SYNTHESIS AND STUDIES OF NEW TITANATES, NIOBATES AND TUNGSTATES WITH LAYERED STRUCTURE

Ph.D. THESIS

by

SONIA RANI

DEPARTMENT OF CHEMISTRY
INDIAN INSTITUTE OF TECHNOLOGY ROORKEE
ROORKEE 247 667, (INDIA)
JUNE, 2019

SYNTHESIS AND STUDIES OF NEW TITANATES, NIOBATES AND TUNGSTATES WITH LAYERED STRUCTURE

A THESIS

Submitted in partial fulfilment of the requirements for the award of the degree

of

DOCTOR OF PHILOSOPHY

in

CHEMISTRY

by

SONIA RANI

DEPARTMENT OF CHEMISTRY
INDIAN INSTITUTE OF TECHNOLOGY ROORKEE
ROORKEE 247 667, (INDIA)
JUNE, 2019

INDIAN INSTITUTE OF TECHNOLOGY ROORKEE
ROORKEE

CANDIDATE'S DECLARATION

I hereby certify that the work which is being presented in the thesis entitled "**SYNTHESIS AND STUDIES OF NEW TITANATES, NIOBATES AND TUNGSTATES WITH LAYERED STRUCTURE**" in partial fulfilment of the requirements for the award of the degree of Doctor of Philosophy and submitted in the Department of Chemistry of the Indian Institute of Technology Roorkee, Roorkee is an authentic record of my own work carried out during a period of July, 2013 to June, 2019 under the supervision of Dr. Tapas Kumar Mandal, Assistant Professor, Department of Chemistry, Indian Institute of Technology Roorkee, Roorkee.

The matter presented in the thesis has not been submitted by me for the award of any other degree of this or any other Institution.

(**SONIA RANI**)

This is to certify that the above statement made by the candidate is correct to the best of my knowledge.

(Tapas Kumar Mandal)
Supervisor

Dated:

CONTENTS

ABSTRACT

Transition metal oxides (TMOs) have constituted an interesting class of inorganic solids that have received considerable attention of solid-state and material chemists for the past several decades. The TMOs with perovskite and related structures have been extensively studied due to their diverse physicochemical properties and applications together with the compositional variations that the flexible perovskite structure can tolerate. Perovskite oxides exhibit a wide range of structural, physical, chemical and electronic properties that are not only of fundamental interest but have useful technological applications. Layered perovskites represent a special class of layered materials that contain ABX_3 perovskite as their basic building block, where A refers to cations in a cubooctahedral cavity of twelve X anions (where X = O, halogen, N, S, and/or H) and B refers to a cation in a BX_6 octahedron. The two most common structural classes of layered oxide perovskites that contain ion-exchangeable cations are Ruddlesden–Popper (R-P) phases, $A_2[A_{n-1}B_nO_{3n+1}]$, and Dion–Jacobson (D-J) phases $A[A_{n-1}B_nO_{3n+1}]$. Aurivillius phases, $Bi_2O_2[A_{n-1}B_nO_{3n+1}]$, represent another class of layered perovskites in which a covalent network of $(Bi_2O_2)^{2+}$ occupies the interlayer galleries. While the three-dimensional perovskites readily form with the 3*d* transition metals of d^n configurations, the layered perovskites are mostly composed of d^0 metal cations of Ti, Nb, Ta, Mo or W. Thus, layered perovskites with complete 3*d* transition metal layers are infrequent especially with the D-J and Aurivillius phases, while a plenty of them exist for the R-P phases.

In the pursuit of interesting physical and chemical properties in the layered perovskites, many researchers have devoted their efforts for the incorporation of transition metals with partially filled *d* orbitals in the layered perovskites, which initially contained only d^0 transition metals in the perovskite layer. While the perovskite structure can support the replacement of *B*-site cations with a large variety of transition (3*d*, 4*d* & 5*d*) and *p*-block elements, the range of such replacements within the perovskite blocks of the layered structure is limited. Moreover, due to the lack of a suitable charge compensating isovalent or aliovalent/heterovalent cation combination, the choice of transition metals are also limited. Moreover, the transition metal incorporation at the perovskite block is possible only in a narrow range of compositions, where the structural integrity can be retained without the formation of any secondary competing phases. It is perceived that the layered perovskite oxides containing mostly d° metals might exhibit

interesting magnetic, ferroelectric and catalytic properties if they are replaced partly with transition metals having unpaired *d*-electrons in their orbital. For example, incorporation of magnetic transition metals in the *B*-site of Aurivillius phases have given rise to interesting photocatalytic and magnetic materials. Exchange of interlayer alkali cations by $3d^n$ transition metals of R-P and D-J oxides have given rise to interesting materials with ferroelectric, ferromagnetic, antiferromagnetic and photocatalytic properties. Furthermore, the R–P and D–J phases have received adequate attention due to their rich interlayer chemistry.

The environmental pollution is a serious problem in today's world, with water contamination being one of the biggest concern worldwide. Removal of harmful matters from wastewater and detoxification of pollutants in surface water, and groundwater are key environmental issues before the humankind. Therefore, removal of pollutants, including organic dyes, from the aqueous medium is essential and techniques, such as; chemical oxidation and adsorption are mostly employed for this purpose. However, the above methods are energy intensive. The emergent technique of photocatalytic degradation can be considered as less energy intense and environment friendly for complete mineralization of dye pollutants into CO_2 and H_2O using semiconductors.

The report of Fujishima and Honda in 1972 on the photo-electrochemical water splitting with TiO_2 (E_g = 3.2 eV) photo-anode under UV-light have triggered intense research activity on semiconductor photocatalysis. But, in most of the cases the photocatalysis reactions were restricted to the UV-radiation. For sustainable photocatalysis, it is important to make use of the visible portion (nearly ~ 46 %) of solar radiation. Toward the development of visible-light-active photocatalysts, several approaches are adopted. A metal or non-metal ion doping in binary or complex oxides, solid-solution formation between a narrow and a wide band gap material etc. have been exploited for the suitable tuning of band gap. Most of the Bi-containing layered perovskites (Aurivillius phases) have exhibited catalytic activity under visible-light irradiation. However, there are only few reports on the visible-light-active photocatalysis involving double-layer Aurivillius phases. Recently, interest in these Aurivillius phase semiconductors has grown due to their superior activity as single-phase oxide photocatalysts. Therefore, we envisaged the study of coupled-substitution of La and transition metals (Cr, Mn, Fe, Co) in the two-layer Aurivillius niobates and Sillén-Aurivillius hybrid titanates and tungstates (both one- and two-layer). The study also reports effects of transition metal incorporation on the structure, band gap,

photocatalytic activity and magnetic properties. The outcome of the investigations are presented in the thesis.

Chapter-2 provides the details of general solid-state synthesis and all the characterization techniques used throughout the course of this investigation along with their experimental procedures. The compounds were synthesized by solid-state reactions employing metal carbonates, oxalates, oxides or oxychlorides as starting materials. The formation of products at every stage of the synthesis were monitored by powder X-ray diffraction (P-XRD) analysis. The morphology and chemical composition of the compounds were characterized by Field Emission-Scanning Electron Microscopy (FE-SEM), Energy Dispersive X-ray Spectroscopy (EDS) and High-Resolution Transmission electron microscopy (HR-TEM) analysis. X-ray photoelectron spectroscopy (XPS) was employed for the determination of the oxidation states of the elements. Further, the optical properties were investigated by UV-vis Diffuse Reflectance Spectroscopy (UV-vis DRS) and the band gap energies were estimated with the help of Tauc plots. The photocatalytic activity of the compounds were tested by following standard procedures using model organic pollutants in aqueous medium and natural sunlight or 250 W medium/high pressure (MP/HP) mercury vapour lamps (MVLs) as radiation source. Scavenger tests were carried out for the detection of reactive species involved in the degradation process. Dye adsorption, zeta potential and photoluminescence (PL) studies were carried out to understand the surface charge effects on adsorption and relative e^-–h^+ recombination effects across a homologous series of catalysts. The experimental details of P-XRD, FE-SEM, EDS, HR-TEM, XPS, Raman, FT-IR, UV-vis DRS, PL, EIS and Zeta potential techniques are discussed in this chapter.

In **Chapter-3**, the solid-state synthesis, characterization and photocatalytic studies of a series of lead-free double-layer Aurivillius niobates, $LaBi_2Nb_{1.5}M_{0.5}O_9$ (M = Cr, Mn, Fe, Co) is reported. The compositions are designed by adopting a heterovalent coupled substitution strategy starting with the parent $SrBi_2Nb_2O_9$. Rietveld structure refinements of the compounds using P-XRD data suggests formation of $3d^n$ transition metal incorporated double-layer Aurivillius niobates. The compounds form in the non-centrosymmetric orthorhombic $A2_1am$ space group and are isostructural with the parent. UV-vis DRS data demonstrates optical absorption in the visible region with absorption edges extending up to ~ 650 nm and with estimated band gaps ranging from 2.25–2.94 eV confirming their sunlight-active nature. While all the compounds show Curie-like paramagnetism in the 5-300 K temperature range and the transition metals in them adopt

high-spin (HS) configurations, the Mn compound stabilizes with a low-spin (LS) configuration, in contrast to others. The stabilization of the LS configuration for the Mn ($3d^4$) compound occurs with an $e_g \rightarrow t_{2g}$ electron redistribution due to the suppression of the first-order Jahn-Teller (FOJT) distortion of MnO_6 octahedra by the dominating second-order Jahn-Teller (SOJT) distortion of the $Nb^{5+}O_6$ ($4d^0$ Nb). The compounds exhibit photocatalytic Rhodamine B (RhB) degradation at pH 2 within 50 –110 minutes under natural sunlight-irradiation and remain stable after five consecutive cycles of photocatalytic degradation maintaining the activity of the catalysts largely intact in the cycles, as exemplified by cycles of photocatalytic degradation studies followed by the post-catalytic P-XRD and XPS analysis of $LaBi_2Nb_{1.5}Cr_{0.5}O_9$. However, the RhB degradation time reduces to 15-30 min when irradiated with a 250 W MP-MVL. It is believed that the heterovalent coupled-substitution strategy adopted herewith will open up possibilities for transforming many other UV-active layered niobates into sunlight-active compounds without using toxic Pb or expensive Ag, while the paramagnetic nature of the compounds will be helpful in post-catalytic magnetic separation of the catalysts.

Chapter-4 deals with the synthesis and characterization of new double-layered Aurivillius perovskite titanates and their photocatalytic activity toward dye degradation. The compounds, $Bi_{3-x}La_xTi_{1.5}W_{0.5}O_9$ (x = 0, 1) and $Bi_{3-x}La_xTiW_{0.67}Fe_{0.33}O_9$ (x = 0, 1), are prepared by conventional solid-state reactions. The composition of the Fe-substituted two-layered Aurivillius titanate, $Bi_{3-x}La_xTiW_{0.67}Fe_{0.33}O_9$ (x = 0, 1), is designed by a coupled substitution strategy involving Fe, Ti and W in $Bi_{3-x}La_xTi_{1.5}W_{0.5}O_9$ (x = 0, 1). The Fe-substitution resulted in a decreased band gap of the compounds (E_g ~ 2.63 & 2.72 eV) from that of the parent, $Bi_3Ti_{1.5}W_{0.5}O_9$ (~3.0 eV). Fe-substitution appeared to help in the suppression of photogenerated e^-–h^+ recombination as evidenced by the PL spectra. While $Bi_{3-x}La_xTi_{1.5}W_{0.5}O_9$ (x = 0, 1) show negligible to little RhB degradation in the acidic aqueous medium under sunlight irradiation, $Bi_{3-x}La_xTiW_{0.67}Fe_{0.33}O_9$ (x = 0, 1) show complete RhB degradation under similar conditions. It appears that poor sunlight absorption and high e^-–h^+ recombination in $Bi_{3-x}La_xTi_{1.5}W_{0.5}O_9$ (x = 0, 1) lead to little or negligible photocatalysis. Moreover, La-substituted compound showed inferior activity as compared to its Bi-analog in contrary to the results observed in other layered Aurivillius titanates where La-substitution resulted in the enhanced photocatalytic activity. This is attributed to the higher zeta potential and consequent adsorption in the Bi-analog as compared to the La-analog of the double-layer titanate. The catalysts are reusable and remain stable after

five photocatalytic cycles of RhB degradation without showing any noticeable loss of activity. The paramagnetic nature of the compounds may be helpful in the post catalytic magnetic separation of the compounds from the solution phase.

In **Chapter-5**, the details of solid-state synthesis, characterization and photocatalytic activity studies of Sillén−Aurivillius phases, $LaBi_3W_{0.67}M_{0.33}O_8Cl$ (M = Mn, Fe) are reported. The La-substituted Sillén−Aurivillius phases, $LaBi_3W_{0.67}M_{0.33}O_8Cl$ (M = Mn, Fe), are synthesized for the first time by solid-state reactions. The P-XRD data indicate that the compounds, $LaBi_3W_{0.67}M_{0.33}O_8Cl$ (M = Mn, Fe), crystallize in the *Cm2m* space group as adopted by the parent $Bi_4W_{0.67}Mn_{0.33}O_8Cl$. The refined lattice parameters of the compounds indicate slight contraction in the *c*-parameter, while the in plane *a* and *b* parameters remained nearly the same on La substitution. Both the compounds exhibit paramagnetic behaviour between 5 and 300 K indicating absence of any magnetic phase transitions in the temperature interval. The UV-vis DRS data established the compounds as visible-light-active semiconductors with the band gap ranging from 2.11-2.41 eV. The photocatalytic activity of the new Sillén−Aurivillius phases is investigated by way of degradation of organic pollutants (RhB and MO) under sunlight irradiation. The compounds show collective degradation of RhB and MO in addition to the photodegradation of individual RhB and MO in the acidic aqueous medium (pH 2). Moreover, the compounds are reusable and stable in the acidic medium even after five consecutive cycles of degradation without any noticeable loss in the activity as evidenced by the cycle tests and post catalytic P-XRD and XPS analyses. Scavenger tests indicate h^+ and $^{\bullet}OH$ radicals as active species that take part in the photocatalytic degradation of RhB and MO.

Chapter-6 deals with the intercalative removal of a pollutant dye, Congo Red, using a three-layer Dion-Jacobson (D-J) perovskite, $KCa_2Nb_3O_{10}$. During the course of this investigation involving transition metal incorporated Dion-Jacobson perovskite compositions derived from $KCa_2Nb_3O_{10}$, it is realized that doping of nearly 16 % of transition metals at the Nb-site do not result in the formation of phase pure D-J compounds. However, during photocatalytic experiments with the parent $KCa_2Nb_3O_{10}$, excellent Congo Red (CR) removal efficiency in the acidic aqueous medium is observed. Detail investigation of the removal process of CR employing $KCa_2Nb_3O_{10}$ have revealed intercalation of CR in the interlayer space of the layered perovskite with concomitant expansion of the lattice along the *c*-axis. Moreover, the process is partly reversible as demonstrated by the de-intercalative release of the CR dye in the alkaline aqueous

medium. Analysis of $KCa_2Nb_3O_{10}$ before and after CR removal by P-XRD, FTIR, EDS, and Raman studies support the intercalative removal and de-intercalative release of the dye. EDS data also indicate ~35-40% proton exchange in the parent $KCa_2Nb_3O_{10}$ during the dye removal process. Accordingly, an acid-base complexation between the protons of the in-situ formed proton-exchanged layered perovskite and the amine group of the CR is attributed for the intercalative removal of the dye from the aqueous medium. In the basic medium, a strong complexation of the proton with the basic OH^- frees the amine groups of the dye, which leads to the release of the CR molecules from the interlayer space of the layered perovskite. The above mechanism of CR removal is in line with earlier reports of Methylene Blue intercalation on protonated-layered perovskites and our study with the protonated forms of the Dion-Jacobson perovskite.

The overall conclusions and future prospects of the current research is presented in **Chapter-7**. The idea of coupled-substitution may be extended in many series of layered perovskites to generate a large number of semiconducting compounds with tenable band gap and interesting photocatalytic and magnetic properties. The substitution of 4*d* and 5*d* transition metals can also be carried out in the layered titanates, niobates and tungstates with appropriate valence adjustments as the 4*d* and 5*d* elements are generally not stable at lower oxidation states that are easily adopted by 3*d* transition metals. Since the present work demonstrated efficient photocatalytic dye degradations and the reported compounds contain various transition metals, alkali/alkaline earth metals and bismuth/lanthanum, they may well be investigated for other environmental pollutant degradations and photocatalytic reactions, such as, water splitting, CO_2 reduction and organic conversions. Thus, the present work hold considerable potential and provide insight for the development of sunlight active semiconductors with enhanced activity.

Acknowledgements

First of all, I sincerely express my heartfelt gratitude to my Ph.D. supervisor Dr. Tapas Kumar Mandal for his invaluable guidance, motivation and encouragement during the entire Ph.D. research. At many stages of the research work, his positive outlook and confidence on my research inspired me and gave confidence to overcome the obstacles. Without his timely help, intellectual input, constructive criticism, careful editing and painstaking efforts, it would not have been possible for me to complete this thesis in the present form. It has been a great pleasure for me to work under his supervision.

I am highly obliged and express my sincere thanks to present Head of the Department Prof. K. R. Justin Thomas as well as former Head of the Department Prof. M. R. Maurya and all other faculty members for their kindness and help. I am grateful to the members of my SRC, Prof. U. P. Singh (Chairman), Dr. P. Jeevanandam (Internal member), Department of Chemistry and Dr. P. Biswas (External member), Department of Chemical Engineering, IIT Roorkee for their valuable suggestions and encouragement to carry out this work.

I am extremely grateful to Head, Institute Instrumentation Centre (IIC) for providing all the necessary instrumental facilities. I greatly appreciate Mr. Shiv Kumar for his help during the FE-SEM measurements. I am also thankful to Mr. Shiv Kumar and Devender Sharma in-charge of XRD and also thankful to in-charge of TEM. I wish to place my sincere thanks to technical and administrate staff of the Department of chemistry. Thank you to Pankaj Kumar and Ankur Sharma who have helped me during the course of my Ph.D. I express my sincere thanks to Mr. Madan Pal, Department of Chemistry, who helped me a lot for the technical arrangements during my presentations in the department.

I would like to thank my seniors and lab mates for creating an interacting and enthusiastic research atmosphere. I wish to thank Dr. Naresh for his valuable discussion and help for work in early days. Thank to Dr. Nishant Gautam, Vandana Meena, Lalit Gangwar, Vijay Alwera, Jaideep Malik, Anil, Shubham, Prachi, Preeti and Megha for their co-operation and support in the Ph.D. duration. I would also like to thank to other members Rita, Anowar, Ambikeshwar, Avnish, Poonam, Sagar and Priyanka.

I also convey my sincere thanks to my mentors some of them are Dr. Ajay Dhiman, Dr. Ruby Phul, Dr. Arun Choudhary, Dr. Tanveer Alam for their true guidance and encouragement to achieve my goals.

Deep in my heart, I appreciate the help of my friends Usha, Pooja, Priyanka, Seema, Pinky, Uttara and Pankaj and some names which I might miss, whose support and criticism help me. All may not be mentioned, but none is forgotten. The memories of this adventurous ordeal will always stay alive and be a source of inspiration for me and my family.

A special thanks to my family. No words can suffice my feelings of gratitude towards my parents for their unconditional love and motivation which remained driving force during the entire period of my study. They helped me a lot reach this stage of life. I want to thank to my elder brother Arun Kumar Karanwal and his wife Shivani Bharti, my younger brother Vipin Karanwal for their encouragement and support.

I can never forget to thanks my husband Mr. Hari Raj, who has always loved me unconditionally and his good examples have taught me to work hard for the things that I aspire to achieve. His determination to his goal encouraged me to look forward beyond any limit. He has lot of contribution in my thesis completion from data analysis to thesis writing. At the end, I would say that he is not only my husband but a good friend too, who always gives constructive criticism on mistakes and motivates me to learn from them.

(Sonia Rani)

List of Figures

List of Tables

List of Publications

1. **Sonia Rani**, Gollapally Naresh and Tapas Kumar Mandal, "Rendering Double-Layer Aurivillius Niobates as Sunlight-Driven Magnetic Photocatalysts" under revision.

2. **Sonia Rani** and Tapas Kumar Mandal, "Iron Incorporated Double Layered Titanates and its La- substituted Analogs: Magnetism and Solar Photocatalysis" (manuscript under preparation).

3. **Sonia Rani** and Tapas Kumar Mandal, "Transition Metal Incorporated New Sillén-Aurivillius A1X1 Layered Tungstates: Magnetism and Solar Photocatalysis" (manuscript under preparation).

4. **Sonia Rani** and Tapas Kumar Mandal, "Housing Pollutants in the Middle of Layered Perovskites" (manuscript under preparation).

List of Conference Proceedings

1. **Sonia Rani** and Tapas Kumar Mandal, Transition Metal Incorporated Two Layer Aurivillius Niobates: Magnetism and Solar Photocatalysis, Solid State Chemistry and Allied Areas (ISCAS-2017), Delhi Technological University, Delhi, India, July 1-3, 2017.

2. **Sonia Rani** and Tapas Kumar Mandal, Transition Metal Incorporated New Sillén-Aurivillius A1X1 Layered Tungstates: Magnetism and Solar Photocatalysis, Shaping the energy Future: Challenges and Opportunities (SEFCO-2018), Indian institute of Petroleum, Dehradun, India, May 11-12, 2018.

Table of Contents

CHAPTER 1. Introduction

This thesis is dedicated to my parents and family.

CHAPTER -1

Introduction

1.1 Introduction

Perovskite and perovskite related structures exhibiting a range of structural, physical, chemical and electronic properties have attracted considerable attention almost over the past few decades from now.[1,2] Layered oxides can be formed with different compositions which results in transformation of their structural and physical properties such as magnetic,[3-5]colossal magnetoresisitance,[6-7] ferroelectric,[8-10] dielectric,[11-15] photocatalytic activity,[16-22] ion exchange[23-26] and superconductivity[27.] This chapter overviews the work presented in the thesis.

1.2 Perovskite

In 1839, German scientist Gustav Rose discovered a mineral in the Ural Mountains in the form of $CaTiO_3$ and is named after Russian mineralogist Aleksevich Lev Perovski. The term 'Perovskite' was used to describe a class of compounds having the same general stoichiometric and connectivity with ($CaTiO_3$). In 1926 at the University of Oslo, $CaTiO_3$ was reported on the first synthesized perovskite by Goldschmidt.[28]

The ideal perovskite Composition has the general formula, ABX_3 with stoichiometry of 1:1:3, where "A" represents heavy metal cation, "B" represents a transition metal cation and "X" represents an anion. In $CaTiO_3$, A is a divalent metal and B is a tetravalent metal. However, the A and B cation have a variety of charges. A large number of perovskite compositions are possible by various combination of cations lattice site. In general, A is an alkali metal/alkaline earth metal or a rare-earth metal element, whereas B is usually a transition metal element or a probable element and X is an anion, such as F^-, Cl^-, Br^-, I^-, S^- and even H^-, etc. but usually O^{2-}.

Fig 1.1 shows ideal perovskite structure. It consists of a network of BO_6 octahedra (B in a 6 fold oxygen coordination) linked through each corner to their neighbors and the A cation occupying the central cubooctahedral void (surrounded by the 12 oxygens) created by the BO_6 corner connected network.[28]

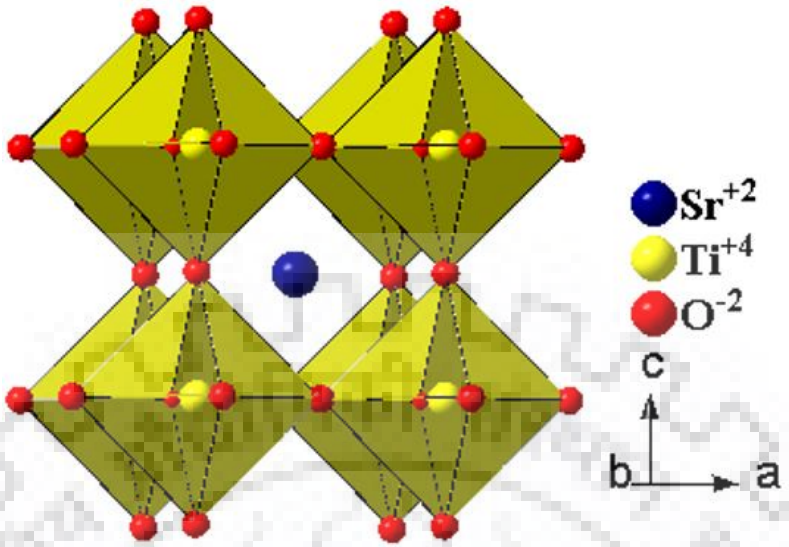

Figure 1.1 Ideal Perovskite Structure

In 1945, the perovskite structure was established by the Irish crystallographer Helen Dick Mcgaw coworkers. They studied the structure of $BaTiO_3$ and determined the unit cell parameters and symmetry.[29,30] Based on the known compounds of perovskite, Mcgaw and her colleagues pointed out that the ionic size difference between A and B atoms may lead to distorted structures.[31] For the explanation and stability of perovskite structures, Goldschmidt had introduced a factor known as "Goldschmidt tolerance factor", t and is given by the expression,[32]

$$t = \frac{r_A + r_O}{\sqrt{2}(r_B + r_O)}$$

where, r_A, r_B, and r_o are the ionic radii of A, B and O, respectively. If t values are in between 0.8 to 1.0, perovskite structure gets stabilized. For t = 1, an ideal perovskite structure forms with no distortions. However, the structure distorts from an ideal perovskite when the value of t deviates from 1.0. Figure 1.1 shows an ideal perovskite structure of $SrTiO_3$.

1.3 Layered Perovskite

Layered perovskite structures are intergrowths of perovskite and other structures. Layered perovskites have infinite two-dimensional slabs of ABX_3 type structure in which slabs are separated by cations or cationic structural units. The thickness of layered perovskite is determined by the number of octahedra (*n*) between the two adjacent sheets of different structures. Therefore we have mono-layered, double-layered, triple-layered etc. perovskite-like oxides which are differentiated by the value of n =1, 2…∞ member corresponds to the typical perovskite structure.

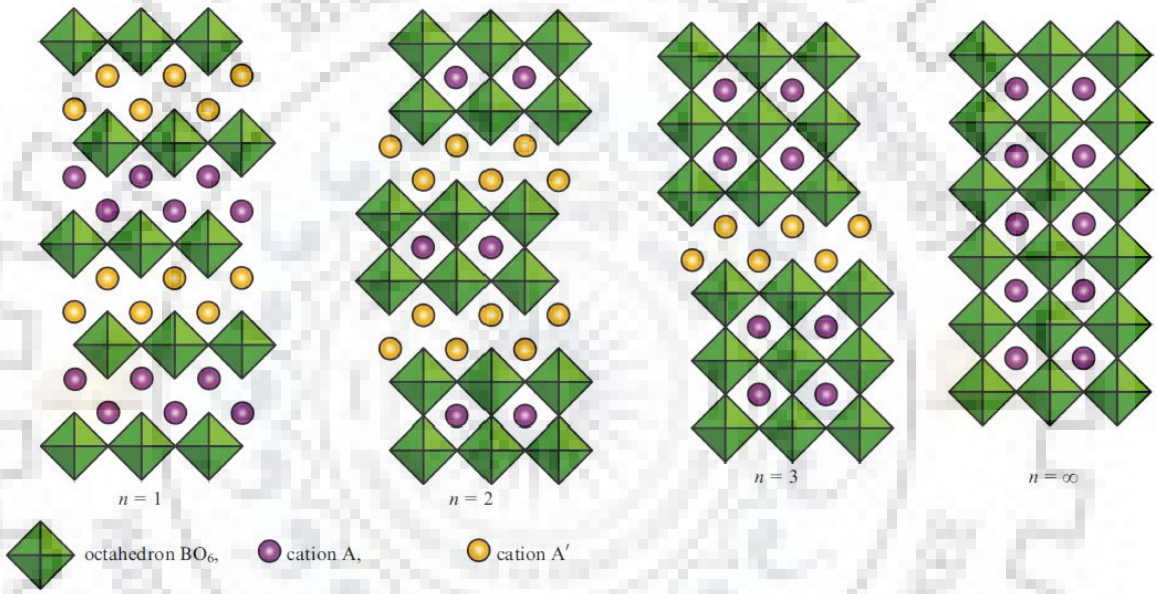

Figure 1.2 Layered perovskite oxides with various perovskite sheet thicknesses (n =1, 2, 3….∞).[33]

The two differentiating characteristics for the layered perovskites are 1) the motif separating the layers, and 2) the offsetting of the layers from each other. Generally, there are three types of layered perovskite structure (Figure 1.3) and usually named after their discoverers.

The general formulas of these phases are as follows:

(i) The Aurivillius phase $(A'_2X_2)(A_{n-1}B_nX_{3n+1})$

(ii) The Dion–Jacobson phase $A'(A_{n-1}B_nX_{3n+1})$

(iii) The Ruddlesden–Popper phase $(A'X)(ABX_3)_n$

where *n* indicates the number of the 2D slabs, e.g. for *n* = 1, the slab is one BX_6 octahedron thick. *n* = 2 means two BX_6 octahedral thick, etc.

1.3.1 Aurivillius Phases

Aurivillius phase constitute a class of layered oxides that are based upon the intergrowth of unit layered bismuth oxide/perovskite layer first described by Aurivillius in 1949.[34] The Aurivillius phases are generally formulated by $[Bi_2O_2]^{2+}[A_{n-1}B_nO_{3n+1}]^{2-}$, where 'n' indicates the thickness of perovskite slabs with a covalent network of $[Bi_2O_2]^{2+}$in between the two dimensional perovskite slabs, where A site is occupied by twelve coordinated cation, e.g. Na, K, Ca, Ba, Pb, Bi, etc., the B site cations mostly occupied by d^0 cation, e.g. Ti, Nb, Ta, W, Mo and sometime substituted with Fe, Ga, Cr etc.[35]

Several mixed Aurivillius phases are reported, having different numbers of perovskite layers in the adjacent blocks alternating in the structure.[25,26] The general formula of such compounds is $[Bi_2O_2]^{2+}[A_{k-1}B_kO_{3k+1}]^{2-}[Bi_2O_2]^{2+}[A'_{m-1}B'_mO_{3m+1}]^{2-}$, where k and m is number of perovskite blocks in adjacent layers and $n = (k+m)/2$.

The substitution of anion by halogens layer have been observed in limited extents. The Aurivillius phases (*n* = 1~8) contain distinct Bi_2O_2, and replacement of Bi by Pb, Tl, Sb and Sn in the separating motif has been reported.[27]

1.3.2 Dion–Jacobson Phase

Dion-Jacobson phases were first reported by Dion, and afterword tremendously studied under the guidance of Jacobson.[29,40.] The general formula of the Dion-Jacobson phases are $A'(A_{n-1}B_nX_{3n+1})$, where A' represents an alkali metal which occupy the interlayer space, the perovskite, A site is typically occupied by alkaline or rare earth metals and B site occupied with a pentavalent transition metal by and large, Niobium or tantalum. $A_{n-1}B_nX_{3n+1}$ represents the common unit of 2D perovskite blocks; where 'n' denotes number of the stacked perovskite unit layer. In this type of structure, the large monovalent A'-cations exist in between the perovskite blocks at the eight-coordinated pseudo-cubic coordination sites. Compounds with '*n*' values of 2-6 have been synthesized.[41] This type compounds have been extensively studied because of their fascinating ionic, intercalation, ion-exchange and luminescence properties.

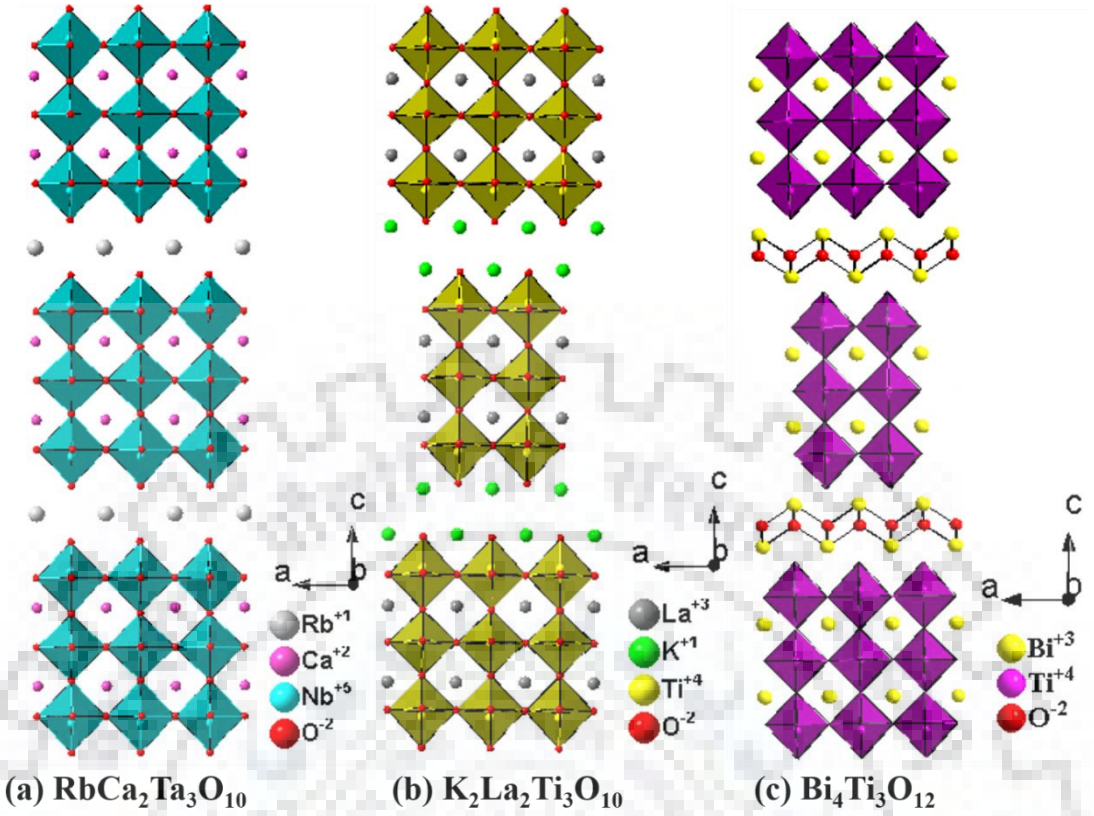

Figure 1.3 Structures of layered perovskite (a) Dion–Jacobson, (b) Ruddlesden–Popper and (c) Aurivillius phases.

1.3.3 Ruddlesden Popper Phase

In 1958, Ruddlesden and Popper studied the structure of $Sr_3Ti_2O_7$ (n = 2)[42] and $Sr_4Ti_3O_{10}$ (n = 3)[43], whereas, the n = 1 member of this series (K_2NiF_4)[44] has reported in 1957.The general formula of the Ruddlesden- Popper (RP) phases can be represented as $A'_2(A_{n-1}B_nO_{3n+1})$, where n represents the thickness of the perovskite block, and the separating motif are two layer of A' cation, where the perovskite slabs $(A_{n-1}B_nO_{3n+1})_n$ are offset with a (1/2, 1/2) displacement along the *a* and *b* axis. In RP phase, the A site is usually occupied with alkaline earth metal or lanthanides while the B site contains 3*d* and 4*d* transition metals of both d^n and d^0 configuration. Figure 1.2 illustrates the crystal structure of RP (n = 1, 2, 3, respectively) phases in comparison with the ideal cubic perovskite, which can be regarded as the $n = \infty$ RP phase. Figure 1.3 displays and compare the three layered perovskites taking the triple-layers (n = 3) perovskite as an example.

1.4 Sillén-Aurivillius phase

In 1986, Ackerman first investigated the structure and synthesis of a new family of Sillén-Aurivillius phases (Bi_3PbWO_8Cl and Bi_4NbO_8Cl).[45] As we know, an Aurivillius phase consist of fluorite-like $[Bi_2O_2]^{2+}$ blocks alternating with perovskite-like $[A_{n-1}B_nO_{3n+1}]^{2-}$ blocks, where 'n' shows the thickness of the octahedral block and in the Sillén phases, $[Bi_2O_2]^{2+}$ or $[BiPbO_2]^{+}$ blocks are inserted between halogen [X] layers. The general formula of a Sillén phases is $[M_2O_2]X_m$, where *m* can be 1 or 2, M site can be occupied by Bi^{3+}, Pb^{2+}, Sr^{2+}, etc., and X represents a halide.[46] Ackerman interconnected these two structurally similar families in a regular manner to produce the new intergrowth family of Sillén-Aurivillius phases and nicknamed these intergrowth phases as "Bipox" phases (bismuth-perovskite-oxyhalide). The Sillén-Aurivillius intergrowth phases have the general formula $[M_2O_2][A_{n-1}B_nO_{3n+1}][M_2O_2][X_m]$. The nomenclature A_nX_m is used for these phases to express the number of perovskite octahedral $[A_n]$ layers and halide $[X_m]$ layers.

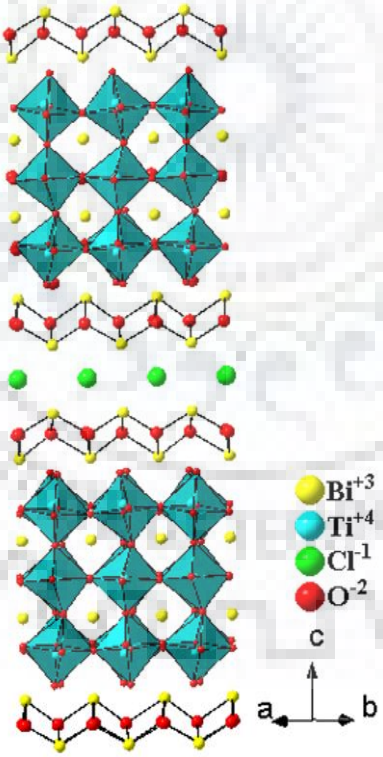

Figure 1.4 Structure of a Sillén-Aurivillius intergrowth phase, $Bi_5PbTi_3O_{14}Cl$.[47]

1.4 Importance of Layered Perovskites

Perovskites and perovskite-like materials exhibit interesting physical and chemical properties and have wide range of applications. These types of material are flexible with different compositions, results in different structures and modified properties. From the early days, transition-metal oxides constituted an interesting class of inorganic solids that have attracted considerable attention of solid-state/materials chemists. Many researchers have investigated the incorporation of transitions metals in the layered perovskites due to their variable interesting properties.[48,49] While the perovskite family can support the replacement of elements with a large number of foreign elements at cation sites as well as anion sites. The range of such replacements within the perovskite blocks of layered perovskites is limited, for the reason that, maintaining of the charge balance is difficult.[33] Moreover, due to the lack of a suitable charge compensating isovalent or aliovalent/heterovalent cation combination, the choice of transition metals are also limited. Moreover, the transition metal incorporation at the perovskite block is possible only in a narrow range of compositions, where the structural integrity can be retained without the formation of any secondary competing phases. It is perceived that the layered perovskite oxides containing mostly *d*° metals might exhibit interesting magnetic, ferroelectric and catalytic properties. An extensive range of compounds in perovskites group include, niobates titanates, and tantalates (d^0) and $3d^n$ transition metals showing numerous unique features. Layered perovskite materials might be exhibits the magnetic, multiferroic, catalytic properties if they have transition metal with unpaired electrons in *d*-orbital.[50-55] For example, incorporation of magnetic transition metal at the B-site of Aurivillius phase have been reported to increase to interesting photocatalytic and magnetic materials. Recently, a number of Aurivillius materials show magnetic properties which contain magnetic transition metal at B site.[56] In RP and DJ phase oxides derived from the $3d^n$ transition metal, which are interesting material for applications in ferroelectric, antiferromagnetic, and high temperature superconductor.[49,57-60]

1.4.1 Ion Exchange Reaction

An obvious strategy for reducing reaction times and lowering reaction temperatures is to prepare more homogeneous mixtures of reagents than the conventional solid state method.

Soft chemistry allows for the manipulation of new compounds at low temperatures (< 500ºC). Topochemical strategies is a part of soft chemistry, that allow to formation of new layered compounds while maintaining the structural feature of the parent compound. Ion exchange, layer extraction, intercalation/deintercalation, grafting, exfoliation, pillaring, layer construction, and substitution reactions are few methods which can used for this purpose.[33,49,61,]

Ion exchange reaction is one of the most fashionable soft chemistry route. Many layered perovskites such as RP phase and DJ phase undergo interlayer ion exchange reactions (Figure 1.5) with retention of structural features of host the structure. DJ phases are similar to RP phases, where the interlayer cation density is half of that in the RP phase. The ion exchange reactions are carried out in solution or in melts of suitable salts of a layered perovskite. Replacement of alkali metal cations from the interlayer space of a layered perovskite with a monovalent cation,[62-65] divalent cation[66] or a complex cationic species[67-70] are known to moderate the properties. Gopalakrishnan *et al.* reported a new series of layered perovskite $A_2Ln_2Ti_3O_{10}$ and their exchange with protons and investigated the Bronsted acidity and intercalation chemistry of $H_2Ln_2Ti_3O_{10}$.[63] Byeon et *al.* reported, the synthesis of $M^{II}_{0.5}LaTiO_4$ and $M^{II}La_2Ti_3O_{10}$ (M= transition metal) via the reaction of metal chlorides with to parent in molten salt media and showed the resulting different colors depending on the metal layer. Ion exchange of transition metal atom occupied half of the tetrahedral sites between the perovskite blocks.[66,71]

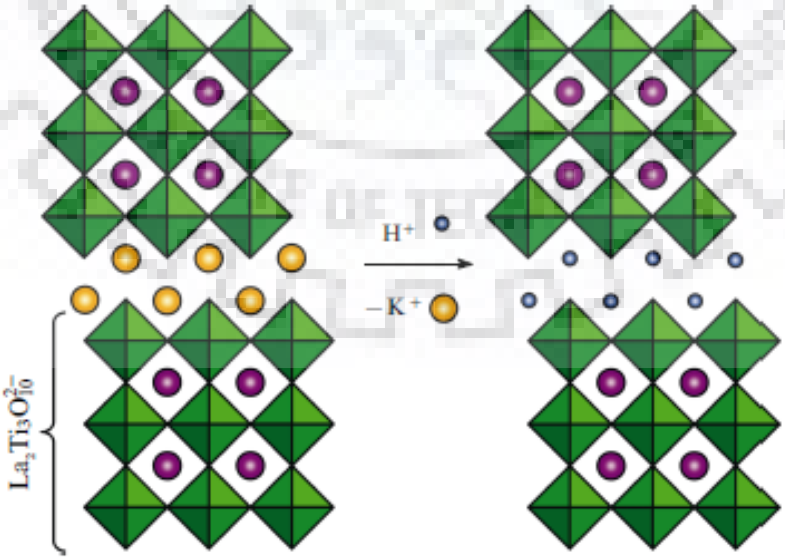

Figure 1.5 Ion exchange reaction in Ruddlesden Popper Phase, $K_2La_2Ti_3O_{10}$.[33]

Wiley's group reported the synthesis of $M_{0.5}LaNb_2O_7$ (M=Fe, Ni, Cu) by ion exchange between $RbLaNb_2O_7$ and MBr_2 (M= Fe, Ni) or $CuCl_2$ at low temperatures. These compounds reaction were structurally similar to the parent compound and all the compounds exhibit paramagnetism.[72] Later, they reported a ion exchange reaction in the triple layered RP series and obtain $Li_{0.3}Ni_{0.85}La_2Ti_3O_{10}$ in an aqueous solution that the compound exhibits ferromagnetism.[57] A silver exchange in $RbLaNb_2O_7$, $RbA_2Nb_3O_{10}$ and $Rb_2La_2Ti_3O_{10}$ with $AgNO_3$ flux at 250º C and all exchanged compounds show photocatalytic activity.[73]Wiley and co-worker investigated the topochemical exchange in layered niobate perovskite and studied their thermal stability. They performed monovalent and divalent cation exchange in a series of double layered niobate $ALaNb_2O_7$ (A= H, Li, Na, K, NH_4 and Ag)[75] by heating them in molten alkali nitrates and further extended this to $ANdNb_2O_7$ and $RbCa_2Nb_3O_{10}$.[59,76]

1.4.2 Intercalation

Intercalation is processes of topochemical synthetic approach that is a reversible process of incorporation of a new species (such as cationic, anionic, organic, polymer etc.) into the interlayer space of layered materials including perovskites (Figure 1.6). There was no change in the structure of layered perovskite after intercalation, only rectilinear dimensions of a crystal increases in the direction usually to the plane of layers.[33,77,78] The reaction mechanisms are based on ion exchange, hydrogen bonding, ion–dipole interactions, acid–base reactions and redox reactions. In the layered-perovskites the intercalation of n-alkylamines in the interlayer spaces in primarily driven by acid base mechanism. Often this method is useful for the synthesis of metastable compounds which cannot be synthesized by conventional solid state synthesis.[33,48,49,79-81]

A variety of guest species such as, alkali metal,[82] metal hydroxide,[83] chalcogenides,[84] organic compounds,[85] and nanoparticles[86] have been successfully intercalated into layered perovskites. Prof. J. B. Wiley at the university of Orleans, USA have reported, a series of mixed valence RP phase $(Li_xVO)La_2Ti_3O_{10}$, that prepared by reductive intercalation reaction.[87] Later, some other compositions were synthesized that include the three step method, in this the initial intercalation/exchange reaction followed by reductive intercalation and oxidative deintercalation, which can lead to the formation of $(Li_2Cl)LaNb_2O_7$,[88] and $(A_2Cl)LaNb_2O_7$ (A = Rb, Cs).[89] This method has also been used in the oxidative intercalation

of chalcogenides, such as H_2S and H_2Se into $RbLaNb_2O_7$[84] and metal hydroxides into layered perovskite resulting $(K_2OH)LaNb_2O_7$, $(Rb_2OH)LaNb_2O_7$, and $(Rb_2OH)Ca_2Nb_3O_{10}$.[83] The intercalation of organic molecules such as alkyl chains, alcohols, amines, and carboxylic acids into the layered oxides or layered perovskites produce inorganic-organic hybrid structures.[33,49,90-93] These resulting hybrids offer interesting magnetic, optical, electrical, and catalytic properties.

1.4.3 Exfoliation of Layered Perovskite

Exfoliation of layered materials has recently become a popular method for the preparation of nano-sized materials. The exfoliation of layered perovskites can give rise to the formation of 2D perovskite nanosheets without compromising the structural integrity of the perovskite layer. For the intercalation, the specific molecule intercalate into the perovskite hosts, surfeit of solvent molecule, for example water, are attracted into the interlayer, such that the layers are completely solvated and separate layer into solution. An example of the exfoliation shown in Figure 1.6. These nanosheets can be utilized as high surface area, materials deposited as thin films, catalytic materials, and high temperature capacitorsetc.[94,95]

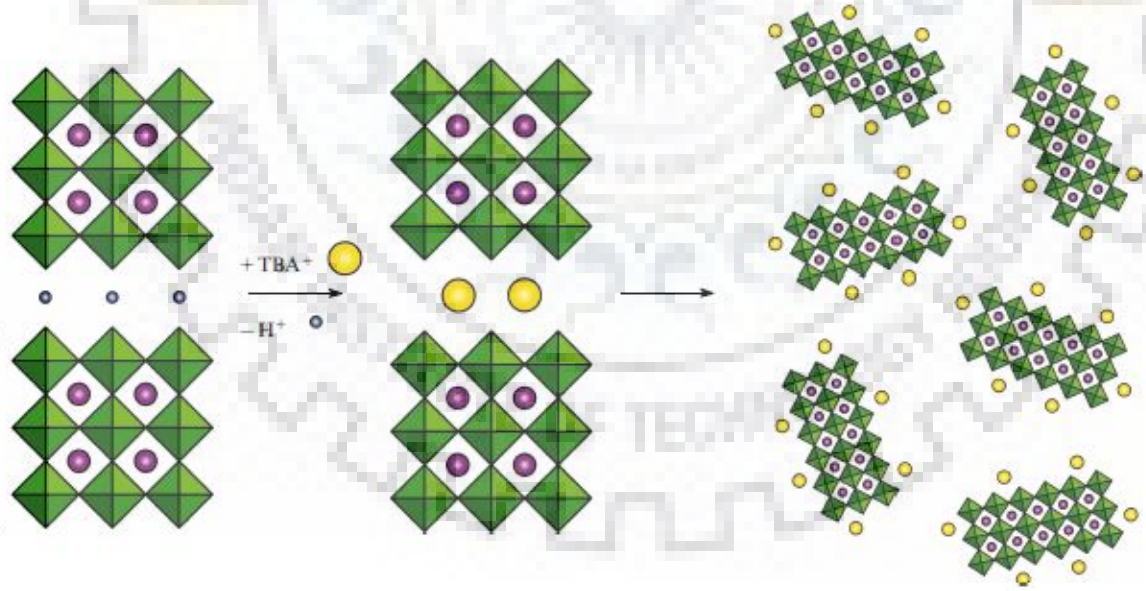

Figure 1.6 Exfoliation of a layered perovskite followed by intercalation of tetrabutyl-ammonium hydroxide by $HCa_2Ta_2O_{10}$.[33]

Treacy and co-workers have initially reported the exfoliation of layered perovskite, by intercalation amines into $KCa_2Nb_3O_{10}$ and observed the formation of single layer nanosheets by electron microscopy.[96] Keller et al. have demonstrated that layered metal oxides can be acid exchanged and exfoliating by TBA^+OH^- (tetrabutyl-ammonium hydroxide).[97] TBA^+OH^- is widely used as exfoliating agent for the protonated layered perovskite.[98-100] However, recently other exfoliated agents have also been reported such as TBP^+OH^- (tetrabutylphosphonium hydroxide) that was more effective for the complete exfoliation of the layered protonic titanate.[101] TEOA, is also used as a exfoliating agent for the preparation of ultra-thin monolayer of $HNbWO_6$ nanosheets.[102]

1.4.4. Transformation of Structure

Solid state metathesis is another convenient method for the structural transformation and interconversion among families of oxide are layered perovskites. The metathesis reaction are generally carried out at relatively lower temperature and for shorter duration in compare to conventional solid state reaction.[33,49,104] An example of the solid state metathesis involving oxides is the transformation of the Ruddlesden-Popper phase, $K_2La_2Ti_3O_{10}$ into the Aurivillius and Dion Jacobson layered perovskite oxides namely, $(Bi_2O_2)La_2Ti_3O_{10}$, $MLa_2Ti_3O_{10}$ (M= Pb, Ba, Sr) and $(VO)La_2Ti_3O_{10}$.These reactions are unique in that they show interlayer cation replacement in the RP phases(in this case K^+) by cationic structural entities such as, $(Bi_2O_2)^+$ and $(VO)^{2+}$ and $(PbBiO_2)^+$.[103] Later, the transformation of the (D-J) phases, $KLaNb_2O_7$ and $RbBiNb_2O_7$ to the corresponding Aurivillius phase, $(PbBiO_2)LaNb_2O_7$ and $(PbBiO_2)BiNb_2O_7$ have been reported by a metathesis reaction with the Sillén phase ($PbBiO_2Cl$).[104]

1.5 Water Pollution and its Decontamination

The Life on the planet is highly dependent on clean water. Water covers the 70% of Earth's surface which contains less portion of fresh water. Only 1% of whole fresh water is accessible by human being. The environmental issues are at high alert in many countries, and water contamination is one of the most emerging on serious problems. Reason of water pollution are various, but the major causes considered to be as agricultural wastes, improper management of industrial effluents, like kind, plastic, textile, coating, printing, cosmetics, paper and rubber etc.[106-109] This affects the human kind as well as the aquatic life. The exponential growth of global population, increasing industrialization and agricultural

activities have increase demand of freshwater. The wastewater released from the household, generated by industries, and agricultural activities contain huge amount of pollutants. According to the World Health Organization (W.H.O) report, around 884 million people still depend upon unimproved water sources – 84% of whom are living in rural areas. By 2025, almost half of the world's population will be part of water-scare areas. In many countries unsafe water is used for drinking, due to which a large part of world population are experiencing the agony of waterborne diseases like as typhoid, hepatitis, and cholera.[110]

Organic pollutants (dyes, phenols, halogenated phenols, BPA, p-Nitrophenol etc.) are the major classes of the water pollutants. Additionally, approx. 7×10^5 tons of organic dyes are being produced annually for use in various industries such as textile, industrial painting, leather goods, cosmetics, plastics and consumer electronics. Around 15% of the non-degradable dyes are produced by industrial wastes during textile finishing and application process. Thus, the removal of harmful matters, from the wastewater including a vast majority of synthetic dyes that subsequently contaminate the surface and ground water is a essential. There are various chemical, physical and biological techniques such as membrane filtration, flocculation, absorption and chemical oxidation which can be used for the removal but they are energy intense.[105,111-115]

The emergent technique of photocatalytic degradation can be considered as lee energy intense and environment friendly, for complete mineralization of the dye pollutants into CO_2 and H_2O. Photocatalysts have gained enormous interest in recent times for their potential application in renewable energy and environmental remediation. As a renewable energy source, sunlight is the effective and attractive energy supplier for the activation of photocatalyst. This method uses a semiconductor and combination of light as photocatalyst to degrade toxic organic pollutants, viruses, bacteria, fungi and algae. In the process these species are degraded through several steps to CO_2, H_2O and inorganic anions. Conversion of solar energy into the clean hydrogen energy by the degradation of organic/inorganic pollutant and water spitting reaction through solar photocatalysis are an emergent research domains. The method is an environmentally friendly technique that can completely degrade the organic pollutants instead of transforming them one to other, as in the case of adsorbent, the photocatalysts are generally inexpensive, chemically stable, non-toxic, non-soluble, photoactive and photostable.[116-122]

1.6 General Principle of Photocatalysis

Photocatalyst is a method that can be used for numerous purposes, like degradation of various organic pollutants from wastewater, hydrogen production, air purification and antibacterial activity. The photocatalyst can defined as, a semiconductor material that absorbs light which is equal or more than ($\lambda \geq E_g$) its band gap (E_g) energy, band gap or energy gap (E_g) is that separate the valence band (VB) and conduction band (CB). In initial step, semiconductor absorbs the sufficient energy of light, which generates electron-hole (e^- and h^+) pairs in the semiconductor. The electrons of the valance band are excited and jumps from valance band to the conduction band, thus creating the holes in the valance band. The photogenerated, electron-hole in the semiconductor can follow several route (Figure 1.7).[121]

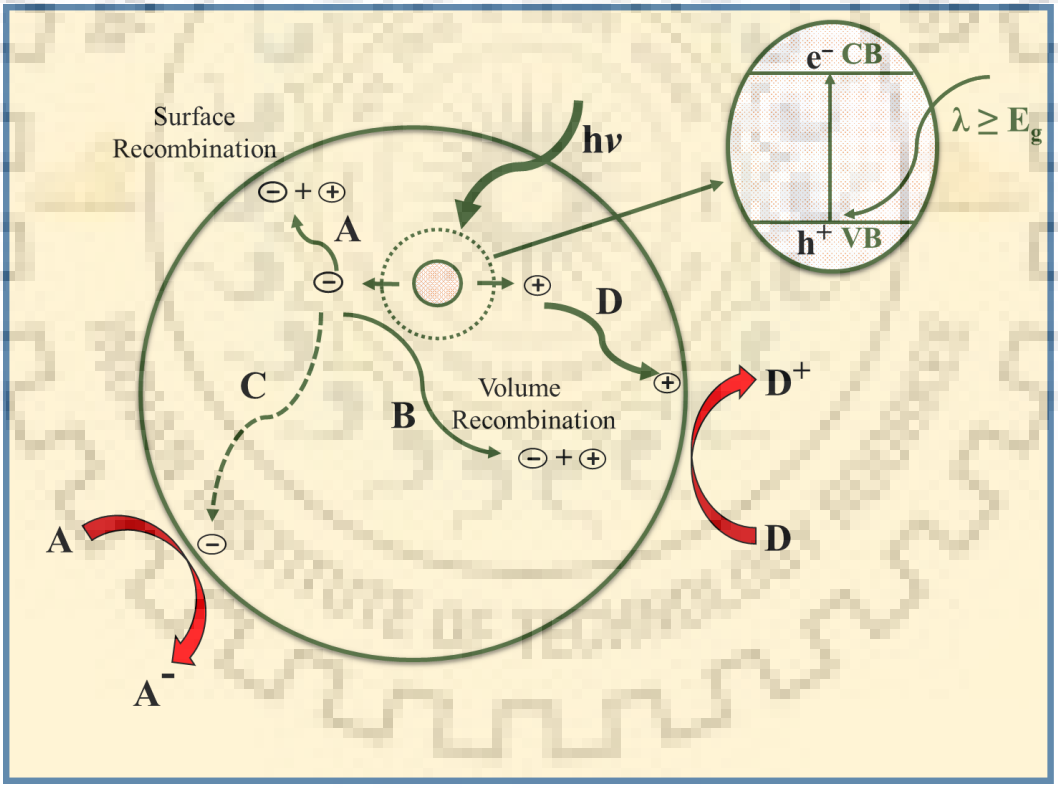

Figure 1.7 General processes involved in photocatalysis.

In second step, the photogenerated charge carries separate and migrate to the surface of the semiconductor that depend upon the several factors, like crystal structure, particle size, crystal defects/electronic structure of the semiconductor. The activity of the semiconductor is higher if the recombination chance of the electron and hole are low. The recombination of the photoinduced charge carriers may occur in the interior of the semiconductor or on the surface of the semiconductor. These electrons and hole recombination may occur in the interior region of the semiconductor (pathway B) or on the surface of the semiconductor and released the absorbed energy in the form of heat (pathway A). In the final step, the generation of the $O_2^{\bullet-}$ radicals, may take place by the photo-reduction of dissolved oxygen by pathway C. Similarly, the generation of $^{\bullet}OH$ radical by the photo-oxidation of (H_2O or OH^-). Both the reactive species (radicals and anions) can react with the organic pollutant to degrade or convert them into CO_2 and H_2O that are completely mineralized byproducts.[117, 123]

1.6.1 Basic Mechanism of Photocatalysis

The photogenerated charge carries (e^- and h^+) of semiconductor photocatalyst that adsorbed react with O_2 and H_2O molecules resulting the generation of the reactive species ($O_2^{\bullet-}$ and $^{\bullet}OH$). The reaction mechanism involved in the generation of the reactive species can be concised by the following steps: [122,124]

(i) Generation of the photogenerated charge carries (e^- and h^+) within the semiconductor on the light irradiation (Eq. 1.1).

$$\text{Semiconductor} + h\nu\ (\lambda \geq E_g) \rightarrow \text{Semiconductor}\ (e^-_{CB} + h^+_{VB}) \quad (1.1)$$

where, e^-_{CB} denotes for conduction band electron and h^+_{VB} denotes to the valence band hole.

(ii) Generation of the $^{\bullet}OH$ radicals, valance band holes can oxidize adsorbed water or hydroxyl group and produce $^{\bullet}OH$ radicals on the surface of the semiconductor (Eq. 1.2 and Eq. 1.3)

$$\text{Semiconductor}\ (h^+_{VB}) + H_2O \rightarrow {}^{\bullet}OH + H^+ + \text{Semiconductor} \quad (1.2)$$

$$\text{Semiconductor}\ (h^+_{VB}) + OH^- \rightarrow {}^{\bullet}OH + \text{Semiconductor} \quad (1.3)$$

(iii) Generation of $O_2^{\bullet-}$ radical anion and photogenerated electron in conduction band react with the adsorbed O_2 and reduce to superoxide radical anion ($O_2^{\bullet-}$) (Eq. 1.4). Further, $O_2^{\bullet-}$ may react with water and produce hydroperoxy radical ($HO_2^{\bullet}$) and hydroxyl anion species (OH^-) (Eq. 1.5).

(v) Moreover the hydroxyl radicals are generated from reaction with water and decomposition of hydrogen peroxide (Eq. 1.6 and Eq. 1.7).

Semiconductor (e_{CB}^-) + $O_2 \rightarrow O_2^{\bullet-}$ + Semiconductor (1.4)

$O_2^{\bullet-} + H_2O \rightarrow HO_2^{\bullet} + OH^-$ (1.5)

$HO_2^{\bullet} + H_2O \rightarrow {}^{\bullet}OH + H_2O_2$ (1.6)

$H_2O_2 \rightarrow 2{}^{\bullet}OH$ (1.7)

(vi) The photo-generated electron and holes can directly react with the organic pollutant and mineralize it into CO_2 and H_2O (Eq. 1.8 and Eq. 1.9).

Organic pollutant + $O_2^{\bullet-} \rightarrow CO_2 + H_2O$ (1.8)

Organic pollutant + ${}^{\bullet}OH \rightarrow CO_2 + H_2O$ (1.9)

1.7 Types of Photocatalytic Reactions

Photocatalytic activity depends on several experimental factors**,** such as radiation source, band gap of the semiconductor catalyst, concentration of pollutant, reaction medium power, amount of catalyst and photoreactor design etc. In general, heterogeneous photocatalysis offers no selectivity towards any specific redox reaction. According to the practical point of view, sunlight driven photocatalyst can be considered as a renewable method for fuel production (water splitting), organic synthesis energetics or environmental remediation and degradation of the harmful substances (water pollutant and air pollutants).[122,125,126] The possibility of photocatalytic activity is dependent on the relative mutual positioning of the reduction potentials and the valance and conduction band gap edges. The complete photocatalytic process, which consists of at least two half-reactions, oxidation and reduction that is possible only when both reduction potentials lie within the top of Valance

bands and bottom of Conduction bands scale.[117,126] Most studies of the photocatalytic properties of layered perovskite-like oxides deals with two types of reactions.

1.7.1 Principle for Water Splitting with semiconductor

For overall water splitting, water molecules are reduced by the photogenerated electrons and holes oxidize the water molecules, to form H_2 and O_2. The positions of the conduction band and valance band edges are important factors for the semiconductor photocatalyst. In semiconductor, the bottom of the conduction band should be more negative than the redox potential of H^+/H_2 (0 eV *vs.* NHE) and the top of the valance band should be more positive than the redox potential of O_2/H_2O (1.23eV*vs.* NHE).[106]

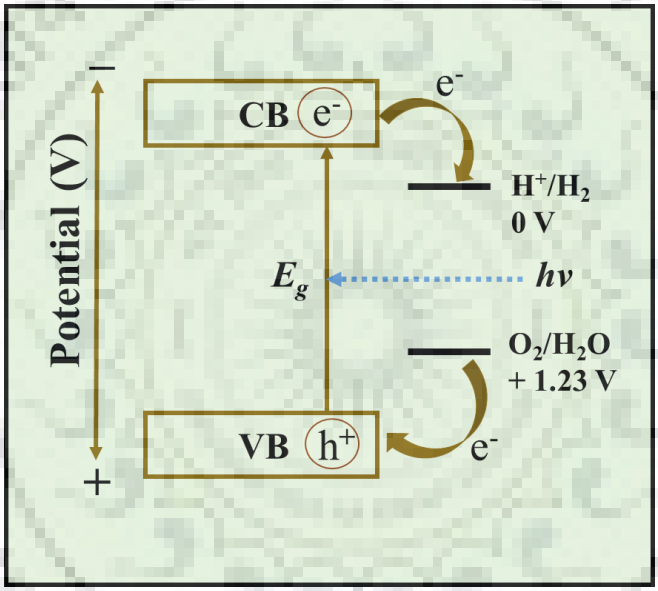

Figure 1.8 Band structure requirement of semiconductor for photocatalytic water splitting.[106]

1.7.2 Principle for Dye degradation with Semiconductor

For dye degradation, the photo absorption of the light by the photocatalyst, charge separation and generation of the reactive species on the surface of the semiconductor play important roles in the generation of charge carriers. The holes can oxidize the H_2O and electrons can reduce the O_2, to produce $^{\bullet}OH$ and $O_2^{\bullet-}$, respectively. If semiconductor band position are suitably placed with respect to the potential generation for $^{\bullet}OH$ ($E_{\bullet OH/H2O}$ = +2.68 eV vs NHE) and $O_2^{\bullet-}$ ($E_{O2/O2\bullet-}$ = +0.13 eV vs NHE).[112] The bottom of the CB of the semiconductor in this case must be more negative than the potential of $O_2/O_2^{\bullet-}$, the top of the

valance band should be more positive as compare to the potential of $^{\bullet}OH/H_2O$ (Figure 1.9). Some other factors that affect the photocatalysis as well, such as charge separation, lifetime of photoinduced charge carriers and charge transfer resistance etc.

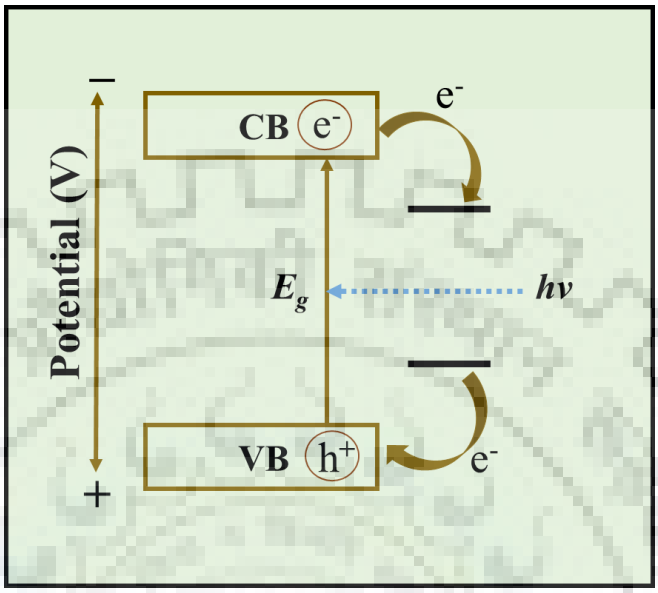

Figure 1.9 Band structure requirement of semiconductor for photocatalytic dye degradation.[122]

1.8 Band Gap Energy

The band gap energy has an important role on the photocatalytic activity. The bandgap energy decides the action spectrum of the photocatalyst. When, the band gap (E_g) energy value is lower, the longer wavelength light in absorbed by the catalyst. If $E_g < 3$ eV, the photocatalyst absorbs the visible light for the excitation of the electron from the valance band to the conduction band and subsequently generates the active species. Moreover, if $E_g > 3$ eV, the photocatalyst absorbs in the UV region. On the basis of the solar spectrum, about a less amount ~ 3–5% falls UV region ($\lambda < 400$ nm) while about 47% visible light ($\lambda < 400$ nm) that reaches on earth. Hence, researchers have the focused their attention on utilization of the solar light due to its natural abundance and sustainability. For harvesting solar energy the band gap of the semiconductor have to be lower than 3.0 eV. However, most of the photocatalyst based on niobates and titanates is active under the UV light only. Continuous efforts are being devotes by many researchers for the development of the visible-light-active

photocatalysts.[117,127-131] Several common approaches that have been developed to narrow down the band gap for harvesting the visible-light in photocatalysis includes the following:

- Metal or /and non-metal ion doping
- Solid solution formation
- New visible-light-active photocatalysts

1.9 Photocatalytic Activity of Layered Perovskites

The photocatalytic properties of layered perovskites with the Ruddlesden-Popper, Dion-Jacobson and Aurivillius structures are being investigated. The main focus of the photocatalytic reactions was water splitting, hydrogen evolution from aqueous solutions of organic compounds and degradation of model organic pollutants (especially the dyes). There are following examples given below in which photocatalytic activities of layered perovskites, their oxides and composite under visible and UV light are described.

1.9.1 Photocatalytic Activity of Layered Titanates

1.9.1.1 Layered Titanates Photocatalysts working under UV Irradiation

Triple layered perovskite- Several photocatalysts that are reported with the Ruddlesden-Popper structure include the single layered and triple layered titanate perovskites, $K_2La_2Ti_3O_{10}$. The structure of $K_2La_2Ti_3O_{10}$, consists of three octahedral perovskite layers separated by two K^+ ions.[132] Takata *et al.* reported the water splitting under UV irradiation by the Ni-loaded hydrated $K_2La_2Ti_3O_{10}$ photocatalyst. It showed fivefold increase in the photocatalytic activity than the pristine (parent) $K_2La_2Ti_3O_{10}$ and better results were obtained in aq. KOH solution with Ni (3.0 wt.%) - $K_2La_2Ti_3O_{10}$.[133] Takata *et al.* also reported the photocatalytic activity of a series of niobate substituted RP phase $A_{2-x}La_2Ti_{3-x}Nb_xO_{10}$ (A= K, Rb, Cs; x = 0, 0.5, 1). The isostructural compound, $Rb_2La_2Ti_3O_{10}$ also showed the activity twice as that of the $K_2La_2Ti_3O_{10}$ and the activity of the $Cs_2La_2Ti_3O_{10}$ was comparable to $Rb_2La_2Ti_3O_{10}$. A partial replacement of Ti^{4+} by Nb^{5+}, $ALa_2Ti_2NbO_{10}$ (A = Rb, Cs) was found to decrease the interlayer hydration capacity and in subsequently photocatalytic activity, whereas intermediate composition, $A_{1.5}La_2Ti_{2.5}Nb_{0.5}O_{10}$ (A = Rb, Cs) retained the interlayer hydration capacity and the photocatalytic activity.[134]

Co-catalyst-loaded $K_2La_2Ti_3O_{10}$ (Cr−Ni−$K_2La_2Ti_3O_{10}$) exhibited higher photocatalytic activity for water splitting under ultraviolet (UV) light.[135] Moreover, a noticeable photocatalytic activity was shown in the aqueous isopropyl alcohol solution by $A_2La_2Ti_3O_{10}$ (A= Li, Na), This is due to the deficiency ability of the intercalated the water molecule.[136] Wang *et al.* have reported the tailoring of the layered perovskite, $K_2La_2Ti_3O_{10}$, by ion-exchange reaction with divalent cations (Ca^{2+}, Sr^{2+}, and Ba^{2+}), and the photocatalytic activities were evaluated by methyl orange and phenol degradation.[137]

1.9.1.2 Layered Titanates Photocatalysts working under Visible Irradiation

Triple layered perovskite- Due to higher band gap of $K_2La_2Ti_3O_{10}$ (E_g ~ 3.5 eV), it can work under UV light ($\lambda < 350$ nm).[133,138] The photocatalytic activity of the catalyst, $K_2La_2Ti_3O_{10}$ can be improved by doping with cation/anion, like as $K_{2-x}La_2Ti_{3-x}Nb_xO_{10}$ ($0 \leqslant x \leqslant 1$),[139] Zinc-(Zn) doped $K_2La_2Ti_3O_{10}$,[140] Vanadium(V)-doped $K_2La_2Ti_3O_{10}$,[141] $K_2La_2Ti_{3-x}M_xO_{10+\delta}$ (M = Fe, Ni, and W),[142] Nitrogen(N)-doped $K_2La_2Ti_3O_{10}$[143] and Sn^{2+} and N^{3-} substituted $K_2La_2Ti_3O_{10}$.[144] Furthermore, $K_2La_2Ti_3O_{10}$-based composite photocatalysts also enhanced the photocatalytic activity in the visible-light irradiation, such as CdS/$K_2La_2Ti_3O_{10}$ have shown enhanced activity for the Rhodamine B dye degradation,[145] $ZnIn_2S_4$/$K_2La_2Ti_3O_{10}$ was used for hydrogen evolution[146] and BiOBr/$K_2La_2Ti_3O_{10}$have shown the photocatalytic activity towards the RhB degradation.[147] Recently, Kawashima *et al.* reported the protonated lanthanum titanium oxide, $H_2La_2Ti_3O_{10}$ and its oxynitride ($H_2La_2Ti_3O_{10-3/2x}N_x$ crystals) for water oxidation activity under visible light.[148]

Four layered perovskite- Most of the Bi-containing layered perovskites i.e. Aurivillius phases exhibited catalytic activity under visible-light irradiation. In Bi-containing compounds, the formation of hybridized valance band mix state (Bi 6*s* and O 2*p*) push up the valance band edge, extending the absorption edge in the visible region.[149,150] Kim *et al.* reported, the visible-light driven photocatalysts with lead substituted four layer Aurivillius phase, $PbBi_4Ti_4O_{15}$, lead substitution has been claimed as a generic method for the visible-light sensitization.[151] The photocatalytic activity of $Bi_5Ti_3FeO_{15}$ (n = 4) has been reported towards RhB, acetaldehyde and isopropyl alcohol degradation in the visible-light irradiation.[152,153] However, Sun *et al.* have reported hierarchical microflowers of $Bi_5Ti_3FeO_{15}$ to show excellent photocatalytic activity towards RhB and acetaldehyde as compared to the bulk compound

($Bi_5Ti_3FeO_{15}$) under similar conditions, the nanoflowers showed higher efficiency because of nanocrysatalline nature and increased surface area.[152]

Furthermore, Naresh *at el.* have synthesized, $Bi_{5-x}La_xTi_3FeO_{15}$ (x = 1, 2), by the conventional solid state method and the compounds exhibited excellent photocatalytic activity towards RhB degradation in the pH 2 under solar light irradiation.[154] The photocatalytic activity of $Bi_5Ti_3FeO_{15}$ were also enhanced by the microstructural modification via partial substitution of Ti^{4+} with Fe^{3+}, $Bi_5Ti_{3-x}Fe_{1+x}O_{15}$ (x = 0–0.6) and $Bi_{5-y}Eu_yFe_{1-x}Ni_xTi_3O_{15}$($x$ = 0, 0.05, 0.10, 0.15, 0.20; y = 0, 0.1, 0.3, 0.5) nanoflowers which showed enhanced degradation of RhB in the visible-light irradiation.[155,156]

Five and higher layered perovskite- Naresh *at el.* have synthesized, the five layer (n = 5) Aurivillius phase, $Bi_{6-x}La_xTi_3Fe_2O_{18}$ (x = 0, 1) have also shown excellent photocatalytic activity in natural solar irradiation. The compounds are efficient toward photocatalytic degradation of dye (RhB) at pH 2 with concomitant complete mineralization of the dye.[157] Later, they reported the new composition that designed by the substitution of Ca, Sr and Pb in A-site of the $Bi_6Ti_4FeO_{18}$. The substituted compound, $Bi_5ATi_4FeO_{18}$ (A = Ca, Sr, and Pb) exhibited excellent selective degradation of RhB-MB at pH 11 and collective photocatalytic degradation of RhB-MB and RhB-RhB 6G at pH 2 under solar light irradiation.[158] Li *et al.* have described the photocatalytic activity of the higher member (n = 6) Aurivillius phase, $Bi_7Fe_3Ti_3O_{21}$ nanoshelves with co-existing ferroelectricity and ferromagnetism properties.[159]

1.9.2 Photocatalytic Activity of Layered Niobates Perovskites

Niobium-based catalysts are a new class of photocatalysts which have shown excellent properties in many applications. Although, Nb has very small differences in the electronegativity and ionic radius as compared to its neighbours elements in the periodic table, but catalytic properties of Nb are very different from others. Therefore, from last two decades, Nb-based catalysts got adequate attention from research community due to their very interesting photocatalytic activities. [160-162]

1.9.2.1 Layered Niobates Photocatalysts working under UV Irradiation

Double layered perovskites- Domen *et al.* were the first researcher group to investigate the activity of double layered niobates, $ALaNb_2O_7$ (A = Cs, Rb, K or H), The compounds was

showed photocatalytic hydrogen evolution form aqueous solution of methanol and oxygen evolution from $AgNO_3$ solution. Double-layered restacked D–J phase niobate nanosheets, $HLaNb_2O_7$ (prepared by the proton exchange reaction of $RbLaNb_2O_7$) were used for photochemical H_2 evolution under ultraviolet irradiation.[163] N. Xu *et al.* have reported the preparation of partially substituted $RbLaNb_2O_7$ by replacing Nb^{5+} with W^{6+} and Ti^{4+} and its phenol degradation activity.[164] Moreover, enhanced photocatalytic activity of interlayered perovskite with a layered perovskite oxide $HLaNb_2O_7$, as host and Ag or Bi as guest by control of the valance band was demonstrated.[165]

A double layered niobates, $ABi_2Nb_2O_9$ (A = Ca, Sr, Ba) were reported as good candidates for photocatalytic water splitting.[166] Later, Citrate method used for the preparation of microcrystalline $ABi_2Nb_2O_9$ (A= Sr, Ba) and photocatalytic activity of the compounds were tested by a way of organic pollutant such as methyl orange [167] and conversion of 4-nitroaniline to p-phenylenediamine under UV- light irradiation.[168]

Triple layered perovskite- The activity of the triple layered niobates, $ACa_2Nb_3O_{10}$ (A = Cs, Rb, K or H) was first studied by the Domen and co-workers. The Niobates showed photocatalytic H_2 evolution from aqueous solution of methanol and O_2 evolution from silver nitrate solution.**[169]** It was demonstrated that the rate of H_2 evolution depends upon the amount of H^+ and K^+ cation substitution in $KCa_2Nb_3O_{10}$. The substitution about 70-80 % have been shown to be increase the activity, this proves that the photocatalytic activity is dependent on the interlayer space. The layered niobate perovskites has not been able to evolve hydrogen and oxygen without any modification.[170] A similar strategy can be seen in silica pillared $Ca_2Nb_3O_{10}$, which was prepared by intercalation of *n*-alkylammonium ion in $KCa_2Nb_3O_{10}$ followed by the incorporation of $Si(OEt)_4$.[171] The specific surface area increased if the varies from 2 to 200 $m^2\ g^{-1}$ after the SiO_2 loading. In silica pillared $Ca_2Nb_3O_{10}$, the activity was increased by ca. 30 times in both aqueous propanol or butanol solution as compared to that with the original $HCa_2Nb_3O_{10}$, though no variance was found in the aqueous methanol solution. The surface area was increased because of restacking of $KCa_2Nb_3O_{10}$ from monolayers which showed the enhanced activity of hydrogen evolution in aqueous solution under UV- light irradiation.[172] The triple layered oxides, such as restacked niobates have shown higher photocatalytic activities as compared to the double layered oxides, similar to precursor unsplit compounds.[163] In case of triple layered niobates, the potassium containing

samples have shown the highest activity. However, in double-layered niobates, the Rb-containing compounds have shown the highest activity.[173]

1.9.2.2 Layered Niobates Photocatalysts Working under Visible Irradiation

Double Layered Perovskites- A double layer Aurivillius compound, $PbBi_2Nb_2O_9$ (PBN) have unique band structure makes $PbBi_2Nb_2O_9$ possess excellent photocatalytic performance under visible-light irradiation. For $PbBi_2Nb_2O_9$ ($E_g \sim 2.8$ eV), the conduction have empty Nb 4*d* and valence bands occupied O 2*p* orbitals, respectively is hybridized with Bi 6s and Pb 6s.[150] Recently $ABi_2Nb_2O_9$ showed the photocatalysts activity towards the photoreduction of 4-nitroaniline,[174,175] isopropyl alcohol degradation to CO_2, Pt-loaded PBN exhibit photoactivity of H_2 evolution with an amount of 7.6 $mmol.g^{-1}h^{-1}$.[150] Cr^{3+}doped $PbBi_2Nb_2O_9$[176] or W^{6+} doped $PbBi_2Nb_2O_9$[177] showed higher quantum yield for H_2 and O_2 generation as compare to the PBN under visible-light irradiation.

Triple Layered Perovskites- $AB_2Nb_3O_{10}$ with a wide band gap (>3.0 eV), often shows higher activity under UV-light, while less activity under visible-light. Some modifications like pillaring, exfoliation or loading co-catalyst, doping of metals can improve the active sites that promote the activity.[178-171] For example, the replacement of Ca^{2+} from the $RbCa_2Nb_3O_{10}$ with lead have shown enhanced catalytic activity under visible high irradiation. The replacement of Rb^+ with the H^+, enhanced the rate of hydrogen evolution.[178] Moreover, the coupled substitution of La^{3+} for Ca^{2+} at B-site in $HCa_2Nb_3O_{10}$ and $K_{0.5}La_{0.5}Ca_{1.5}Nb_3O_{10}$ have been shown to enhanced the photocatalytic activity.[151,179] The activity of $KSr_2Nb_3O_{10}$ and $HPb_2Nb_3O_{10}$ have been enhanced by the doping a suitable amount of Cr. [180,181]

The compound, $CsBa_2M_3O_{10}$ (M = Ta, Nb) and oxynitrides $CaTaO_2N$, $SrTaO_2N$, $BaTaO_2N$, $LaTiO_2N$ and $LaTaON_2$) were synthesized using flux method and investigated the photocatalytic activities towards the removal of caffeine from wastewater.[182] However, N-doped $CsM_2Nb_3O_{10}$ (M = Ba and Sr) showed significantly higher photocatalytic activity against the degradation of MB as compared to the corresponding parent oxides. Nitrogen is the most popular dopant because of its appropriate ionic radius similar to oxygen and the partial replacement of O^{2-} by N^{3-} narrows the band-gap of the parent oxides by shifting their valence band upward.[183] The nanosheets, $KCa_2Nb_{3-x}Rh_xO_{10-\delta}$ have been exhibited the higher photocatalytic efficiency than their parent counterparts,[184] due to high crystallinity, large

specific surface area, and shortened distance for photogenerated e^- and h^+ to easily move to the surface without recombination. Some heterojunction photocatalysts 2D/0D material and exfoliated nanosheets (2D-2D g-C_3N_4/$K^+Ca_2Nb_3O_{10}$[185] and 0D/2D Au nanoparticles/$KCa_2Nb_3O_{10}$[186]) have showed remarkable photocatalytic activity degraded the organic pollutant, tetracycline hydrochloride.

1.9.3 Photocatalytic Activity of Layered Tungstates Perovskite

Aurivillius phases have been extenseively studied as photocatalysts that absorbs visible light. The most of studies including mono-layered phase isostructural to Bi_2MoO_6, and Bi_2WO_6.[187] The Bi_2WO_6 structure is a homologous of the Bi_2MoO_6 structure. For Bi_2WO_6 (E_g = 2.7 eV) showed the absorption of visible light, with the transition of an electron from the valence band (Bi 6*s* and O 2*p* orbitals) to conduction band (W5*d* orbitals). Several strategies have been developed, so the improved photocatalyst activity, like noble metal deposition (Ag-loaded Bi_2WO_6, Ag nanoparticles loaded Bi_2WO_6),[187,188] ion doping (Fe- doped Bi_2WO_6, Cu-doped)[189,190] nanocomposite and heterostructure construction[191-198] with Bi_2WO_6 and so on.

1.10 Methods to Synthesize Metal Oxides

A variety of synthetic methods are available in the literature for the synthesis of metal oxides. Some of the commonly used methods include the following.

- Ceramic
- Reactive grinding
- Hydrothermal
- Sol-gel
- Microwave
- Sonochemical

Solid state method or ceramic method is the most commonly used route for the synthesis of inorganic solids. In this method, the stoichiometric amount of precursor materials, such as, binary metal oxides and/or simple metal salts (e.g. oxalates, oxides, carbonates, nitrates, etc.) are weighed and ground the mixture thoroughly in an agate mortar and pestle or by ball milling. The ground mixture is transferred to an alumina or silica boat or crucible and heated

at high temperatures for random durations. First, the reaction occurs at the contact points among component phases and then proceeds through inter diffusion between precursor particles to form final product phases. Because of very low diffusion coefficient of solids (~ 10^{-12} cm^2 s^{-1}), a high temperature is required for the diffusion controlled reactions. For the volatile and/or sensitive precursor materials, atmosphere (argon/nitrogen gas) controlled sealed tube is used for the reactions to avoid the contact of O_2 or moisture. Sometimes multiple steps of grinding and heating are required for breaking the courser grain of starting materials/products which helps in lowering the diffusion barrier between the grains. In the solid state reaction, initial reactants or precursors have different structures. Therefore, nucleation process is difficult due to lot of bond breaking, bond reforming and structural reorganizations that takes place during the reaction. In addition, introduction of impurity in the samples is very common during the physical processing (grinding, ball milling, and compression). Thus, it is found that high purity and homogeneity is difficult to obtain by solid state route/ceramic routes. Despite some of the drawbacks of solid state routes, it is most usable method for synthesizing new materials. In the present study, solid state route method is extensively used to synthesis new perovskite based layered oxides. In the study, we have used both direct reactions (one step) as well as multistep reactions to get the final product.

REFERENCES

1. Centi, G.; Perathoner, S. Catalysis by Layered Materials: A review. *Microporous Mesoporous Mater*. **2008**, *107*, 3–15.

2. Schaak, R. E.; Mallouk, T. E. Topochemical Synthesis of Three-Dimensional Perovskites from Lamellar Precursors. *J. Am. Chem. Soc.* **2000**, ***122***, 2798–2803.

3. Raju, K.; Song, M. S.; Lee, J. Y. Crystal Structure and Magnetic Properties of $La_{2-x}(Sr_{0.5}Ca_{0.5})_{1+x}Mn_2O_7$ (x = 0.6, 0.8 and 1.0) Ruddlesden–Popper Manganites. *J. Magn. Magn. Mater*. **2014**, *358*, 119–122.

4. Wu, M.; Tian, Z.; Yuan, S.; Huang, Z.; Magnetic and Optical Properties of the Aurivillius phase $Bi_5Ti_3FeO_{15}$. *Mater. Lett.* **2012**, *68*, 190–192.

5. Tezuka, K.; Hinatsu, Y. Magnetic Properties of Layered Perovskites $NaLnTiO_4$ (Ln = Sm, Eu, and Gd). *J Solid State Chem.* **1998**, *138*, 342–346.

6. Moritomo, Y.; Asamitsu, A.; Kuwahara, H.; Tokura, Y. Gaint Magnetoresistance of Manganese Oxides with a Layered Perovskite Structure. *Nature* **1996**, *380*, 141–144.

7. Zhang, J.; Wang, F.; Zhang, P.; Yan, Q. Effect of Fe Doping on Magnetic Properties and Magnetoresistance in $La_{1.2}Sr_{1.8}Mn_2O_7$. *J. Appl. Phys.***1999**, *86*, 1604–1606.

8. Porob D. G.; Maggard, P. A. Synthesis of Textured $Bi_5Ti_3FeO_{15}$ and $LaBi_4Ti_3FeO_{15}$ Ferroelectric Layered Aurivillius Phases by Molten-Salt Flux Methods. *Mater. Res. Bull.* **2006**, *41*, 1513-1519.

9. Blake, S. M.; Falconer, M. J.; McCreedy, M.; Lightfoot, P. Cation Disorder in Ferroelectric Aurivillius Phases of the Type $Bi_2ANb_2O_9$ (A= Ba, Sr, Ca). *J. Mater. Chem.* **1997**, *7(8)*, 1609–1613.

10. Kusainova, A. M.; Lightfoot, P.; Zhou, W.; Stefanovich, S. Y.; Mosunov, A. V.; Dolgikh, V. A. Ferroelectric Properties and Crystal Structure of the Layered Intergrowth Phase $Bi_3Pb_2Nb_2O_{11}Cl$. *Chem. Mater.* **2001**, *13*, 4731–4737.

11. Battle, P. D.; Green, M. A.; Laskey, N. S.; Millburn, J. E.; Rosseinsky, M. J.; Sullivan, S. P.; Vente, J. F. Coupled Metal-Insulator and Magnetic Transitions in $LnSr_2Mn_2O_7$ (Ln = La, Tb).*Chem. Commun*. **1996**, 767–768.

12.Kusainova, A. M.; Stefanovich, S. Y.; Dolgikh, V. A.; Mosunov, A. V.; Hervoches, C. H.; Lightfoot, P. Dielectric Properties and Structure of Bi_4NbO_8Cl and Bi_4TaO_8Cl. *J. Mater. Chem*. **2001**, *11*, 1141–1145

13. Yim, H.; Yoo, S. Y.; Nahm, S.; Hwang, S. J.; Yoon, S. J.; Choi, J. W. Synthesis and Dielectric Properties of $HCa_2Nb_3O_{10}$ Layered Structure Ceramics. *Ceram. Int.* **2013**, *39*, S611–S614.

14. Ima, M.; Kim, D. H.; Kweon, S. H.; Lee, W. H.; Nahm, S. Synthesis and Effect of Ba^{2+} Ions on the Dielectric Properties of the Layered Perovskite $KSr_2NaNb_4O_{13}$ Ceramics. *Mater. Res. Bull*. **2018**, *105*, 246–252.

15. Li, B. W.; Osada, M.; Ebina, Y.; Akatsuka, K.; Fukuda, K.; Sasaki, T. High Thermal Robustness of Molecularly Thin Perovskite Nanosheets and Implications for Superior Dielectric Properties. *ACS Nano* **2014**, *8*, 5449–5461.

16. Yang, J.; Wang, Y.; Zhao, X.; Dai, J.; Mo, S. Synthesis of Uniform Bi_2WO_6-Reduced Graphene Oxide Nanocomposites with Significantly Enhanced Photocatalytic Reduction Activity *J. Phys. Chem. C* **2015**, *119*, 3068−3078

17. Ganguly, A.; Anjaneyulu, O.; Ojha, K; Ganguli, A. K. Oxide-based Nanostructures for Photocatalytic and Electrocatalytic Applications. *Cryst. Eng. Comm.* **2015**, *17*, 8978 –9001.

18. Liu, X.; Xu, L.; Huang, Y.; Qin, C.; Qin, L.; Seo. H. J. Improved Photochemical Properties of Aurivillius $Bi_5Ti_3FeO_{15}$ with Partial Substitution of Ti^{4+} with Fe^{3+}. *Ceram. Int.* **2017**, *43*, 12372–12380.

19. Dutta, D. P.; Tyagi, A. K. Facile Sonochemical Synthesis of Ag Modified $Bi_4Ti_3O_{12}$ Nanoparticles with Enhanced Photocatalytic Activity under Visible Light. *Mater. Res. Bull.* **2016**, *74*, 397-407.

20. Fujito, H.; Kunioku, H.; Kato, D.; Suzuki, H.; Higashi, M.; Kageyama, H.; Abe, R. Layered Perovskite Oxychloride Bi_4NbO_8Cl: A Stable Visible Light Responsive Photocatalyst for Water Splitting. *J. Am. Chem. Soc.* **2016**, *138*, 2082–2085.

21. Oka, M.; Miseki, Y.; Saito, K.; Kudo, A. Photocatalytic Reduction of Nitrate Ions to Dinitrogen Over Layered Perovskite $BaLa_4Ti_4O_{15}$ using Water as an Electron Donor. *Appl. Catal. B: Environ*. **2015**, *179*, 407–411

22. Ge, W.; Fu, Z.; Li, X.; Wang, J.; Zhu, Z.; Liu, M.; Peng, R.; Lu, Y. Optimizing the Photocatalysis in Ferromagnetic $Bi_6Fe_{1.9}Co_{0.1}Ti_3O_{18}$ Nanocrystal by Morphology Control. *RSC Adv.* **2015**, *5*, 54165–54170.

23. Kobayashi, Y.; Tian, M.; Eguchi, M.; Mallouk, T. E. Ion-Exchangeable, Electronically Conducting Layered Perovskite Oxyfluorides. *J. Am. Chem. Soc.* **2009**, *131*, 9849–9855.

24. Sato, M.; Abo, J.; Jin, T. Structure Examination of $NaLaNb_2O_7$ Synthesized by Soft Chemistry. *Solid State Ionics* **1992**, *57*, 285–293.

25. Patino, M. A.; Smith, T.; Zhang, W.; Halasyamani, P. S.; Hayward. M. A. Cation Exchange in a 3D Perovskite-Synthesis of $Ni_{0.5}TaO_3$. *Inorg. Chem.* **2014**, *53*, 8020−8024.

26. Uma, S.; Bhat, V.; Gopalakrishnan, J. Synthesis of Layered Perovskite Oxides, $ACa_{2-x}La_xNb_{3-x}Ti_x0_{10}$ (A = K, Rb, Cs), and Characterization of New Solid Acids, $HCa_{2-x}La_xNb_{3-x}Ti_xO_{l0}$ ($0 < x \leq 2$), Exhibiting Variable Bronsted Acidity. *Chem. Mater.* **1993**, *5*, 132-136.

27. Kawaguchi, T.; Horigane, K.; Itoh, Y.; Kobayashi, K.; Horie, R.; Kambe, T.; Akimitsu, J. Crystal Structure and Superconducting Properties of $KSr_2Nb_3O_{10}$. *Physica B* **2018**, *536*, 830–832.

28. Attfield, J. P.; Lightfoot, P.; Morris, R. E. Perovskites. *Dalton Trans.* **2015**, *44*, 10541–10542

29. Megaw, H. D. Crystal Structure of Barrium Titanite. *Nature* **1995**, *155*, 484–485.

30. Megaw, H. D. Temperature Changes in the Crystal Structure of Barium Titanium Oxide. *Proc. R. Soc. A* **1947**, *189*, 261–283.

31. Megaw, H. D. Crystal Structure of Double Oxides of the Perovskite Type. *Proc. Phys. Soc*. 1946, *58* 133–152.

32. Goldschmidt V. M. Die Gesetze der Krystallochemie. Naturwissenschaften. *Nature. sci.* **1926**, *14*, 477–485.

33. Rodionov, I. A.; Zvereva, I. A. Photocatalytic Activity of Layered Perovskite-like Oxides in Practically Valuable Chemical Reactions. *Russ. Chem. Rev.* **2016**, *85*, 248–279.

34. Aurivillius, B. Mixed Bismuth Oxides with Layer Lattices, the Structure Type of $CaNb_2Bi_2O_9$. *Arki. Kemi* **1949**, *1*, 463–480.

35. Ismunandar; Hunter, B. A.; Kennedy. B. J. Cation Disorder in the Ferroelectric Aurivillius Phase $PbBi_2Nb_2O_9$ an Anomalous Dispersion X-ray Diffraction Study. *Solid State Ionics* **1998**, *112*, 281–289.

36. Kikuchi, T.; Watanabe, A.; Uchida, K. A Family of Mixed-Layer type Bismuth Compounds. *Mat. Res. Bull.* **1977**, *12*, 299–304.

37. Snedden, A.; Charkin, D. O.; Dolgikh, V. A.; Lightfoot. P. Crystal Structure of the 'Mixed-Layer' Aurivillius Phase $Bi_5TiNbWO_{15}$. *J. Solid State Chem.* **2005**, *178*, 180–184.

38. Raghavan, C. M.; Kim, J. W.; Choi, J. Y.; Kim, J. W.; Kim, S. S. Effects of Donor W^{6+}-Ion Doping on the Microstructural and Multiferroic Properties of Aurivillius $Bi_7Fe_3Ti_3O_{21}$Thin Film. *Appl. Surf. Sci.* **2015**, *346*, 201–206.

39. Dion, M., The New Phase Families M(I)M2(II)Nb_3O_{10} with Perovskite Sheets. *Mat. Res. Bull.* **1981**, *6*, 1429–1435.

40. Jacobson, A. J.; Johnson, W. J.; Lewandowski. J. T. Interlayer Chemistry between thick Transition-Metal Oxide Layers: Synthesis and Intercalation Reactions of $K[Ca_2Na_{n-3}Nb_nO_{3n+1}]$. *Inorg. Chem.* **1985**, *24*, 3727–3729.

41. Li, B. W.; Osada, M.; Ebina, Y.; Ozawa, T. C.; Ma, R.; Sasaki, T. Impact of Perovskite Layer Stacking on Dielectric Responses in $KCa_2Na_{n-3}Nb_nO3_{n+1}$ (n = 3 – 6) Dion–Jacobson Homologous Series. *Appl. Phys. Lett.* **2010**, *96*, 182903 (1–3).

42. Ruddlesden, S. N.; Popper, P. The Compound $Sr_3Ti_2O_7$ and Its Structure. *ActaCrystallogr.* **1958**, *11*, 54–55.

43. Ruddlesden, S. N.; Popper, P. New Compounds of the K_2NiF_4 Type. *ActaCrystallogr.* **1957,** *10*, 538–539.

44. Balz, D.; Plieth, K. Die Struktur Des Kaliumnickel-Fluorids K_2NiF. *ActaCrystallogr.* **1954**. *7*, 545–551.

45. Ackerman, J. F. The Structures of Bi_3PbWO_8Cl and Bi_4NbO_8Cl and the Evolution of the Bipox Structure Series. *J. Solid State Chem.* **1986**, *62*, 92–104.

46. Suzuki, H.; Kunioku, H.; Higashi, M.; Tomita, O.; Kato, D.; Kageyama, H.; Abe, R. Lead Bismuth Oxyhalides $PbBiO_2X$ (X = Cl, Br) as Visible-Light-Responsive Photocatalysts for Water Oxidation: Role of Lone Pair Electrons in Valence Band Engineering. *Chem. Mater.* **2018**, *30*, 5862–5869.

47. Kusainova, A. M.; Stefanovich, S. Y.; Irvine, J. T. S.; Lightfoot, P. Structure–Property Correlations in the New Ferroelectric $Bi_5PbTi_3O_{14}Cl$ and Related Layered Oxyhalide Intergrowth Phases. *J. Mater. Chem.* **2002**, *12*, 3413–3418.

48. Raymond E. Schaak and Thomas E. Mallouk. Perovskites by Design: A Toolbox of Solid-State Reactions. *Chem. Mater.* **2002**, *14*, 1455–1471.

49. Uppuluri, R.; Gupta, A. S.; Rosas, A. S.; Mallouk, T. E. Soft chemistry of Ion-Exchangeable Layered Metal Oxides. *Chem. Soc. Rev.* **2018**, *47*, 2401–2430.

50. Bhuvanesh, N. S. P.; Gopalakrishnan, J. Solid-State Chemistry of Early Transition-Metal Oxides containing d^0 and d^1 Cations. *J. Mater. Chem*. **1997**, *7*, 2297–2306.

51. Porob D. G.; Maggard, P. A. A Rapid Flux-Assisted Synthetic Approach Towards the Bandgap Engineering of Layered Perovskites. *Chem. Mater.* **2007**, *19*, 970–972.

52. Hwang, D. W.; Kim, H. G.; Lee, J. S.; Kim, J.; Li, W.; Oh, S. H. Photocatalytic Hydrogen Production from Water over M-Doped $La_2Ti_2O_7$ (M = Cr, Fe) under Visible Light Irradiation ($\lambda > 420$ nm). *J. Phys. Chem. B* **2005**, *109,* 2093-2102.

53. Liu, S.; Miiller, W.; Liu, Y.; Avdeev, M.; Ling, C. D. Sillen−Aurivillius Intergrowth Phases as Templates for Naturally Layered Multiferroics. *Chem. Mater.* **2012,** *24*, 3932−3942.

54. Chen, Z.; Jiang, X.; Zhu, C.; Shi, C.; Chromium-Modified $Bi_4Ti_3O_{12}$ Photocatalyst: Application for Hydrogen Evolution and Pollutant Degradation. *Appl. Catal. B: Environ.* **2016**, *199*, 241–251.

55. Zhao, H.; Wang, H.; Cheng, Z.; Fu, Q.; Tao, H.; Maa, Z.; Jia, T.; Kimura, H.; Li, H.; Electric and Magnetic Properties of Aurivillius-Phase Compounds: $Bi_5Ti_3XO_{15}$ (X = Cu, Mn, Ni, V). *Ceram. Int.* **2018**, *11*, 44−47.

56. Koval, V.; Skorvanek, I.; Viola, G.; Zhang, M.; Jia, C.; Yan, H. Crystal Chemistry and Magnetic Properties of Gd-Substituted Aurivillius-Type $Bi_5FeTi_3O_{15}$ Ceramics. *J. Phys. Chem. C* **2018**, *122*, 15733−15743.

57. Neiner, D.; Spinu, L.; Golub, V.; Wiley, J. B. Ferromagnetism in Topochemically Prepared Layered Perovskite $Li_{0.3}Ni_{0.85}La_2Ti_3O_{10}$. *Chem. Mater.* **2006**, *18*, 518−524.

58. Lichtenberg, F.; Herrnberger, A.; Wiedenmann. K. Synthesis, Structural, Magnetic and Transport Properties of Layered Perovskite-Related Titanates, Niobates and Tantalates of the Type $A_nB_nO_{3n-2}$, $A'A_{k-1}B_kO_{3k+1}$ and $A_mB_{m-1}O_{3m+1}$.*Prog. Solid State Chem.* **2008,** *36*, 253−387.

59. Arney, D.; Maggard, P. A. Effect of Platelet-Shaped Surfaces and Silver-Cation Exchange on the Photocatalytic Hydrogen Production of $RbLaNb_2O_7$. *ACS Catal.* **2012**, *2*, 1711−1717.

60. Raju, K.; Song, M.S.; Lee, J.Y. Crystal Structure and Magnetic Properties of $La_{2-x}(Sr_{0.5}Ca_{0.5})_{1+x}Mn_2O_7$ (x = 0.6, 0.8 and 1.0) Ruddlesden–Popper Manganites. *J. Magn.Magn. Mater.* **2014**, *358*, 119–122.

61. Uma, S.; Gopalakrishnan, J. $K_{1-x}La_xCa_{2-x}Nb_3O_{10}$, a Layered Perovskite Series with Variable Interlayer Cation Density, and $LaCaNb_3O_{10}$, a Novel Layered Perovskite Oxide with No Interlayer Cations. *J Solid State Chem.* **1993**, *102*, 332–339.

62. Dion, M.; Ganne, M.; Tournoux, M. Nouvelles Familles de Phases $MIMIINb_3O_{10}$ a Feuillets "Perovskites". *Mater. Res. Bull.* **1981**, *16*, 1429–1435.

63. Gopalakrishnan, J.; Bhat. V.$A_2Ln_2Ti_3O_{10}$ (A = K or Rb; Ln = La or Rare Earth): A New Series of Layered Perovskites Exhibiting Ion Exchange. *Inorg. Chem.* **1987**, *26*, 4329–4301.

64. Jacobson, J.; Lewandowski, J.T.; Johnson. J. W. Ion Exchange Reactions of the Layered Solid Acid $HCa_2Nb_3O_{lo}$ with Alkali Metal Cations. *Mat. Res. Bull.* **1990**, *25*, 679–686.

65. Uma, S.; Raju, A. R.; Gopalakrishnan, J. Bridging the Ruddlesden-Popper and the Dion-Jacobson Series of Layered Perovskites: Synthesis of Layered Oxides, $A_{2-x}La_2Ti_{3-x}Nb_xO_{10}$ (A = K, Rb), Exhibiting Ion Exchange. *J. Mater. Chem.* **1993**, *3*, 709–713.

66. Hyeon, A. K. Byeon, S. H. Synthesis and Structure of New Layered Oxides, $M^{II}La_2Ti_3O_{10}$ (M = Co, Cu, and Zn). *Chem. Mater.* **1999**, *11*, 352–357.

67. Kim, S. Y.; Oh, J. M.; Park, J. C.; Byeon, S. H. Structure of New Layered Oxides $M^{II}_{0.5}LaTiO_4$ (M = Co, Cu, and Zn) Synthesized by the Ion-Exchange Reaction. *Chem. Mater.* **2002**, *14*, 1643–1648.

68.Kodenkandath, T. A.; Lalena, J. N.; Zhou, W. L.; Carpenter, E. E.; Sangregorio, C.; Falster, A. U.; Simmons, W. B.; Connor, C. J.; Wiley, J. B. Assembly of Metal-Anion Arrays within a Perovskite Host. Low-Temperature Synthesis of New Layered Copper-Oxyhalides, $(CuX)LaNb_2O_7$, X = Cl, Br. *J. Am. Chem. Soc.* **1999**, *121*, 10743–10746.

69. Viciu, L.; Koenig, J.;Spinu, L.; Zhou, W. L.; Wiley. J. B. Insertion of a Two-Dimensional Iron-Chloride Network between Perovskite Blocks. Synthesis and Characterization of the Layered Oxyhalide, $(FeCl)LaNb_2O_7$. *Chem. Mater.* **2003**, *15*, 1480–1485.

70. Josepha, E. A.; Farooq, S.; Mitchell, C. M.; Wiley. J. B. Synthesis and Thermal Stability Studies of a Series of Metastable Dion–Jacobson Double-Layered Neodymium-Niobate Perovskites. *J. Solid State Chem.* **2014**, *216*, 85–90.

71.Montasserasadi, D.; Granier, M. W.; Spinu, L.; Rai, S. C.; Zhou, W.; Wiley, J. B. Synthesis and Characterization of the Rare-Earth Dion–Jacobson Layered Perovskites, $APrNb_2O_7$ (A = Rb, Cs and CuCl). *Dalton Trans*. **2015**, *44*, 10654-10660.

72. Viciu, L.; Liziard, N.; Golub, V.; Kodenkandath, T. A.; Wiley, J. B. Transition-metal Dion-Jacobson layered perovskites, $M_{0.5}LaNb_2O_7$. *Mater. Res. Bull.* **2004**, *39*, 2147–2154.

73. Boltersdorf, J.; Maggard, P. A. Silver Exchange of Layered Metal Oxides and Their Photocatalytic Activities. *ACS Catal.* **2013**, *3*, 2547−2555.

74. Jacobson, A. J.; Lewandowski, J. T.; Johnson. J. W. Ion Exchange of the Layered Perovskite $KCa_2Nb_3O_{10}$ by Protons. *J. Less Common Met.* **1986**, *116*, 137–146.

75. Hermann, A. T.; Wiley, J. B. Thermal stability of Dion–Jacobson Mixed-Metal-Niobate Double-Layered Perovskites *Mater. Res. Bull.* **2009**, *44*, 1046–1050.

76. Guertin, S. L.; Josepha, E. A.; Montasserasadi, D.; Wiley, J. B. Thermal Stability and High Temperature Polymorphism of Topochemically-Prepared Dion–Jacobson Triple-Layered Perovskites. *J. Alloy. Compd.* **2015**, *647*, 370–374.

77. Gopalakrishnan, J.; Bhat, V. $A_2Ln_2Ti_3O_{10}$ (A = Potassium or Rubidium; *Ln* = Lanthanum or Rare Earth): A New Series of Layered Perovskites Exhibiting Ion Exchange. *Inorg. Chem*. **1987**, *26*, 4299–4301.

78. Bisio, C.; Nocchetti, M.; Leroux, F. Recent Developments in Intercalation Compounds: Chemistry and Applications. *Dalton Trans.* **2018**, *47*, 2838–2840.

79. Jacobson, A. J.; Johnson. J. W.; Lewandowski, J. T. Interlayer Chemistry between Thick Transition-Metal Oxide Layers: Synthesis and Intercalation Reactions of $K[Ca_2Na_{n-3}Nb_nO_{3n+1}]$ ($3 \leq n \leq 7$). *Inorg. Chem.* **1985**, *24*, 3727–3729.

80. Jacobson, A. J.; Lewandowski, J. T.; Johnson. J. W. Ion Exchange of the Layered Perovskite $KCa_2Nb_3O_{10}$ by Protons. *J. Less Common Met.***1986**, *116*, 137–146.

81. Gopalakrishnan, J.; Bhat, V.; Raveau, B. $A^ILaNb_2O_7$: A New Series of Layered Perovskites Exhibiting Ion Exchange and Intercalation Behavior. *Mater. Res. Bull.* **1987**, *22*, 413–417.

82. Didier, C.; Guignard, M.; Suchomel, M. R.; Carlier, D.; Darriet, J.; Delmas, C. Thermally and Electrochemically Driven Topotactical Transformations in Sodium Layered Oxides Na_xVO_2. *Chem. Mater*. **2016**, *28*, 1462–1471.

83. Montasserasadi, D.; Mohanty, D.; Huq, A.; Heroux, L.; Payzant, E. A.; Wiley, J. B. Topochemical Synthesis of Alkali-Metal Hydroxide Layers within Double- and Triple-Layered Perovskites. *Inorg. Chem.* **2014**, *53*, 1773–1778.

84. Ranmohotti, K. G. S.; Montasserasadi, M. D.; Choi, J.; Yao, Y.; Mohanty, D.; Josepha, E. A.; Adireddy, S.; Caruntu, G.; Wiley, J. B. Room Temperature Oxidative Intercalation with Chalcogen Hydrides: Two Step Method for the Formation of Alkali-Metal Chalcogenide Arrays within Layered Perovskite. *Mater. Res. Bull.* **2012**, *47*, 1289–1294.

85. Tefaghi, S. A.; Veiga, E. T.; Amand, G.; Wiley, J. B. Rapid Topochemical Modification of Layered Perovskites via Microwave Reactions. *Inorg. Chem.* **2016**, *55*, 1604–1612.

86. Hata, H.; Kubo, S.; Kobayashi, Y.; Mallouk, T. E. Preparation of a Blue Luminescent Nanosheet Derived from Layered Perovskite $Bi_2SrTa_2O_9$. *J. Am. Chem. Soc.* **2007**, *129*, 3064–3065.

87. Neiner, D.; Sweany, R. L.; Golub, V.; Wiley, J. B. Structure and Properties of Mixed Valence Titanates, $(Li_xVO)La_2Ti_3O_{10}$. *J. Mater. Chem.* **2006**, *16*, 186–191.

88. Viciu, L.; Kodenkandath, T. A.; Wiley, J. B. Construction of a Double-Layered Tetrahedral Network within a Perovskite Host: Two-Step Route to the Alkali-Metal-Halide Layered Perovskite, $(Li_xCl)LaNb_2O_7$. *J. Solid State Chem.* **2007**, *180*, 583–588.

89. Choi, J.; Zhang, X.; Wiley, J. B. Building Alkali-Metal-Halide Layers within a Perovskite Host by Sequential Intercalation: $(A_2Cl)LaNb_2O_7$ (A = Rb, Cs). *Inorg. Chem.* **2009**, *48*, 4811–4816.

90. Matsuda, T.; Miyamae, N.; Takeuchi, M. Intercalation of Various Alcohols in $HLaNb_2O_7$. *Bull. Chem. Soc. Jpn.***1993**, *66*, 1551–1553.

91. Takahashi, S.; Nakato, T.; Hayashi, S.; Sugahara, Y.; Kuroda, K. Formation of Methoxy-Modified Interlayer Surface via the Reaction between Methanol and Layered Perovskite $HLaNb_2O_7.xH_2O$. *Inorg. Chem.* **1995**, *34*, 5065–5069.

92. Wang, Y.; Wang, C. H.; Wang, L. L.; Hao, Q. Y.; Zhu, X. B.; Chen, X. H.; Tang, K. B. Preparation of Interlayer Surface Tailored Protonated Double-Layered Perovskite $H_2CaTa_2O_7$ with n-Alcohols, and Their Photocatalytic Activity. *RSC Adv.* **2014**, *4*, 4047–4054.

93. Toihara, N.; Yoneyama, Y.; Shimada, A.; Tahara, S.; Sugahara, Y. Intercalation of Triethylphosphine Oxide Bearing a Phosphoryl Group into Dion–Jacobson-Type Ion-Exchangeable Layered Perovskites. *Dalton Trans.* **2015**, *44*, 3002–3008.

94. Bizeto, M. A.; Shiguiharab, A. L.; Constantino, V. R. L. Layered Niobate Nanosheets: Building Blocks for Advanced Materials Assembly. *J. Mater. Chem.* **2009**, *19*, 2512–2525.

95. Kim, Y. H.; Kim, H. J.; Osada, M.; Li, B. W.; Ebina, Y.; Sasaki, T. 2D Perovskite Nanosheets with Thermally-Stable High-κ Response: A New Platform for High-Temperature Capacitors. *ACS Appl. Mater. Interfaces* **2014**, *6*, 19510−19514.

96. Treacy, M. M. J.; Rice, S. B.; Jacobson, A. J.; Lewandowski, J. T. Electron Microscopy Study of Delamination in Dispersions of the Perovskite-Related Layered Phases $K[Ca_2Na_{n-3}Nb_nO_{3n+1}]$: Evidence for Single-Layer Formation. *Chem. Mater.* **1990**, *2*, 281.

97. Keller, S. W.; Kim, H. N.; Mallouk, T. E. Layer-by-Layer Assembly of Intercalation Compounds and Heterostructures on Surfaces: Toward Molecular "Beaker" Epitaxy. *J. Am. Chem. Soc.* **1994**, *116*, 8817–8818.

98. Sasaki, T.; Watanabe, M.; Hashizume, H.; Yamada, H.; Nakazawa, H. Macromolecule-like Aspects for a Colloidal Suspension of an Exfoliated Titanate. Pairwise Association of Nanosheets and Dynamic Reassembling Process Initiated from It. *J. Am. Chem. Soc.* **1996**, *118*, 8329–8335.

99. Schaak, R. E.; Mallouk, T. E. Prying Apart Ruddlesden-Popper Phases: Exfoliation into Sheets and Nanotubes for Assembly of Perovskite Thin Films. *Chem. Mater.* **2000**, *12*, 3427–3434.

100. Schottenfeld, J. A.; Kobayashi, Y.; Wang, J.; Macdonald, D. D.; Mallouk, T. E. Proton-Conducting Films of Nanoscale Ribbons Formed by Exfoliation of the Layer Perovskite $H_2SrTa_2O_7$. *Chem. Mater.* **2008**, *20*, 213–219.

101. Sasaki, T.; Watanabe, M. Osmotic Swelling to Exfoliation. Exceptionally High Degrees of Hydration of a Layered Titanate. *J. Am. Chem. Soc.* **1998**, *120*, 4682–4689.

102. Liu, Y.; Xiong, J.; Luo, S.; Liang, R.; Qin, N.; Liang, S.; Wu, L. Ultrathin $HNbWO_6$ nanosheets: facile synthesis and enhanced hydrogen evolution performance from photocatalytic water splitting. *Chem. Commun.* **2015**, *51*, 15125-15128.

103. Gopalakrishnan, J.; Sivakumar, T.; Ramesha, K.; Thangadurai, V.; Subbanna, G. N. *J. Am. Chem. Soc.* **2000**, *122*, 6237–6241.

104. Sivakumara, T.; Gopalakrishnana, J. Transformation of Dion–Jacobson Phase to Aurivillius Phase: Synthesis of $(PbBiO_2)MNb_2O_7$ (M = La, Bi). *Mat. Res. Bull.* **2005**, *40*, 39–45.

105. Hoffmann, M. R.; Martin, S. T.; Choi, W.; Bahnemann, D. W. Environmental Applications of Semiconductor Photocatalysis. *Chem. Rev.* **1995**, *95*, 69-96.

106. Kalogirou, S. A. Seawater Desalination using Renewable Energy Sources. *Prog. Energy Combust. Sci.* **2005**, *31*, 242-281.

107. Zhang, H.; Chen, G.; Bahnemann. D. W. Photoelectrocatalytic Materials for Environmental Applications. J. *Mater. Chem.* **2009,** *19*, 5089–5121.

108. Zhang, D.; Li, G.; Yu, J. C. Inorganic Materials for Photocatalytic Water Disinfection. *J. Mater. Chem.* **2010**, *20*, 4529-4536.

109. Hashim, N.; Natarajan, P.; and Ray, K. A.; Intrinsic Kinetic Study for Photocatalytic Degradation of Diclofenac under UV and Visible Light. *Ind. Eng. Chem. Res.* **2014**, *53*, 18637−18646

110. Shiklomanov, I.A.; Appraisal and Assessment of World Water Resources. *Water International*. **2000**, 25, 11-32.

111. Zhou, L.; Gao, C.; Xu, W. Magnetic Dendritic Materials for Highly Efficient Adsorption of Dyes and Drugs. *ACS Appl. Mater. Interfaces* **2010**, *2*, 1483-1491.

112. Kim, W. J.; Pradhan, D.; Min, B.-K.; Sohn, Y. Adsorption/Photocatalytic Activity and Fundamental Natures of BiOCl and $BiOCl_xI_{1-x}$ Prepared in Water and Ethylene Glycol Environments, and Ag and Au-doping Effects. *Appl. Cat. B: Envoirn.* **2014**, *147*, 711-725.

113. Na, Y.; Kim, Y. I.; Cho, D. W.; Pradhan, D.; Sohn, Y. Adsorption/Photocatalytic Performances of Hierarchical Flowerlike $BiOBr_xCl_{1-x}$ Nanostructures for Methyl Orange, Rhodamine B and Methylene Blue. *Mater. Sci. Semicond. Process.* **2014**, *27*, 181-190

114. Dong, S.; Feng, J.; Fan, M.; Pi, Y.; Hu, L.; Han, X.; Liu, M.; Sun, J.; Sun, J. Recent Developments in Heterogeneous Photocatalytic Water Treatment using Visible Light Responsive Photocatalysts: A Review. *RSC Adv*. **2015**, *5*, 14610–14630.

115. Sharma, M.; Vaidya, S.; Ganguli, A. K. Enhanced Photocatalytic Activity of g-C_3N_4-TiO_2 Nanocomposites for Degradation of Rhodamine B dye. *J Photochem. Photobiol. A: Chem*. **2017**, *335*, 287–293.

116. Osterloh, F. E. Inorganic Materials as Catalysts for Photochemical Splitting of Water. *Chem. Mater*. **2008**, *20*, 35–54.

117. Kudo, A.; Miseki, Y. Heterogeneous Photocatalyst Materials for Water Splitting. *Chem. Soc. Rev.*, **2009**, *38*, 253–278.

118. Chen, X.; Shen, S.; Guo, L.; Mao, S. S. Semiconductor-Based Photocatalytic Hydrogen Generation. *Chem. Rev.* **2010**, *110*, 6503–6570.

119. Ma, Y.; Wang, X.; Jia, Y.; Chen, X.; Han, H.; Li, C. Titanium Dioxide-Based Nanomaterials for Photocatalytic Fuel Generations. *Chem. Rev*. **2014**, *114*, 9987–10043.

120. Ajmal, A.; Majeed, I.; Malik, R.N.; Idriss, H.; and Nadeem, M.A.; Principles and mechanisms of photocatalytic dye degradation on TiO_2 based photocatalysts: a comparative overview. *RSC Adv*. **2014**, *4*, 37003–37026.

121. Linsebigler, A. L.; Lu, G.; Yates, J. T. Photocatalysis on TiO_2 Surfaces: Principles, Mechanisms, and Selected Results. *Chem. Rev*. **1995**, *95*, 735-758.

122. Chen, C.; Ma W.; Zhao, J. Semiconductor-mediated photodegradation of pollutants under visible-light irradiation. *Chem. Soc. Rev*. **2010**, *39*, 4206-4219

123. Bora, L. V.; Mewada, R. K. Visible/solar light active photocatalysts for organic effluent treatment: Fundamentals, mechanisms and parametric review. *Renew. Sustain. Energ. Rev.* **2017**, *76*, 1393–1421

124. Chong, M.N.; Jin, B.; Chow, C. W. K. Recent developments in photocatalytic water treatment technology: A review. *Water Research*. **2010**, *44*, 2997-3027.

125. Gogate, P. R.; Pandit, A. B. A Review of Imperative Technologies for Wastewater Treatment: Oxidation Technologies at Ambient Conditions. *Advances in Environmental Research*. **2004**, *8*, 501–551.

126. J. Sa, Fuel Production with Heterogeneous Catalysis (Boca Raton, FL: CRC Press, **2015**).

127. Chatterjee, D.; Dasgupta, S.; Visible light Induced Photocatalytic Degradation of Organic Pollutants. *J. Photochem. Photobiol. C: Photochem. Rev.* **2005**, 6,186–205.

128. Jang, J. S.; Kim, H. G.; Lee, J. S. Heterojunction Semiconductors: A Strategy to Develop Efficient Photocatalytic Materials for Visible Light Water Splitting. *Catal. Today* **2012**, *185*, 270−277.

129. Roy, N.; Park, Y.; Sohn, Y.; Leung, K. T.; Pradhan, D. Green Synthesis of Anatase TiO_2 Nanocrystals with Diverse Shapes and their Exposed Facets-Dependent Photoredox Activity. *ACS Appl. Mater. Interfaces* **2014**, *6*, 16498–16507.

130. Roy, N.; Sohn, Y.; Leung, K. T.; Pradhan, D. Engineered Electronic States of Transition Metal Doped TiO_2 Nanocrystals for Low Over potential Oxygen Evolution Reaction. *J. Phys. Chem. C* **2014**, *118*, 29499−29506.

131. Oshima, T.; Ichibha, T.; Qin, K. S.; Muraoka, K.; Vequizo, J. J. M.; Hibino, K.; Kuriki, R.; Yamashita, S.; Hongo, K.; Uchiyama, T.; Fujii, K.; Lu, D.; Maezono, R.; Yamakata, A.; Kato, H.; Kimoto, K.; Yashima, M.; Uchimoto, Y.; Kakihana, M.; Ishitani, O.; Kageyama, H.; Maeda, K. Undoped Layered Perovskite Oxynitride $Li_2LaTa_2O_2N$ for Photocatalytic CO_2 Reduction with Visible Light. *Angew. Chem. Int. Ed.* **2018**, *57*, 8154–8158.

132. Gopalakrishnan, J.; Bhat, V. $A_2Ln_2Ti_3O_{10}$ (A = K or Rb; Ln = La or Rare Earth): A New Series of Layered Perovskites Exhibiting Ion Exchange. *Inorg. Chem.* **1987**, *26*, 4329–4301.

133. Takata, T.; Shinohara, K.; Tanaka, A.; Hara, M.; Kondo, J. N.; Domen, K. A Highly Active Photocatalyst for Overall Water Splitting with a Hydrated Layered Perovskite Structure. *J. Photochem. Photobiol.* A **1997**, *106*, 45–49.

134. Takata, T.; Furumi, Y.; Shinohara, K.; Tanaka, A.; Hara, M.; Kondo. J. N.; Domen. K. Photocatalytic Decomposition of Water on Spontaneously Hydrated Layered Perovskites. *Chem. Mater*. **1997**, *9*, 1063–1064.

135. Thaminimulla, C. T. K.; Takata, T.; Hara, M.; Kondo, J. N.; Domen, K. Effect of Chromium Addition for Photocatalytic Overall Water Splitting on Ni–$K_2La_2Ti_3O_{10}$. *J Catal.* **2000**, *196*, 362–365.

136. Rodionov, I. A.; Silyukov, O. I.; Utkina, T. D.; Chislov, M. V.; Sokolova, Y. P.; Zvereva, I. A. Photocatalytic Properties and Hydration of Perovskite-Type Layered Titanates $A_2Ln_2Ti_3O_{10}$ (A = Li, Na, K; Ln = La, Nd). *Russ. J. Gen. Chem.* **2012**, *82*, 1191–1196

137. Wang, Y.; Lai, X.; Lü, X.; Li, Y.; Liu, Q.; Lin, J.; and Huang, F.; Tailoring the photocatalytic activity of layered perovskites by opening the interlayer vacancy via ion-exchange reactions. *CrystEngComm.* **2015**, *17*, 8703–8709.

138. Ikeda, S.; Hara, M.; Kondo, J. N.; Domen, K.; Preparation of $K_2La_2Ti_3O_{10}$ by polymerized complex method and photocatalytic decomposition of water. *Chem. Mater.* **1998**, *10*, 72–77.

139. Huang, Y.; Wu, J.; Wei, Y.; Hao, S.; Huang, M.; Lin, J. Synthesis and photocatalytic activity of hydrated layered perovskite $K_{2-x}La_2Ti_{3-x}Nb_xO_{10}$ ($0 \leqslant x \leqslant 1$) and protonated derivatives. *Scr. Mater*. **2007**, *57*, 437−440.

140. Ya, H. Y.; Yuan, Q. C.; Zhou, L. Y.; Jie, L. Study on the photocatalytic activity of $K_2La_2Ti_3O_{10}$ doped with zinc (Zn). *Appl. Surf. Sci*. **2009**, *255*, 8419−8424.

141. Yang, Y.; Chen, Q.; Yin, Z.; Li, J. Study on the Photocatalytic Activity of $K_2La_2Ti_3O_{10}$ Doped with Vanadium (V). *J. Alloys Compd.* **2009**, *488*, 364−369.

142. Wang, B.; Li, C.; Hirabayashi, D.; Suzuki, K. Hydrogen evolution by photocatalytic decomposition of water under ultraviolet− visible irradiation over $K_2La_2Ti_{3-x}M_xO_{10+\delta}$ perovskite. *Int. J. Hydro. Energy*. **2010**, *35*, 3306−3312.

143. Huang, Y.; Wei, Y.; Cheng, S.; Fan, L.; Li, Y.; Lin, J.; Wu, J. Photocatalytic Property of Nitrogen-doped Layered Perovskite $K_2La_2Ti_3O_{10}$. *Sol. Energy Mater. Sol. Cells* **2010**, *94*, 761−766.

144. Kumar, V.; Uma, S.; Govind. Investigation of Cation (Sn^{2+}) and Anion (N^{3-}) Substitution in favor of Visible Light Photocatalytic Activity in the Layered Perovskite $K_2La_2Ti_3O_{10}$. *J. Hazard. Mater.* **2011**, *189*, 502−508.

145. Cui, W.; Liu, L.; Ma, S.; Liang, Y.; Zhang, Z. CdS-sensitized $K_2La_2Ti_3O_{10}$ composite: a new photocatalyst for hydrogen evolution under visible light irradiation. *Catal. Today* . **2013**, *207*, 44−49.

146. Cui, W.; Guo, D.; Liu, L.; Hu, J.; Rana, D.; Liang, Y. Preparation of $ZnIn_2S_4/K_2La_2Ti_3O_{10}$ composites and their photocatalytic H_2 evolution from aqueous Na_2S/Na_2SO_3 under visible light irradiation. *Catal. Commun.* **2014**, *48*, 55−59.

147. Cui, W.; An, W.; Liu, L.; Hu, J.; Liang, Y. A Novel Nano-sized BiOBr Decorated $K_2La_2Ti_3O_{10}$ with Enhanced Photocatalytic Properties under Visible Light. *J. Solid State Chem.* **2014**, *215*, 94−101.

148. Kawashima, K.; Hojamberdiev, M.; Wagata, H.; Yubuta, K.; Domen, K.; Teshima, K. Protonated Oxide, Nitrided, and Reoxidized $K_2La_2Ti_3O_{10}$ Crystals: Visible-Light-Induced Photocatalytic Water Oxidation and Fabrication of Their Nanosheets. *ACS Sustain. Chem. Eng.* **2017**, *5*, 232−240.

149. Akihiko, K.; Satoshi, H.; H_2 or O_2 Evolution from Aqueous Solutions on Layered Oxide Photocatalysts Consisting of Bi^{3+} with $6s^2$ Configuration and d^0 Transition Metal Ions. *Chem. Lett.***1999**, *28*, 101103-1104.

150. Kim. H. G.; Hwang. D. W.; and Lee. J. S.; An Undoped, Single-Phase Oxide Photocatalyst Working under Visible Light. *J. Am. Chem. Soc*. **2004**, *126*, 8912-8913.

151. Kim, H. G.; Becker, O. S.; Jang, J. S.; Ji, S. M.; Borse, P. H.; Lee. J. S. A generic method of visible light sensitization for perovskite-related layered oxides: Substitution effect of lead. *J Solid State Chem.* **2006**, *179*, 1214-1218.

152. Sun, S.; Wang, W.; Xu, H.; Zhou, L.; Shang, M.; Zhang, L. $Bi_5FeTi_3O_{15}$ Hierarchical Microflowers: Hydrothermal Synthesis, Growth Mechanism, and Associated Visible-Light-Driven Photocatalysis. *J. Phys. Chem. C* **2008**, *112*, 17835–17843.

153. Jang, J. S.; Yoon, S. S.; Borse, P. H.; Lim, K. T.; Hong, T. E.; Jeong, E. D.; Jung, O. S.; Shim, Y. B.; Kim, H. G. Synthesis and Characterization of Aurivillius Phase $Bi_5Ti_3FeO_{15}$ Layered Perovskite for Visible Light Photocatalyst. *J Ceram. Soc. of Jpn*. **2009**, *117*, 1268-1272.

154. Naresh, G.; Mandal, T. K. Excellent Sun-Light-Driven Photocatalytic Activity by Aurivillius Layered Perovskites, $Bi_{5-x}La_xTi_3FeO_{15}$ (x = 1, 2). *ACS Appl. Mater. Interfaces* **2014**, *6*, 21000−21010.

157. Liu, X.; Xu, L.; Huang, Y.; Qin, C.; Qin. L.; Seo, H. J. Improved Photochemical Properties of Aurivillius $Bi_5Ti_3FeO_{15}$ with Partial Substitution of Ti^{4+} with Fe^{3+}. *Ceram. Int.* **2017**, *43*, 12372–12380.

156. Sun, H.; Yao, T.; Xie, X.; Lu, Y.; Wang, Y.; Xu, Z.; Han, J.; Chen, X. Ni, Eu-Co Doping Effect on the Photocatalytic Activity and Magnetic Recyclability in Multifunctional Single-Phase Photocatalysts $Bi_5FeTi_3O_{15}$. *J Colloid and Interface Sci.* **2019**, *534*, 499–508.

157. Naresh, G.; Mandal, T. K. Efficient COD Removal Coinciding with Dye Decoloration by Five- Layer Aurivillius Perovskites under Sunlight-Irradiation. *ACS Sustainable Chem. Eng*. **2015**, *3*, 2900-2908.

158. Naresh, G.; Malik, J.; Meena, V.; Mandal, T. K. pH Mediated Collective and Selective Solar Photocatalysis by a series of Layered Aurivillius Perovskites. *ACS Omega* **2018**, *3*, 11104-11116.

159. Li, X.; Ju, Z.; Li, F.; Huang, Y.; Xie, Y.; Fu, Z.; Knized, R. J.; Lu, Y. Visible Light Responsive $Bi_7Fe_3Ti_3O_{21}$ Nanoshelf Photocatalysts with Ferroelectricity and Ferromagnetism. *J. Mater. Chem. A* **2014**, *2*, 13366–13372.

160. Kumar, S.; Parthasarathy, R.; Singh, A. P.; Wickman, B.; Thirumald, M.; Ganguli, A. K. Dominant {100} Facet Selectivity for Enhanced Photocatalytic Activity of $NaNbO_3$ in $NaNbO_3$/CdS Core/Shell Heterostructures. *Catal. Sci. Technol.* **2017**, *7*, 481–495.

161. Kumar, S.; Malik, T.; Sharma, D.; Ganguli, A. K. $NaNbO_3/MoS_2$ and $NaNbO_3/BiVO_4$ Core−Shell Nanostructures for Photoelectrochemical Hydrogen Generation. *ACS Appl. Nano Mater.* **2019**, *25*, 2651−2662.

162. Ogawa, K.; Nakada, A.; Suzuki, H.; Tomita, O.; Higashia, M.; Saeki, A.; Kageyama, H.; Abe, R. Flux Synthesis of Layered Oxyhalide Bi_4NbO_8Cl Photocatalysts for Efficient Z-scheme Water Splitting Under Visible Light. *ACS Appl. Mater. Interfaces* **2019**, *11*, 5642–5650.

163. Maeda, K.; Mallouk, T. E. Comparison of Two- and Three-Layer Restacked Dion–Jacobson Phase Niobate Nanosheets as Catalysts for Photochemical Hydrogen Evolution. *J. Mater. Chem.* **2009,** *19*, 4813–4818.

164. Xu, N.; Takei, T.; Miura, A.; Kumada, N. Photocatalytic Activities of Layered Niobate Perovskite with Substitution of Ti and W for Nb. *J ion exchange* **2014**, *4*, 242–247.

165. Xu, N.; Takei, T.; Miura, A.; Kumada, N. Preparation and Phase Transformation of Ag or Bi Ion-Exchanged Layered Niobate Perovskite and Their Photocatalytic Properties. *J ceram. Soc. Jpn.* **2015**, *123*, 690–694.

166. Li, Y.; Chen, L.; Zhang, H.; Lv, Z. Band Structure and Photocatalytic Activities for H2 Production of $ABi_2Nb_2O_9$ (A= Ca, Sr, Ba). *Int. J. Hydrogen Energy* **2010**, *35*, 2652–2656.

167. Wu, W.; Liang, S.; Wang, X.; Bi, J.; Liu, P.; Wu, L. Synthesis, Structures and Photocatalytic Activities of Microcrystalline $ABi_2Nb_2O_9$ (A = Sr, Ba) Powders. *J. Solid State Chem.* **2011**, *184*, 81–88.

168. Wu, W.; Liang, S.; Chen, Y.; Shen, L.; Zheng, H.; Wu. L. High Efficient Photocatalytic Reduction of 4-Nitroaniline to p-Phenylenediamine over Microcrystalline $SrBi_2Nb_2O_9$. *Catal. Commun*. **2012**, *17*, 39–42

169. Domen, K.; Yoshimura, J.; Sekine, T.; Tanaka, A.; Onishi, T. A Novel Series of Photocatalysts with an Ion-Exchangeable Layered Structure of Niobate, *catal. Lett*. **1990**, *4*, 339–344.

170. Takata, T.; Tanaka, T.; Hara, M.; Kondo, J. N.; Domen, K. Recent Progress of Photocatalysts for Overall Water Splitting. *Catal. Today* **1998**, *44*, 17–26.

171. Ebina, Y.; Tanaka, A.; Kondo, J. N.; Domen. K. Preparation of Silica Pillared $Ca_2Nb_3O_{10}$ and Its Photocatalytic Activity. *Chem. Mater*. **1996**, *8*, 2534–2538.

172. Ebina, Y.; Sasaki, T.; Harada, M.; Watanabe, M. Restacked Perovskite Nanosheets and Their Pt-Loaded Materials as Photocatalysts. *Chem. Mater*. **2002**, *14*, 4390–4395.

173 Burovikhina, A. A.; Rodionov, I. A.; Chislov, M. V.; Porotnikov, D. A.; Zvereva, I. A. Photocatalytic Activity of Layered Niobates $ANdNb_2O_7$ (A = H, Li, Na, Rb, Cs). I*nt. J. Nanotechnol*. **2016**, *13*, 158–167.

174. Wu. W.; Liu, G.; Liang, S.; Chen, Y.; Shen, L.; Zheng, H.; Yuan, R.; Hou, Y.; Wu, Ling. Efficient Visible-Light-Induced Photocatalytic Reduction of 4-Nitroaniline over Nanocrystalline $PbBi_2Nb_2O_9$. *J catal.* **2012**, *290*, 13–17.

175. Wu, W.; wen, L.; Shen, L.; Liang, R.; Yuan, R.; Wu. L. A New Insight into the Photocatalytic Reduction of 4-Nitroaniline to p-Phenylenediamine in the Presence of Alcohols. *Appl. Catal. B: Environ*. **2013**, *130*, 163–167.

176. S Hong, S. J.; Borse, P. H.; Ji, S. M.; Jang J. S.; Lee. J. S. Structure of $PbBi_2Nb_2O_9$ and Its Cr-Doped Layered Perovskite System and Their Photocatalytic Activities. *J. Kor. Phys. Soc*. **2007**, *51*, S27–S31.

177. Kim, H. G.; Borse H. P.; Jang, J. S.; Jeong, E. D.; Lee, J. S. Enhanced photochemical properties of electron rich W-doped $PbBi_2Nb_2O_9$ layered perovskite material under visible-light irradiation. *Mater. Lett.* **2008**, *62*, 1427–1430.

178. J Yosbimura, J.; Ebina, Y.; Kondo, J.; Domen, K.; Visible Light Induced Photocatalytic Behavior of a Layered Perovskite Type Niobate, $RbPb_2Nb_30_{10}$. *J. Phys. Chem.* **1993**, *97*, 1970–1973.

179. Huang, Y.; Xie, Y.; Fan, L.; Li, Y.; Wei, Y.; Lin, J.; Wu. J. Synthesis and Photochemical Properties of La-Doped $HCa_2Nb_3O_{10}$. *Int. J Hydro. Energy* **2008**, *33*, 6432–6438.

180. Hu, Y.; Guo, P.; Guo, L.; Synthesis and Photocatalytic Properties of Cr-Doped $KSr_2Nb_3O_{10}$ for Hydrogen Production. *Int. J Hydro. Energy* **2012**, *37*, 1007–1013.

181. Hu, Y.; Shi, J.; Guo, L. Enhanced Photocatalytic Hydrogen Production Activity of Chromium Doped Lead Niobate under Visible-Light Irradiation. *Appl. Catal. A: General* **2013**, *468*, 403– 409.

182. Czech, B.; Hojamberdiev, M. Visible-Light-Driven Photocatalytic Activity of Three-Layer Perovskite Dion Jacobson Phase $CsBa_2M_3O_{10}$ (M= Ta, Nb) and Oxynitride Crystals in the Removal of Caffeine from Model Wastewater. *J Photochem. Photobiol A Chem*. **2016**, *324*, 70–80.

183. Reddy, J. R.; Kurra, S.; Guje, R.; Palla, S. Veldurthi, N. K.; Ravi, G.; Vithal, M. Photocatalytic Degradation of Methylene Blue on Nitrogen Doped Layered Perovskites, $CsM_2Nb_3O_{10}$ (M = Ba and Sr). *Ceram. Int.* **2015**, *41*, 2869–2875.

184. Okamoto, Y.; Ida, S.; Hyodo, J.; Hagiwara, H.; Ishihara, T. Synthesis and Photocatalytic Activity of Rhodium-Doped Calcium Niobate Nanosheets for Hydrogen Production from a Water/Methanol System without Cocatalyst Loading. *J. Am. Chem. Soc.* **2011**, *133*, 18034–18037.

185. Jiang, D.; Wang, T.; Xu, Q.; Li, D.; Meng, S.; Chen, M. Perovskite Oxide Ultrathin Nanosheets/g-C_3N_4 2D-2D Heterojunction Photocatalysts with Significantly Enhanced Photocatalytic Activity Towards the Photodegradation of Tetracycline. *Appl. Catal. B: Environ.* **2017**, *201*, 617–628.

186. Jiang, D.; Wen, B.; Xu, Q.; Gao, M.; Li, D.; Chen, M. Plasmonic Au Nanoparticles/$KCa_2Nb_3O_{10}$ nanosheets 0D/2D heterojunctions with enhanced photocatalytic

activity towards the degradation of tetracycline hydrochloride. *J. Alloy and compound* **2018**, *762*, 38–45.

187. Zhang, Z. J.; Wang, W. Z.; Gao, E. P.; Sun, S. M.; Zhang, L. Photocatalysis Coupled with Thermal Effect Induced by SPR on Ag-Loaded Bi_2WO_6 with Enhanced Photocatalytic Activity. *J. Phys. Chem. C* **2012,** *116*, 25898−25903.

188. Ren, J.; Wang, W. Z.; Sun, S. M.; Zhang, L.; Chang, J. Enhanced Photocatalytic Activity of Bi_2WO_6 Loaded with Ag Nanoparticles under Visible Light Irradiation. *Appl. Catal. B* **2009**, *92*, 50−55.

189. Guo, S.; Li, X. F.; Wang, H. Q.; Dong, F.; Wu, Z. B. Fe-Ions Modified Mesoporous Bi_2WO_6 Nanosheets with High Visible Light Photocatalytic Activity. *J. Colloid Interface Sci.* **2012**, *369*, 373−380.

190. Wang, J.; Gao, X. M.; Fu, F.; Zhang, L. P.; Wu, Y. F. Photocatalytic Degradation of Phenol-Containing Wastewater over Cu-Bi_2WO_6 Composite under Visible Light Irradiation. *J. Residuals Sci. Technol.* **2012**, 9, 101−106.

191. He, D. Q.; Wang, L. L.; Xu, D. D.; Zhai, J. L.; Wang, D. J.; Xie, T. F. Investigation of Photocatalytic Activities over Bi_2WO_6/$ZnWO_4$ Composite under UV Light and Its Photoinduced Charge Transfer Properties. *ACS Appl. Mater. Interfaces* **2011**, *3*, 3167−3171.

192. Gui, M. S.; Zhang, W. D.; Chang, Y. Q.; Yu, Y. X. One-Step Hydrothermal Preparation Strategy for Nanostructured WO_3/Bi_2WO_6 Heterojunction with High Visible Light Photocatalytic Activity. *Chem. Eng. J.* **2012**, *197*, 283−288.

193. Li, H. Q.; Cui, Y. M.; Hong, W. S. High Photocatalytic Performance of BiOI/Bi_2WO_6 toward Toluene and Reactive Brilliant Red. *Appl. Surf. Sci.* **2013**, *264*, 581−588.

195. Tian, Y. L.; Chang, B. B.; Lu, J. L.; Fu, J.; Xi, F. N.; Dong, X. P. Hydrothermal Synthesis of Graphitic Carbon Nitride−Bi_2WO_6 Heterojunctions with Enhanced Visible Light Photocatalytic Activities. *ACS Appl. Mater. Interfaces* **2013**, *5*, 7079−7085.

196. Huang, H. W.; Wang, S. B.; Tian, Na.; Zhang, Y. H. A One-Step Hydrothermal Preparation Strategy for Layered $BiIO_4/Bi_2WO_6$ Heterojunctions with Enhanced Visible Light Photocatalytic Activities. *RSC Adv*. **2014**, *4*, 5561−5567.

197. Singh, A.; Dutta, D. P.; Roy, M.; Tyagi, A. K.; Fulekar, M. H. Sonochemical Synthesis, Characterization, and Photocatalytic Properties of $Bi_{2-2x}Sb_xWO_6$ Nanorods. *J. Mater. Sci.* **2014**, *49*, 2085-2097.

198. Uma, S.; Singh, J.; Thakral, V. Facile Room Temperature Ion-Exchange Synthesis of Sn^{2+} Incorporated Pyrochlore-Type Oxides and Their Photocatalytic Activities. *Inorg. Chem.* **2009**, *48*, 11624–11630.

CHAPTER -2

Characterization Techniques

Characterization Techniques

All the synthesized niobates, tungstates and titanates reported here were characterized by an array of advanced analytic techniques. These include powder X-Ray diffraction (P-XRD), Field emission-scanning electron microscopy (FE-SEM), Selected area electron diffraction (SEAD), transmission electron microscopy (TEM), Energy Dispersive Spectroscopy (EDS), Fourier transform Infrared spectroscopy (FT-IR), Ultraviolet-visible diffuse reflectance spectroscopy (UV-vis DRS), superconducting quantum interference device (SQUID) magnetometry, Photoluminescence (PL) spectroscopy, Electrochemical impedance spectroscopy (EIS) and zeta–potential. The formation of products at every stage of the synthesis were monitored by P-XRD analysis. The morphology and chemical composition of the compounds were characterized by FE-SEM, EDS and HR-TEM analysis. XPS was employed for the determination of the oxidation states of the elements. Further, the optical properties were investigated by UV-vis DRS and the band gap energies were estimated with the help of Tauc plots. Dye adsorption, zeta potential and PL studies were carried out to understand the surface charge effects on the adsorption and relative e^{-}–h^{+} recombination effects across a homologous series of catalysts. The experimental details of P-XRD, FE-SEM, EDS, HR-TEM, XPS, Raman, FT-IR, UV-vis DRS, PL, EIS and Zeta potential techniques and the details of the instrument used along with a brief description of the basic principles are discussed in this chapter.

2.1 Powder X-ray Diffraction

Powder X-ray diffraction is a commonly used analytical technique to characterize the solid compounds. It is mostly used to differentiate between crystalline and amorphous compound, for phase identification, measurement of phase purity and determination of unit cell parameters etc. As every compound shows its own characteristic fingerprint P-XRD pattern, this is highly powerful in identifying the structure type based on the diffraction pattern. The principle of X- ray diffraction is based the on constructive and destructive interference of radiations diffracted by a solid sample when a beam of monochromatic X- ray falls on it. The interaction of the crystalline sample with the incident X-ray produces

diffractive rays and a constructive interference occurs when the Bragg condition is satisfied as given by the Bragg's law.

$$n\lambda = 2d\sin\theta \quad (2.1)$$

where, λ is the wavelength of the incident X-ray beam, d stands for interplanar spacing between diffracting planes, θ is the incident angle and *n*, is any integer known as the order of diffraction.[1]

In the present work, P-XRD pattern of the samples were recorded using a Bruker AXS D8 Advance diffractometer operating at 40 kV and 30 mA, using graphite monochromatized Cu-Kα radiation (λ = 1.54Å) and Smart Lab, Rigaku, Japan with Co–Kα (1.78 Å) in the range 2θ = 5–90°. For P-XRD measurements, few hundred milligrams of powder sample were placed in the sample holder and the surface of the sample was smoothened with the help of a glass slide.

The collected diffraction data of the prepared compounds were analyzed by comparing the observed data with the standard diffraction data files (JCPDS-PDF). The unit cell parameters of all the newly prepared compounds were calculated by least-squares refinement of the observed reflections with the help of PROSZKI program.[2] 'Powder Cell 2.4' software was used for the simulation of the X-ray diffraction patterns.[3] The crystal structure data, such as space group, atomic position, occupancy and thermal parameters required for the simulation of powder patterns were taken from the model structures, the refined lattice parameters were taken from the least-square refinement.

Rietveld refinements of the structures were carried by using the FULLPROF program Suite.[4] The Rietveld refinement was performed with experimental P-XRD data and this method is based on the minimization of a residual function based on the difference between the observed and calculated intensity data. For this purpose, a slow scan P-XRD data collected over a period of 6-8 hours using Cu-Kα (λ = 1.54 Å) radiation in the angular range of 10-90º. For refinement runs, cell parameters and the background coefficients along with zero-shift were refined first. Then subsequently, the profile parameters, atomic positions, thermal parameters, occupancy etc. were refined more or less in the same sequence for all the structures.

2.2 Field-Emission Scanning Electron Microscopy and Energy Dispersive X-ray Spectroscopy (FE-SEM and EDS)

Field emission - scanning electron microscopy (FE-SEM) is a type of electron microscopic technique that not only is used to get information about the particle morphology and surface topography of the samples, but chemical composition of the samples as well if used with an energy dispersive detector (EDD).[5,6] It is well known that the electron microscopy, in general, is a more advanced microscopic technique in comparison to the simple optical microscopy due to its high magnification, resolution and depth of focus that is achievable as it uses high energy electrons beam as radiation source. In the FE-SEM, magnetically controlled electrons beam are directed towards the specimen with help of various types of lenses, such as condenser and objective lenses. When incident electron beam falls on the specimen, different types of signals such as, back scattered electrons (BSE), secondary electrons (SE), X-rays etc. are emitted from the specimen. The secondary electrons generated from the sample are used to produce the image of the sample, whereas, BSE and X-ray are used for compositional and elemental analysis.

The EDS mode was used for the elemental composition and mapping analysis of all the synthesized samples. X-ray spectra were collected from the large area of the sample as well as from individual crystallites. The elemental composition was estimated based on the average elemental ratio at several locations of the sample to confirm the homogeneity. The elemental mapping was carried out to determine the distribution of the elements in a selected area of the samples. For the preparation of samples for SEM analysis, specimen powders were smeared on the double-sided adhesive carbon tapes pasted on the aluminum stubs. For the electrical conductivity, gold coating was carried out using gold sputtering technique under argon atmosphere. For the present study, the morphology and elemental compositions were analyzed with Carl Zeiss, Ultra 55 FE-SEM (Germany), operating at 20 kV.

2.3 High Resolution - Transmission Electron Microscopy (HR-TEM)

Transmission Electron Microscope (TEM) is an electron microscope in which a high-energy electron beam passes through a thin specimen. The electron beam interacts with the specimen during the transmission and a highly magnified image is formed on to the

fluorescent screen or to be detected by a charged coupled device camera. Several electromagnetic lenses contained in the microscope column control the electron beam. These lenses are used to regulate the size and angular spread of the electron beam. Two different modes of operation are used by changing position of projector lens called image mode and the other is the diffraction mode.[7]

In the diffraction mode, selected area electron diffraction (SAED) patterns were recorded and the diffraction spots were indexed to confirm the crystal structures and lattice spacing as ascertained from P-XRD analysis. In the image mode, images of thin sample were taken to observe the morphology and particle size. In addition, the high-resolution mode was used to determine the direct image of atomic planes called lattice fringes.

In our study, TEM images with high-resolution lattice fringes and SAED pattern were recorded using both FEI-TECHNAI G^2 operating with an accelerating voltage of 200 kV and a JEOL FE (3200FS HRTEM) operating at 300 kV accelerating voltage. For the TEM analysis, about 3 mg of finely powdered sample were dispersed in 2-3 mL of ethanol in a agate mortar-pestle and ground for 15 minutes. One drop of the suspension was put on a carbon coated copper grid with the help of a micropipette and allowed to dry in air a day before the microscopy experiment was carried out.

2.4 X-Ray Photoelectron Spectroscopy

X-Ray Photoelectron Spectroscopy (XPS) is most usable surface analysis technique, which can be applied to a broad range of materials. It has been also popularly known as Electron spectroscopy for chemical analysis (ESCA). The XPS technique is used for the qualitative and quantitative analysis of chemical compounds based on the oxidation state of various chemical elements present on the surface of the material being studied. The average depth of analysis for an XPS measurement is approximately 5 nm. XPS is performed by exciting the sample surface by a beam of monochromatic X-ray, usually of from an Al-K_α or Mg-K_α source, which causes photoelectrons to be emitted from the sample surface. Electron energy analysis by the instrument with a hemispherical analyzer one can estimate the energy of the photoelectrons emitted and deduce its respective elemental identity and chemical state

that helps in qualitative and quantitative analysis. XPS usually requires a very high or ultra-high vacuum conditions (P =10^{-8} to 10^{-9} mbar).[8]

In the present work, spectra were recorded with an X-ray photoelectron spectrometer, PHI 5000 VersaProbe III operating with monochromatic Al-K_α ($h\nu$ = 1486.6 eV) and Mg-K_α ($h\nu$ = 1253.3 eV) X-ray source. All the binding energies were corrected with reference to the C 1s peak at 284.8 eV. The MULTIPAK software was used for the peak analysis and de-convolution studies.

2.5 Fourier Transform - Infrared (FT-IR) Spectroscopy

Fourier Transform – Infrared (FT-IR) spectroscopy is a readily available and widely applicable spectroscopy method used for obtaining chemical information about the functional group present in organic molecules and mostly polymers. The basic principle of FT-IR spectroscopy is based on the interaction of infrared light with molecules.[9] The FTIR spectrum is formed by the energy absorptivity of chemical bands. The following relation is used to calculate the energy content of the light, which is directly proportional to its wavenumber:

$$E = hcw \tag{2.2}$$

where, E is energy of incident radiation, *w* is the wavenumber, *h* is the Planck's constant (6.63 × 10^{-34} J s^{-1}) and *c* is the speed of light (3.0 ×10^{8} m s^{-1}). The range of wavenumbers between 4000 and 400 cm^{-1} is defined as the mid-infrared range and mostly used to study the fundamental vibrations. All materials above absolute zero of temperature (-273.15 °C) emit infrared (IR) light. When the infrared light is focused on a molecule, it can be absorbed by the molecule causing fundamental vibrations in the atomic bonds of appropriate frequency. Since, specific atomic groups absorb infrared light of particular wavenumbers; therefore, based on this, the molecular structure can be identified.

The plot of measured infrared absorbance versus wavenumber is called the infrared spectrum. The intensity of the IR absorption band is proportional to the rate of change of the dipole moment in a molecule, with respect to the displacement of atoms.

A NICOLET 6700 FT-IR (Thermo Scientific) infrared spectrometer was used to analyze the samples by IR spectroscopy. KBr was used as a reference. Sample for IR analysis was prepared by mixing of a pinch of sample with KBr and pressed into a transparent pellet.

2.6 Raman Spectroscopy

Raman spectroscopy is a technique mostly similar to the IR spectroscopy. However, IR activity arises due the changing dipole moment in a molecule whereas; the Raman signal arises due to the change in polarizability of the molecule by same interactions. [10,11] Thus, both techniques are useful in identifying the type of molecular vibration present in a test sample. When the light passes through a medium, some part of the light scatters and deviates. However, most of the scattered light shows original energy but some of the photons of the scattered light shows loss or gain in the original energy. When the energy remains unchanged during the scattering process, the phenomenon is called Rayleigh scattering or elastic scattering. However, when energy shows loss or gain during scattering process, it is called Raman scattering or inelastic scattering process.

During the interaction of light with molecules, molecules get excited and relax back. If the molecules relax back to the same vibrational level, the light will have the same energy (frequency) similar to the incident light, known as Rayleigh scattering. If molecules return to a higher or lower vibrational level, the molecule will have absorbed or released some vibrational energy ($h\nu_1$), called Raman scattering. In this case, the electronic state remains the same, but vibrational state changes. When the molecules return to a higher vibrational energy level, it is called Stokes Raman scattering ($h\nu_o$-$h\nu_1$), and when the molecules return to a lower vibrational level the process is called Anti-Stokes Raman scattering ($h\nu_o$+$h\nu_1$), where, ν_o and ν_1 corresponds to the wave number of each vibrational mode, and h is the Planck`s constant.[9]

In the present work, Renishaw inVia Raman spectrometer (Serial no. 021R88) using an Ar ion laser (514 nm) were used for the Raman measurements. The spectrophotometer is equipped with a confocal microscope through different objective lenses with a spectral resolution of $1cm^{-1}$.

2.7 Photoluminescence (PL)

The photoluminescence measurement was carried out at room temperature using Fluoromax-4 spectrofluorometer. For this purpose, 10 mg of the photocatalyst was suspended in 10 ml methanol and sonicated for 10 minutes. The samples were excited at an excitation

wavelength of 315 nm and the excitation and emission slit width 5 nm were used. The PL emissions spectra gave indirect information about the recombination of the photo-generated electron hole. The higher the electron-hole recombination, the higher would be the luminescence intensity for a semiconductor, provided other scattering events and non-radiative processes are very same in the compounds.

2.8 Electrochemical Impedance Spectroscopy (EIS)

Electrochemical impedance test was conducted using a galvanostate (model; Versastat 3, PAR) based on a conventional three electrode assembly. In the experiment, the catalyst was mixed with graphite paste as the working electrode; Pt wire was used as the counter electrode and Ag/AgCl (3 M KCl) as the reference electrode. For the electrolyte, 10 mM $K_3[Fe(CN)_6]$ solution containing 0.1 M KCl was used. All tests were carried out in the frequency range of 0.02 Hz to 100 kHz at 0.24 V and the amplitude of the applied sinusoidal potential perturbation of ±5 mV.

2.9 UV-Vis Diffuse Reflectance Spectroscopy (UV-Vis DRS)

UV-Vis DRS is a widely used technique to study the optical properties for powder solid materials. UV –Vis DRS spectra of synthesized compounds were recorded using a Shimadzu UV-2450 UV-Vis spectrophotometer within the wavelength range 240-800 nm employing an integrating sphere. The technique involves the measurement of diffuse reflected light from all possible specular reflections. For a typical experiment, 40 mg of the powder sample and 4 gm of $BaSO_4$ were taken and mixed well with a mortar-pestle by grinding thoroughly for 15-20 minutes. $BaSO_4$ was used as a reference material for the baseline correction. After that, the mixture was pressed in sample holder with the help of the cylindrical glass slide. Then, the sample holder was put into the integrating sphere of spectrophotometer to record the reflectance spectrum. According to the Kubelka-Munk (K-M) theory, the reflectance data were converted to absorptions.[12]

$$F(R_\infty)=(1-R_\infty)^2/2R_\infty \quad (2.3)$$

where, $F(R_\infty)$ is the Kubelka-Munk function and R is diffuse reflectance. The band gap of the samples were calculated by extrapolating the linear portion of the absorption coefficient versus energy using the below expression.[13]

$$(\alpha h\nu)^{1/n} = A(h\nu - E_g) \quad (2.4)$$

The above expression is called the Tauc equation. where A, E_g, $h\nu$ and α are proportionality constant, band gap, incident light frequency and absorption coefficient, respectively. The exponent value n, determines the nature of electronic transition; for indirect transition, $n = 2$ and for a direct transition, $n = ½$ were used.[14,15]

2.10 Photocatalytic Activity Test

The photocatalytic activity of catalyst were examined by the dye degradation at various pH. For this, RhB, MO and CR were selected as model dye and natural light irradiation, High Pressure Mercury Vapor Lamp (HPMVL 250 W) and Medium Pressure Mercury Vapor Lamp (MPMVL 250 W) were used as radiation source for the degradation of dye solutions. The pH (2, 7 and 11) of the dye solution was adjusted by adding of dil. HCl and NaOH. For sunlight driven studies, the catalyst degradation experiments were conducted at IIT Roorkee (29°51′ N; 77°53′ E), and the solar Direct Normal Irradiance (DNI) of sunlight-irradiation was ~ 216 W/m^2 in the month of October, 2016 (Chapter-3), ~ 248 W/m^2 in the month of April, 2017 (Chapter-4), ~ 143 W/m^2 in the month of May, 2016 (Chapter 5). For the degradation experiment, 100 mL of the dye solution (1×10^{-5} M, with appropriate pH) and 100 mg of powder photocatalyst were taken in a 250 ml beaker. Before sunlight irradiation, the dye-catalyst suspensions were magnetically stirred in the dark for a definite time, to ensure the adsorption-desorption equilibrium between the dye and photocatalyst. Later, the of dye-catalyst suspension was placed in the direct sunlight irradiation. During the degradation experiments, dye concentration was measured by taking 5 mL suspension at regular time intervals and centrifuging the suspension at 8000 rpm to remove the catalyst particles and recording the absorption of the filtrates using a Shimadzu 2450 UV-visible spectrophotometer. To maintain the constant volume the suspension of dye-catalyst, dye solution was put back into the beaker after collecting the absorbance data. For degradation efficiency calculation and self-degradation correction, a blank test (without the catalyst) was

also performed under the same condition. The degradation efficiencies of the catalysts were calculated using the following expression:

$$\text{Degradation (\%)} = (1 - C/C_0) \times 100 \quad (2.5)$$

where, C_0 and C is the initial concentration and concentration of the dye at different time intervals, respectively.

2.10.1 Chemical Oxygen Demand Test

To analysis the COD of the dye solution before and after the photocatalysis, COD measurements were carried out by using UV-visible spectrophotometer and a digestion unit (DRB 200, HACH, USA). To calculate the photodegradation efficiency, the following expression was used:

$$\text{Photodegradation efficiency} = \frac{\text{Initial COD} - \text{Final COD}}{\text{Initial COD}} \times 100 \quad (2.6)$$

2.10.2 Scavenger Test

To detect the reactive species (•OH, h^+ and $O_2^{\bullet-}$) involved in the photocatalytic dye degradation under the sunlight, scavenger tests were performed. In this experiment, prior to the addition of the catalyst in the dye solution, different scavengers were added to the dye solution. For this study, tertiary butyl alcohol (t-BuOH), ammonium oxalate (AO), and benzoquinone (BQ) were employed as •OH, h^+ and $O_2^{\bullet-}$ scavenger, respectively.[16] The experimental procedure for the reactive species was same as described above in the photodegradation studies.

2.10.3 Catalyst Stability and Photocatalytic Cycle Test

The stability of the catalyst was investigated by performing the cycle test of photocatalytic degradation in the acidic medium with the same catalyst and recording the P-XRD of recovered catalyst. For this experiment, dye solution (100 mL of 1×10^{-5} M) and a fixed amount of catalyst (100 mg) were taken and the photocatalytic degradation studies were carried out by the similar manner as mentioned above in the activity test. For cycle test, after

the first cycle, the catalyst was recovered with the help of centrifuge. For the second cycle, a fresh solution of the dye was used to the recover catalyst suspension subjected to magnetic stirring in the dark for adsorption-desorption equilibrium followed by photocatalytic degradation under direct sunlight-irradiation. The same process was continued for other cyclic runs. After the last cycle test, the catalyst was separated and dried. The catalyst thus obtained was also subjected to P-XRD and XPS analysis to evaluate the crystalline and chemical stability of the catalysts under the reaction conditions.

REFERENCES

1. West, A. R. Solid State Chemistry and Its Applications. Wiley Publishers, **2011**.

2. Losocha, W.; Lewinski, K. PROSZKI- A System of Programs for Powder Diffraction Data Analysis. *J. Appl. Crystallogr.* **1994**, *27*, 437–438.

3. Kraus, W.; Nolze, G. POWDER CELL - A Program for the Representation and Manipulation of Crystal Structures and Calculation of the Resulting X-ray Powder Patterns. *J. Appl. Crystallogr*. **1996**, *29*, 301–303.

4. Rietveld, H. M. A Profile Refinement Method for Nuclear and Magnetic Structures. *J. Appl. Cryst*. **1969**, *2*, 65–71.

5. Wetzig, K.; Schulze, D. In Situ Scanning Electron Microscopy in Materials Research. AkademieVerlag **1995**.

6. Joy, C. D. Scanning Electron Microscopy Characterization of Materials. Curr. Opin. Solid State Mater. Sci. **1997**, *2*, 465–468.

7. Pennycook, S. J.; Eds. Williams, D. B.; Carter, C. B. Transmission Electron Microscopy: A Text Book for Materials Science. Microscopy and Microanalysis **2010**, *16*, 111–111.

8.Moulder, J. F.; Stickle, W. F.; Sobol, P, E.; Bomben, K. D. Handbook of X- ray Photoelectron Spectroscopy. Published by, Perkin-Elmer Corporation, **1992**.

9. D. Bougeard et al. Infrared and Raman Spectroscopy: methods and applications, published by Wiley VCH Verlag GmbH, **1995**.

10. Long, D. A. Raman Spectroscopy. Published by McGraw-Hill Book Company, **1977**.

11. Ferraro, J. R.; Nakamoto, K.; Brown, C. W. Introductory Raman Spectroscopy. Published by Academic Press, **1994**.

12. Kubelka, P.; Munk, F. EinBeitragzurOptik der Farbanstriche. Z. *Tech. Phys.* **1931**, *12*, 593–601.

13. Tauc, J.; Grigorovic, R.; Vancu, A. Optical Properties and Electronic Structure of Amorphous Germanium. *Phys. Status Solidi* **1966**, *15*, 627–637.

14. Kim, M. R.; Kang, Y.; Jang, D. Synthesis and Characterization of Highly Luminescent CdS@ZnS Core−Shell Nanorods. *J. Phys. Chem. C* **2007**, *111*, 18507–18511.

15. Joshi, U. A.; Maggard, P. A. $CuNb_3O_8$: A p-Type Semiconducting Metal Oxide Photoelectrode. *J. Phys. Chem. Lett.* **2012**, *3*, 1577–1581.

16. Kumar, S.; Parthasarathy, R.; Singh, A. P.; Wickman, B.; Thirumald, M.; Ganguli, A. K. Dominant {100} Facet Selectivity for Enhanced Photocatalytic Activity of $NaNbO_3$ in $NaNbO_3$/CdS core/shell Heterostructures. *Catal. Sci. Technol.* **2017**, *7*, 481–495.

CHAPTER -3

Double-Layer Aurivillius Niobates as Sunlight Active Photocatalyst: Synthesis, Magnetism and Photocatalytic Activity

Double-Layer Aurivillius Niobates as Sunlight Active Photocatalyst: Synthesis, Magnetism and Photocatalytic Activity

3.1 INTRODUCTION

Utilization of solar energy using semiconducting oxides for renewable energy generation, catalytic conversions and environmental remediation has gained a great deal of attention as prime areas of inorganic materials research. In recent years, a wide range of oxides are reported as important photocatalysts owing to their prospective applications in the production of hydrogen, breakdown of environmental pollutants and wastewater treatment.[1-4] Organic pollutants (such as, phenols, dyes etc.) are substantially present in wastewater effluents of industries such as textile, organic dye-stuffs, adhesives, leather goods, pharmaceuticals etc., and adversely affect the human and aquatic life. Therefore, removal of organic pollutants from aqueous medium is essential and a variety of techniques, such as, chemical oxidation, reduction, biodegradation, adsorption and photocatalytic degradation have been used for their removal. Photocatalytic degradation can be considered as an environment friendly technique for complete mineralization of pollutants/organic dyes into CO_2 and H_2O using semiconductors.[5,6] After Fujishima and Honda's report of water splitting with TiO_2 (E_g = 3.2 eV) photocatalyst under UV-light in 1972,[10,7] vast majority of photocatalytic research were conducted utilizing UV-light. The abundance of visible-light (~ 43%) and scarcity of UV- light (~ 5%) in the solar radiation restricts the practical application of TiO_2 and other UV-active photocatalysts under natural sunlight. Various strategies are adopted by researchers to reduce the band gap of UV-active semiconductors so as to make them visible-light active.[6,8-18]

While the compositional modifications of semiconducting oxides are quite common in three dimensional oxides, they are infrequent in case of layered oxides especially with the perovskite structure. This is primarily due to the inherent difficulty in stabilizing the layered structure after compositional variations even with a small amount of substitution in the perovskite block particularly when the perovskite layer thickness is low. The difficulty may arise while dealing with the charge compensation of the substituent due to the limited choice of the A-site cations. In addition, often the inherent and competing phase stability of the $3d^n$

transition metal containing ternary perovskites under the reaction condition makes the formation of phase pure layered perovskites difficult. Nevertheless, many layered perovskites exhibiting a wide range of structural, physical, chemical and electronic properties have been reported during the past two decades.[19-43] These perovskites have attracted current attention due to their interesting magnetic, [23,24,30,36] ferroelectrics, [20,25,35,41] dielectric[22,23,25,30,33,34,39] multiferroic[29,34,37,38] and photocatalytic[26,28,31,32,36,37,40,42,43] properties. In this context, the photocatalytic activities of Aurivillius phases are noteworthy. This is primarily due to their visible-light-driven activity and excellent chemical stability.[-31,32,36,37,40,42-44]

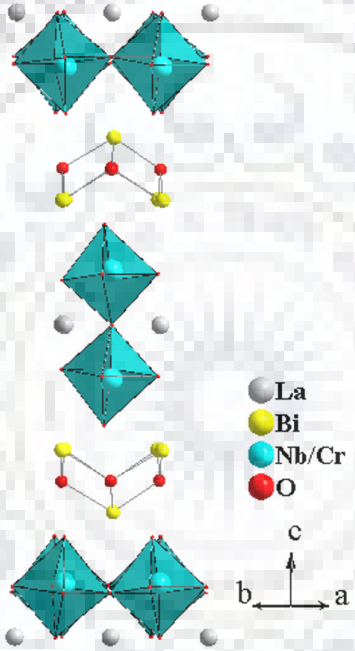

Figure 3.1 Crystal structure of $LaBi_2Nb_{1.5}Cr_{0.5}O_9$.

In the recent past, photocatalytic activity of few Bi-containing double layered niobates, $ABi_2Nb_2O_9$ (A = Ca, Sr, Ba), are investigated for water splitting and environmental remediation purposes mainly under UV-light.[45-47] However, visible-light-driven activity is also reported with a lead substituted double layered Aurivillius niobate, $PbBi_2Nb_2O_9$, where the substitution of lead has been claimed as a generic method for visible light sensitization.[48-50]Along similar lines, Ag exchange in the Dion-Jacobson niobate, $RbLaNb_2O_7$, has been shown to exhibit visible-light-driven photocatalytic activity.[51,52] But, only in few cases heterovalent substitutions of Aurivillius niobates are reported. [20,53-55]To the best of our knowledge, there seems to be only one report with thorough structural characterization of a

$3d^n$ metal substituted double layered Aurivillius niobate, which can be thought of as heterovalent coupled substitution of $SrBi_2Nb_2O_9$ to form $Bi_3Fe_{0.5}Nb_{1.5}O_9$ by replacing Sr with Bi at the A-site and part of Nb with Fe at the B-site maintaining the overall cationic charge.[23] Moreover, the solubility of the B-site substituent seems to be limited in the double-layer Aurivillius structure.

While many layered perovskites with visible-light activity are known in case of titanates, only few are reported with the niobates. In line with our group's current research interests, we have envisaged the synthesis of lead free $3d^n$ metal substituted double-layer Aurivillius niobates through coupled substitution of both *A*- and *B*-sites to develop visible-light active photocatalysts. The phase formation, stability and structure of the $3d^n$ metal incorporated Aurivillius niobates are reported herein. The strategy has helped us to extend the absorption edges into the visible region (up to ~ 650 nm and beyond) in the new layered niobates, as compared to that at near UV-region (~ 400 nm) of the parent, $SrBi_2Nb_2O_9$. The photocatalytic activities are investigated by way of RhB degradation under sunlight and their performances are compared in the light of PL, EIS, ζ-potential and adsorption studies. In addition, the transition metal doping in the non-magnetic niobates has imparted paramagnetism that may help in the magnetic separation of the catalysts from the reaction medium. Interestingly, an interplay of FOJT and SOJT distortion has resulted in the stabilization of Mn compound in the LS state while the Fe and Co compounds form with the HS configurations. The details of these investigations are reported in the paper.

3.2 EXPERIMENTAL SECTION

3.2.1 Materials and Synthesis

The compounds, $LaBi_2Nb_{1.5}M_{0.5}O_9$ (M = Cr, Mn, Fe, Co) were synthesized by solid state reactions starting from Bi_2O_3 (Sigma-Aldrich, ≥ 98.0%), La_2O_3 (Sigma-Aldrich, 99.99%), (preheated at 950°C), Nb_2O_5 (Sigma-Aldrich, 99.99%), CrO_3 (Sigma-Aldrich, 99.9%) and $MnC_2O_4.2H_2O$, Fe_2O_3 (prepared by heating $FeC_2O_4.2H_2O$, Sigma-Aldrich, 99%) and $CoC_2O_4.2H_2O$. $MnC_2O_4.2H_2O$ and $CoC_2O_4.2H_2O$ were prepared in the laboratory by precipitation method starting from the corresponding transition metal salts [$Mn(NO_3)_2{\cdot}H_2O$, Sigma-Aldrich, 97%, and $Co(NO_3)_2{\cdot}6H_2O$, Sigma-Aldrich, 98%] and oxalic acid

$(COOH)_2.2H_2O$. In a typical synthesis, stoichiometric quantities of starting materials were thoroughly ground in a mortar and the mixture was calcined in air at 800, 900, 950 and 1050 °C for 12 h each with intermediate grinding. $SrBi_2Nb_2O_9$ was synthesized using the above mentioned condition as well as following the procedure

3.2.2 Photocatalytic Activity and Cycle Test

Photocatalytic activity of the reported compounds was investigated by way of dye degradation. For this purpose, Rhodamine B (RhB) was chosen as the model dye. Natural sunlight, high pressure MVL, medium pressure MVL were used as radiation source for the photocatalytic degradation of 1×10^{-5} M RhB aqueous solution. For sunlight driven studies all the photocatalytic experiments were carried out during the same time on consecutive days in the month of October, 2016 (having solar Direct Normal Irradiance ~ 216 W/m^2 during the month) at IIT Roorkee (29°51′ N; 77°53′ E). The degradation studies were performed over $LaBi_2Nb_{1.5}M_{0.5}O_9$ (M = Cr, Mn, Fe, Co) at various pH (pH 2, 7 and 11). In a typical experiment, 100 mg of powdered catalyst were dispersed in 100 mL of dye solution and stirred magnetically for 1h in the dark before photocatalysis. Thereafter, the dye-catalyst suspensions were exposed to the natural sunlight and 5 mL aliquots were withdrawn at regular time intervals, centrifuged at 8000 rpm (to remove solid particles) and absorbance data of the filtrate so obtained were recorded on a Shimadzu 2450 UV-vis spectrophotometer. For the photocatalytic degradation cycle tests, the once used catalyst was separated by centrifuge and a fresh 100 mL dye solution was added to it and the above procedure was repeated under the same experimental conditions. Moreover, a blank experiment without catalysts was carried out under identical conditions to exclude any self-degradation of the dye and make necessary correction to the degradation data.

3.2.3 Carbon Oxygen Demand (COD) Test

COD experiments were carried with a digestion unit (DRB 200, HACH, USA) and a UV-Visible spectrophotometer. COD data help to find out the mineralization of dye solution at different stages. For this, multiple sets of degradation experiments were carried out with the same amount of dye and catalyst. The dye-catalyst suspensions were exposed to sunlight

for different time intervals and aliquots were collected for the analysis. The photocatalytic degradation efficiency was calculated from the COD data using the following expression:

$$\text{Photodegradation efficiency} = \frac{\text{Initial COD} - \text{Final COD}}{\text{Initial COD}} \times 100$$

3.2.4 Adsorption and ζ-Potential Measurements

Adsorption studies were carried out for the determination of the amount of dye molecule adsorbed over the solid catalysts at different pH. For this, 100 mg of catalyst was dispersed in 100 mL of 1×10^{-5} M dye solution and stirred in the dark. Then, at every 30 min time interval, 5 mL of suspension was sampled, centrifuged for 2 min to remove the catalyst particles and the absorbance of the centrifugate was recorded using a Shimadzu 2450 UV-Vis spectrophotometer. The data were collected until the equilibrium adsorption (maximum adsorption) was reached. ζ-potential measurements for the compounds, $LaBi_2Nb_{1.5}M_{0.5}O_9$ (M = Cr, Mn, Fe, Co), were performed on a Malvern Zeta Sizer Nano ZS90 at different pH (2, 5, 7, 9 and 11) for exploring the character of surface charge on the semiconductor oxides. For this, 10 mg of catalyst was taken in 10 mL water of appropriate pH and the suspension was sonicated for 2 minutes prior to ζ-potential measurements.

3.2.5 Scavenger Tests

Scavenger tests were performed to understand the role of reactive species in RhB degradation under sunlight irradiation. For this study, tertiary butyl alcohol (t-BuOH), ammonium oxalate (AO), and benzoquinone (BQ) were used as •OH, h^+ and $O_2^{\bullet-}$ scavenger, respectively. In this experiment, 100 mg of catalyst was suspended in 100 mL of dye solution and after the addition of appropriate scavengers the suspension was stirred and adsorption equilibrated prior to the photocatalytic degradation studies.

3.3 RESULTS AND DISCUSSION

3.3.1 P-XRD Analysis

The P-XRD patterns of $LaBi_2Nb_{1.5}M_{0.5}O_9$ (M = Cr, Mn, Fe, Co) niobates are shown in Figure 3.2. The P-XRD data for all the compounds are similar and in agreement with the formation of double-layer Aurivillius niobates isostructural with the parent $SrBi_2Nb_2O_9$ (JCPDS PDF # 49-0607). In fact, all the compounds are nearly phase pure excepting that small amounts of unidentified impurities are detected at 2θ of 28.05° for Cr and Co and at 29.30° for Mn. All the diffraction peaks excepting these impurities are indexable in the orthorhombic $A2_1am$ space group as assigned for the parent $SrBi_2Nb_2O_9$. The indexed PXD data for all compounds are given in Tables 3.1, and 3.2 respectively.

The Rietveld structure refinement for all the compounds were carried out with the room temperature P-XRD data in the $A2_1am$ space group. The structural data of $SrBi_2Nb_2O_9$[56] were used as the initial input for the refinements. The $SrBi_2Nb_2O_9$ structure consists of double layer perovskite slabs of composition $[SrNb_2O_7]^{2-}$ with corner connected NbO_6 octahedra that are interleaved by fluorite-like $[Bi_2O_2]^{2+}$ layers. For structure refinements, initially La was placed exclusively at the A-site (in place of Sr) and the transition metal M (Cr, Mn, Fe or Co) was statistically incorporated at 25% of the B-sites. The refinement runs with statistical distribution of La both at A- and Bi-sites (i.e. in the $[Bi_2O_2]$-layer) did not yield better result in terms of improved reliability factors as compared to those with La exclusively occupying the A-site. Thus, all later refinements are performed by restricting all the La at the perovskite *A*-site and Bi in the $[Bi_2O_2]$- layers. To maintain the stability of the refinement runs and attain convergence all the general atomic positions are refined one by one. However, whenever possible convergences are achieved by refining multiple atom positions and their thermal parameters together. The observed, calculated and difference profiles for $LaBi_2Nb_{1.5}M_{0.5}O_9$ (M = Cr, Mn, Fe, Co) are shown in Figure 3.4. The Rietveld refined positional, thermal and occupancy parameters for all the compounds are given in Table 3.3. Table 3.3 shows the Rietveld refined lattice parameters along with the reliability factors obtained at the final convergence cycle. The crystal structures drawn from the refined coordinates are shown in Figure 3.

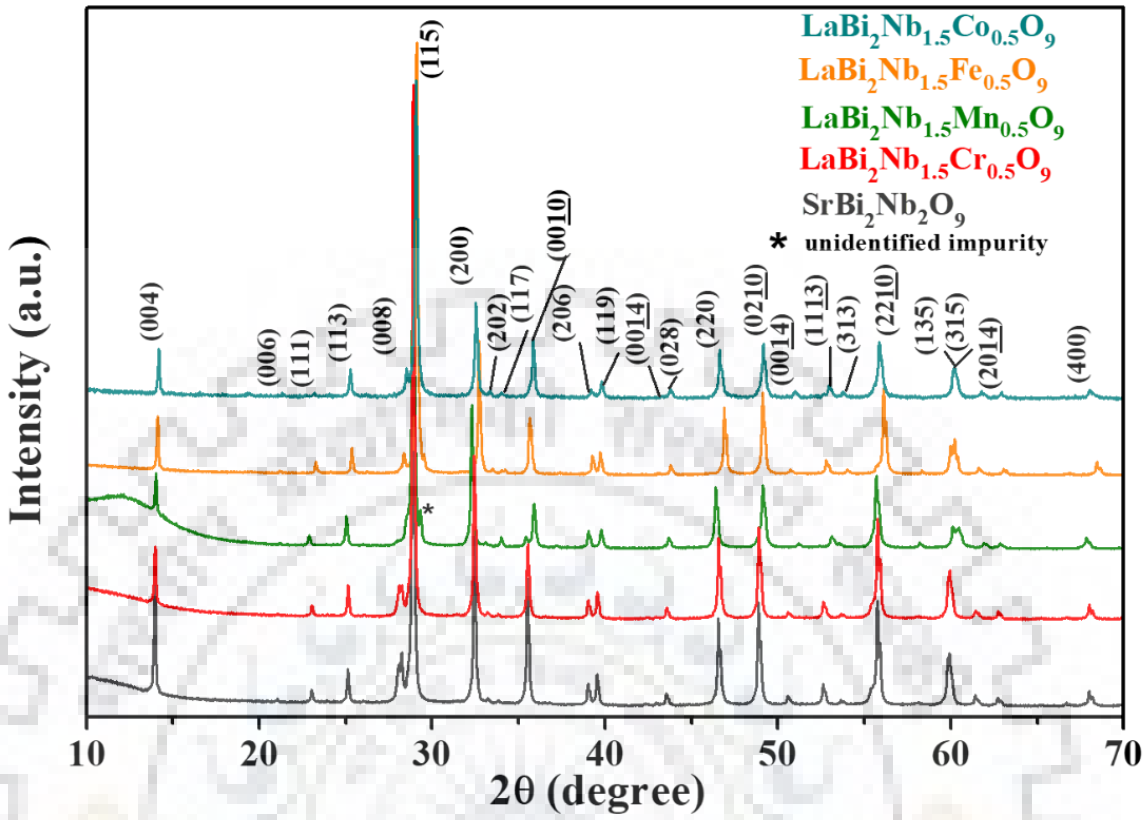

Figure 3.2 P-XRD patterns of $LaBi_2Nb_{1.5}M_{0.5}O_9$ (M = Cr, Mn, Fe, Co).

Table 3.1 Indexed P-XRD Data for $LaBi_2Nb_{1.5}M_{0.5}O_9$ (M = Cr, Mn)

$LaBi_2Nb_{1.5}Cr_{0.5}O_9$				$LaBi_2Nb_{1.5}Mn_{0.5}O_9$			
h k l	d_{obs}(Å)	d_{calc} (Å)	I_{obs}	*h k l*	d_{obs}(Å)	d_{calc} (Å)	I_{obs}
0 0 4	6.270	6.293	10	0 0 4	6.185	6.185	6
0 0 6	4.190	4.195	1	0 0 6	4.120	4.123	1
1 1 1	3.818	3.819	3	1 1 1	3.835	3.843	3
1 1 3	3.510	3.516	5	1 1 3	3.514	3.518	5
0 0 8	3.143	3.146	4	0 0 8	3.093	3.092	4
1 1 5	3.066	3.069	100	1 1 5	3.058	3.058	100
2 0 0	2.736	2.738	32	2 0 0	2.747	2.749	30
2 0 2	2.674	2.675	1	2 0 2	2.683	2.683	1
1 1 7	2.626	2.626	1	1 1 7	2.614	2.615	1
0 0 10	2.498	2.498	18	0 0 10	2.478	2.473	12
2 0 6	2.290	2.290	6	2 0 6	2.288	2.287	6
1 1 9	2.160	2.159	5	1 1 9	2.244	2.244	5
0 2 8	2.060	2.061	3	0 2 8	2.058	2.056	3
2 2 0	1.939	1.939	20	2 2 0	1.939	1.939	19
0 2 10	1.847	1.847	23	0 2 10	1.840	1.840	21
0 0 14	1.784	1.784	2	0 0 14	1.767	1.767	2
1 1 13	1.721	1.721	5	1 1 13	1.710	1.709	5
1 3 3	1.698	1.698	1	1 3 3	1.703	1.703	1
1 3 5	1.639	1.639	23	1 3 5	1.641	1.642	23
3 1 5	1.639	1.638	23	3 1 5	1.640	1.640	23
2 2 10	1.531	1.532	14	2 2 10	1.528	1.529	14
2 0 14	1.496	1.496	1	2 0 14	1.485	1.486	1
1 3 9	1.471	1.471	2	1 3 9	1.471	1.470	2
4 0 0	1.371	1.371	3	4 0 0	1.375	1.374	3

$LaBi_2Nb_{1.5}Cr_{0.5}O_9$; a = 5.486(1), b = 5.487(1), c = 24.981(6) Å

$LaBi_2Nb_{1.5}Mn_{0.5}O_9$; a = 5.498(1), b = 5.505(1), c = 24.749(2) Å

Table 3.2 Indexed P-XRD Data for $LaBi_2Nb_{1.5}M_{0.5}O_9$ (M = Fe, Co)

$LaBi_2Nb_{1.5}Fe_{0.5}O_9$				$LaBi_2Nb_{1.5}Co_{0.5}O_9$			
h k l	d_{obs}(Å)	d_{calc} (Å)	I_{obs}	*h k l*	d_{obs}(Å)	d_{calc} (Å)	I_{obs}
0 0 4	6.246	6.245	8	0 0 4	6.338	6.310	10
0 0 6	4.160	4.163	14	0 0 6	4.198	4.207	1
1 1 1	3.832	3.833	1	1 1 1	3.860	3.853	3
1 1 3	3.515	3.516	3	1 1 3	3.543	3.537	5
0 0 8	3.121	3.122	6	0 0 8	3.160	3.155	5
1 1 5	3.064	3.064	6	1 1 5	3.089	3.085	100
2 0 0	2.742	2.743	100	2 0 0	2.759	2.757	34
2 0 2	2.679	2.679	30	2 0 2	2.695	2.694	1
1 1 7	2.626	2.626	1	1 1 7	2.647	2.647	1
0 0 10	2.498	2.498	1	0 0 10	2.526	2.524	17
2 0 6	2.290	2.290	18	2 0 6	2.307	2.306	6
1 1 9	2.160	2.159	6	1 1 9	2.278	2.276	5
0 2 8	2.060	2.061	5	0 2 8	2.076	2.075	3
2 2 0	1.939	1.939	3	2 2 0	1.949	1.949	20
0 2 10	1.847	1.847	20	0 2 10	1.862	1.861	23
0 0 14	1.784	1.784	23	0 0 14	1.801	1.803	2
1 1 13	1.721	1.721	2	1 1 13	1.737	1.738	5
1 3 3	1.698	1.698	5	1 3 3	1.707	1.707	1
1 3 5	1.639	1.639	1	1 3 5	1.647	1.647	28
3 1 5	1.639	1.638	23	3 1 5	1.647	1.648	28
2 2 10	1.531	1.532	14	2 2 10	1.552	1.543	18
2 0 14	1.496	1.496	1	2 0 14	1.508	1.509	1
1 3 9	1.471	1.471	2	1 3 9	1.480	1.480	2
4 0 0	1.371	1.371	3	4 0 0	1.378	1.378	4

$LaBi_2Nb_{1.5}Fe_{0.5}O_9$; a = 5.476(1), b = 5.477(1), c = 25.179(6) Å

$LaBi_2Nb_{1.5}Co_{0.5}O_9$; a = 5.516(1), b = 5.512(1), c = 24.244(2) Å

The in-plane lattice parameters (*a* and *b*) of the $3d^n$ metal substituted niobates largely remain unchanged due to the heterovalent coupled substitution across the series, Cr, Mn, Fe and Co, while the *c*-parameter shows an unusual contraction for the Mn compound. This appears striking given the near equal ionic radii of Nb^{5+}, Fe^{3+} and Mn^{3+} (ca. 0.64 Å) and slightly smaller ionic radii of Cr^{3+} and Co^{3+} (ca. 0.61 Å). The bond length variations (Figure 3.5) are consistent with the above facts. However, the unequal bonds both in the *a*-*b* plane and in the *c*-direction are due to more prominent SOJT distortion of the $4d^0$ Nb^{5+}, because in the present double layer niobates the $3d^n$ transition metal content is only 25%. Therefore, the SOJT effect is expected to dominate the octahedral distortion and consequent bond length variations. Overall octahedral distortion (Table 3.6) and the bond length variation in the transition metal incorporated double layer niobates are similar to those of other layered niobates.[56,58]

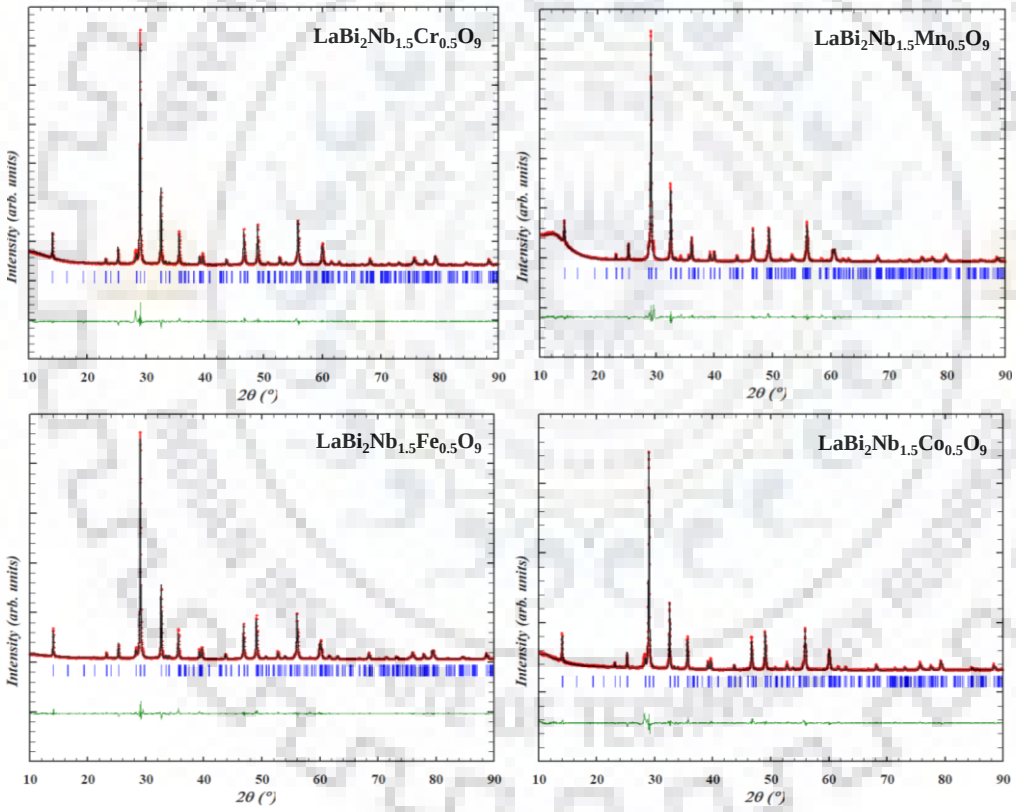

Figure 3.3 Rietveld refinement from P-XRD data for $LaBi_2Nb_{1.5}Mn_{0.5}O_9$ (M = Cr, Mn, Fe, Co). Observed (×), calculated (–) and difference (at bottom) profiles are shown. Vertical bars below the profile mark the Bragg reflection positions.

The anomalously small *c*-parameter in $LaBi_2Nb_{1.5}Mn_{0.5}O_9$ may be due to competing effects of second order Jahn-Teller (SOJT) distortion of $Nb^{5+}(4d^0)O_6$ octahedra and a first

order Jahn-Teller (FOJT) distortion of Mn^{3+}(high spin $3d^4$)O_6 octahedra. Interestingly, a detail analysis of the axial and equatorial bonds of the distorted MnO_6 octahedra shows the smallest difference between the average axial and the equatorial bond distances, although the reverse is expected due a Jahn-Teller elongation effect from a d^4 Mn^{3+} cation. This may probably indicate some sort of electron redistribution in the Mn-3*d* orbital under the competing effects of FOJT and SOJT, wherein the SOJT wins over the FOJT effect due to the higher percentage of Nb in the compound.

Table 3.3 Positional, Thermal and Occupancy Parameters for $LaBi_2Nb_{1.5}M_{0.5}O_9$ (M= Cr, Mn, Fe, Co)

Site	Atom	Coordinates	Cr	Mn	Fe	Co	Occ.
		y	0.244(1)	0.243(1)	0.246(2)	0.246(1)	
		B	0.89	0.89	0.89	0.89	
8b	Bi	*x*	0.497(2)	0.491(1)	0.496(4)	0.506(5)	1
		y	0.732(5)	0.736(2)	0.741(1)	0.742(1)	
		z	0.200(2)	0.200(1)	0.201(5)	0.200(1)	
		B	1.7	1.65	1.57	1.57	
8b	Nb/M	*x*	0.502(4)	0.496(2)	0.495(2)	0.507(2)	0.75/0.25
		y	0.754(2)	0.749(2)	0.760(2)	0.751(1)	
		z	0.412(1)	0.412(3)	0.412(4)	0.411(1)	
		B	0.35	0.35	0.35	0.35	
4a	O1	*x*	0.459(1)	0.460(2)	0.471(1)	0.467(3)	1
		y	0.212(1)	0.220(5)	0.212(3)	0.212(1)	
		B	1.70	1.70	1.70	1.70	
8b	O2	*x*	0.465(1)	0.468(1)	0.473(1)	0.469(5)	1
		y	0.797(1)	0.796(2)	0.803(1)	0.768(2)	
		z	0.339(5)	0.340(5)	0.339(3)	0.339(5)	
		B	1.20	1.20	1.20	1.20	
8b	O3	*x*	0.740(5)	0.735(3)	0.743(1)	0.731(1)	1
		y	-0.005	-0.005	-0.005	-0.005	
		z	0.249(1)	0.252(1)	0.249(2)	0.248(2)	
		B	0.89	0.89	0.89	0.89	
8b	O4	*x*	0.682(3)	0.679(1)	0.672(1)	0.690(5)	1
		y	0.959(2)	0.959(4)	0.965(4)	0.952(1)	
		z	0.081(2)	0.084(1)	0.083(1)	.0844(2)	
		B	0.50	0.50	0.50	0.50	
8b	O5	*x*	0.738(4)	0.727(1)	0.734(1)	0.742(1)	1
		y	0.992(5)	0.975(1)	0.982(3)	0.967(3)	
		z	0.571(4)	0.569(2)	0.567(3)	0.567(2)	
		B	0.60	0.60	0.60	0.60	

Table 3.4 Rietveld Refined Lattice Parameters and Reliability Factors for $LaBi_2Nb_{1.5}M_{0.5}O_9$ (M = Cr, Mn, Fe, Co)

Parameters	Cr	Mn	Fe	Co
***a*(Å)**	5.5034(1)	5.5018(1)	5.4824(1)	5.4969(1)
***b*(Å)**	5.5019(1)	5.5078(1)	5.4825(1)	5.4974(1)
***c*(Å)**	25.195(1)	24.859(1)	25.213(1)	25.170(1)
$R_{p\ (\%)}$	4.00	4.05	4.14	4.42
$R_{wp\ (\%)}$	6.34	6.59	5.63	6.71
$R_{expt\ (\%)}$	2.29	2.59	2.92	2.78
$R_{Bragg\ (\%)}$	4.59	4.00	3.56	4.79
$R_{F\ (\%)}$	3.93	3.11	3.59	5.18

Table 3.5 Bond Types and Bond Lengths for $LaBi_2Nb_{1.5}M_{0.5}O_9$ (M = Cr, Mn, Fe, Co).

Bond Type	Cr	Mn	Fe	Co
M/Nb-O_1	2.219	2.187	2.238	2.242
M/Nb-O_2	1.885	1.818	1.857	1.844
M/Nb-O_4	1.906	1.890	1.889	1.935
M/Nb-O_4	2.120	2.088	2.161	2.071
M/Nb-O_5	1.888	1.837	1.865	1.826
M/Nb-O_5	2.056	2.170	2.077	2.186
Bi-O_3	2.263	2.227	2.288	2.218
Bi-O_3	2.279	2.241	2.272	2.242
Bi-O_3	2.324	2.343	2.343	2.376
Bi-O_3	2.403	2.420	2.419	2.425

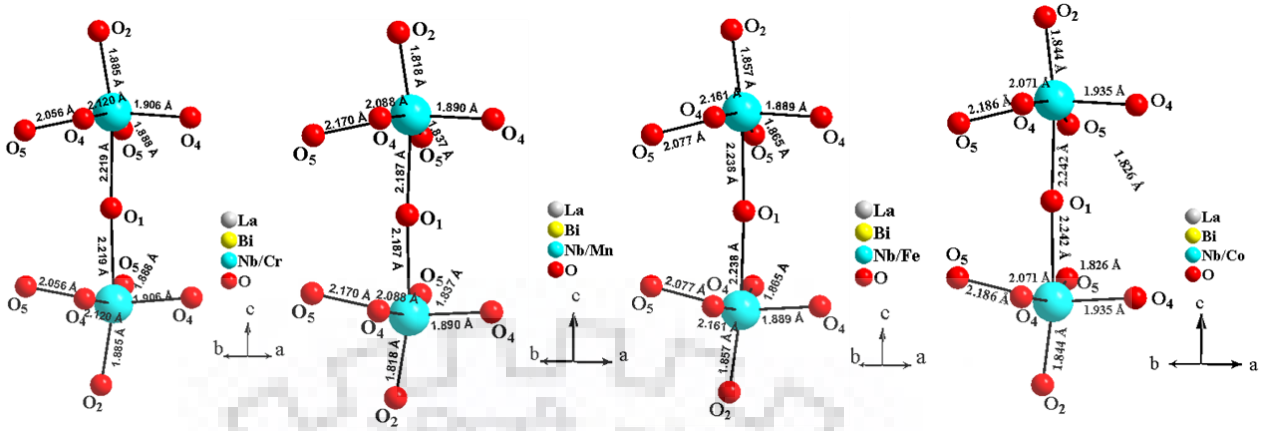

Figure 3.4 Octahedral coordination environment of the double-layer perovskite block for $LaBi_2Nb_{1.5}M_{0.5}O_9$ (M = Cr, Mn, Fe and Co).

Table 3.6 Octahedral Distortion Parameters, Average Axial, Equatorial and Difference Bond Distances for $LaBi_2Nb_{1.5}M_{0.5}O_9$ (M = Cr, Mn, Fe, Co).

Compounds	Octahedral distortion parameter (Δ_o)	Average axial bond distance (d_{avg}^{ax}/Å)	Average equatorial bond distance (d_{avg}^{eq}/Å)	Difference (d_{avg}^{ax}) - (d_{avg}^{eq})
$LaBi_2Nb_{1.5}Cr_{0.5}O_9$	0.0244	2.0520	1.9925	0.0590
$LaBi_2Nb_{1.5}Mn_{0.5}O_9$	0.0359	2.0025	1.9962	0.0065
$LaBi_2Nb_{1.5}Fe_{0.5}O_9$	0.0340	2.0475	1.9980	0.0495
$LaBi_2Nb_{1.5}Co_{0.5}O_9$	0.0381	2.0430	2.0045	0.0380

3.3.2 FE-SEM and EDS Analysis

FE-SEM images and corresponding EDS spectra are shown in Figure 3.5. The crystallite size ranges from few hundred nanometers to few micrometers. The images reveal the microstructure of agglomerated crystallites with relatively more homogenous size distribution for the Cr and Fe, while seemingly large variation is observable in case of Mn and Co compounds. The EDS spectra show slightly higher atomic percentage of Bi and lower atomic percentage for Nb than their expected nominal proportions. This may be due to the

overlapping X-ray lines of Bi-Mα_1 and Nb-Lγ_1. However, the elemental mapping (Figure 3.6) analysis indicated good sample homogeneity showing uniform distribution of the constituent elements in a rectangular imaging area (also shown in the bright filed image) for all the samples.

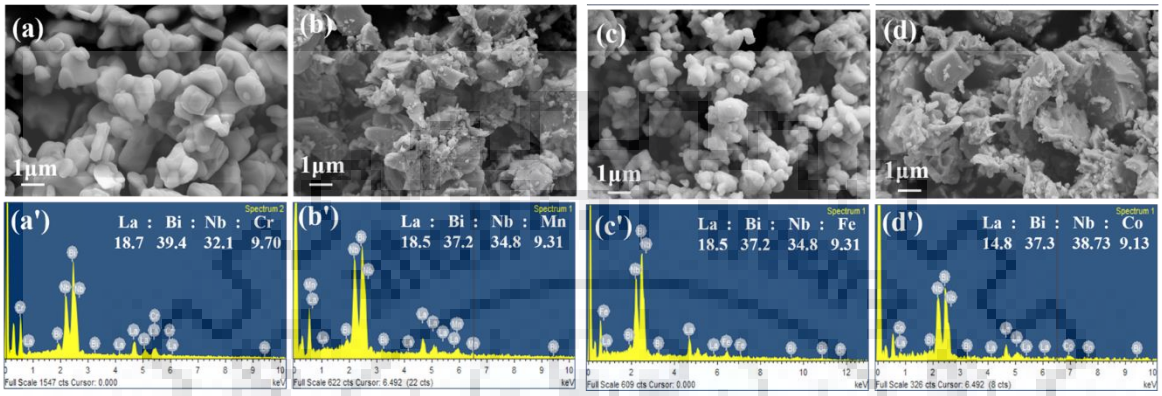

Figure 3.5 FE-SEM image and corresponding EDS spectra of (a) & (a') $LaBi_2Nb_{1.5}Cr_{0.5}O_9$, (b) & (b') $LaBi_2Nb_{1.5}Mn_{0.5}O_9$, (c) & (c') $LaBi_2Nb_{1.5}Fe_{0.5}O_9$, and (d) & (d') $LaBi_2Nb_{1.5}Co_{0.5}O_9$.

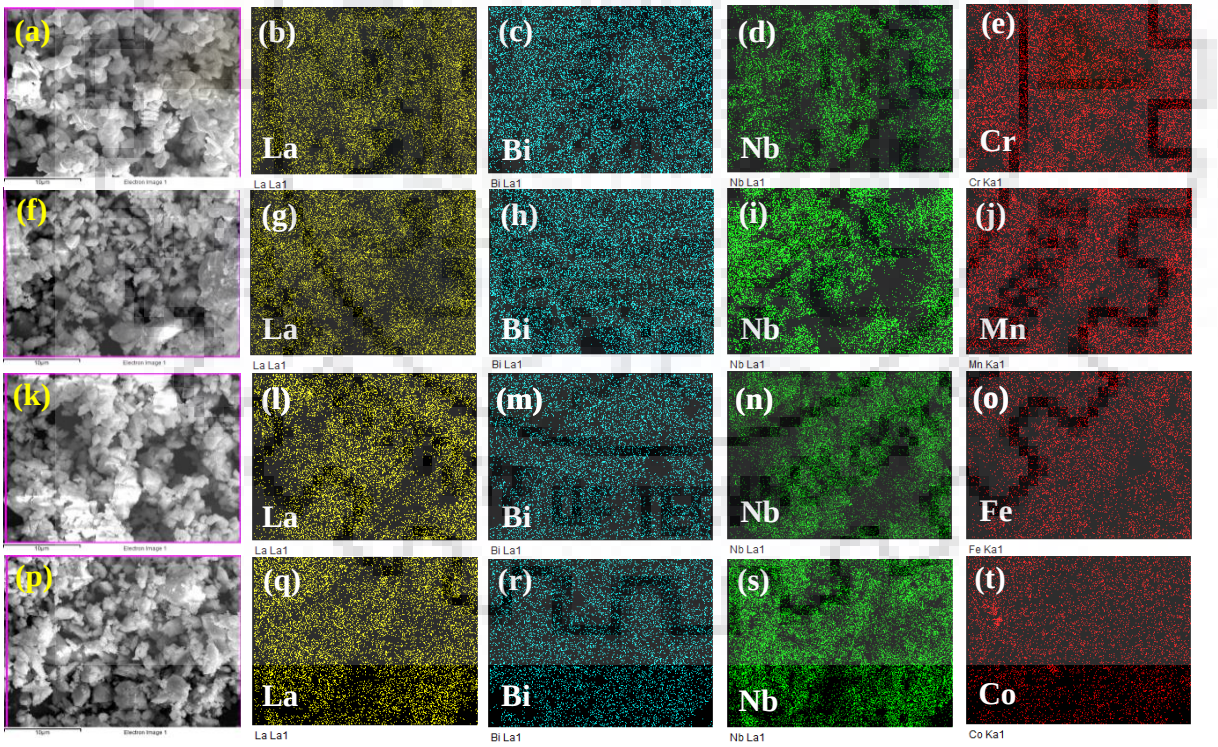

Figure 3.6 EDS elemantal mapping of La, Bi, Nb and M (M = Cr, Mn, Fe, Co) for $LaBi_2Nb_{1.5}M_{0.5}O_9$. The left panel shows the corresponding bright field SEM images.

3.3.3 TEM Analysis

Since the compounds are isostructural, the TEM data for a representative member, $LaBi_2Nb_{1.5}Fe_{0.5}O_9$, is shown in Figure 3.7 together with its FE-SEM image. The HR-TEM image exhibits lattice fringes with a spacing of ~ 0.387 nm. This is in agreement with the distance between two corner connected octahedra in the *a-b* plane of the double layer niobates. SAED data indicates its polycrystalline nature and the indexing of few representative diffraction spots are consistent with the symmetry and crystal system as confirmed by the P-XRD analysis.

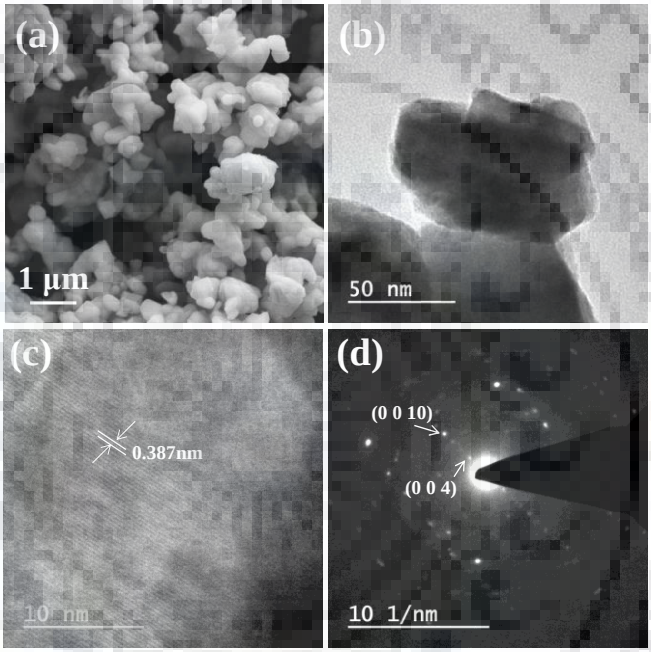

Figure 3.7 (a) SEM, (b) TEM, (c) HR-TEM images and (d) SAED pattern of $LaBi_2Nb_{1.5}Fe_{0.5}O_9$.

3.3.4 XPS Analysis

XPS of the compounds with the corresponding transition metal peaks are shown in Figure 3.8. The transition metal 2p spectra show two peak features consistent with the $2p_{3/2}$ and $2p_{1/2}$ spin-orbit coupled doublets. The range of binding energy of the peaks are in conformity with the single oxidation state i.e. M^{3+} for all the transition metals studied here.[59-61] Moreover, the La-3*d*, Nb-3*d* and Bi-4*f* peaks and their binding energies in the survey spectra confirmed the presence of these elements and their oxidation states as +3, +5 and +3, respectively, in all the compounds.

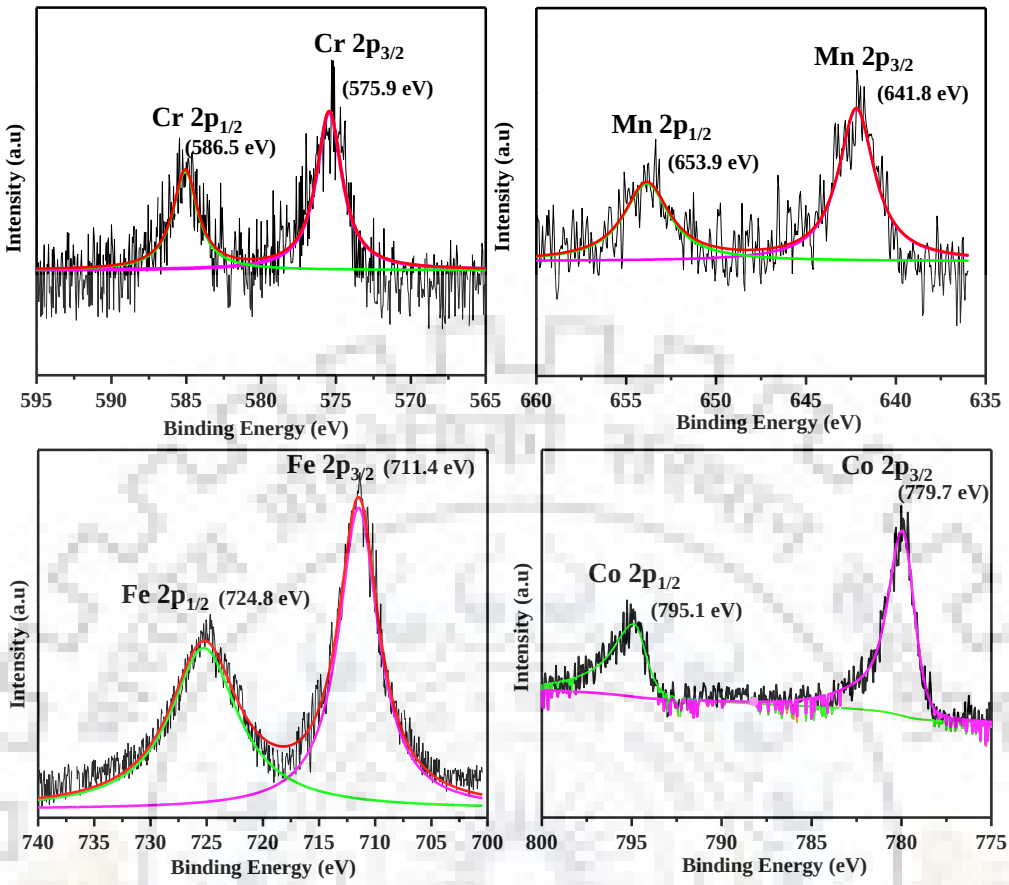

Figure 3.8. XPS spectra of $LaBi_2Nb_{1.5}M_{0.5}O_9$ (M = Cr, Mn, Fe, Co) showing respective transition metal peaks.

3.3.5. Magnetic Properties

The field cooled (FC) magnetization data of the as prepared $LaBi_2Nb_{1.5}M_{0.5}O_9$ (M = Cr, Mn, Fe, Co) are shown in Figure 3.9. The compounds show paramagnetic behavior with no indication of magnetic phase transition or ordering in the temperature range 5-300 K. The compounds display nearly Curie-law paramagnetism in the entire temperature range. This can be understood from the low concentration and disordered nature of M^{3+} amidst the diamagnetic matrix of Nb^{5+} cations leaving the M^{3+} mostly in a lattice of isolated non-interacting spins within the perovskite block of the double layer niobate. Although, few nearest neighbor pairs or larger clusters of magnetic ions may be present as it occurs in dilute magnetic semiconductors.

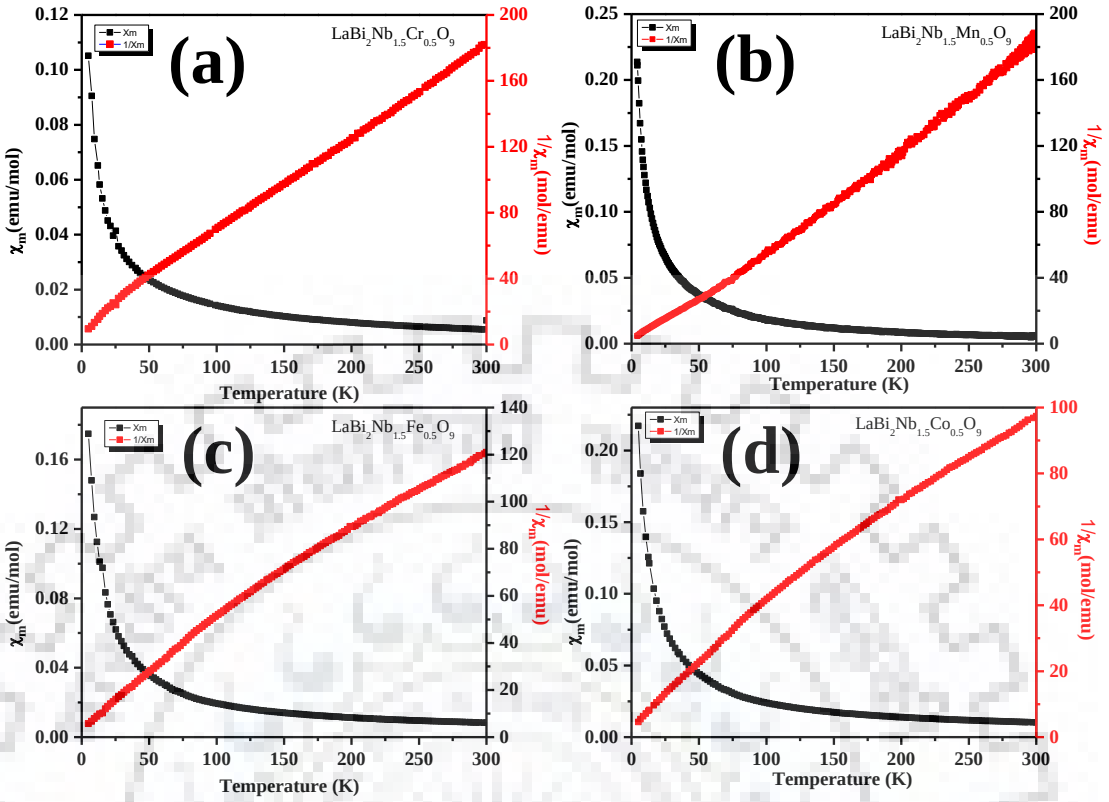

Figure 3.9. Magnetic susceptibility data for $LaBi_2Nb_{1.5}M_{0.5}O_9$ (M = Cr, Mn, Fe, Co).

Additional to the dilute nature of the M^{3+} spins within the perovskite blocks, each perovskite block itself is further separated by the $[Bi_2O_2]$-layers from the neighboring blocks thus preventing magnetic interactions in-between the perovskite blocks, prevailing the paramagnetic behavior. But, slight deviations from pure Curie behavior may not be completely overlooked. This may primarily be due to dominant antiferromagnetic correlations between existing nearest neighbor pairs and extended interactions within a cluster. The paramagnetic moments per formula unit calculated from the inverse susceptibility vs. temperature FC data for the compounds are more or less in agreement (excepting the Mn compound) with the corresponding calculated magnetic moments (Table 3.7) from spin-only formula assuming all M^{3+} in their high spin states. In case of the Mn compound, the observed paramagnetic moment (3.6 μ_B) is surprisingly smaller than that calculated from the spin-only formula (4.9 μ_B). Keeping in mind, the unusual contraction of the *c*-parameter in the Mn compound, the low moment can be explained as a magnetic moment collapse with a redistribution of electron from $e_g \rightarrow t_{2g}$ in corroboration with a volume collapse.[62]

3.3.6. UV-vis DRS Analysis

The UV-vis DRS for $LaBi_2Nb_{1.5}M_{0.5}O_9$ (M = Cr, Mn, Fe, Co) are shown in Figure 3.10. The data indicates extension of absorption edges deep into the visible region due to coupled substitution of La and M (Cr, Mn, Fe and Co) in the parent $SrBi_2Nb_2O_9$, a near UV absorber. The compounds show absorption edges with a two-step feature excepting in case of Fe, where a three step feature can be seen. The higher energy edge (~ 380 – 400 nm) is nearly merged with the absorption edge of the parent $SrBi_2Nb_2O_9$ corresponding to the transition from the Bi6s states to the empty 4d states of Nb.[45,55] The extended edge that appears in the range 450 - 650 nm with wide band features corresponds to transitions from O2p states to 3d states of the transition metals. The primary band gap (E_g) was calculated from the Tauc plot assuming direct band gap transition (Table 3.6). The higher edge energies are also given in Table S3 along with the E_g values for all the compounds. On transition metal incorporation the compounds became visible-light absorber and thus suitable for investigating their activities in solar photocatalysis.

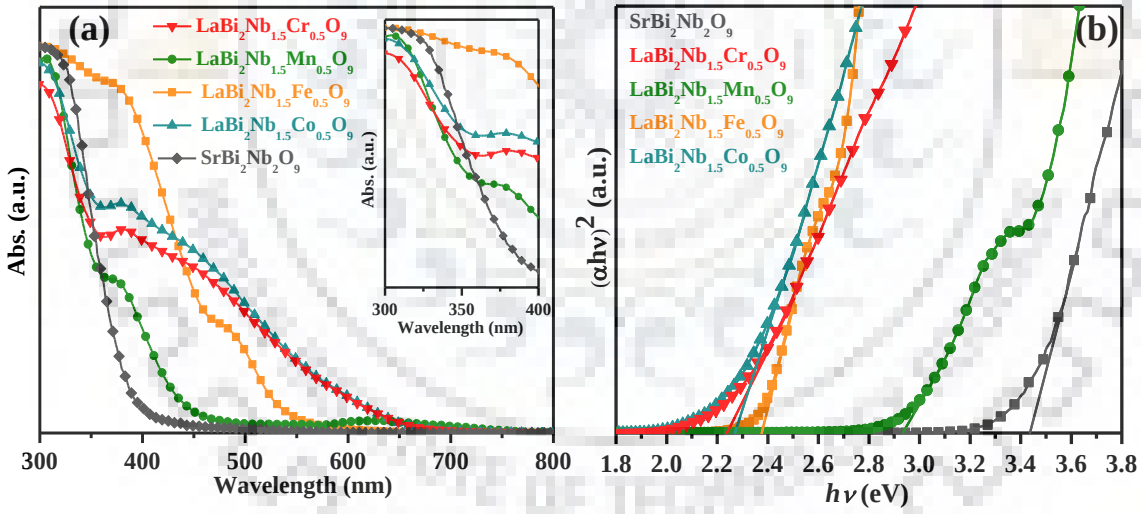

Figure 3.10 (a) UV-vis DRS of $LaBi_2Nb_{1.5}M_{0.5}O_9$ (M = Cr, Mn, Fe, Co), (b) Tauc plots for the estimation of band gap. The inset of (a) shows the higher energy absorption edges.

3.3.7 PL Analysis

Figure 9 shows the PL spectra of the compounds measured at room temperature. Generally, the PL emissions give information about recombination of the photo-generated charge carriers. Broad PL emissions are observed in the wavelength range 440-510 nm with the highest intensity emission at around 468 nm. According to PL data, one would expect the activity order as $LaBi_2Nb_{1.5}Cr_{0.5}O_9$ > $LaBi_2Nb_{1.5}Co_{0.5}O_9$ > $LaBi_2Nb_{1.5}Mn_{0.5}O_9$ > $LaBi_2Nb_{1.5}Fe_{0.5}O_9$ since the photocatalytic activity also depends on the abundance of generated charge carriers (electron-holes) on photo-excitation. Moreover, higher PL intensity signifies greater extent of charge carrier recombination. This decreases the overall number of e^-/h^+ that reaches the surface and takes part in the reactive species generation and consequently the photocatalytic efficiency of a catalyst. The strong emission in case of Fe is due to an intermediate energy band edge (intra-band) emission which also corroborates with the sharp absorption edge in the UV-vis DRS of the Fe compound. Moreover, the high emission intensities at 400 nm and below for the Mn as well as for Co and Cr compounds can be corroborated with their UV-vis DRS data having a sharp higher energy band edge, which is absent in case of the Fe compound.

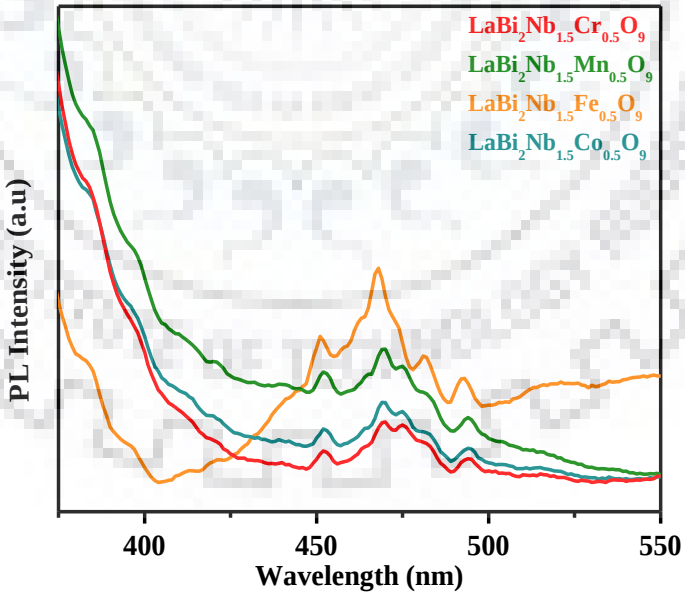

Figure 3.11. PL spectra of $LaBi_2Nb_{1.5}M_{0.5}O_9$ (M = Cr, Mn, Fe, Co) at room temperature.

Table 3.7 Observed and Calculated Magnetic Moments, Band Gaps and Edge Energies for $LaBi_2Nb_{1.5}M_{0.5}O_9$ (M = Cr, Mn, Fe, Co).

Compounds	Observed μ_{obs} (BM)	Expected $\mu_{spin\ only}$ (BM)	Band Gap and Edge Energies (eV) E_{edge} (1)	E_{edge} (2)	E_{edge} (3)
$SrBi_2Nb_2O_9$	---	---	3.42	---	---
$LaBi_2Nb_{1.5}Cr_{0.5}O_9$	3.8	3.9	2.25	3.53	---
$LaBi_2Nb_{1.5}Mn_{0.5}O_9$	3.6	4.9 (HS)	2.94	3.45	---
$LaBi_2Nb_{1.5}Fe_{0.5}O_9$	5.3	5.9 (HS)	2.37	2.73	3.47
$LaBi_2Nb_{1.5}Co_{0.5}O_9$	5.1	4.9 (HS)	2.29	3.48	---

3.3.8. EIS Analysis

EIS studies can evaluate the charge transfer resistance and separation efficiency of the photogenerated charge carriers. The EIS data for the double layered niobates, $LaBi_2Nb_{1.5}M_{0.5}O_9$ (M = Cr, Mn, Fe, Co), are shown in Figure 3.12. The samples show a semicircular part and a linear part, which is indicative of a complex equivalent circuit for the Randles cell controlled both by the charge transfer and diffusion process. Assuming a simplified Randles cell for the semicircular part the charge transfer resistance (R_{CT}) is estimated from the diameter of the semicircle. The Cr compound shows the smallest R_{CT} of 0.687 kΩ while higher values of 0.703, 1.55 and 2.36 kΩ are obtained for Co, Mn and Fe, respectively. A smaller R_{CT} is expected to facilitate the migration of photogenerated charge carriers and thus enhance the photocatalytic activity at the semiconductor surface. Thus, according to EIS data $LaBi_2Nb_{1.5}Cr_{0.5}O_9$ is believed to have the most favorable charge transfer to show the highest activity that decreases in the order, $LaBi_2Nb_{1.5}Cr_{0.5}O_9 > LaBi_2Nb_{1.5}Co_{0.5}O_9 > LaBi_2Nb_{1.5}Mn_{0.5}O_9 > LaBi_2Nb_{1.5}Fe_{0.5}O_9$.

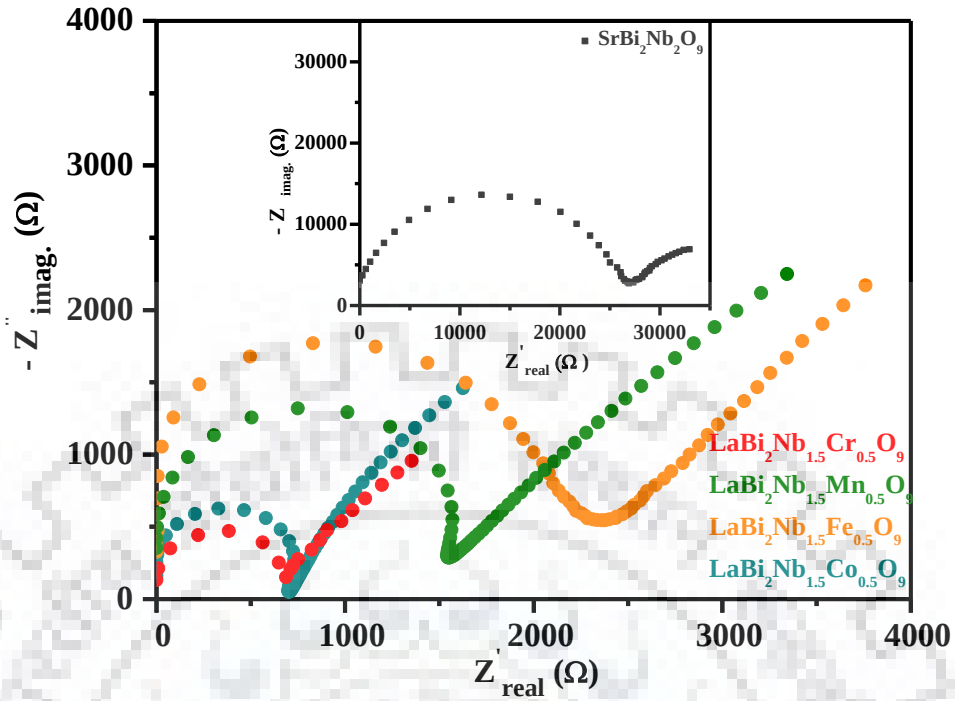

Figure 3.12. Nyquist impedance plots for $LaBi_2Nb_{1.5}M_{0.5}O_9$ (M = Cr, Mn, Fe, Co) and $SrBi_2Nb_2O_9$ (inset).

3.3.9. Photocatalytic Activity Studies

To explore the photocatalytic activity of $LaBi_2Nb_{1.5}M_{0.5}O_9$ (M= Cr, Mn, Fe, Co) compounds at different pH (2, 7 and 11) under UV-Vis light and natural sunlight-irradiation RhB dye was selected as a model pollutant. The compounds show photocatalytic degradation of RhB at pH 2 and the results are presented in Figure 3.13. Under visible light illumination, RhB was completely degraded much quickly as compare to the sunlight irradiation. The compounds took 50-110 min for complete degradation of RhB at pH 2 (Figure 3.13 a) under sunlight irradiation and 15-30 min in Visible lamp (MPMVL) (Figure 3.13) But, the compounds did not show any degradation at pH 7 and 11 (Figure 3.13 (c) and 3.13 (d). For the sake of comparison the degradation data for the parent compound, $SrBi_2Nb_2O_9$, is also given. The UV-vis absorption data for the degradation at pH 2 clearly show some shifting of the characteristic RhB peak (Figure 3.14 and 3.15) toward the later stages of degradation is probably due to de-ethylation of RhB.[62]The photostability study did not show any self-degradation of RhB at pH 2 and hence no correction to the absorption data has been made.

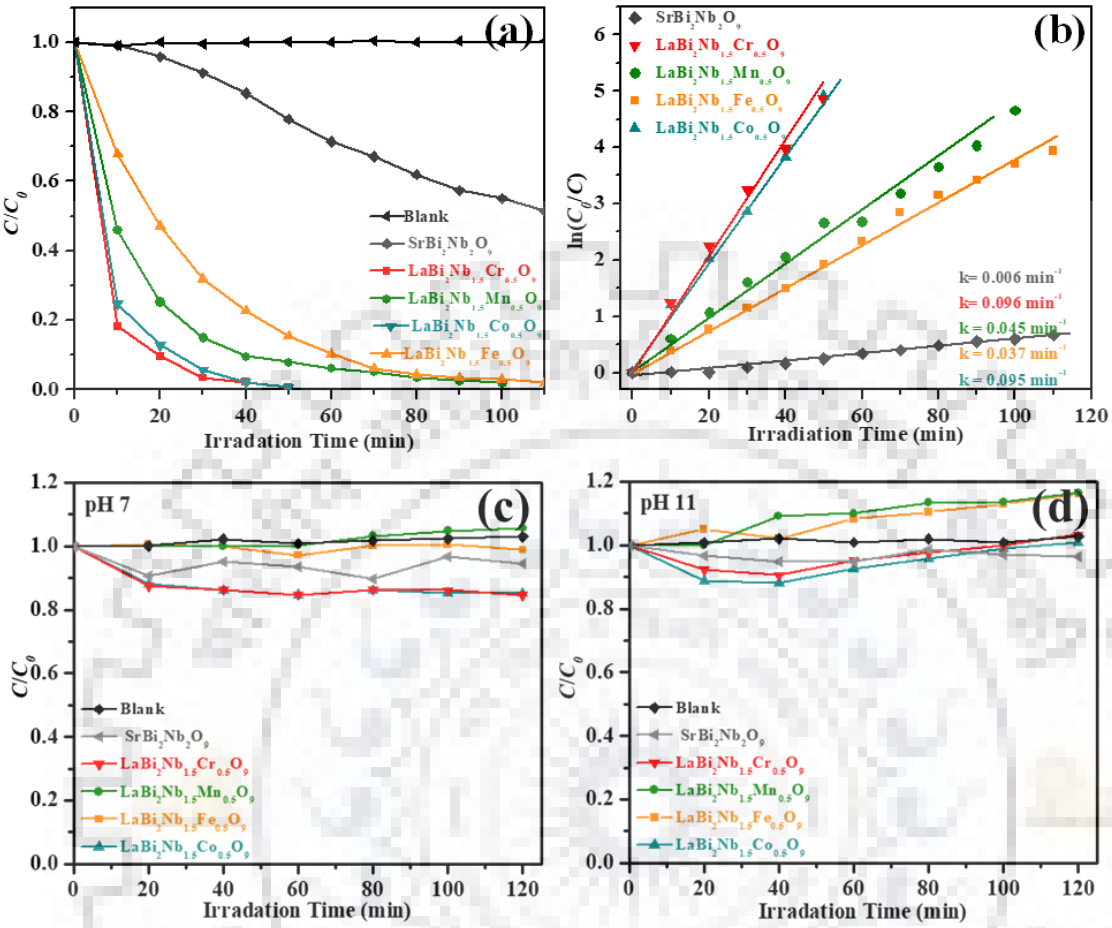

Figure 3.13. (a) Photocatalytic degradation of RhB at pH 2. (b) The plot of ln(C_0/C) as a function of time.

The photocatalytic RhB degradation kinetics over $LaBi_2Nb_{1.5}M_{0.5}O_9$ (M = Cr, Mn, Fe, Co) was modeled using Langmuir-Hinshelwood equation.[63]

$$\ln(C_0/C) = kt$$

where, C_0 is the initial RhB concentration, C is the RhB concentration at time t, and k is the rate constant.

Figure 3.13 (b) and 3.16 (b) shows a linear plot between ln(C_0/C) and irradiation time, indicating the photocatalytic degradation to follow a pseudo-first-order kinetics. The degradation rate of compounds much higher in Visible light illumination as compare to the sunlight irradiation. The degradation rate constants are calculated to be 0.096, 0.044, 0.037 and 0.095 min^{-1} for the Cr, Mn, Fe and Co-incorporated niobates, respectively. A rate constant of 0.006 $min^{-1}$for the parent $SrBi_2Nb_2O_9$ may primarily be due to its inefficiency of solar light absorption in the visible region.

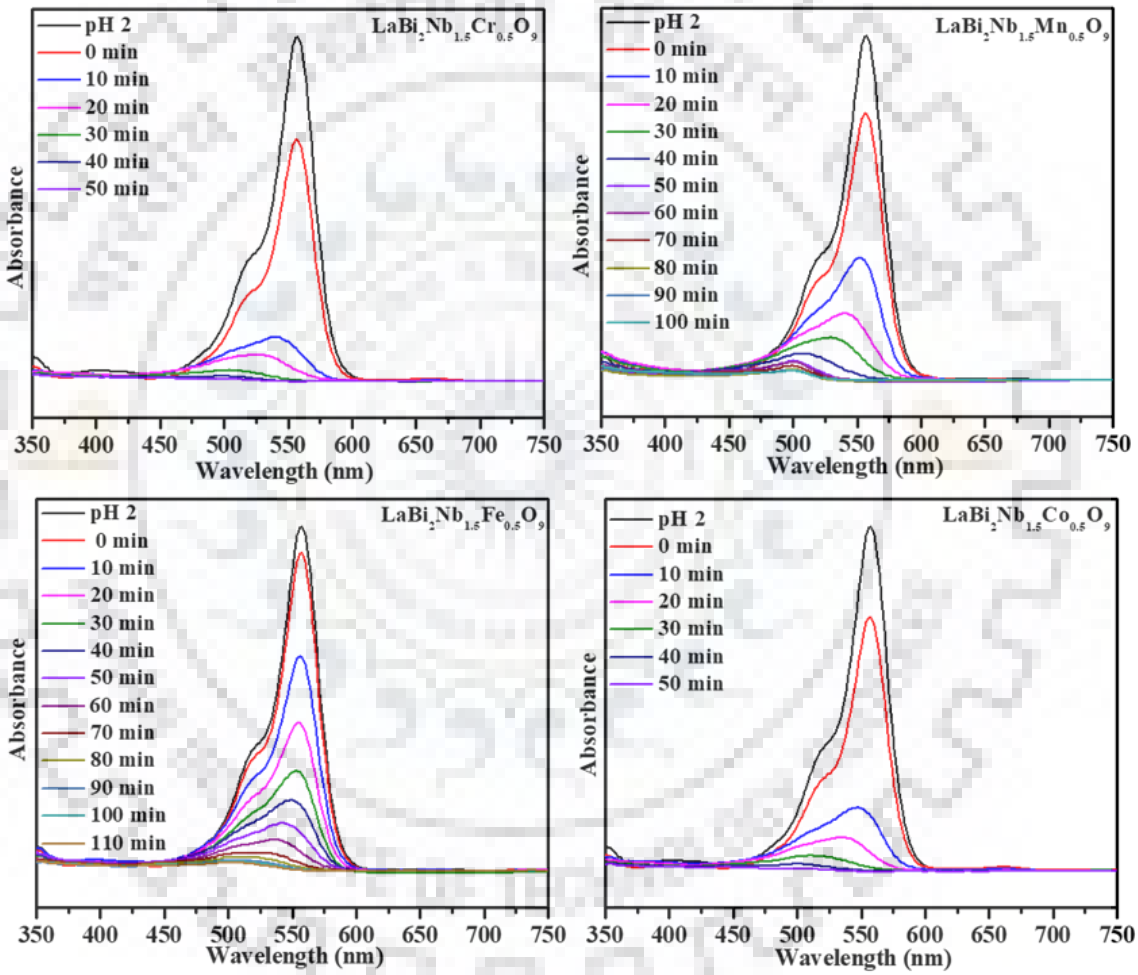

Figure 3.14 RhB degradation over $LaBi_2Nb_{1.5}M_{0.5}O_9$, (M = Cr, Mn, Fe and Co) at pH 2 under solar irradiation.

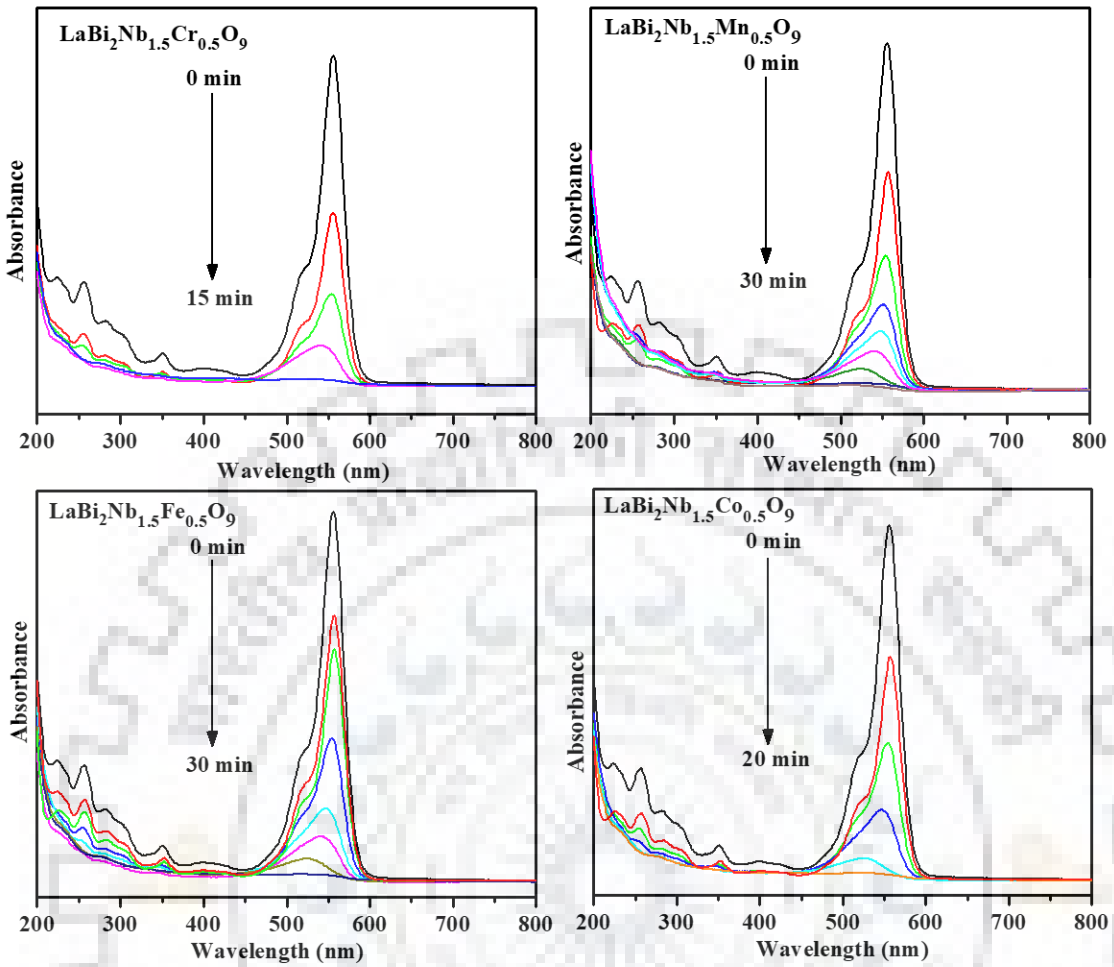

Figure 3.15 RhB degradation over $LaBi_2Nb_{1.5}M_{0.5}O_9$, (M = Cr, Mn, Fe and Co) at pH 2 under medium pressure mercury vapour lamp (Visible light).

The percentage COD removal data in combination with C_0/C with time (Figure 3.17) at pH2 shows nearly complete dye mineralization concordant with dye decoloration. In Figure 3.18, The parent compound, $SrBi_2Nb_2O_9$ has been shown complete degradation in UV light but low degradation shown in the presence of the visible light. However the incorporation La and transition metal in $SrBi_2Nb_2O_9$ makes visible light active compound.

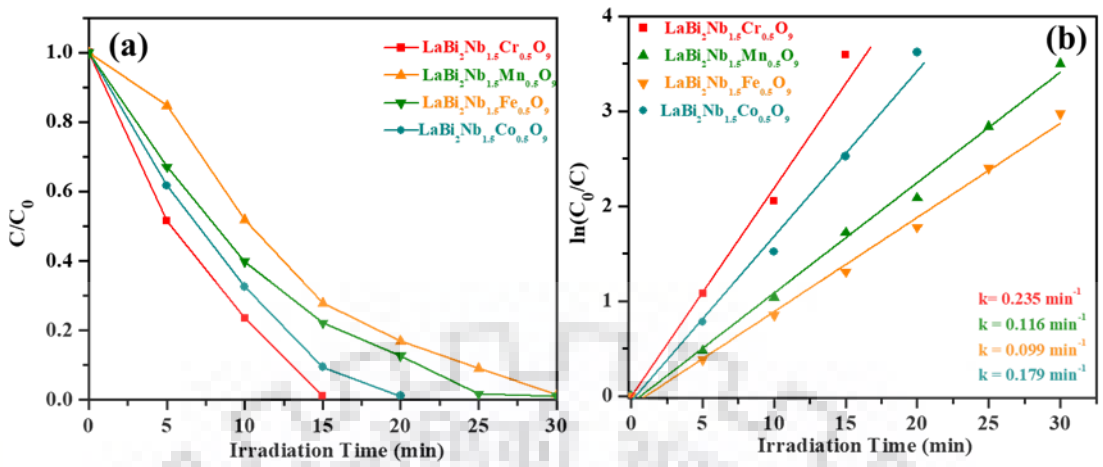

Figure 3.16 (a) Photocatalytic degradation of RhB over $LaBi_2Nb_{1.5}M_{0.5}O_9$, (M = Cr, Mn, Fe and Co) at pH 2 under medium pressure mercury vapour lamp. (b) The plot of $\ln(C_0/C)$ as a function of time.

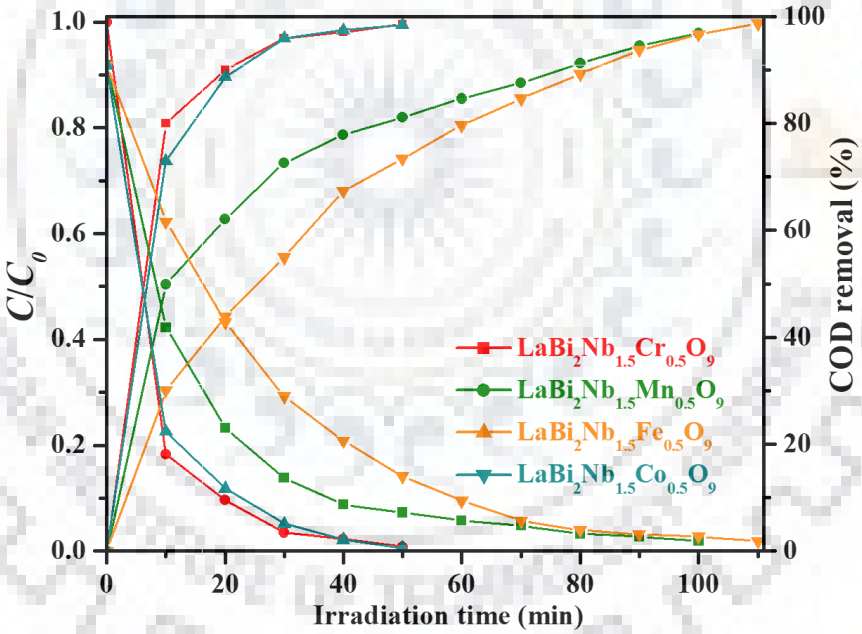

Figure 3.17 Photocatalytic degradation of RhB and COD removal efficiency with time by $LaBi_2Nb_{1.5}M_{0.5}O_9$ (M = Cr, Mn, Fe, Co) at pH 2 under sunlight.

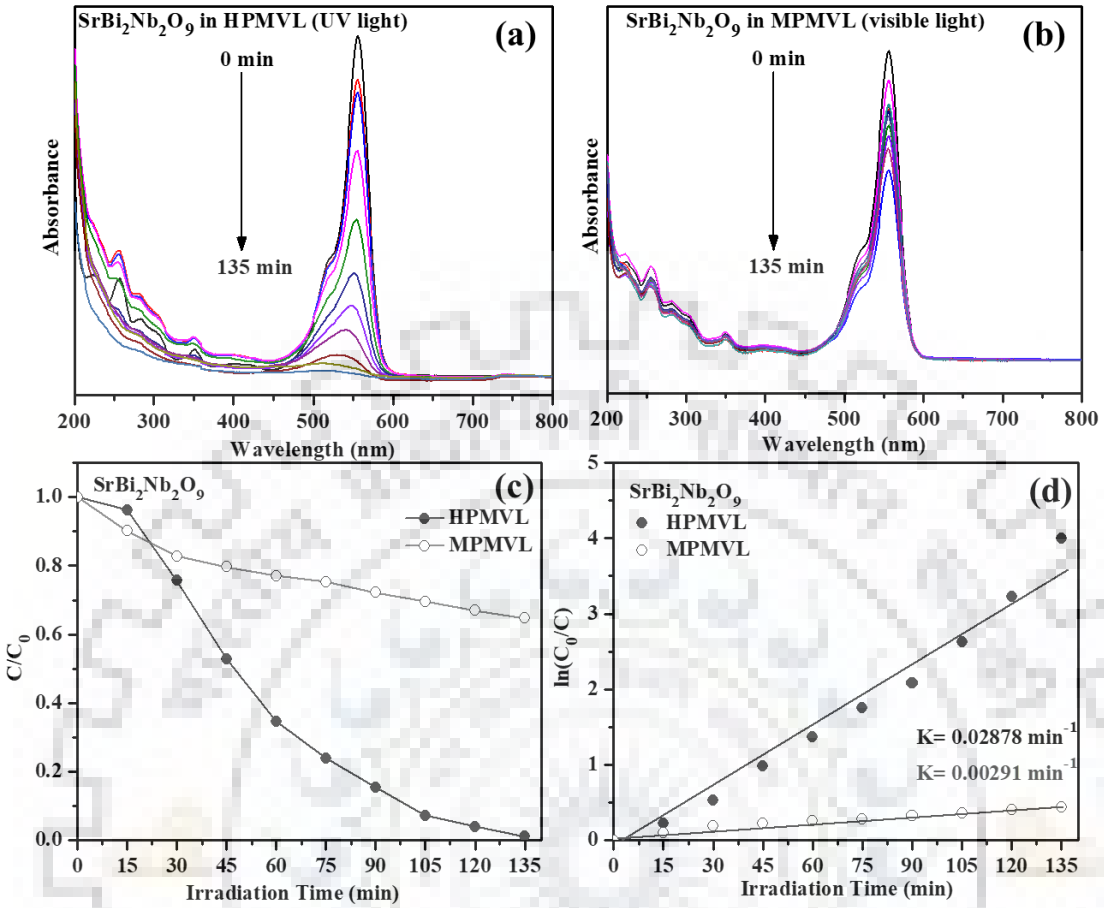

Figure 3.18 RhB degradation over $SrBi_2Nb_2O_9$ at pH 2 under (a) high pressure mercury vapour lamp (HPMVL), (b) medium pressure mercury vapour lamp (MPMVL), (c) Photocatalytic degradation of RhB at pH 2 under HPMVL and MPMVL. (d) The plot of $\ln(C_0/C)$ as a function of time.

3.3.10 Role of Adsorption

To evaluate the role of RhB adsorption on the photocatalytic activity, we have performed adsorption tests at different pH in the dark. The adsorption data (Figure 3.19) indicates a relatively large extent of adsorption in the acidic medium, while that in the neutral and alkaline media was much less. Interestingly, the adsorption results at pH 2 are in agreement with the order of RhB degradation making $LaBi_2Nb_{1.5}Cr_{0.5}O_9$ as the most active photocatalyst with the activity decreasing in the order, $LaBi_2Nb_{1.5}Cr_{0.5}O_9 > LaBi_2Nb_{1.5}Co_{0.5}O_9 > LaBi_2Nb_{1.5}Mn_{0.5}O_9 > LaBi_2Nb_{1.5}Fe_{0.5}O_9$. While the adsorption test explains the activity order and enhanced activity of the compounds in the acidic medium, negligible activity of the

Mn compound at pH 7 is not explainable purely based on adsorption. This may indicate additional role of the pH in the generation of reactive species and mechanistic pathways of degradation.

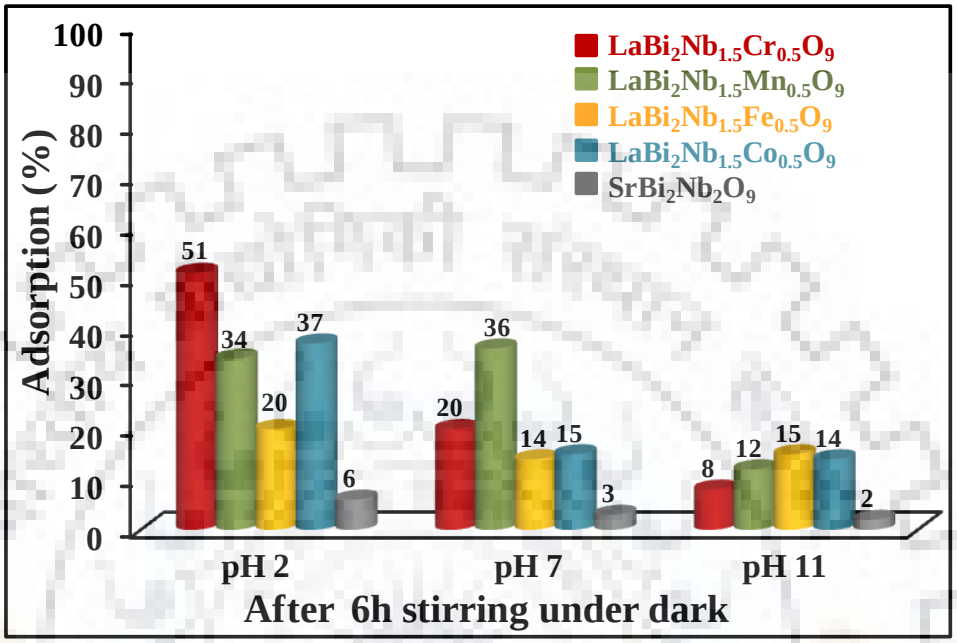

Figure 3.19 Percentage adsorption of RhB with $LaBi_2Nb_{1.5}M_{0.5}O_9$ (M = Cr, Mn, Fe, Co) at different pH.

3.3.11 ζ- Potential

Surface charge of the catalyst plays an important role in the dye adsorption. The variation of ζ- potential as a function of pH is shown in Figure 3.20. The maximum positive ζ-potentials are observed in the acidic medium, whereas negative ζ-potentials are noticed in the neutral and alkaline media. The maximum adsorption of RhB in the acidic medium is attributed to more positive ζ-potential of the catalysts. The negatively charged carboxylic acid groups of RhB can electrostatically interact with the positively charged catalysts at pH 2. At pH 7 and 11, the catalyst surface is negatively charged and the negatively charged carboxylic acid groups of RhB will be repelled. However, the reduced extent of adsorption of RhB at pH 7 and 11 is due to the electrostatic interaction between the negatively charged catalyst and positively charged N-diethyl end of RhB.[38] Surprisingly, the highest adsorption at pH 7 is observed for the Mn compound, which showed the least negative ζ-potential at this pH. This

might have its origin in the crystal structure where the local environment of the Mn octahedra is way different from the transition metal octahedra of others.

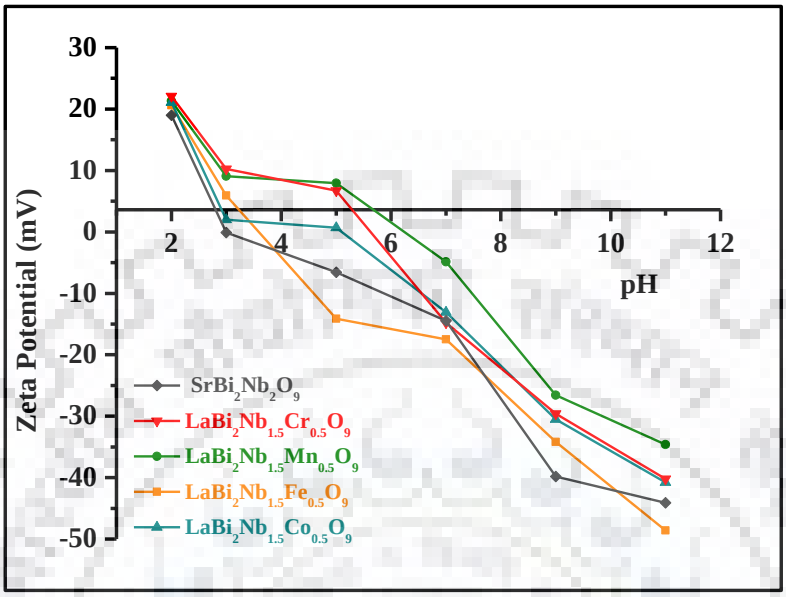

Figure 3.20 ζ- Potential of $LaBi_2Nb_{1.5}M_{0.5}O_9$ (M = Cr, Mn, Fe, Co) catalysts at different pH.

3.3.12. Catalyst Reusability and Stability

Reproducibility and stability of catalysts are among the important parameters that need to be evaluated for their repeated use. The reusability of the catalysts is evaluated by performing five consecutive cycles of RhB degradation over the most active catalyst, namely, $LaBi_2Nb_{1.5}Cr_{0.5}O_9$ under solar irradiation (Figure 16). The extent of RhB degradation varied from slightly more over 99% (1^{st} cycle) to 97% (5^{th} cycle) within 50 min of solar irradiation. The result suggests no noticeable activity loss over the cycles and up to the 5^{th} cycle. The 2% decrease in the activity is attributed to the unavoidable loss of the catalyst during the cycling study. The stability of the catalyst after the 5^{th} cycle is evaluated by P-XRD and XPS study (Figure 3.21). The P-XRD pattern of the recovered compound after five cycles of RhB degradation revealed high crystallinity as original without any additional peaks (Figure 3.21 a). This indicated high photocatalytic stability of the catalyst in the acidic pH. In Figure 3.21 (c-d), the XPS survey scan and Cr2p data for the pristine and post-catalytic Cr-compounds are compared. The XPS data show the presence of lanthanum, bismuth, niobium and chromium in the same chemical state after five cycles of RhB degradation, substantiating the

photocatalytic stability of the compound. The spectrum of Cr 2p with Gauss-Lorentz curve fitting (Figure 3.21 d) both before and after photocatalysis indicated presence of Cr^{3+} only. Considering Cr as more vulnerable among all other elements present under the reaction condition, retention of its chemical state further demonstrated good stability and reusability of the catalyst.

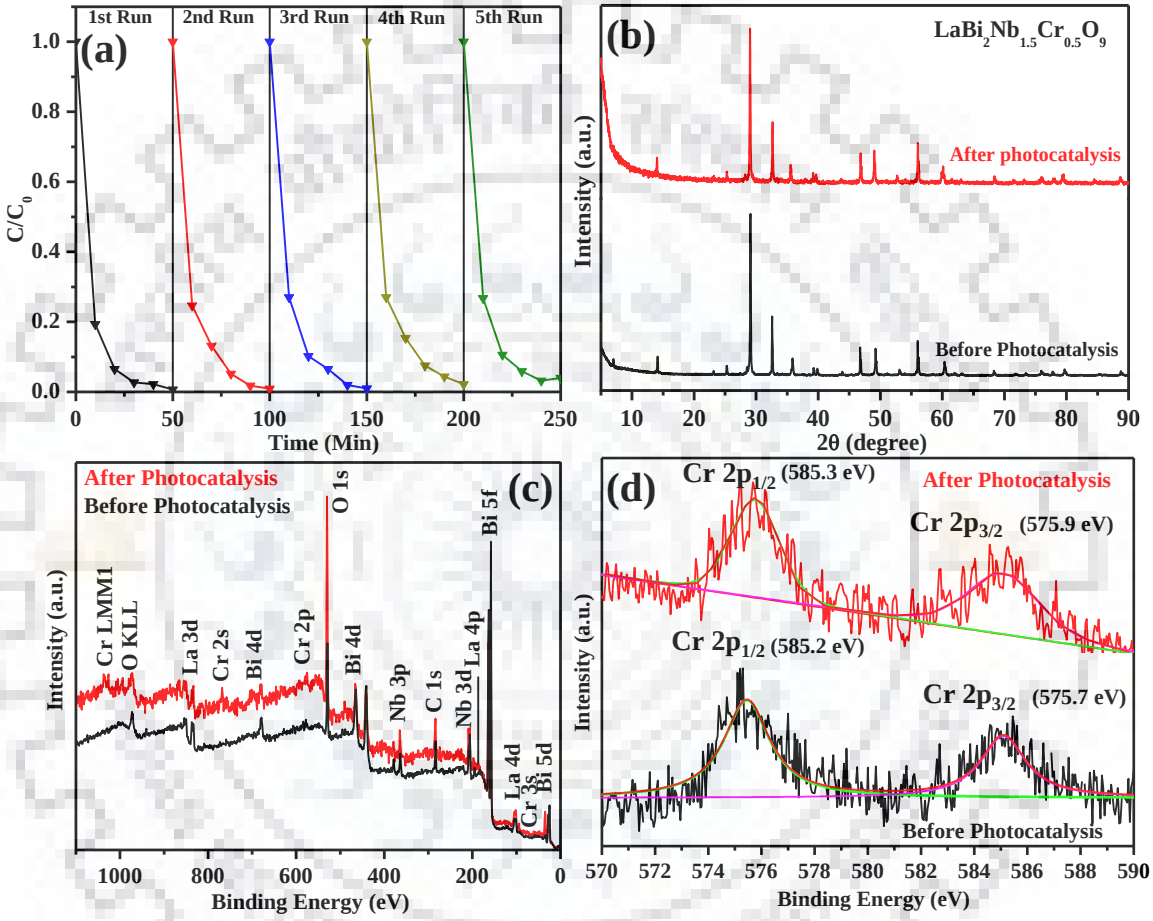

Figure 3.21 (a) Time profiles of RhB degradation for five successive cycles with $LaBi_2Nb_{1.5}Cr_{0.5}O_9$. (b) PXD patterns of $LaBi_2Nb_{1.5}Cr_{0.5}O_9$ before and after photocatalytic degradation. XPS spectra of catalyst before and after degradation: (c) XPS survey spectra and (b) high-resolution XPS of Cr 2p.

3.3.13. Role of Reactive Species

In general, the reactive species such as, holes, $O_2^{\bullet-}$ (superoxide radical anions) and $^{\bullet}OH$ (hydroxyl radical) are expected to be involved in the photodegradation of the dye. To

find out the dominant reactive species which play active role in the degradation process, degradation experiments are carried out in presence of tertiary butyl alcohol (t-BuOH), benzoquinone (BQ), and ammonium oxalate (AO) as $^{\bullet}OH$, $O_2^{\bullet-}$ and h^+ scavengers, respectively. It can be seen from Figure 3.22 that the photodegradation of RhB is greatly inhibited in presence of AO (h^+ scavenger), while the degradation is suppressed to significant and moderate extents in presence of t-BuOH and BQ, respectively. This ascertained the role of h^+ as the main reactive species, whereas $O_2^{\bullet-}$ and $^{\bullet}OH$ played significant to moderate roles in the RhB degradation.

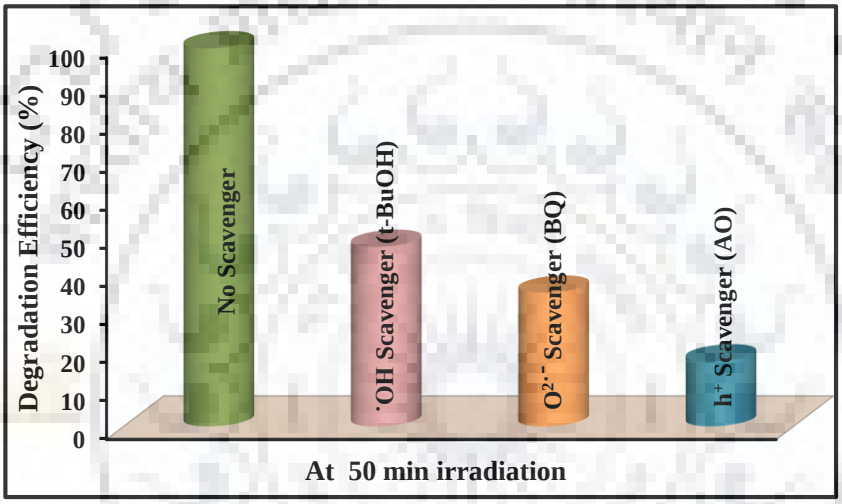

Figure 3.22 Effect of different scavengers on the degradation of RhB over$LaBi_2Nb_{1.5}Cr_{0.5}O_9$ under sunlight-irradiation

3.3.14. Energy Level Diagram and Mechanism of Photocatalysis

The band edge positions of $LaBi_2Nb_{1.5}Cr_{0.5}O_9$ were calculated empirically according to the following equations.[64]

$$E_{CB} = \chi(A_aB_bC_c) - \tfrac{1}{2}E_g + 0.059(pH_{ZPC} - pH) + E_0$$

$$E_{VB} = E_{CB} + E_g$$

where, E_{CB} is the conduction band edge potential and $\chi(A_aB_bC_c)$ is the absolute electronegativity (*AE*; defined as the geometric mean of the electronegativity of the

constituent atoms) of the semiconductor ($A_aB_bC_c$), E_g is the band gap, pH_{ZPC} is the zero point of charge for the compound taken by the zeta potential values, E_0 is the scale factor with respect to *NHE* scale (– 4.5 eV) and E_{VB} is the valence band edge potential. The *AE* value for$LaBi_2Nb_{1.5}Cr_{0.5}O_9$ is calculated to be 6.02 eV. With the help of above equations, the conduction band potential, E_{CB} (1), valence band potential, E_{VB}, and the potential for the next higher energy conduction band edge, E_{CB} (2) (corresponding to the 2nd absorption edge in the UV-vis DRS) are calculated at different pH, and are given in Table S4. The potential for the generation of $^{\bullet}OH$ ($E_{\bullet OH/H2O}$= + 2.68 eV *vs. NHE*), $O_2^{\bullet-}$ ($E_{O2/O2\bullet-}$= + 0.13 eV *vs. NHE*) and HOMO-LUMO levels of RhB (E_{HOMO} = 0.95 eV and E_{LUMO} = – 1.42 eV) were taken from the recently reported literature.[65,66]

As illustrated in Figure 3.23, under sunlight irradiation, the electrons in the valence band of $LaBi_2Nb_{1.5}Cr_{0.5}O_9$are excited to the conduction bands and leaves holes in the valence band. The photoinduced electrons in the E_{CB}(1) cannot produce $O_2^{\bullet-}$ from dissolved O_2 by photoreduction process, because the E_{CB}(1) (+ 1.24 eV vs. NHE) is more positive than the potential for the generation of $O_2^{\bullet-}$ ($E_{O2/O2\bullet-}$= + 0.13 eV *vs. NHE*). But, the electrons in the E_{CB} (2) can produce $O_2^{\bullet-}$due to its less positive potential (– 0.04 eV vs. NHE) than that of $E_{O2/O2\bullet-}$. Moreover, the holes in the E_{VB} can oxidize H_2O to produce $^{\bullet}OH$, because the E_{VB} is more positive (+ 3.49 eV vs. NHE) than the potential for the generation of $^{\bullet}OH$ ($E_{\bullet OH/H2O}$= + 2.68 eV *vs. NHE*). Additionally, the E_{VB} of the semiconductor is located below the HOMO level of RhB, which favors the h^+ transfer from the semiconductor to the adsorbed RhB molecules. Further, the E_{CB} and LUMO levels of the dye are in a favorable position to promote photosensitization process. Thus, all the reactive species (holes, $O_2^{\bullet-}$ and $^{\bullet}OH$ radicals) can play a role in the degradation of RhB under sunlight irradiation. The scavenger experiments of RhB degradation is in agreement with the above as expected from the energy level positioning.

At this juncture, it is worthwhile to notice the weakest activity of the Fe compound in comparison to all others. This is in line with the high PL intensity, weak RhB adsorption and high R_{CT} of the Fe compound. Interestingly, the Mn compound features close to that of the Fe compound in terms of activity, despite its stronger RhB adsorption comparable to that of the Co compound. This is mainly due to its higher PL intensity as compared to Cr or Co analog

and a higher R_{CT}, which is more than double to that of Cr or Co compound. The overall higher PL intensity of the Mn and Fe compounds as compared to those of Co and Cr is attributed to the presence of sharp intermediate band edges for the Mn and Fe compounds. It appears that the enhanced PL intensity of Mn and Fe is due to the intermediate band edge recombination, which in turn reduces the photocatalytic activity of Fe and Mn compounds to a significant extent as compared to the Cr and Co analogs. The highest activity, on the other hand, for the Cr-compound is due to the collective effects of reduced carrier recombination, efficient charge transport and enhanced dye adsorption. This is also consistent with holes, $O_2^{\bullet-}$ and $^{\bullet}OH$ radicals being the reactive species involved in the degradation process.

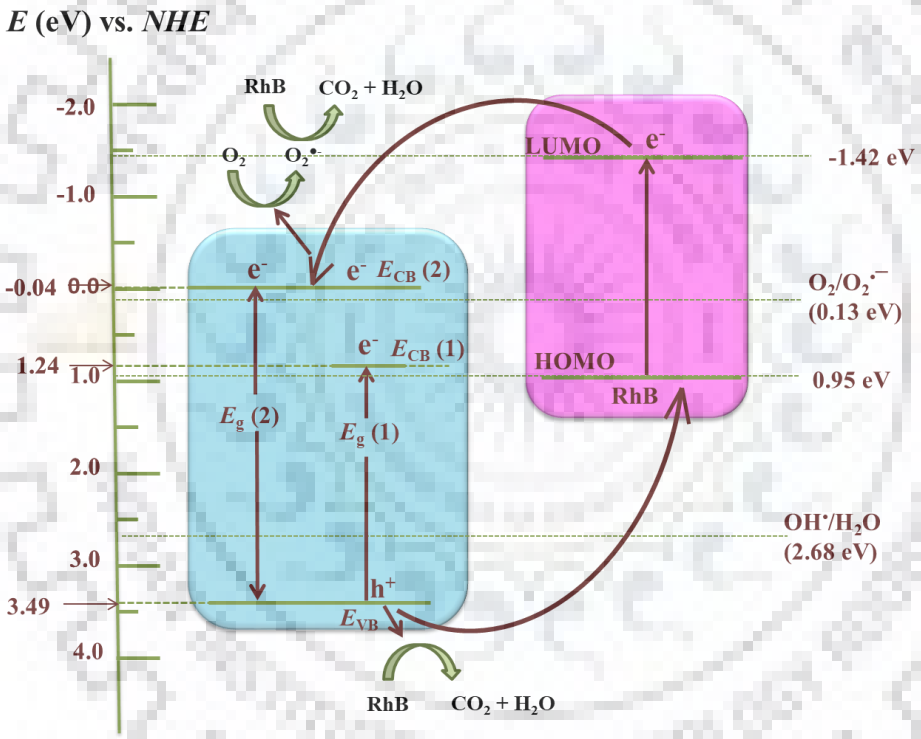

Figure 3.23. Schematic energy level diagram of $LaBi_2Nb_{1.5}Cr_{0.5}O_9$ with respect to potential (vs. NHE) of $^{\bullet}OH/H_2O$, $O_2/O_2^{\bullet-}$ and the HOMO–LUMO levels of RhB.

Moreover, a systematic study of the specific surface area of the compounds and its correlation with the dye adsorption indicates that the extent of adsorption is not directly related to the surface area of the compounds. It is generally accepted that enhanced dye adsorption occurs with increasing surface area. It is believed that, in addition to the surface area additional

factors like local coordination environment, octahedral distortion or the bond polarization may play important roles in determining the extent of dye adsorption. Moreover, realizing the fact that the overall photocatalytic activity of a catalyst is a complex function of several factors, the experimental activity order of a series of compounds cannot be understood simply based on one parameter in isolation, rather it must be understood in the context of the relative contribution of various parameters and their comparative effects on the overall activity.

In summary, A series of double-layer Aurivillius niobates, $LaBi_2Nb_{1.5}M_{0.5}O_9$ (M = Cr, Mn, Fe, Co), with heterovalent coupled substitution of La and $3d^n$ transition metals are reported. The coupled substitution strategy is lead-free and all the compounds are sunlight-active with absorption edges extending up to ~ 650 nm with band gaps ranging from 2.25 – 2.94 eV. The new layered niobates crystallize in the same non-centrosymmetric $A2_1am$ space group as that of $SrBi_2Nb_2O_9$. Despite adopting the same structure, $LaBi_2Nb_{1.5}Mn_{0.5}O_9$ showed an unusual contraction of the *c*-parameter and a subsequent magnetic moment collapse, ascribed to a redistribution of $e_g \rightarrow t_{2g}$ electron originating from a complex interplay of FOJT and SOJT interaction, with the later winning over the former. While all the compounds exhibited sunlight-driven Rhodamine B degradation and COD removal within 110 minutes, the Cr compound showed rapid degradation and concordant COD removal within 50 minutes of sunlight irradiation. The degradation cycle study with the Cr analog indicated excellent catalyst stability and recyclability under the experimental conditions with five consecutive cycles. The paramagnetic nature of the compounds will be helpful in the post-catalytic magnetic separation of the catalysts. The work will open up possibilities in developing other lead-free Aurivillius niobates and tantalates for solar photocatalysis.

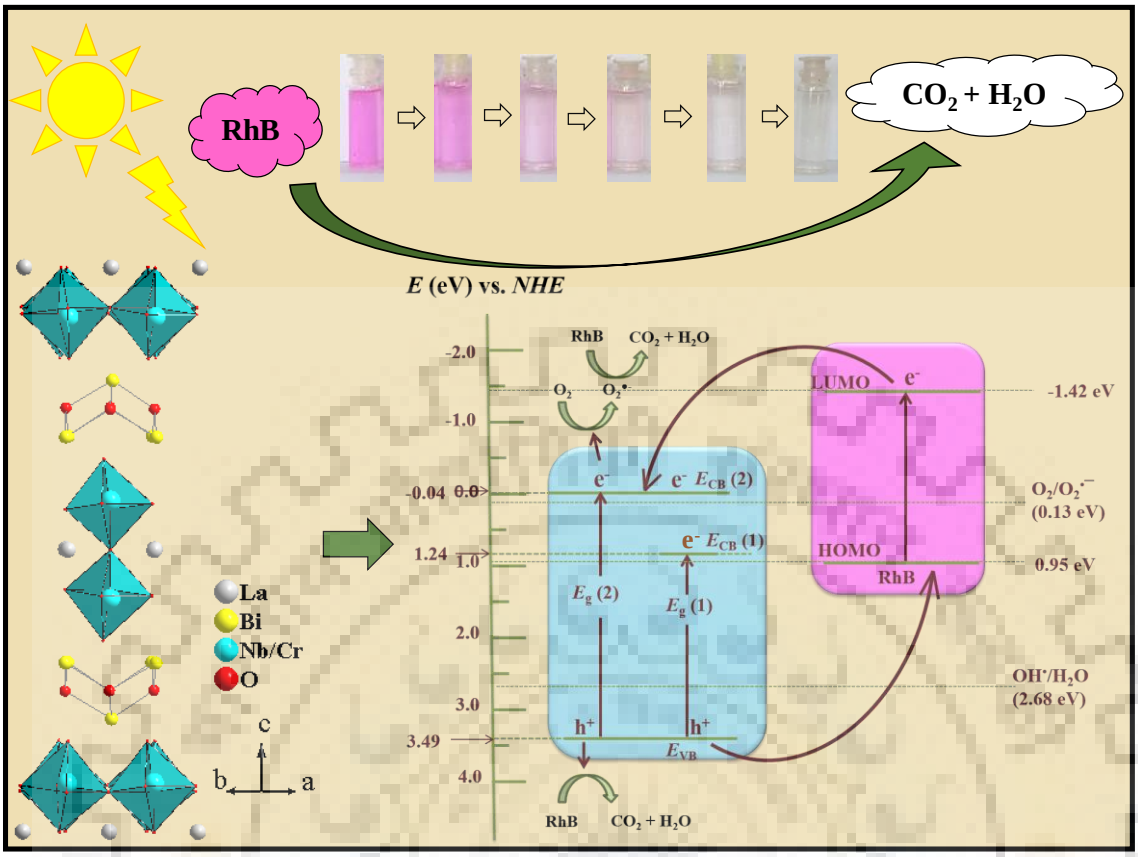
RhB
CO2 + H2O
E (eV) vs. NHE
-2.0
-1.0
-0.04
0.0
1.24
1.0
2.0
3.0
3.49
4.0
RhB
CO2 + H2O
O2
O2•
e-
e- ECB (2)
e- ECB (1)
Eg (2)
Eg (1)
h+
h+
EVB
LUMO
HOMO
RhB
-1.42 eV
O2/O2•−
(0.13 eV)
0.95 eV
OH•/H2O
(2.68 eV)
La
Bi
Nb/Cr
O
c
b
a

REFERENCES

1. Wang, W.; Tadé, M. O.; Shao, Z. Research Progress of Perovskite Materials in Photocatalysis and Photovoltaics Related Energy Conversion and Environment Treatment. *Chem. Soc. Rev.* **2015**, *44*, 5371-5408.

2. Chen, X.; Shen, S.; Guo, L.; Mao, S. S. Semiconductor-Based Photocatalytic Hydrogen Generation. *Chem. Rev.* **2010**, *110*, 6503-6570.

3. Luo, B.; Liu, G.; Wang, L. Recent Advances in 2D Materials for Photocatalysis. *Nanoscale* **2016**, *8*, 6904-6920.

4. Zhang, X.; Peng, T.; Song, S. Recent Advances in Dye-sensitized Semiconductor Systems for Photocatalytic Hydrogen Production. *J. Mater. Chem.* **2016**, *4*, 2365-2402.

5. Hoffmann, M. R.; Martin, S.T.; Choi, W.; Bahnemann, D.W. Environmental Applications of Semiconductor Photocatalysis. *Chem. Rev.* **1995**, *95*, 69-96.

6. Kudo, A.; Miseki, Y. Heterogeneous Photocatalyst Materials for Water Splitting. *Chem. Soc. Rev.* **2009**, *38*, 253-278.

7. Fujishima, A.; Honda, K. Electrochemical Photolysis of Water at a Semiconductor Electrode. *Nature* **1972**, *238*, 37-38.

8. Zou, Z.; Ye, J.; Sayama, K.; Arakawa, H. Direct Splitting of Water under Visible Light Irradiation with an Oxide Semiconductor Photocatalyst. *Nature* **2001**, *414*, 625-627.

9. Asahi, R.; Morikawa, T.; Ohwaki, T.; Aoki, K.; Taga, Y. Visible-Light Photocatalysis in Nitrogen-Doped Titanium Oxides. *Science* **2001**, *293*, 269-271.

10. Maeda, K.; Takata, T.; Hara, M.; Saito, N.; Inoue, Y.; Kobayashi, H.; Domen, K. GaN:ZnO Solid Solution as a Photocatalyst for Visible-Light-Driven Overall Water Splitting. *J. Am. Chem. Soc.* **2005**, *127*, 8286-8287.

11. Ni, M.; Leung, M. K. H.; Leung, D.Y.C.; Sumathy, K. A Review and Recent Developments in Photocatalytic Water-Splitting Using TiO_2 for Hydrogen Production. *Renewable Sustainable Energy Rev.* **2007**, *11*, 401-425.

12. Zhang, H.; Chen, G.; Bahnemann, D. W. Photoelectrocatalytic Materials for Environmental Applications. *J. Mater. Chem.* **2009**, *19*, 5089-5121.

13. Choi, W. S.; Chisholm, M. F.; Singh, D. J.; Choi, T.; Jellison Jr., G. E.; Lee, H. N. Wide Bandgap Tunability in Complex Transition Metal Oxides by Site-Specific Substitution. *Nat. Commun.* **2012**, *3*, 689.

14. Xu, X.; Randorn, C.; Efstathiou, P.; Irvine, J. T. S. A Red Metallic Oxide Photocatalyst. *Nat. Mater.* **2012**, *11*, 595-598.

15. Tong, H.; Ouyang, S.; Bi, Y.; Umezawa, N.; Oshikiri, M.; Ye, J. Nano-photocatalytic Materials: Possibilities and Challenges. *Adv. Mater.* **2012**, *24*, 229-251.

16. Banerjee, S,; Pillai S. C.;, Falaras, P.; O'Shea, K. E.; Byrne, J.A.; Dionysiou, D. D. New Insights into the Mechanism of Visible Light photocatalysis. *J. Phys. Chem. Lett.* **2014**, *5*, 2543-2554.

17. Yaghoubi, H.; Li, Z.; Chen, Y.; Ngo, H. T.; Bhethanabotla, V. R.; Joseph, B.; Ma, S.; Schlaf, R.; Takshi, A. Toward a Visible Light-Driven Photocatalyst: The Effect of Midgap-States-Induced Energy Gap of Undoped TiO_2 Nanoparticles. *ACS Catal.* **2015**, *5*, 327-335.

18. Dong, S.; Feng, J.; Fan, M.; Pi, Y.; Han, X.; Liu, M.; Sun, J.; Sun, J. Recent Developments in Heterogeneous Photocatalytic Water Treatment using Visible Light-Responsive Photocatalysts: A Review. *RSC Adv.* **2015**, *5*, 14610-14630.

19. Schaak, R. E.; Mallouk, T. E.; Perovskites by Design: A Toolbox of Solid-State Reactions. *Chem. Mater.* **2002**, *14*, 1455-1471.

20. Moon, S.-Y.; Choi, K. S.; Jung, K. W.; Lee, H.; Jung, D. Ferroelectric Properties of Substituted Aurivillius Phases $SrBi_2Nb_{2-x}M_xO_9$ (M = Cr, Mo). *Bull. Korean Chem. Soc.* **2002**, *23*, 1463-1466.

21. Mandal, T. K.; Sivakumar T.; Augustine, S.; Gopalakrishnan, J. Heterovalent Cation-Substituted Aurivillius Phases, $Bi_2SrNaNb_2TaO_{12}$ and $Bi_2Sr_2Nb_{3-x}M_xO_{12}$ (M = Zr, Hf, Fe, Zn). *Mater. Sci. Engg. B* **2005**, *121*, 112-119.

22. Kalaiselvi, B. J.; Sridarane, R.; Murugan, R. Dielectric Properties of $Sr_{0.8}Bi_{2.2}(V_{0.2}Nb_{0.8})_2O_9$ Ceramic. *Mater. Sci. Eng. B.* **2006**, *127*, 224-227.

23. Lufaso, M.W.; Schulze, W.A.; Misture, S.T.; Vanderah, T.A.; Crystal Structure, Magnetic, and Dielectric Properties of Aurivillius-type $Bi_3Fe_{0.5}Nb_{1.5}O_9$. *J. Solid State Chem.* **2007**, *180*, 2655-2660.

24. McCabe, E.E.; Greaves, C. Structural and Magnetic Characterization of Aurivillius Material $Bi_2Sr_2Nb_{2.5}Fe_{0.5}O_{12}$. *J. Solid State Chem.* **2008**, *181*, 3051-3056.

25. Fang, P.; Fan H.; Li, J.; Jia, X., Liang, F. The Dielectric Properties and the Relaxation Phase Transition of Copper Substituted $SrBi_2Nb_2O_9$ Ferroelectric Ceramics. *Solid State Commun.* **2009**, *149*, 2074-2077.

26. Yao, W.; Huang, C.; Ye, J. Hydrogen Production and Characterization of $MLaSrNb_2NiO_9$ (M = Na, Cs, H) Based Photocatalysts. *Chem. Mater.* **2010**, *22*, 1107-1113.

27. Wang, B.; Li, C.; Hirabayashi, D.; Suzuki, K. Hydrogen Evolution by Photocatalytic Decomposition of Water under Ultraviolet-Visible Irradiation over $K_2La_2Ti_{3-x}M_xO_{10+\delta}$ Perovskite. *Int. J. Hydrogen Energy* **2010**, *35*, 3306-3312.

28. Kumar, V.; Govind,; Uma, S.; Investigation of Cation (Sn^{2+}) and Anion (N^{3-}) Substitution in favor of Visible Light Photocatalytic Activity in the Layered Perovskite $K_2La_2Ti_3O_{10}$. *J. Hazard. Mater.* **2011**, *189*, 502-508.

29. Liu, S.; Miller, W.; Liu, Y.; Avdeev, M.; Ling, C. D. Sillen-Aurivillius Intergrowth Phases as Templates for Naturally Layered Multiferroics. *Chem. Mater.* **2012**, *24*, 3932-3942.

30. Zuo, X.; Yang, J.; Yuan, B.; Song, D.; Tang, X.; Zhang, K.; Zhu, X.; Song, W.; Dai, J.; Sun, Y. Structural, Magnetic and Dielectric Properties of the Aurivillius Phase $Bi_6Fe_{2-x}Mn_xTi_3O_{18}$ ($0 \le x \le 0.8$). *RSC Adv.* **2014**, *4*, 46704-46709.

31. Naresh, G.; Mandal, T. K. Excellent Sun-Light-Driven Photocatalytic Activity by Aurivillius Layered Perovskites, $Bi_{5-x}La_xTi_3FeO_{15}$ (x = 1, 2). *ACS Appl. Mater. Interfaces* **2014**, *6*, 21000-21010.

32. Naresh, G.; Mandal, T. K. Efficient COD Removal Coinciding with Dye Decoloration by Five- Layer Aurivillius Perovskites under Sunlight-Irradiation. *ACS Sustainable Chem. Eng*. **2015**, *3*, 2900-2908.

33. Singh, R.; Luthra, L.; Rawat, R.S.; Tandon R. P. Structural, Dielectric and Piezoelectric Properties of $SrBi_2Nb_2O_9$ and $Sr_{0.8}Bi_{2.2}Nb_2O_9$ Ceramics. *Ceram. Int*. **2015**, *14*, 4468-4478.

34. Bai, W.; Chen, C.; Yang, J.; Zhang, Y.; Qi, R.; Huang, R.; Tang, X.; Duan, C.-G.; Chu, J. Dielectric behaviors of Aurivillius $Bi_5Ti_3Fe_{0.5}Cr_{0.5}O_{15}$ Multiferroic Polycrystals: Determining the Intrinsic Magnetoelectric Responses by Impedance Spectroscopy. *Sci. Rep.* **2015**, *5*, 17846.

35. Shi, K.; Peng, L.; Li, M.; Zhou, J.; Jiang, K.; Zhang, J.; Hu, Z.; Dong, Z.; Chu, J. Structural Distortion, Phonon Behavior and Electronic Transition of Aurivillius Layered Ferroelectric $CaBi_2Nb_{2-x}W_xO_9$ ceramics. *J. Alloys Compd.* **2015**, *653*, 168-174.

36. Ge, W.; Fu, Z.; Li, X.; Wang, J. Zhu, Z.; Liu, M.; Peng, R.; Lu, Y. Optimizing the Photocatalysis in Ferromagnetic $Bi_6Fe_{1.9}Co_{0.1}Ti_3O_{18}$ Nanocrystal by Morphology Control. *RSC Adv.* **2015**, *5*, 54165-54170.

37. Li, X.; Zhu, Z.; Li, F.; Huang, Y.; Hu, X.; Huang, H.; Peng, R.; Zhai, X. F.; Fu, Z.; Lu, Y. Multifunctional Single-Phase Photocatalysts: Extended Near Infrared Photoactivity and Reliable Magnetic Recyclability. *Sci. Rep.* **2015**, *5*, 15511.

38. Wang, J.; Fu, Z.; Peng, R.; Liu, M.; Sun, S.; Huang, H.; Li, L.; Knize, R. J.; Lu, Y. Low Magnetic Field Response Single-phase Multiferroics under High Temperature. *Mater. Horiz.* **2015**, *2*, 232-236.

39. Yin, W.; Chen, C.; Bai, W.; Yang, J.; hang, Y.; Tang, X.; Duana, Y. G.; Chu. J. Dielectric Behavior Dependence on Temperature and Cr-doping Contents of Aurivillius $Bi_5Ti_3FeO_{15}$ Ceramics. *Ceram. Int.* **2016**, *42*, 4298-4305.

40. Fujito, H.; Kunioku, H.; Kato, D.; Suzuki, H.; Higashi, M.; Kageyama, H.; Abe, R. Layered Perovskite Oxychloride Bi_4NbO_8Cl: A Stable Visible Light Responsive Photocatalyst for Water Splitting. *J. Am. Chem. Soc*. **2016**, *138*, 2082-2085.

41. Zhang, Q.; Liu, J.; Sun, H.; Wang, X.; Hao, X.; An, S. Luminescence Photoswitching of Ho-doped $Na_{0.5}Bi_{2.5}Nb_2O_9$ Ferroelectrics: The Luminescence Readout Process. *J. Mater. Chem. C*, **2017**, *5*, 807-816.

42. Pandey, A.; Naresh, G.; Mandal, T. K. Sunlight Responsive New Sillèn-Aurivillius A1X1 Hybrid Layered Oxyhalides with Enhanced Photocatalytic Activity. *Sol. Energy Mater. Sol. Cells* **2017**, *161*, 197-205.

43. Liu, X.; Xu, L.; Huang, Y.; Qin, C.; Qin, L.; Seo, H. J. Improved Photochemical Properties of Aurivillius $Bi_5Ti_3FeO_{15}$ with Partial Substitution of Ti^{4+} with Fe^{3+}. *Ceram. Int.* **2017**, *43*, 12372-12380.

44. Naresh, G.; Malik, J.; Meena, V.; Mandal, T. K. pH Mediated Collective and Selective Solar Photocatalysis by a series of Layered Aurivillius Perovskites. *ACS Omega* **2018**, *3*, 11104-11116.

45. Li, Y.; Chen, L.; Zhang, H.; Lv, Z. Band Structure and Photocatalytic Activities for H_2 Production of $ABi_2Nb_2O_9$ (A= Ca, Sr, Ba). *Int. J. Hydrogen Energ*. **2010**, *35*, 2652.

46. Wu, W.; Liang, S.; Wang, X.; Bi, J.; Liu, P.; Wu, L. Synthesis, Structures and Photocatalytic Activities of Microcrystalline $ABi_2Nb_2O_9$ (A = Sr, Ba) Powders. *J. Solid State Chem*. **2011**, *184*, 81-88.

47. Kim, J. H.; Hwang, K. T.; Kim, U. S.; Kang, Y. M. Photocatalytic Characteristics of Immobilized $SrBi_2Nb_2O_9$ film for Degradation of Organic Pollutants. *Ceram. Int.* **2012**, *38*, 3901-3906.

48. Kim, H. G.; Hwang, D. W.; Lee, J. S. An Undoped, Single-Phase Oxide Photocatalyst Working under Visible Light. *J. Am. Chem. Soc.* **2004**, *126*, 8912-8913.

49. Wu, W.; Liu, G.; Liang, S.; Chen, Y.; Shen, L.; Zheng, H.; Yuan, H.; Hou, Y.; Wu, L. Efficient Visible-Light-Induced Photocatalytic Reduction of 4-Nitroaniline to p-Phenylenediamine over Nanocrystalline $PbBi_2Nb_2O_9$. *J. Catal.* **2012**, *290*, 13-17.

50. Kim, H. G.; Becker, O. S.; Jang, J. S.; Ji, S. M.; Borse, P. H. Lee, J. S. A generic Method of Visible Light Sensitization for Perovskite-related Layered Oxides: Substitution Effect of Lead. *J. Solid State Chem.* **2006**, *179*, 1214-1218.

51. Arney, D.; Maggard, P. A. Effect of Platelet Shaped Surfaces and Silver-Cation Exchange on the Photocatalytic Hydrogen Production of $RbLaNb_2O_7$. *ACS Catal.* **2012**, *2*, 1711-1717.

52. Xu, N.; Takei, T.; Miura, A.; Kumada, N. Preparation and Phase Transformation of Ag or Bi Ion-exchanged Layered Niobate Perovskite and their Photocatalytic Properties. *J. Cer. Soc. Jpn.* **2015**, *123*, 690-694.

53. Hong, S. J.; Borse, P. H.; Ji, S.M.; Jang, J. S.; Lee, J. S.; Structure of $PbBi_2Nb_2O_9$ and Its Cr- Doped Layered Perovskite System and Their Photocatalytic Activities. *J. Korean. Phys. Soc.* **2007**, *51*, S27-S31.

54. Kim, H. G.; Borse, P. H.; Jang, J. S.; Jeong, E. D.; Lee, J. S. Enhanced Photochemical Properties of Electron Rich W-Doped $PbBi_2Nb_2O_9$ Layered Perovskite Materials Under Visible Light Irradiation. *Mater. Lett.* **2008**, *62*, 1427-1430.

55. Jiang, L.; Ni, S.; Liu, G.; Xu, X. Photocatalytic Hydrogen Production over Aurivillius Compound Bi_3TiNbO_9 and its Modifications by Cr/Nb Co-doping. *Appl. Cat. B: Environ.* **2017**, *217*, 342-352.

56. Ismunandar.; Kennedy, B. J. Structure of $ABi_2Nb_2O_9$ (A = Sr, Ba): Refinement of Powder Neutron Diffraction Data. *J. Solid State Chem.* **1996**, *126*, 135-141.

57. Rietveld, H. M. A Profile Refinement Method for Nuclear and Magnetic Structures. J. Appl. Cryst. **1969**, 2, 65-71.

58. Blake, S. M.; Falconer, M. J.; McCreedy, M.; Lightfoot, P. Cation Disorder in Ferroelectric Aurivillius Phase of the type $Bi_2ANb_2O_9$ (A = Ba, Sr, Ca). *J. Mater. Chem.* **1997**, *7*, 1609-1613.

59. Harrison, P. G.; Lloyd, N. C.; Daniell, W. The Nature of the Chromium Species Formed during the Thermal Activation of Chromium-Promoted Tin (IV) Oxide Catalysts: An EPR and XPS Study. *J. Phys. Chem. B* **1998**, *102*, 10672-10679.

60.Kar, P,; Sardar, S.; Ghosh, S.; Parida, M. R.; Liu, B.; Mohammed, O. F.; Lemmens, P.; Pal, S. K. Nano surface engineering of Mn_2O_3 for potential light-harvesting application. *J. Mater. Chem. C*, **2015**, *3*, 8200-8211.

61. Lukashuk, L.; Yigit, N.; Rameshan, R.; Kolar, E.; Teschner, D.; Havecker, M.; Gericke, A. K.; Schlögl, R.; Föttinger, K.; Rupprechter, G. Operando Insights into CO Oxidation on Cobalt Oxide Catalysts by NAP-XPS, FTIR, and XRD. *ACS Catal*. **2018**, *8*, 8630−8641.

62. Kuneŝ, J.; Lukoyanov, A. V.; Anisimov, V. I.; Scalettar, R. T.; Pickett, W. E. Collapse of Magnetic Moment drives the Mott Transition in MnO. *Nature Materials* **2008**, *7*, 198-202.

63. Fu, H.; Pan, C.; Yao, W.; Zhu, Y. Visible-Light-Induced Degradation of Rhodamine B by Nanosized Bi_2WO_6. *J. Phys. Chem. B.* **2005**, *109*, 22432-22439.

64. Xu, Y.; Schoonen, M. A. A. The Absolute Energy Positions of Conduction and Valence Bands of Selected Semiconducting Minerals. *Am. Mineral.* **2000**, *85*, 543-556.

65. Kumar, S.; Surendar, T.; Baruah, A.; Shanker, V. Synthesis of a Novel and Stable g-C_3N_4–Ag_3PO_4 Hybrid Nanocomposite Photocatalyst and Study of the Photocatalytic Activity under Visible Light Irradiation. *J. Mater. Chem. A* **2013**, 1, 5333-5340.

66. Pan, L.; Zou, J.J.; Liu, X. Y.; Liu, X. J.; Wang, S.; Zhang, X.; Wang, L. Visible−Light−Induced Photodegradation of Rhodamine B over Hierarchical TiO_2: Effects of Storage Period and Water-Mediated Adsorption Switch. *Ind. Eng. Chem. Res.* **2012**, *51*, 12782-12786.

CHAPTER -4

Iron Incorporated Double Layered Titanates-Tungstates and its La- substituted Analogs: Magnetism and Solar Photocatalysis

Iron Incorporated Double Layered Titanates and its La-substituted Analogs: Magnetism and Solar Photocatalysis

4.1 INTRODUCTION

The development of photocatalysts has got adequate attention in the scientific community due to its overwhelming potential in addressing issues related to environment pollution and energy generation by utilizing abundant solar energy.[1,2] In the regard, the Aurivillius phase oxides are noteworthy in showing enhanced photocatalytic activity with respect to water splitting and sunlight driven pollutant degradation. Many studies have been reported on oxides containing Bi^{3+} for photocatalytic activity in the visible light.[3-12] The Bi plays important role in these materials, with possible hybridization of Bi 6*s* and O 2*p* the up-lifting of valance band edge reduces the band gap and is also responsible for the high mobility of the electron and holes, which helps in the photodegradation process.[4,13]

Among various Bi^{3+} containing oxides, which show photocatalytic activity in visible light, Aurivillius phases have special properties.[3-12,14,15] The Aurivillius phases consist of alternating stacks of perovskite blocks interleaved by the fluorite-like Bi_2O_2 layers. The general formula of these layered perovskites is $(Bi_2O_2)[A_{n-1}B_nO_{3n+1}]$, where *n* is the number of perovskite block. Some of the Aurivillius materials that have been reported to show photocatalytic activity in the visible-light, are Bi_2WO_6,[16-18] Bi_2MoO_6,[19,20] Bi_3TiNbO_9,[21] $Bi_3Ti_4O_{12}$,[22] $BiVO_4$,[13,23] and $PbBi_2Nb_2O_9$.[24-26] They have been used for degradation of organic pollutants, water splitting and CO_2 reduction under visible light.

The double-layer titanate Aurivillius phases, $Bi_3Ti_{1.5}W_{0.5}O_9$, have drawn the attraction for its dielectric, ferroelectric and luminescence properties.[27-30] The nanosheets and nanoparticle of $Bi_6Ti_3WO_{18}$, prepared by the sol-gel method, showed photocatalytic activity towards RhB degradation under visible-light.[31,32] Due to the involvement of perovskite slab, the Aurivillius compounds are amenable to various compositional modification. For example, by the doping of transition metal the compounds becomes strong visible light absorber with reduced band gap and efficient for photocatalytic reaction, such as, degradation of pollutants, hydrogen production etc.[21,22,33]

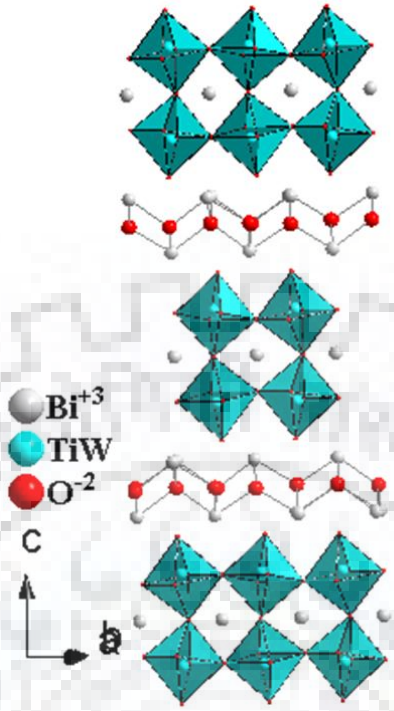

Figure 4.1 Structure of two-layer Aurivillius perovskite, $Bi_3Ti_{1.5}W_{0.5}O_9$.

In this work, the effect of co-substitution of La and Fe on the structural, magnetic, optical and photocatalytic activity of two-layer Aurivillius perovskites, $Bi_3Ti_{1.5}W_{0.5}O_9$ is investigated. The solid-state synthesis of $Bi_{3-x}La_xTi_{1.5}W_{0.5}O_9$ (x = 0, 1), $Bi_{3-x}La_xTiW_{0.67}Fe_{0.33}O_9$ (x = 0, 1), and their characterization by P-XRD, FE-SEM, TEM etc. are described. The Fe-substituted compounds, $Bi_{3-x}La_xTiW_{0.67}Fe_{0.33}O_9$ (x = 0, 1) show paramagnetic behavior in the 5-300 K temperature range. UV-vis DRS data exhibits reduce the band gap on Fe-substitution in $Bi_3Ti_{1.5}W_{0.5}O_9$. The photocatalytic activity of the compound were checked by the degradation of RhB at pH 2 under sunlight-irradiation and their photostability on recycling is also reported in this chapter. The details of synthesis, characterization and RhB degradation over $Bi_{3-x}La_xTi_{1.5}W_{0.5}O_9$ (x = 0, 1), $Bi_{3-x}La_xTiW_{0.67}Fe_{0.33}O_9$ (x = 0, 1) are described.

4.2 EXPERIMENTAL SECTION

4.2.1 Materials and Synthesis

To prepare $Bi_{3-x}La_xTi_{1.5}W_{0.5}O_9$ (x = 0, 1) and $Bi_{3-x}La_xTiW_{0.67}Fe_{0.33}O_9$ (x = 0, 1), Bi_2O_3 (Sigma-Aldrich, ≥ 98.0%), La_2O_3 (Sigma-Aldrich, 99.99%), TiO_2 (Sigma-Aldrich, 99.8%), WO_3 (Sigma-Aldrich, ≥ 99.0%), $FeCl_2{\cdot}4H_2O$ (Sigma-Aldrich, ≥ 99.0%) and oxalic acid (Merck ≥ 99.0%) were used as raw materials. All analytical grade reagents were used as purchased without any further purification. In the degradation experiments, double distilled water is used throughout.

The compounds $Bi_2LaTi_{0.5}W_{1.5}O_9$ and $Bi_{3-x}La_xTiW_{0.67}Fe_{0.33}O_9$ (x = 0, 1) are synthesized using solid-state route. Stoichiometric quantities of Bi_2O_3, La_2O_3 (preheated at 950 °C), TiO_2, WO_3 and $FeC_2O_4{\cdot}2H_2O$ were mixed thoroughly in an agate mortar for 1h. The powder mixture was then calcined at 800 °C for 7 h followed by 900 °C for 7 h with intermittent grinding. $FeC_2O_4{\cdot}2H_2O$ was synthesized by co-precipitation method in aqueous medium, by mixing equimolar solution $FeCl_2{\cdot}4H_2O$ and oxalic acid. Similarly, $Bi_3Ti_{1.5}W_{0.5}O_9$ is prepared by solid-state route using stoichiometric mixture of Bi_2O_3, TiO_2, WO_3 and $FeC_2O_4{\cdot}2H_2O$ as reported.[27]

4.2.2 Dye Adsorption Studies

The adsorption of RhB on the catalyst surface at different pH was determined by stirring of catalyst suspensions in RhB solution to accomplish adsorption-desorption equilibrium in the dark. The absorption experiments was carried out to determine, the concentration of the initial and final dye solution was measured by adsorption measurement with UV-Vis spectrophotometer.

4.2.3 Photocatalytic Activity Test

Photocatalytic activities of the as prepared compounds were carried out in natural sunlight by RhB degradation at different pH. For the test, the RhB solution was prepared in aqueous medium and the pH values (2, 3, 7 and 11) of the solutions were adjusted by addition of dilute HCl or NaOH according to the requirement. The degradation experiments were

carried out at IIT Roorkee (29°51′ N; 77°53′ E) under similar conditions in the month of April, 2017 with solar Direct Normal Irradiance (DNI) of ~ 248 W/m^2. For the degradation study, 100 mL RhB solution (1×10^{-5} M) of appropriate pH was taken in a 250 mL beaker and to this 100 mg powder of photocatalyst was added. To achieve adsorption-desorption equilibrium between the photocatalyst and RhB, the dye-catalyst suspensions were magnetically stirred in the dark at 400 rpm. Thereafter, the solution of dye-catalyst suspension was kept in direct sunlight-irradiation. The dye concentration during the degradation experiments was checked by taking 5 mL of suspension at regular time intervals and this suspension was centrifuged at 8500 rpm to remove the catalyst particles. The centrifugate was used for the absorption measurement and after the measurement test at each interval, the dye solution was put back into the solution to minimize the error due to the loss of RhB and catalysts, by keeping the volume of the dye constant. For self-degradation correction and calculation of degradation efficiency, a blank test was also carried out with the RhB solution of same concentration without the catalyst under sunlight-irradiation. The photocatalytic degradation efficiencies of the catalysts were calculated using the following equation

$$\text{Degradation (\%)} = (1 - C/C_0) \times 100 \quad (4.1)$$

where C_0 and C are the initial dye concentrations and dye concentration at different time intervals, respectively.

4.2.4 Catalyst Stability and Photocatalytic Cycle Test

Several cycles of photodegradation with the same catalyst in the acidic medium were carried out followed by the P-XRD analysis of the recovered catalyst to investigate the stability. For this, the photocatalytic degradation studies were carried out through similar processes as activity test by taking 0.1 g of catalyst in 100 mL of 1×10^{-5} M RhB solution. For cycle test, after first cycle, the catalyst was separated by centrifugation and recovered from the centrifuge tube into a beaker with the help of a fresh 100 mL of 1×10^{-5} M RhB solution. Thereafter, obtained dye-catalyst suspension was stirred by magnetic stirring in the dark for 1 h. Then the solution was exposed to the direct sunlight-irradiation for the second cycle test. Similarly, the procedure was repeated for other cycle also. After five cycles, the catalyst was separated, dried and subjected to P-XRD analysis.

4.3.5 Detection of Reactive Species

The reactive species, which are responsible for the photodegradation process, were investigated through the scavenger tests. For that, suitable scavenger was mixed in the catalyst-dye suspension and rest of the photodegradation experiment was followed as described in the activity test. Herein, ammonium oxalate (AO), benzoquinone (BQ) and tertiary butyl alcohol (t-BuOH) were used as h^+, $O_2^{\bullet-}$ and $^{\bullet}OH$ scavengers.

4.3 RESULTS AND DISCUSSION

4.3.1 P-XRD Analysis

The P-XRD patterns of the as prepared compounds, $Bi_{3-x}La_xTi_{1.5}W_{0.5}O_9$ (x = 0, 1), $Bi_{3-x}La_xTiW_{0.67}Fe_{0.33}O_9$ (x = 0, 1) are shown in Figure 4.2. The experimental P-XRD patterns are matched with the standard JCPDS data (JCPDS PDF # 31-0204) which confirms the formation of single phase two-layer Aurivillius perovskites. All observed peaks in the synthesized compounds are indexed in the orthorhombic $A2_1am$ space group [27].

The least-squares refined lattice parameters for the compounds are given in Table 4.1. The indexed P-XRD data for $Bi_3Ti_{0.5}W_{1.5}O_9$, $Bi_3TiW_{0.67}Fe_{0.33}O_9$, $Bi_2LaTi_{0.5}W_{1.5}O_9$ and $Bi_2LaTiW_{0.67}Fe_{0.33}O_9$ are shown in Tables 4.2, 4.3, 4.4 and 4.5, respectively.

Table 4.1 Lattice Parameters and Band Gap of $Bi_{3-x}La_xTi_{1.5}W_{0.5}O_9$ (x = 0, 1) and $Bi_{3-x}La_xTiW_{0.67}Fe_{0.33}O_9$ (x = 0, 1)

Compound	Lattice parameters (Å)		
	a	*b*	*c*
$Bi_3Ti_{1.5}W_{0.5}O_9$	5.364(2)	5.389(2)	24.89(1)
$Bi_3TiW_{0.67}Fe_{0.33}O_9$	5.387(3)	5.371(4)	24.99(1)
$Bi_3LaTi_{1.5}W_{0.5}O_9$	5.441(2)	5.428(1)	24.86(4)
$Bi_3LaTiW_{0.67}Fe_{0.33}O_9$	5.425(1)	5.432(2)	25.03(1)

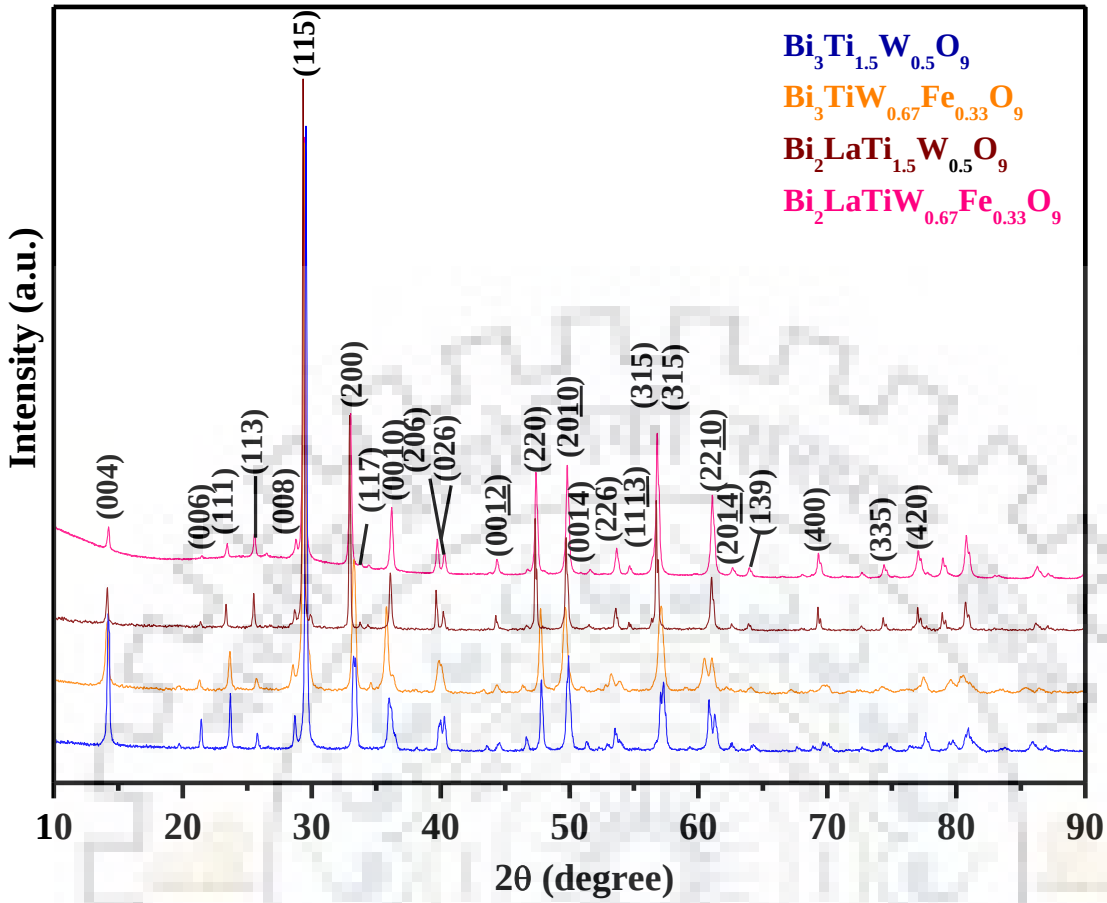

Figure 4.2 P-XRD patterns of $Bi_{3-x}La_xTi_{1.5}W_{0.5}O_9$ (x = 0, 1) and $Bi_{3-x}La_xTiW_{0.67}Fe_{0.33}O_9$ (x = 0, 1)

The P-XRD simulation data indicates that the La–substitution in $Bi_3Ti_{1.5}W_{0.5}O_9$ at the A-site and coupled substitution of Fe, Ti and W in $Bi_{3-x}La_xTi_{1.5}W_{0.5}O_9$ (x = 0, 1) at the B-site of the perovskite block. For the simulation, the structural data of $Bi_3Ti_{1.5}W_{0.5}O_9$ was used as an initial input with *A2₁am* space group.[28] Figure 4.1 shows the crystal structure of $Bi_3Ti_{1.5}W_{0.5}O_9$, The observed P-XRD data of $Bi_2LaTi_{1.5}W_{0.5}O_9$ matches very well with the simulated data. The compound, $Bi_3Ti_{1.5}W_{0.5}O_9$ contains two types of bismuth, Bi(1) and Bi(2), while Bi(1) is present in $[Bi_2O_2]^{2+}$ layer and Bi(2) lie in the A-site of the perovskite block. The simulation data have shown that the La occupy the Bi(1) site and 16% of Fe is substituted at the B-site of the perovskite in the perovskite block. The data simulation used in the given in Tables 4.6, 4.7 and Figure 4.3 shows the comparison of the simulated P-XRD pattern and observed data.

Table 4.2 Indexed P-XRD Data for $Bi_3Ti_{1.5}W_{0.5}O_9$.

h k l	d_{obs}(Å)	d_{calc} (Å)	I_{obs}
0 0 4	6.203	6.222	12
0 0 6	4.139	4.148	1
1 1 1	3.751	3.758	2
1 1 3	3.454	3.456	8
0 0 8	3.107	3.111	4
1 1 5	3.020	3.021	100
2 0 0	2.691	2.694	29
2 0 2	2.649	2.650	1
1 1 7	2.616	2.616	1
0 0 10	2.488	2.489	15
2 0 6	2.253	2.252	6
1 1 9	2.235	2.236	5
0 2 8	2.030	2.031	3
2 2 0	1.944	1.944	14
0 2 10	1.825	1.825	20
0 0 14	1.784	1.786	2
1 1 13	1.710	1.710	5
1 3 3	1.675	1.675	1
1 3 5	1.612	1.611	18
3 1 5	1.606	1.606	18
2 2 10	1.521	1.522	13
2 0 14	1.486	1.486	1
1 3 9	1.453	1.453	2
4 0 0	1.362	1.363	3

a = 5.364(2), b = 5.389(2), c = 24.89(1) Å.

Table 4.3 Indexed P-XRD Data for $Bi_3TiW_{0.67}Fe_{0.33}O_9$.

h k l	d_{obs}(Å)	d_{calc} (Å)	I_{obs}
0 0 4	6.243	6.249	7
0 0 6	4.165	4.167	1
1 1 1	3.757	3.760	3
1 1 3	3.462	3.460	6
0 0 8	3.124	3.124	3
1 1 5	3.027	3.027	100
2 0 0	2.691	2.693	27
2 0 2	2.648	2.649	1
1 1 7	2.603	2.603	1
0 0 10	2.499	2.499	12
2 0 6	2.261	2.262	6
1 1 9	2.242	2.243	5
0 2 8	2.040	2.040	3
2 2 0	1.950	1.950	15
0 2 10	1.832	1.832	21
0 0 14	1.785	1.785	2
1 1 13	1.716	1.716	5
1 3 3	1.681	1.683	1
1 3 5	1.612	1.612	20
3 1 5	1.608	1.609	20
2 2 10	1.526	1.526	14
2 0 14	1.488	1.488	1
1 3 9	1.451	1.451	2
4 0 0	1.358	1.358	3

a = 5.387(3), b = 5.371(4), c = 24.99(1) Å.

Table 4.4 Indexed P-XRD Data for $Bi_3LaTi_{1.5}W_{0.5}O_9$.

h k l	d_{obs}(Å)	d_{calc} (Å)	I_{obs}
0 0 4	6.237	6.216	6
0 0 6	4.152	4.144	2
1 1 1	3.803	3.803	4
1 1 3	3.490	3.486	6
0 0 8	3.110	3.108	1
1 1 5	3.042	3.040	100
2 0 0	2.717	2.714	32
2 0 2	2.638	2.638	1
1 1 7	2.592	2.592	1
0 0 10	2.485	2.486	11
2 0 6	2.270	2.270	2
1 1 9	2.230	2.231	6
0 2 8	2.040	2.040	4
2 2 0	1.919	1.921	25
0 2 10	1.835	1.847	24
0 0 14	1.772	1.772	1
1 1 13	1.721	1.721	2
1 3 3	1.703	1.703	5
1 3 5	1.625	1.625	1
3 1 5	1.621	1.621	23
2 2 10	1.521	1.521	19
2 0 14	1.483	1.482	1
1 3 9	1.458	1.458	2
4 0 0	1.355	1.355	5

a = 5.441(2), b = 5.428(1), c = 24.86(4) Å.

Table 4.5 Indexed P-XRD Data for $Bi_2LaTiW_{0.67}Fe_{0.33}O_9$

h k l	d_{obs}(Å)	d_{calc} (Å)	I_{obs}
0 0 4	6.251	6.248	8
0 0 6	4.171	4.168	1
1 1 1	3.812	3.838	3
1 1 3	3.498	3.496	6
0 0 8	3.126	3.124	2
1 1 5	3.051	3.046	100
2 0 0	2.722	2.724	35
2 0 2	2.658	2.658	1
1 1 7	2.602	2.602	1
0 0 10	2.503	2.503	13
2 0 6	2.277	2.275	6
1 1 9	2.250	2.250	5
0 2 8	2.049	2.049	3
2 2 0	1.922	1.922	21
0 2 10	1.838	1.838	23
0 0 14	1.781	1.782	2
1 1 13	1.716	1.716	4
1 3 3	1.685	1.658	1
1 3 5	1.642	1.6	1
3 1 5	1.624	1.624	28
2 2 10	1.521	1.522	16
2 0 14	1.488	1.491	1
1 3 9	1.459	1.459	2
4 0 0	1.357	1.358	4

a = 5.425(1), b = 5.432(1), c = 25.03(1) Å.

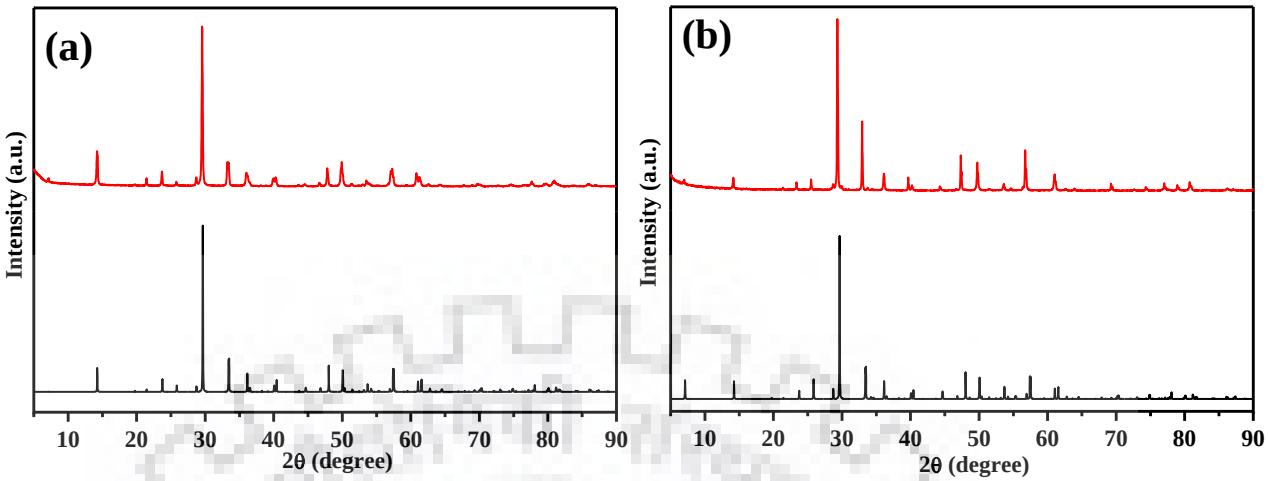

Figure 4.3 Observed (top) and simulated (bottom) P-XRD pattern of (a) $Bi_3TiW_{0.67}Fe_{0.33}O_9$ and (b) $Bi_3LaTi_{1.5}W_{0.5}O_9$.

Table 4.6 Atomic Position, Site Occupancy and Thermal Parameters used for P-XRD Pattern Simulation of $Bi_3TiW_{0.67}Fe_{0.33}O_9$.

Atom	*x*	*y*	*z*	Occ.	B (temp)
Bi1	0.000	0.258	0.000	1	2.05
Bi2	0.511	0.766	0.198	1	1.26
Ti/W/Fe	0.549	0.746	0.418	0.5/0.335/0.165	0.33
O1	0.815	0.689	0	1	0.89
O2	0.779	0.997	0.250	1	0.94
O3	0.559	0.703	0.341	1	1.36
O4	0.778	0.969	0.070	1	1.11
O5	0.854	0.958	0.585	1	1.09

Table 4.7 Atomic Position, Site Occupancy and Thermal Parameters used for P-XRD Pattern Simulation of $Bi_2LaTi_{1.5}W_{0.5}O_9$

Atom	*x*	*y*	*z*	Occ.	B (temp)
La	0.000	0.258	0.000	1	2.05
Bi2	0.511	0.766	0.198	1	1.26
Ti/W	0.549	0.746	0.418	0.75/0.25	0.33
O1	0.815	0.689	0	1	0.89
O2	0.779	0.997	0.250	1	0.94
O3	0.559	0.703	0.341	1	1.36
O4	0.778	0.969	0.070	1	1.11
O5	0.854	0.958	0.585	1	1.09

4.3.2 FE-SEM and EDS Analysis

FE-SEM images and corresponding EDS spectra of $Bi_{3-x}La_xTi_{1.5}W_{0.5}O_9$ (x = 0, 1) and $Bi_{3-x}La_xTiW_{0.67}Fe_{0.33}O_9$ (x = 0, 1) are shown in Figure 4.4. The SEM images show uniform morphology in the entire region of imaging with plate like morphology, which is expected in the layered compound. Moreover, the particles exist with a large degree of agglomeration of the crystallites. The particle size of the platelets show large variation from several hundred nanometers to few micrometers. The elemental composition of the compound analyzed by EDS at several crystallites, both on area and spot basis are in good arrangement with the expected atomic percentage.

4.3.3 FE-SEM-EDS Elemental Mapping Analysis

EDS mapping (Figure 4.5) have revealed the elemental distribution in $Bi_{3-x}La_xTi_{1.5}W_{0.5}O_9$ (x = 0, 1) and $Bi_{3-x}La_xTiW_{0.67}Fe_{0.33}O_9$ (x = 0, 1), in a selected area of FE-SEM image. The elemental mapping indicates the homogeneous distribution of the constituent elements in a selected rectangular area for all the samples. The images clearly show that the amount of Ti decreases and amount of W increases in the Fe incorporated compounds, while the amount of Bi decreases in the La incorporated compounds.

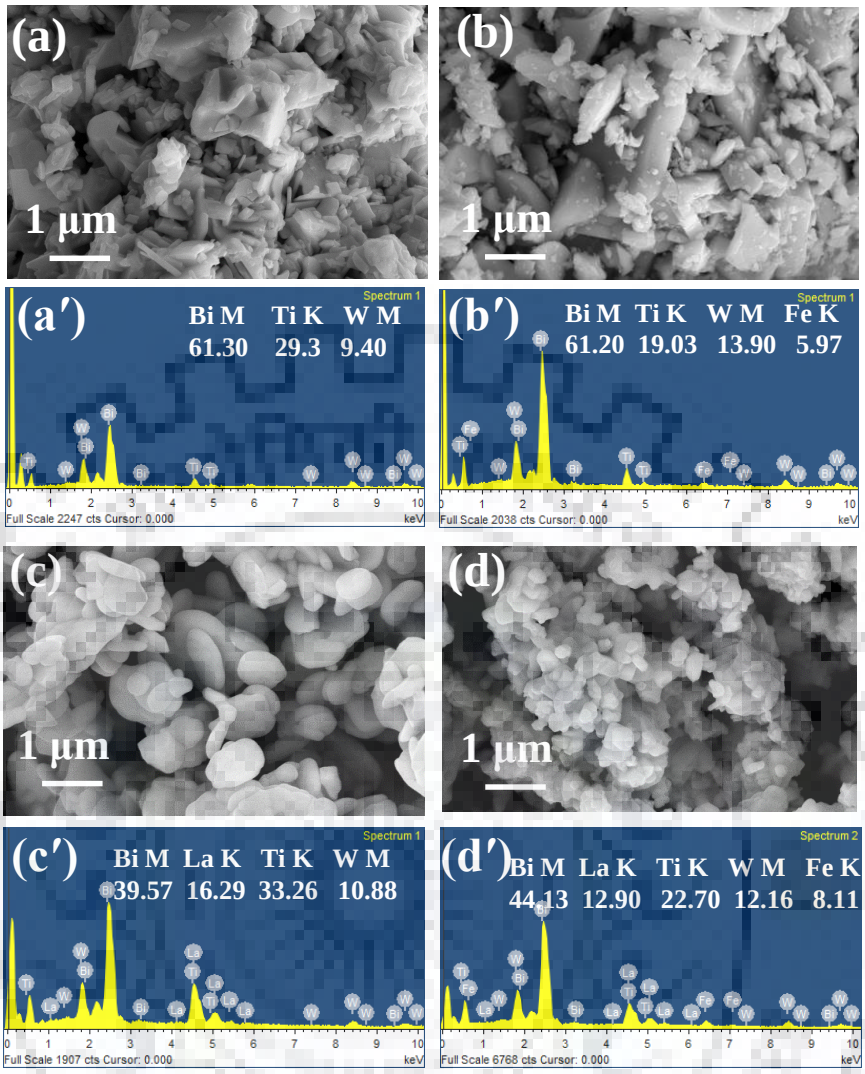

Figure 4.4 FE-SEM images and EDS data of (a) & (a') of $Bi_3Ti_{1.5}W_{0.5}O_9$, (b) & (b') $Bi_3TiW_{0.67}Fe_{0.33}O_9$, (c) & (c') $Bi_3LaTi_{1.5}W_{0.5}O_9$ and (d) & (d') $Bi_2LaTiW_{0.67}Fe_{0.33}O_9$.

4.3.4 TEM Analysis

The TEM data of compound, $Bi_2TiW_{0.67}Fe_{0.33}O_9$, is shown in Figure 4.6. The lattice fringe spacing is ~ 0.388 nm as shown by HR-TEM image this is equivalent to the distance between two corner connected octahedra in the a-b plane of the compound. The polycrystalline nature of the compound shown by SAED data and indexing of few diffraction spots are consistent with the crystal symmetry in accordance with the P-XRD analysis.

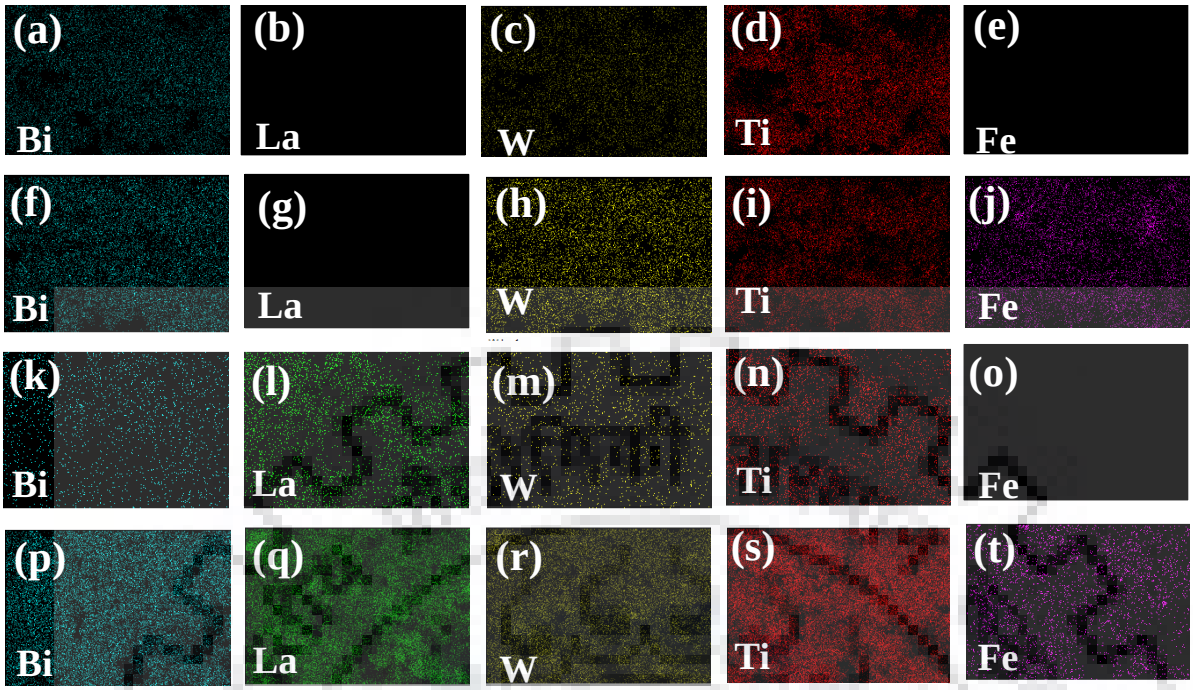

Figure 4.5 EDS elemental mapping of $Bi_3Ti_{1.5}W_{0.5}O_9$ (a-e), $Bi_3TiW_{0.67}Fe_{0.33}O_9$ (f-j), $Bi_3LaTi_{1.5}W_{0.5}O_9$ (k-o), and $Bi_2LaTiW_{0.67}Fe_{0.33}O_9$ (p-t).

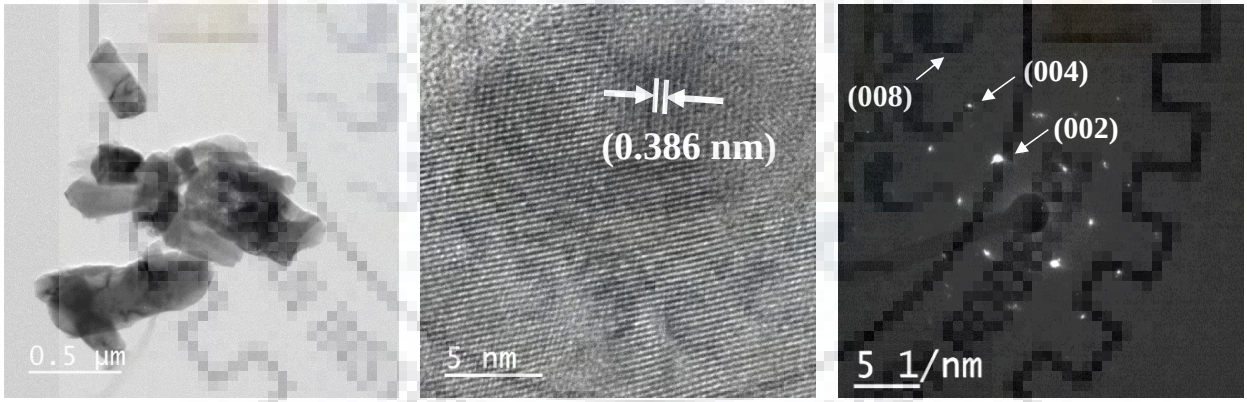

Figure 4.6 TEM images and SAED pattern of $Bi_3TiW_{0.67}Fe_{0.33}O_9$.

4.3.5 Magnetic Properties

Figure 4.7 shows the field cooled (FC) data of the as prepared compounds $Bi_3TiW_{0.67}Fe_{0.33}O_9$ and $Bi_2LaTiW_{0.67}Fe_{0.33}O_9$. Both the compound show paramagnetic nature with no magnetic phase transition in the temperature range 5-300 K. The calculated magnetic moment indicated the presence of Fe^{3+} in the high spin state.

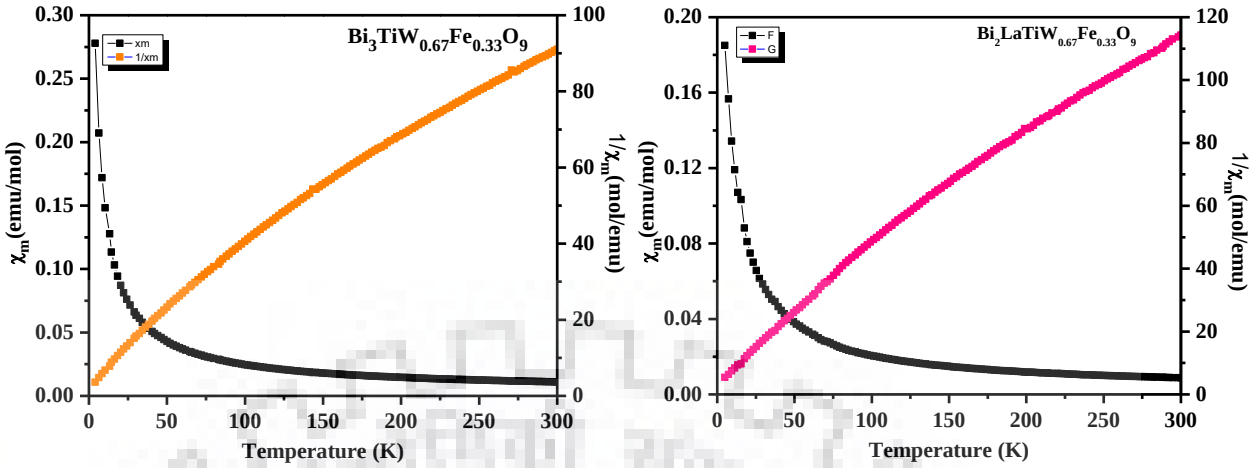

Figure 4.7 Magnetic susceptibility data for $Bi_3TiW_{0.67}Fe_{0.33}O_9$ and $Bi_2LaTiW0.67Fe_{0.33}O_9$.

4.3.6 UV-vis DRS Analysis

The UV-vis DRS data for $Bi_{3-x}La_xTi_{1.5}W_{0.5}O_9$ (x = 0, 1) and $Bi_{3-x}La_xTiW_{0.67}Fe_{0.33}O_9$ (x = 0, 1) are shown in Figure 4.8. The data show the absorption edges for the compounds above 400 nm ($\lambda_{abs.}$ > 400 nm) and confirm that the compounds absorb in the visible region. The coupled substituted compound $Bi_{3-x}La_xTiW_{0.67}Fe_{0.33}O_9$ (x = 0, 1), show two clear absorption edges. The primary absorption edge is attributed to the transition from the valance band mix sates of (Bi-6*s* and O-2*p*) and Fe t_{2g} to conduction band (Ti-3*d* and W-4*d*) while the extended edge corresponding to Fe e_g conduction band that probably lies in between. The band gap energies (E_g) are estimated from the plot of $(\alpha h\nu)^2$ versus $h\nu$ and the value of band gap is given in Table 4.8. Since the all compounds are visible light absorbers, it suggested their potential use in visible-light-driven photocatalysis.

Table 4.8 Calculated Band gap for $Bi_{3-x}La_xTi_{1.5}W_{0.5}O_9$ (x = 0, 1), $Bi_{3-x}La_xTiW_{0.67}Fe_{0.33}O_9$ (x = 0, 1).

Compound	Band Gap (eV)	
	E_g (1)	E_g (2)
$Bi_3Ti_{1.5}W_{0.5}O_9$	3.00	-
$Bi_3TiW_{0.67}Fe_{0.33}O_9$	2.63	3.00
$Bi_2LaTi_{1.5}W_{0.5}O_9$	3.03	-
$Bi_2LaTiW_{0.67}Fe_{0.33}O_9$	2.72	3.01

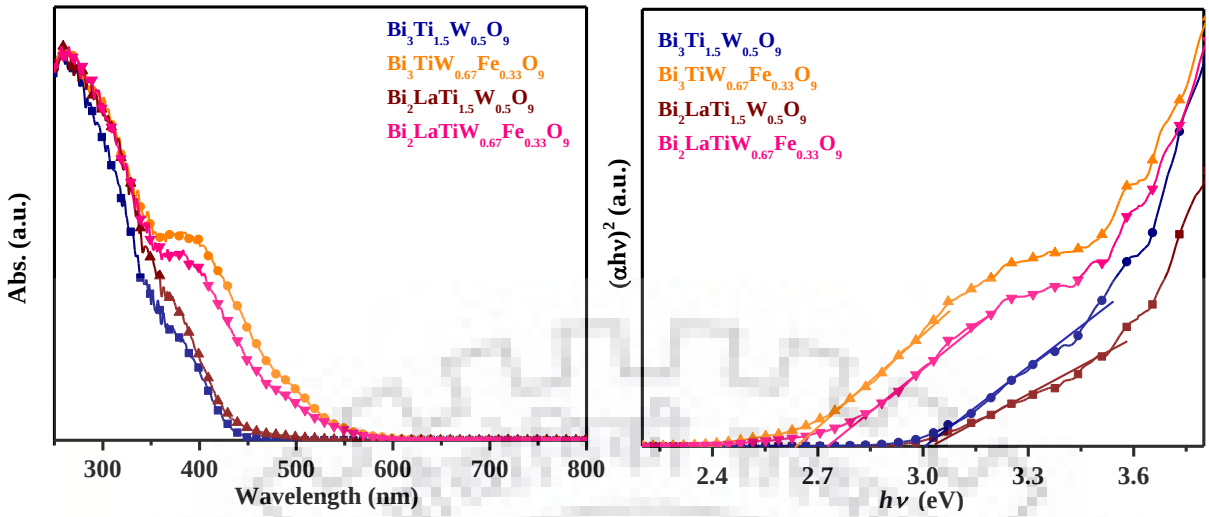

Figure 4.8 (a) UV-vis diffuse reflectance spectra of $Bi_{3-x}La_xTi_{1.5}W_{0.5}O_9$ (x = 0, 1) and $Bi_{3-x}La_xTiW_{0.67}Fe_{0.33}O_9$ (x = 0, 1).

4.3.7 PL Analysis

The photocatalytic activity of the semiconductor catalysts is directly related to the life time and recombination rate of photogenerated e^-–h^+ pairs. Since, the intensity of PL spectra is related to recombination rate of photogenerated charge carrier governed by the relative emission. Therefore, lower PL intensity reduced recombination and longer lifetime of the photogenerated e^-–h^+ pair provided the non-radiative emission are assumed to be very similar in the homologous series of compounds. The concentrations of the reactive species are affected by the enhanced or reduced e^-–h^+ recombination which indirectly affects the photocatalytic activity. The PL data of $Bi_{3-x}La_xTi_{1.5}W_{0.5}O_9$ (x = 0, 1) and $Bi_{3-x}La_xTiW_{0.67}Fe_{0.33}O_9$ (x = 0, 1) are shown in Figure 4.9. The broad emission range from 410 to 575 nm is found for the compounds with a peak around 470 nm. The larger concentration and longer lifetime of electron hole pairs can be corroborated with the lower PL intensity for $Bi_3TiW_{0.67}Fe_{0.33}O_9$. Therefore, PL results are in focus of higher photocatalytic degradation efficiency of $Bi_3TiW_{0.67}Fe_{0.33}O_9$ as compared to the parent compound $Bi_3Ti_{1.5}W_{0.5}O_9$. The PL results are indicated that, both the Fe-containing compound will show high photocatalytic activity as compare to the non-Fe compounds.

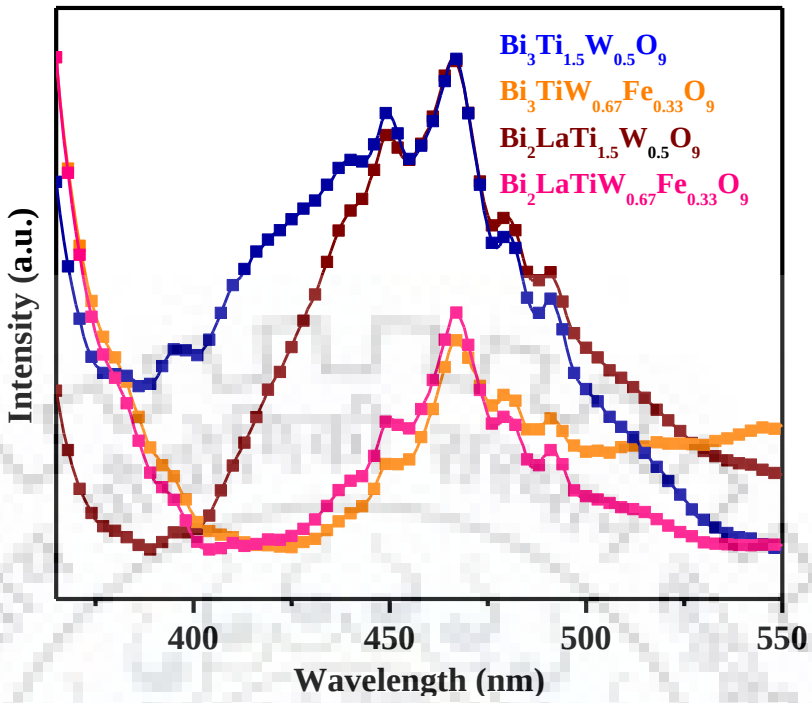

Figure 4.9 PL spectra of $Bi_{3-x}La_xTi_{1.5}W_{0.5}O_9$ (x = 0, 1) and $Bi_{3-x}La_xTiW_{0.67}Fe_{0.33}O_9$ (x = 0, 1)

4.3.8 Sun-Light-Driven Photocatalytic Activity

The photocatalytic activity of the compounds, $Bi_{3-x}La_xTi_{1.5}W_{0.5}O_9$ (x = 0, 1) and $Bi_{3-x}La_xTiW_{0.67}Fe_{0.33}O_9$ (x = 0, 1) are determined by the degradation of RhB and tests are conducted at various pH values (2, 7 and 11) under solar light (Figure 4.10). $Bi_{3-x}La_xTiW_{0.67}Fe_{0.33}O_9$ (x = 0, 1) show complete degradation of RhB within 90-160 minute at pH 2, while $Bi_{3-x}La_xTi_{1.5}W_{0.5}O_9$ (x = 0, 1) exhibit negligible photocatalytic degradation (Figure 4.11). However, there is no significant degradation of the dye at higher pH values of 7 and 11 and no photocatalytic activity. The photostability of the dye was tested by performing degradation test in absence of the catalysts at similar conditions.

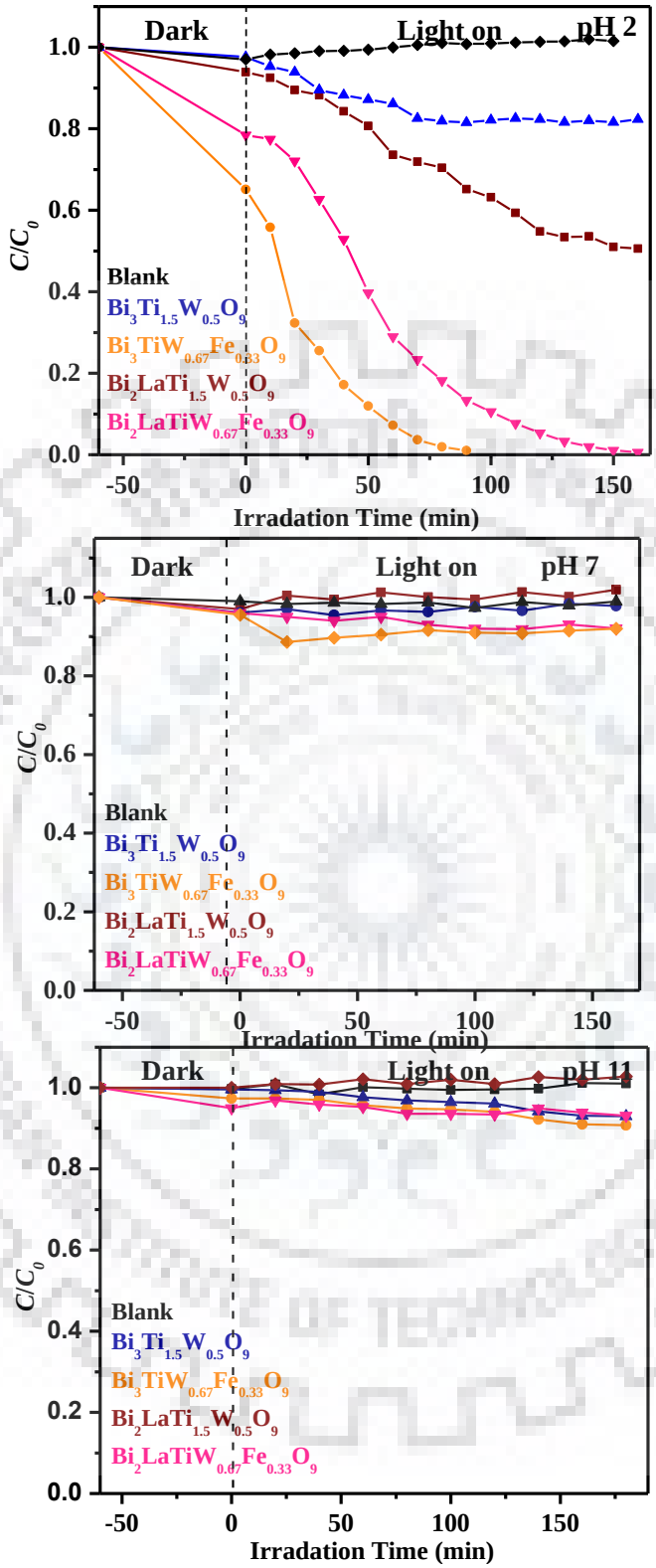

Figure 4.10 Photocatalytic degradation of RhB at different pH by $Bi_{3-x}La_xTi_{1.5}W_{0.5}O_9$ (x = 0, 1), $Bi_{3-x}La_xTiW_{0.67}Fe_{0.33}O_9$ (x = 0, 1).

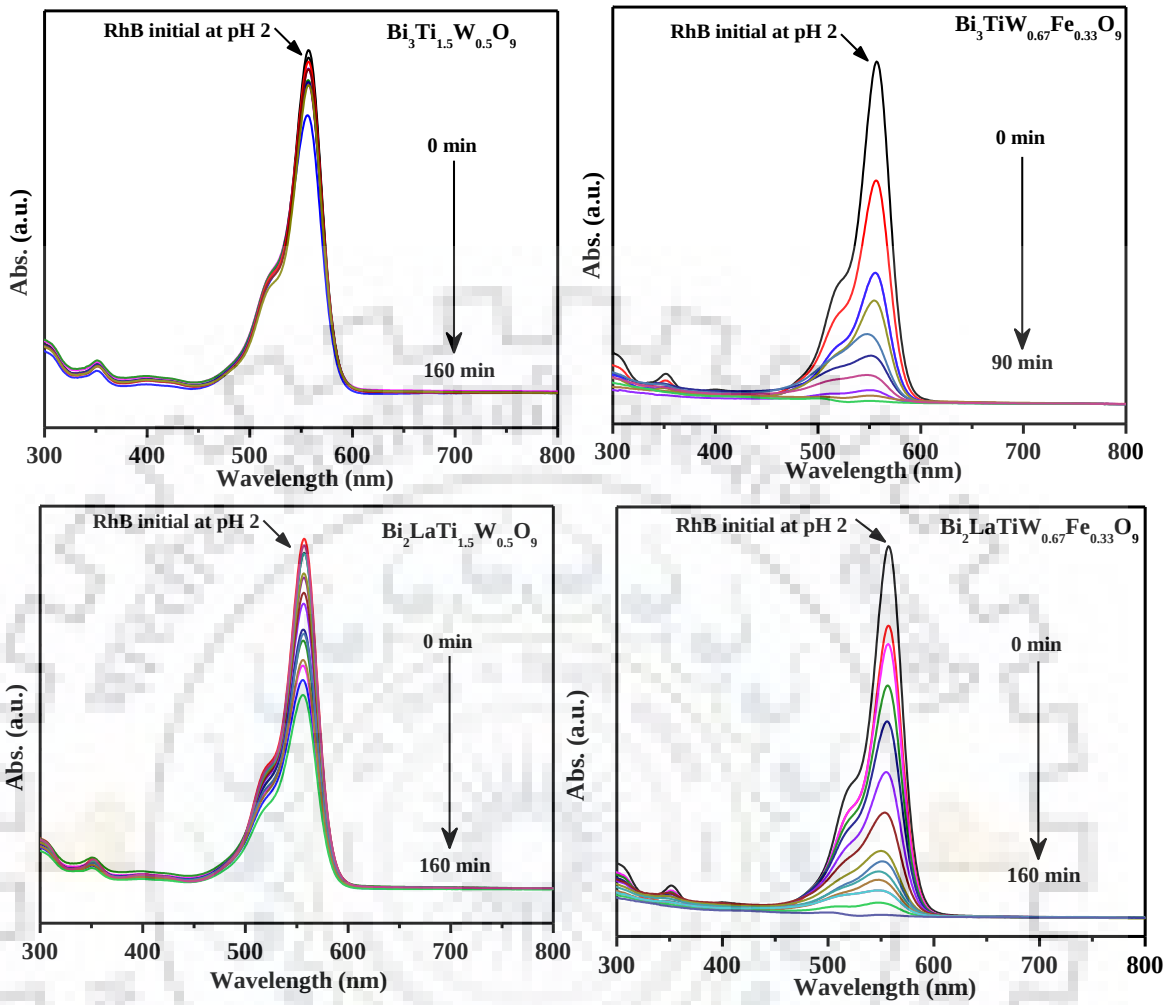

Figure 4.11 UV-vis absorption spectra of the aqueous RhB solutions during photocatalysis $Bi_{3-x}La_xTi_{1.5}W_{0.5}O_9$ (x = 0, 1) and $Bi_{3-x}La_xTiW_{0.67}Fe_{0.33}O_9$ (x = 0, 1).

The kinetic data of RhB degradation under sunlight irradiation over $Bi_{3-x}La_xTi_{1.5}W_{0.5}O_9$ (x = 0, 1) and $Bi_{3-x}La_xTiW_{0.67}Fe_{0.33}O_9$ (x = 0, 1) catalysts were fitted with Langmuir-Hinshelwood rate expression followed the pseudo first order kinetics.[34]

$$\ln(C_0/C) = kt \qquad (4.3)$$

where, C_0 and C is the initial and final concentration of concentration at time t and k is the pseudo-first-order rate constant. It can be seen from the linear plot of $\ln(C_0/C)$ vs. irradiation time (t) for $Bi_{3-x}La_xTi_{1.5}W_{0.5}O_9$ (x = 0, 1) and $Bi_{3-x}La_xTiW_{0.67}Fe_{0.33}O_9$ (x = 0, 1), that photocatalytic RhB degradation follows a first-order kinetics. The slope of the $\ln(C_0/C)$ versus

t plot was used to calculate the degradation rate constants (*k*). The compound $Bi_3TiW_{0.67}Fe_{0.33}O_9$, revealed higher degradation rate constant, as compare to other on shown in Figure 4.12.

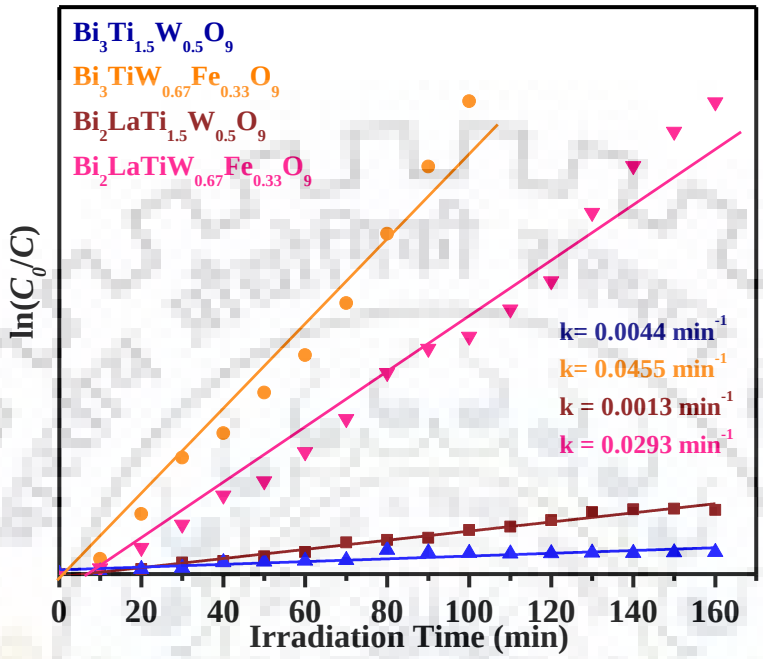

Figure 4.12 The plot of ln(C_0/C) as a function of time over $Bi_{3-x}La_xTi_{1.5}W_{0.5}O_9$ (x = 0, 1) and $Bi_{3-x}La_xTiW_{0.67}Fe_{0.33}O_9$ (x = 0, 1).

4.3.9 Catalyst Stability and Photocatalytic Cycle Studies

The stability and reusability of the photocatalysts were verified by repeating the RhB degradation process for four cycles and details of the process are given in the Experimental Section. The data of dye degradation of $Bi_3TiW_{0.67}Fe_{0.33}O_9$, over four catalytic cycles are presented in the Figure 4.13 (a) .The results shows that about ~ 99 % of RhB are degraded within 90 min of every cycle under sunlight-irradiation. The complete decolorization of the dye solution indicated no observable loss of activity of the catalyst as shown in Figure 4.13(a).

Figure 4.13(b) show the P-XRD patterns of $Bi_3TiW_{0.67}Fe_{0.33}O_9$, which was retrieved after fourth cycle of photocatalysis run. From the P-XRD data, it was clear that the catalyst did not decompose or degrade during dye degradation. In addition, the excellent stability of the catalysts is demonstrated under complete retention of crystallinity as observed in the P-XRD analysis.

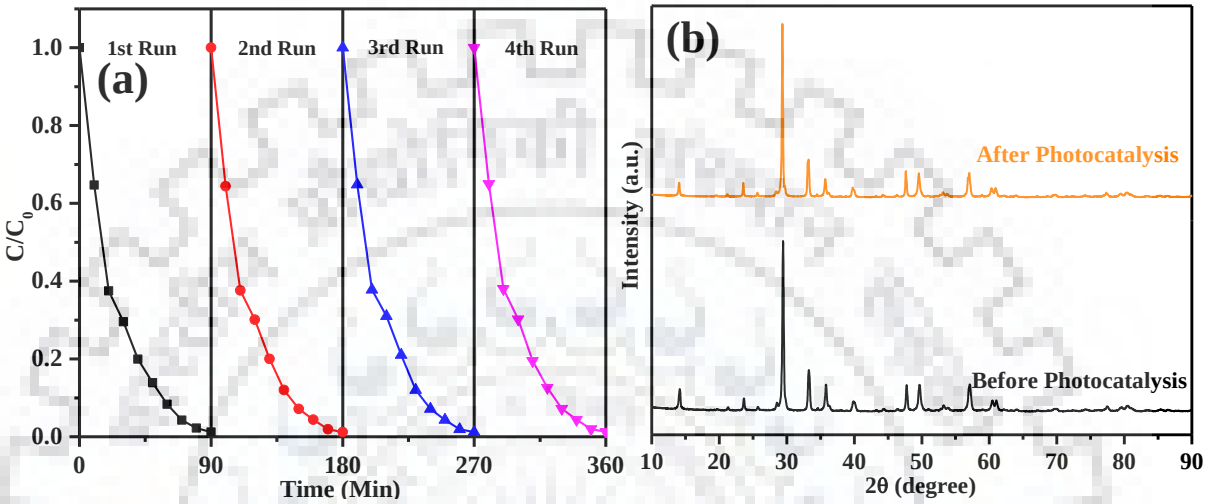

Figure 4.13 (a) Time profiles of RhB degradation for four successive cycles with $Bi_3TiW_{0.67}Fe_{0.33}O_9$ and (b) P-XRD of $Bi_3TiW_{0.67}Fe_{0.33}O_9$ before and after photocatalysis.

4.3.10 Detection of Reactive Species

To understand the photocatalytic degradation mechanism of RhB under sunlight-irradiation over $Bi_3TiW_{0.67}Fe_{0.33}O_9$, the radical and hole trapping experiments called scavenger tests are performed with different scavengers. In the photocatalytic dye degradation process, hydroxyl radicals ($^{\bullet}OH$), superoxide radical anions ($O^{2\bullet-}$) and holes (h^+) are the mainly reactive species that take part in the reaction.[34] When ammonium oxalate (AO) was used as the hole scavenger, the photocatalytic degradation of RhB is drastically suppressed as shown in Figure 4.14. Whereas, the RhB degradation is retarded to a moderate extent, when benzoquinone (BQ) and tertiary butyl alcohol ($^{\bullet}OH$ scavenger) are used during degradation process and the results are shown in Figure 4.14. Therefore, it can be concluded that h^+ play a significant role in the photocatalytic degradation of RhB over $Bi_3TiW_{0.67}Fe_{0.33}O_9$ under natural sunlight, while $^{\bullet}OH$ and $O^{2\bullet-}$ play minor roles.

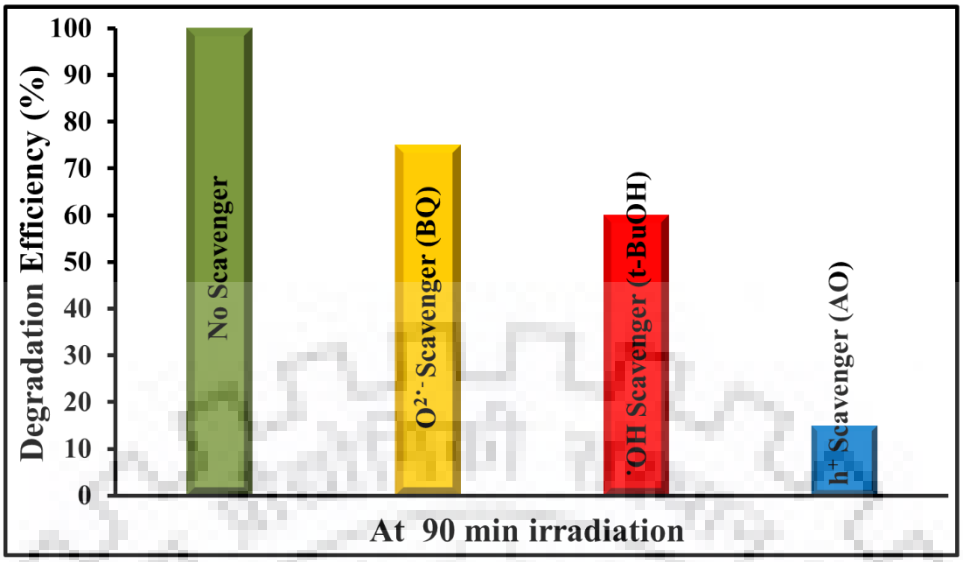

Figure 4.14 Scavengers test on the degradation of RhB in presence of $Bi_3TiW_{0.67}Fe_{0.33}O_9$ under sunlight-irradiation.

4.3.11 Mechanistic Insights for Enhanced Photocatalytic Activity

It is well known that for semiconductor photocatalysis with dyes adsorption of dye on the surface of the photocatalyst take place as a primary process, when on photoexcitation e^--h^+ are generated on oxidative breakdown of the dye molecule occur on action of the generated reactive species. The high activity of the catalyst in degradation process is further investigated with the help of energy level alignments of the photocatalyst band edges with respect to the potential of $^{\bullet}OH/H_2O$, $O_2/O_2^{\bullet-}$ and HOMO-LUMO levels of the RhB. To calculate the minima of the conduction band (E_{CB}) and maxima of valence band (E_{VB}) of the semiconductor photocatalysts, the following expressions were used.[35]

$$E_{CB} = \chi(A_aB_bC_c) - \tfrac{1}{2}\, E_g + E_0 \qquad (4.4)$$

$$E_{VB} = E_{CB} + E_g \qquad (4.5)$$

where, band gap of semiconductor is denoted by E_g, potential of conduction band by E_{CB}, potential of valence band by E_{VB}, the scale factor by E_0 (taken as – 4.5 eV) with respect to the normal hydrogen electrode (*NHE*) scale, and the absolute electronegativity (*AE*) of the semiconductor, $A_aB_bC_c$ is denoted by $\chi(A_aB_bC_c)$. The *AE* of a compound semiconductor is determined by the geometric mean of the *AE* of the constituent atoms.

For the calculation, the values of AE are taken as 4.69, 3.45, 4.40, 4.06 and 7.54 for Bi, Ti, W, Fe and O, respectively.[36] The potential of $^{\bullet}OH/H_2O$ (+ 2.68 eV *vs*. *NHE*), $O_2/O_2^{\bullet-}$ (+ 0.13 eV *vs*. *NHE*) and HOMO-LUMO levels of RhB (E_{HOMO} = 0.95 eV and E_{LUMO} = – 1.42 eV) were taken from the literature.[37,38] The energy level diagram of $Bi_3TiW_{0.67}Fe_{0.33}O_9$ with respect to the potential of $^{\bullet}OH/H_2O$, $O_2/O_2^{\bullet-}$ and HOMO-LUMO levels of RhB are shown in Figure 4.15.

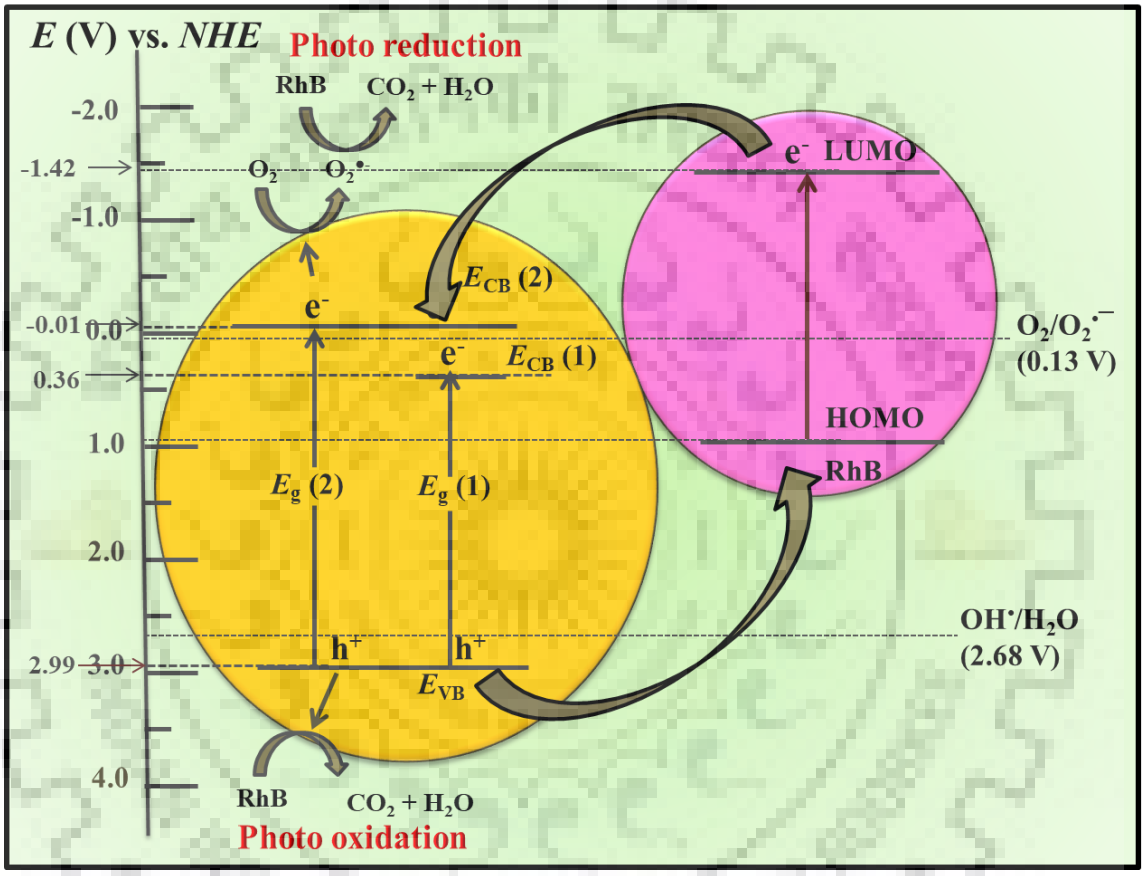

Figure 4.15 Schematic energy level diagram of $Bi_3TiW_{0.67}Fe_{0.33}O_9$ with respect to the $^{\bullet}OH/H_2O$, $O_2/O_2^{\bullet-}$ level and HOMO-LUMO levels of RhB.

In the energy level diagram, the position of valance band is more positive (E_{VB} = + 2.99 V vs. NHE) than the potential of $^{\bullet}OH/H_2O$ indicating that the semiconductor can oxidize the H_2O and generate of $^{\bullet}OH$ ($E_{\bullet OH/H2O}$= + 2.68 V *vs. NHE*). Moreover, the HOMO level of RhB is situated above the E_{VB} of the semiconductor that helps in the transfer of h^+ from the semiconductor to the adsorbed RhB molecules. However, the photogenerated electron in the $E_{CB}(1)$ is not in a suitable position for the for photoreduction process, forming of the $O_2^{\bullet-}$

from adsorbed dissolved O_2 (because the position of the $E_{CB}(1)$ (+ 0.36 V vs. NHE) is more positive than the potential required for generation of $O_2^{\bullet-}$ ($E_{O2/O2\bullet-}$= + 0.13 V *vs*. *NHE*)). Moreover the $E_{CB}(2)$ has less positive potential (– 0.01 eV vs. NHE) than the potential of $E_{O2/O2\bullet-}$ which can generate the $O_2^{\bullet-}$ by the photoreduction of O_2. The scavenger test of RhB degradation is supportive of above explanation as expected from the energy level positioning, the reactive species h^+ play a significant role in the degradation of RhB under sunlight irradiation.

4.3.12 ζ- Potential and Role of Adsorption

The dye adsorption and zeta potential measurement are carried out to understand the effect of surface charge on dye adsorption and its consequent effect on photocatalysis. It is believed that, the adsorption of dye at the surface of the photocatalyst semiconductor plays a significant role in h^+-mediated dye degradation. The adsorption experiment are performed at different pH in the dark. The adsorption data indicate that the maximum adsorption of dye on the surface of the catalyst take place in the acidic medium for $Bi_3TiW_{0.67}Fe_{0.33}O_9$, and $Bi_2LaTiW0_{.67}Fe_{0.33}O_9$, however the compound $Bi_3Ti_{1.5}W_{0.5}O_9$ and $Bi_2LaTi_{1.5}W_{0.5}O_9$ show negligible adsorption (Figure 4.16 b). In pH 7 and pH 11, the compounds exhibit negligible adsorption. This is directly, reflected in the enhanced activity of the compounds in the acidic medium (pH 2). According to the adsorption data, $Bi_3TiW_{0.67}Fe_{0.33}O_9$ is expected to show the highest rate of RhB degradation among all the double layer titanates, respectively.

The surface charge of the catalysts are determined by measuring the ζ- potential. It play an important role in the adsorption of the dye at the surface of the catalyst. Variation of ζ- potential for $Bi_{3-x}La_xTi_{1.5}W_{0.5}O_9$ (x = 0, 1) and $Bi_{3-x}La_xTiW_{0.67}Fe_{0.33}O_9$ (x = 0, 1) as a function of pH are shown in Figure 4.16 (a). The compounds show variation from more positive ζ- potentials to more negative potential from acidic to alkaline pH. The extent of adsorption are explained on the basis of electrostatic interaction between the dye molecule and surface charge of the catalyst. Their modes of their adsorption are explained in the previous chapters. According to the adsorption data, the activity of the compounds follow the decreasing trend, $Bi_3TiW_{0.67}Fe_{0.33}O_9$ > $Bi_2LaTiW_{0.67}Fe_{0.33}O_9$ > $Bi_2LaTi_{1.5}W_{0.5}O_9$ > $Bi_3Ti_{1.5}W_{0.5}O_9$.

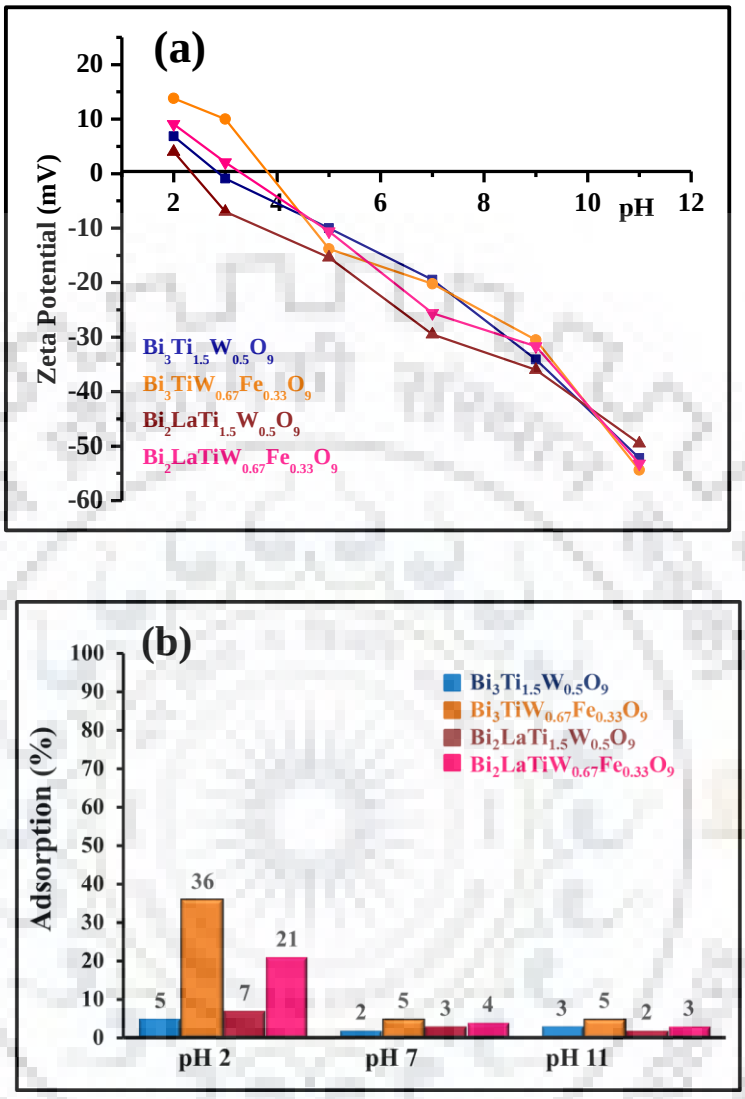

Figure 4.16 (a) ζ- potential of $Bi_{3-x}La_xTi_{1.5}W_{0.5}O_9$ (x = 0, 1) and $Bi_{3-x}La_xTiW_{0.67}Fe_{0.33}O_9$ (x = 0, 1) at different pH. (b) Adsorption of RhB over the catalysts.

In summary, the double-layered titanate and their La-substituted analogs, $Bi_{3-x}La_xTi_{1.5}W_{0.5}O_9$ (x = 0, 1) and $Bi_{3-x}La_xTiW_{0.67}Fe_{0.33}O_9$ (x = 0, 1) are synthesized by conventional solid state reaction and the photocatalytic activity are demonstrated towards RhB degradation at pH 2. The Fe-substituted compound, $Bi_{3-x}La_xTiW_{0.67}Fe_{0.33}O_9$ (x = 0, 1) show reduced the band gap (E_g ~ 2.63 and 2.72) as compared to the parent compound $Bi_3Ti_{1.5}W_{0.5}O_9$ (E_g ~ 3.00). With the help of PL spectra, it is apprehended that $Bi_{3-x}La_xTiW_{0.67}Fe_{0.33}O_9$ (x = 0, 1) exhibit enhanced charge separation and slow down the recombination of photoinduced

electron holes. The photocatalytic activity of the catalyst, $Bi_{3-x}La_xTiW_{0.67}Fe_{0.33}O_9$ (x = 0, 1) show complete degradation of RhB in the acidic medium (pH 2), while $Bi_{3-x}La_xTi_{1.5}W_{0.5}O_9$ (x = 0, 1) show negligible degradation under sunlight irradiation. Moreover, the more positive ζ-potential helps in enhanced dye adsorption, therefore a high rate of degradation. The reusability experiments indicates that the catalyst remain stable after four consecutive degradation cycle with no observable loss of the activity of catalysts. Here, scavenger experiments reveal that, h^+ play the dominant role in the degradation process. The paramagnetic behavior of the compounds can be useful in the post catalytic separation of the catalysts from the reaction medium.

REFERENCES

1. Fox, M. A.; Dulay, M. T.; Heterogeneous Photocatalysis. *Chem. Rev.* **1993**, *93*, 341–357.

2. Hoffmann, M. R.; Martin, S.T.; Choi, W.; Bahnemann, D.W. Environmental Applications of Semiconductor Photocatalysis. *Chem. Rev.* **1995**, *95*, 69–96.

3. Kudo, A.; Hijii, S. H_2 or O_2 Evolution from Aqueous Solution on Layered Oxide Photocatalysts Consisting of Bi^{3+} with $6s^2$ Configuration and d^0 Transition Metal Ions. *Chem. Lett.* **1999**, *28*, 1103–1104

4. Kim, H. G.; Hwang, D. W.; Lee, J. S. An Undoped, Single-Phase Oxide Photocatalyst Working under Visible Light. *J. Am. Chem. Soc.* **2004**, *126*, 8912–8913.

5. Wu. W.; Liu, G.; Liang, S.; Chen, Y.; Shen, L.; Zheng, H.; Yuan, R.; Hou, Y.; Wu, Ling. Efficient Visible-Light-Induced Photocatalytic Reduction of 4-Nitroaniline over Nanocrystallines $PbBi_2Nb_2O_9$. *J. Catal.* **2012**, *290* 13–17.

6. Wu, W.; wen, L.; Shen, L.; Liang, R.; Yuan, R.; Wu. L. A New Insight into the Photocatalytic Reduction of 4-Nitroaniline to p-Phenylenediamine in the Presence of Alcohols. *Appl. Catalysis B: Environ.* **2013**, *130*, 163–167.

7. Fu, H.; Pan, C.; Yao, W.; Zhu, Y. Visible-Light-Induced Degradation of Rhodamine B by Nanosized Bi_2WO_6. *J. Phys. Chem. B*, **2005**, *109*, 22432–22439.

8. Yin, H.; Zhou, A.; Chang, N.; Xu, X. Characterization and Photocatalytic Activity of Bi_3TiNbO_9 Nanocrystallines Synthesized by Sol–Gel Process. *Mater. Res. Bull.* **2009**, *44*, 377–380.

9. Ma, H.; Shen, J.; Shi, M.; Lu, X.; Li, Z.; Long, Y.; Li, N.; Ye, M. Significant Enhanced Performance for Rhodamine B, Phenol and Cr(VI) Removal by Bi_2WO_6 Nanocomposites via Reduced Graphene Oxide Modification. *Appl. Catal. B: Environ.* **2012**, *121*, 198–205.

10. Xu, N.; Takei, T.; Miura, A.; Kumada, N. Preparation and Phase Transformation of Ag or Bi Ion-exchanged Layered Niobate Perovskite and their Photocatalytic Properties. *J. Cer. Soc. Jpn.* **2015**, *123*, 690–694.

11. Liu, X.; Xu, L.; Huang, Y.; Qin, C.; Qin, L.; Seo, H. J. Improved Photochemical Properties of Aurivillius $Bi_5Ti_3FeO_{15}$ with Partial Substitution of Ti^{4+} with Fe^{3+}. *Ceram. Int.* **2017**, *43*, 12372–12380.

12. Yin, X.; Li, X.; Gu, W.; Zou, W.; Liu, H.; Zhu, L.; Fu, Z.; Lu, Y. Morphology Effect on Photocatalytic Activity in $Bi_3Fe_{0.5}Nb_{1.5}O_9$. *Nanotech.* **2018**, *29*, 265706 (1–10).

13. Oshikiri, M.; Boero, M.; Ye, J.; Zou, Z.; Kido, G. Electronic Structures of Promising Photocatalysts $InMO_4$ (M = V, Nb, Ta) and $BiVO_4$ for Water Decomposition in the Visible Wavelength Region. *J. Chem. Phys.* **2002**, *117*, 7313–7318.

14. Naresh, G.; Mandal, T. K. Excellent Sun-Light-Driven Photocatalytic Activity by Aurivillius Layered Perovskites, $Bi_{5-x}La_xTi_3FeO_{15}$ (x = 1, 2). *ACS Appl. Mater. Interfaces* **2014**, *6*, 21000–21010.

15. Naresh, G.; Mandal, T. K. Efficient COD Removal Coinciding with Dye Decoloration by Five- Layer Aurivillius Perovskites under Sunlight-Irradiation. *ACS Sustainable Chem. Eng.* **2015**, *3*, 2900–2908.

16. Zhang, N.; Ciriminna, R.; Pagliaro, M.; Xu, Y. J. Nanochemistry-Derived Bi_2WO_6 Nanostructures: Towards Production of Sustainable Chemicals and Fuels Induced by Visible Light. *Chem. Soc. Rev.* **2014**, *43*, 5276–5287.

17. Huang, H.; Cao, R.; Yu, S.; Xu, K.; Hao, W.; Wang, Y.; Dong, F.; Zhang, T.; Zhang, Y. Single-Unit-Cell Layer Established Bi_2WO_6 3D Hierarchical Architectures: Efficient Adsorption, Photocatalysis and Dye-Sensitized Photoelectrochemical Performance. *Appl. Catal. B Environ.* **2017**, *219*, 526–537.

18. Shanbogh, P. P.; Swain, D.; Narayana, C.; Rao, A.; Sundaram. N. G. Distinct Phase Formation of $BiREWO_6$ (RE = La−Yb) Nanoparticles by a One Step Hydrothermal Synthesis and Their Photocatalytic Applications. *Cryst. Growth Des.* **2018**, *18*, 1935−1939.

19. Li, H.; Li, W.; Wang, F.; Liu, X.; Ren, C. Fabrication of Two Lanthanides Co-doped Bi_2MoO_6 Photocatalyst: Selection, Design and Mechanism of Ln^1/Ln^2 Redox Couple for Enhancing Photocatalytic Activity. *Appl. Catal. B Environ.* **2017**, *217*, 378–387.

20. Song, J. M.; Hu, H. Q.; Wang, X. Z.; Zhao, S. J.; Shi, Y. L.; Ren, M. S. Hydrothermal Synthesis, Characterization and Photocatalytic Activities of $Bi_2Mo_xW_{1-x}O_6$ Solid Solution. *J. Inorg. Mater.* **2013**, *28*, 1275–1280.

21. Jiang, L.; Ni, S.; Liu, G.; Xu. X. Photocatalytic Hydrogen Production over Aurivillius Compound Bi_3TiNbO_9 and its Modifications by Cr/Nb Co-doping. *Applied Catalysis B: Environ.* **2017**, *217*, 342–352.

22. Zhang, H.; Chen, G.; Li. X. Synthesis and Visible Light Photocatalysis Water Splitting Property of Chromium-Doped $Bi_4Ti_3O_{12}$. *Solid State Ionics* **2009**, *180*, 1599–1603.

23. Tokunaga, S.; Kato, H.; Kudo, A. Selective Preparation of Monoclinic and Tetragonal $BiVO_4$ with Scheelite Structure and Their Photocatalytic Properties. *Chem. Mater.* **2001**, *13*, 4624–4628.

24. Kim, H. G.; Becker, O. S.; Jang, J. S.; Ji, S. M.; Borse, P. H.; Lee, J. S. A generic Method of Visible Light Sensitization for Perovskite-related Layered Oxides: Substitution Effect of Lead. *J. Solid State Chem.* **2006**, *179*, 1214–1218.

25. Hong, S. J.; Borse, P. H.; Ji, S.M.; Jang, J. S.; Lee, J. S.; Structure of $PbBi_2Nb_2O_9$ and Its Cr- Doped Layered Perovskite System and Their Photocatalytic Activities. *J. Korean. Phys. Soc.* **2007**, *51*, S27–S31.

26. Kim, H. G.; Borse, P. H.; Jang, J. S.; Jeong, E. D.; Lee, J. S. Enhanced Photochemical Properties of Electron Rich W-Doped $PbBi_2Nb_2O_9$ Layered Perovskite Materials Under Visible Light Irradiation. *Mater. Lett.* **2008**, *62*, 1427–1430.

27. Luo, S.; Noguchi, Y.; Miyayama, M.; Kudo. T. Rietveld Analysis and Dielectric Properties of Bi_2WO_6-$Bi_4Ti_3O_{12}$ Ferroelectric System. *Mater. Res. Bull.* **2001**, *36*, 531–540.

28. Hyatt, N. C.; Reaney, I. M.; Knight. K. S. Ferroelectric-Paraelectric Phase Transition in the n = 2 Aurivillius Phase $Bi_3Ti_{1.5}W_{0.5}O_9$ A Neutron Powder Diffraction Study. *Phys. Rev. B.* **2005**, *71*, 024119 (1–7).

29. Zhang, Y.; Li, J.; Chai, X.; Wang, X.; Li, Y.; Yao. X. Enhanced Electrical Properties, Color-Tunable Up-conversion Luminescence, and Temperature Sensing Behaviour in Er-Doped $Bi_3Ti_{1.5}W_{0.5}O_9$ Multifunctional Ferroelectric Ceramics. *J. Appl. Phys.* **2017**, *121*, 124102(1–7).

30. Zhang, Y.; Chai, X.; Li, J.; Wang, X.; Li, Y.; Yao. X. Enhanced Up-conversion Luminescence and Excellent Temperature Sensing Properties in Yb^{3+} Sensitized Er^{3+}-Doped $Bi_3Ti_{1.5}W_{0.5}O_9$ Multifunctional Ferroelectric Ceramics. *J. Alloys and Comp.* **2018**, *735*, 473–479.

31. Chen, W.; Gao, W.; Xia, Y.; Liang, S.; Bi, J.; Zhou, L.; Wu, L.; Liu, M. Low-Temperature Synthesis and Visible Light-Driven Photocatalytic Activity of $Bi_6Ti_3WO_{18}$ Nanosheet Photocatalyst. *J. Alloys and Comp.* **2017**, *718*, 471–477.

32. Mi, L.; Feng, Y.; Cao, L.; Xue, M.; Qin, C.; Huang, Y.; Qin, L.; Seo, H. J. Photocatalytic Ability of $Bi_6Ti_3WO_{18}$ Nanoparticles with a Mix-Layered Aurivillius Structure. *J. Nanopart Res.* **2018**, *20*, 2–14.

33. Zuo, X.; Zhu, S.; Bai, J.; He, E.; Hui, Z.; Zhang, P.; Song, D.; Song, W.; Yang, J.; Zhu, X.; Dai, J. Enhanced Multiferroicity and Narrow Band Gap in B-site Co-Doped Aurivillius $Bi_5FeTi_3O_{15}$. *Ceram. Int.* **2019**, *45*, 137–143.

34. Fu, H.; Pan, C.; Yao, W.; Zhu, Y. Visible-Light-Induced Degradation of Rhodamine B by Nanosized Bi_2WO_6. *J. Phys. Chem. B.* **2005**, *109*, 22432–22439.

35. Lv, J.; Kako, T.; Zou, Z.; Ye, J. Band Structure Design and Photocatalytic Activity of In_2O_3/N−$InNbO_4$ Composite. *Appl. Phys. Lett.* **2009**, *95*, 032107–032109.

36. Pearson, R. G. Absolute Electronegativity and Hardness: Application to Inorganic Chemistry. *Inorg. Chem.* **1988**, *27*, 734–740.

37. Kumar, S.; Surendar, T.; Baruah, A.; Shanker, V. Synthesis of a Novel and Stable g-C_3N_4–Ag_3PO_4 Hybrid Nanocomposite Photocatalyst and Study of the Photocatalytic Activity under Visible Light Irradiation. *J. Mater. Chem. A* **2013**, *1*, 5333–5340.

38. Pan, L.; Zou, J.J.; Liu, X. Y.; Liu, X. J.; Wang, S.; Zhang, X.; Wang, L. Visible−Light−Induced Photodegradation of Rhodamine B over Hierarchical TiO_2: Effects of Storage Period and Water-Mediated Adsorption Switch. *Ind. Eng. Chem. Res.* 2012, 51, 12782-12786.

CHAPTER -5

Transition Metal Incorporated New Sillén-Aurivillius A1X1 Layered Tungstates: Magnetism and Solar Photocatalysis

Transition Metal Incorporated New Sillén-Aurivillius A1X1 Layered Tungstates: Magnetism and Solar Photocatalysis

5.1 INTRODUCTION

Visible-light photocatalysis may be considered as a sustainable process, which may provide solution for many environmental issues such as degradation of harmful pollutants in industrial effluents, water decontamination and hydrogen generation etc.[1-4] In recent years, for environmental remediation purposes various transition metal oxide based photocatalysts have been investigated.[5-8] Although, TiO_2 is a benchmark photocatalyst, it has significant limitations. A large number of new semiconductor photocatalysts have been discovered as promising alternatives.[9-11] In dealing with organic pollutants, mainly dyes, degradation or removal of dye could be attained by adsorption, or complete conversion into non-toxic inorganic fragments such as CO_2 and H_2O, known as mineralization. The process, of photocatalytic degradation, however, involve several steps, such as light absorption by semiconductor photocatalyst, generation of electron-hole pair , separation and recombination of photo excited charge carriers (e^- and h^+) and finally, charge transfer to reactants or O_2/H_2O to form reactive oxygen species.[12] Recently, Bi-containing layered oxides have been reported as efficient semiconductor photocatalysts working under visible-light.[13-15] This is primarily due to the hybridization of Bi-6*s* with O-2*p* in these compounds that pushes up the valance band edge and thus extends the absorption edge to the visible region and exhibit high photoactivity under visible light.[16,17]

A new class of bismuth based layered oxyhalides, BiOX (X = Cl, Br) with a Sillén X2 structure have recently been investigated for photocatalytic applications.[18-21] Among the other Bi-based layered perovskites are the Aurivillius phase that are also found to possess high photocatalytic activity.[22-25] Due to the similarity in structure of the Aurivillius and Sillén phases (the presence of common Bi_2O_2 layer), the intergrowth of Aurivillius and Sillén structures can be conceived. The general formula of the Sillén-Aurivillius (S-A) phase can be denoted as $[Bi_2O_2][A_{n-1}B_nO_{3n+1}][Bi_2O_2][X]_m$ (n = 1, m = 1, A = Pb^{2+}, Sr^{2+}; B = Nb, Ta etc.) where '*n'* denotes the thickness of the perovskite block and '*m'* denotes the number of halide units in between the layers. The structure of the S-A phase is commonly denoted by AnXm.

Bi_4NbO_8Cl (with n =1 and m =1) is a compound of this series, first reported by Aurivillius. But, John Ackerman was the first person to describe the A1X1 structure correctly.[26,27] To date, several compounds within this family have been reported e.g., Bi_4MO_8X (M= Nb^{5+}, Ta^{5+} and X = Cl, Br),[28,29] $Bi_3Pb_2Nb_2O_{11}Cl$ (A2X1)[30] $Bi_4M'_xM_{1-x}O_8X$ (M = W^{6+}, M ′ =Ti^{4+}, Mn^{3+}, Fe^{3+}, Cu; X= Cl, Br),[31-34] and $Bi_5PbTi_3O_{14}Cl$ (A2X1).[35] These compounds had thoroughly been investigated for their structural characterization and their dielectric as multiferroics properties. Currently, these materials have gained a renewed interest due to their enhanced photocatalytic properties achieved by tailoring their composition and band gap.[15,36] Kusainova *et al*. have established the crystal structure of Bi_4TaO_8Cl, which is isostructural with Bi_4NbO_8Cl, and have studied its dielectric properties.[37] Lin *et al*. have reported Bi_4NbO_8Cl, with a visible band gap exhibiting UV-visible light-driven photocatalysis.[38] Recently, Bi_4TaO_8Cl has been evaluated for water splitting.[39] Moreover, R. Abe and co-workers have studied the series of isostructural oxyhalides, Bi_4MO_8X (M = Nb, Ta; X = Cl, Br), to examine the substitution effects of cations and anions on the band structure and resulting photocatalytic activity.[40]

Currently, Mandal and co-workers have reported, La-substituted Sillén-Aurivillius layered oxyhalides, Bi_3LaNbO_8Cl and Bi_3LaNbO_8Br exhibiting excellent photocatalytic performance under sunlight irradiation. The objective of the present work was to synthesize La-substituted Sillén−Aurivillius phases, $LaBi_3W_{0.67}M_{0.33}O_8Cl$ (M = Mn, Fe), through the coupled substitution strategy. The compounds are synthesized successfully by conventional solid-state reactions. The photocatalytic activity of the new Sillén−Aurivillius phases have been investigated by way of degradation of organic dye pollutants (RhB, MO) under sunlight irradiation. The details of the investigation are described in the subsequent sections of this chapter.

5.2 EXPERIMENTAL SECTION

5.2.1 Materials and Synthesis

The Sillén-Aurivillius phases, $LaBi_3W_{0.67}M_{0.33}O_8Cl$ (M = Mn, Fe), were prepared by the conventional solid-state reactions. For this purpose, La_2O_3 (Sigma-Aldrich, 99.99%), (preheated at 950°C), Bi_2O_3 (Sigma-Aldrich, ≥ 98.0%), WO_3, Mn_2O_3 (laboratory prepared by thermal decomposition of $MnC_2O_4.2H_2O$), Fe_2O_3 (prepared by thermal decomposition

$FeC_2O_4.2H_2O$, Sigma-Aldrich, 99%) and BiOCl were used as starting materials. $MnC_2O_4.2H_2O$ was prepared by the co-precipitation of equimolar aqueous solutions of $Mn(NO_3)_2.6H_2O$ (Sigma-Aldrich, ≥ 98.0%), and oxalic acid ($C_2H_2O_4.2H_2O$ Himedia, ≥ 99.5%). Stoichiometric quantities of the starting materials were ground in agate mortar-pastel for 1h, and the resulting mixture was pressed into pellets. The pellets were taken in an alumina boat and heated in a tube furnace at 720ºC for 24 h and 12 h with an intermediate grinding and pelletizing. For comparison, the parent $Bi_4W_{0.67}Mn_{0.33}O_8Cl$ was also prepared by the solid-state reaction.[32]

BiOCl was prepared by a solution precipitation method. For this excess amount of Bi_2O_3 was first dissolved in 3N HCl to form $BiCl_3$-HCl and subsequently, a large volume of Millipore water was added to the $BiCl_3$-HCl solution. The pH of the solution was adjusted to 2-3 with the help of liquid NH_3. The white color collidal solution was stirred for 40 min at room temperature, settled, filtered and washed several times with Millipore water until no traces of Cl^- were present in the filtrate. The white precipitate was dried in air at 40º C for overnight.

5.2.2 Photocatalytic Degradation and Cyclic Test

The photocatalytic activity of the compounds, $LaBi_3W_{0.67}M_{0.33}O_8Cl$ (M = Mn, Fe) were evaluated through the degradation of Rhodamine B (cationic dye) and Methyl orange (anionic dye) under sunlight irradiation. These organic dyes are generally regarded as water pollutants. For photocatalytic activity experiment, 1×10^{-5} M dye (RhB and MO) solutions were used. The experiments were carried out in our institute, IIT Roorkee (29°51′ N; 77°53′ E) during the month of May 2016 having direct normal irradiance (DNI) ~ 143 W/m^2. Photocatalytic degradation of individual RhB, MO and collective degradation of MO and RhB mixture were performed over the catalysts, ($LaBi_3W_{0.67}M_{0.33}O_8Cl$; M = Mn, Fe), in sun-light radiation at pH 2, 7 and 11. To test the degradation performance of the catalysts, 100 mg of the powder sample were dispersed in 100 mL of dye solution. Then, the suspension was kept under magnetic stirring at 320 rpm for 1h in the dark. After that, the suspensions were exposed to the natural sunlight and at regular time intervals 5 ml of this solution were withdrawn, centrifuged at 9000 rpm (to separate the catalysts from the suspension) for 2 minutes and the absorbance of the filtrate was recorded. For the cyclic measurements, the catalyst used in the

first cycle were recovered and washed with deionized water. Then a fresh dye solution was added to the catalyst and degradation experiments were carried out under the same condition as mentioned above. The efficiency of the catalysts for dye degradation was calculated by the following expression:

$$\% \text{ of degradation} = (1 - C/C_0) \times 100 \quad (5.1)$$

where, C_0 is the initial concentration of dye and C is the dye concentration at any time (*t*).

5.2.3 ζ-potential and Dye Adsorption Studies

To characterize the surface charge of the semiconductor, ζ-potential measurements for $LaBi_3W_{0.67}M_{0.33}O_8Cl$ (M = Mn, Fe) were carried out with Malvern Zeta Sizer Nano ZS90 at various pH (2, 5, 7, 9, 11 and 13). For this purpose, 10 mg of catalysts were dispersed in 10 mL of Millipore water of different pH and sonicated before recording the ζ-potential. Adsorption studies were performed to establish adsorption-desorption equilibrium and to ensure maximum amount of dye absorption over the solid catalyst surface at different pH. For this measurement, 100 mg of catalyst was dispersed in 100 mL of 1×10^{-5} M dye solution and stirred in the dark for 6 h. During this, 5 ml aliquots of the solution were withdrawn at regular time intervals, centrifuged for 2 min (to remove the catalyst particles) and absorbance of the centrifugate was recorded. The withdrawn solution was put back in the beaker after the measurement along with the catalysts to maintain the catalyst to dye volume ratio nearly constant.

5.2.4 Scavenger Tests

To understand the role of reactive species in the degradation of dye, the scavenger tests were performed. In this experiment, different scavengers were added to the RhB solution prior to the addition of the catalyst. In a typical experiment, 10 mM scavenger species were added to the dye suspension. Tertiary butyl alcohol (t-BuOH), benzoquinone (BQ) and ammonium oxalate (AO) were used for •OH, $O_2^{\bullet-}$ and h^+ scavenger, respectively.[36,37] For this purpose, 0.96 mL of t-BuOH, 0.18 g of BQ and 0.14 g of solid AO were added to 100 mL dye solution to make a scavenger concentration of 10 mM in each case. A similar experimental procedure was followed for the determination of the reactive species as describe above.

5.3 RESULTS AND DISCUSSION

5.3.1 Powder X-ray Diffraction (P-XRD)

The P-XRD pattern of the synthesized compounds are shown in Figure 5.1. The preliminary analysis of the P-XRD patterns indicated formation of Sillén-Aurivillius intergrowth phases similar to the orthorhombic $Bi_4W_{0.67}Mn_{0.33}O_8Cl$ reported in the literature.[32] Although, all the peak in the pattern could be indexed in the orthorhombic system, indicating formation of phase pure compound, presence of a small amount of δ-Bi_2O_3 impurity phase was apparent. All the peaks in the observed P-XRD pattern (excluding the impurity peak) were indexed in the *Cm2m* space group.

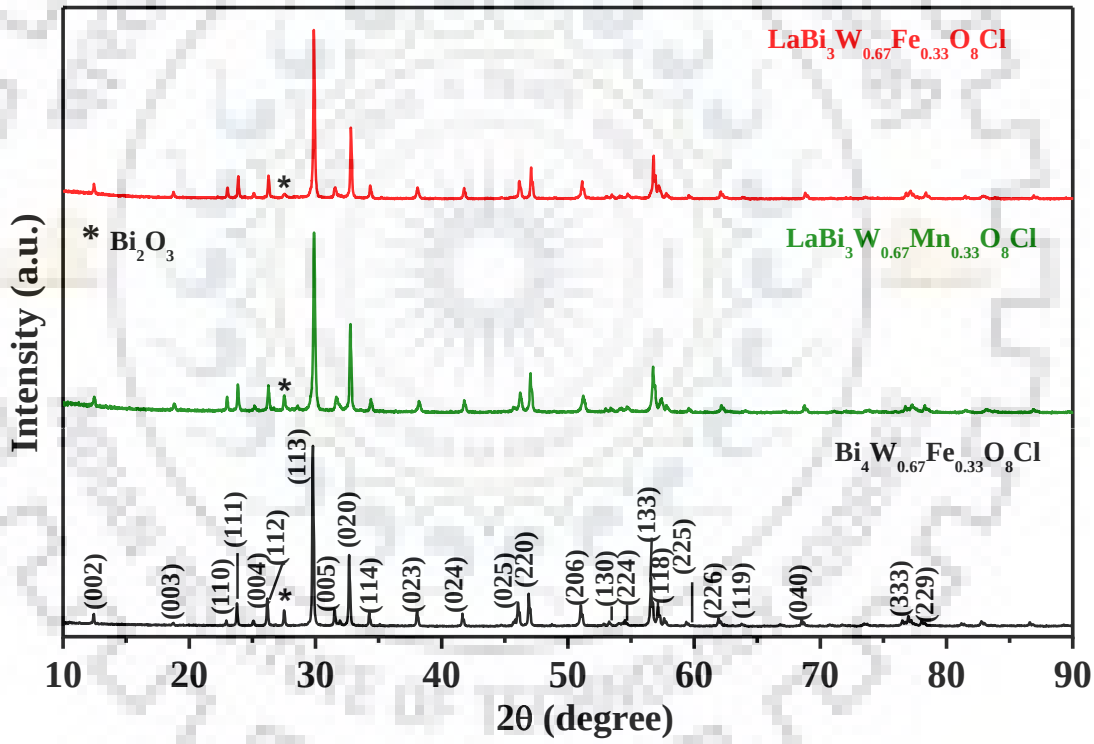

Figure 5. 1 P-XRD patterns of $LaBi_3W_{0.67}M_{0.33}O_8Cl$ (M = Mn, Fe).

The least-squares refined lattice parameters of the synthesized compounds are presented in Table 5.1. A close look at the refined unit cell parameters indicate a slight contraction in the '*a*' and '*c*' parameters in comparison to the parent compound,

$Bi_4W_{0.67}Mn_{0.33}O_8Cl$. The indexed P-XRD data of $Bi_3LaW_{0.67}M_{0.33}O_8Cl$ (M = Mn, Fe) are given in Figures 5.2 and 5.3, respectively.

Table 5.1. Lattice Parameters of $Bi_3LaW_{0.67}M_{0.33}O_8Cl$ (M = Mn, Fe).

Compound	Lattice parameters (Å)		
	a	***b***	***c***
$Bi_4W_{0.67}Mn_{0.33}O_8Cl$	5.467(3)	5.466(2)	14.159(1)
$LaBi_3W_{0.67}Mn_{0.33}O_8Cl$	5.461(1)	5.457(6)	14.133(4)
$LaBi_3W_{0.67}Fe_{0.33}O_8Cl$	5.461(1)	5.466(6)	14.138(1)

The P-XRD simulation studies of the compounds, $LaBi_3W_{0.67}M_{0.33}O_8Cl$ (M = Mn, Fe), based on the model structure indicate La-substitution at the Bi_2O_2 layer. The atomic coordinates of $Bi_4W_{0.67}Mn_{0.33}O_8Cl$ were used as an initial model with *Cm2m* space group. Figure 5.3 shows the crystal structure of $LaBi_3W_{0.67}Fe_{0.33}O_8Cl$. The structure displays the intergrowth nature of the Aurivillius phases by alternating layer sequence of the fluorite-type $[Bi_2O_2]^{2+}$ and $[A_{n-1}B_nO_{3n+1}]^{2-}$ perovskite sheets interleaved by a halide layer. In the structure, two types of bismuths, Bi(1) and Bi(2), are present. Bi(1) is neighboring to the Cl sheet, whereas Bi(2) is closer to the $(W/Fe)O_6$ octahedral layer. The simulation data indicates occupancy of La (~ 25 %) at the Bi(2) site of the $[Bi_2O_2]^{2+}$ layers situated near the perovskite block. The positional parameters, occupancy and thermal factors used in the simulation are given in Table 5.4. Figure 5.2 displays the comparison between the simulated P-XRD pattern and the observed data.

Table 5.2 Indexed P-XRD Data for $LaBi_3W_{0.67}Mn_{0.33}O_8Cl$.

h k l	d_{obs}(Å)	d_{calc} (Å)	I_{obs}
0 0 2	7.067	7.066	7
0 0 3	4.716	4.710	4
1 1 0	3.864	3.860	5
1 1 1	3.728	3.724	10
0 0 4	3.535	3.533	2
1 1 2	3.390	3.387	13
1 1 3	2.986	2.986	100
0 0 5	2.825	2.826	10
0 2 0	2.729	2.728	40
1 1 4	2.605	2.606	6
0 0 6	2.354	2.355	7
0 2 4	2.160	2.159	7
0 2 5	1.962	1.963	13
2 2 0	1.930	1.930	19
2 0 6	1.783	1.783	13
1 3 0	1.726	1.726	2
2 2 4	1.694	1.693	3
1 3 3	1.620	1.620	30
1 1 8	1.606	1.606	2
2 2 5	1.594	1.594	5
1 3 4	1.550	1.550	3
2 2 6	1.492	1.493	7
1 1 9	1.454	1.454	2
0 4 0	1.364	1.364	5
3 3 3	1.241	1.241	3
2 2 9	1.218	1.218	3

a = 5.461(1), b = 5.457(6), c = 14.133(4) Å.

Table 5.3 Indexed P-XRD Data for $LaBi_3W_{0.67}Fe_{0.33}O_8Cl$.

h k l	d_{obs}(Å)	d_{calc} (Å)	I_{obs}
0 0 2	7.102	7.069	7
0 0 3	4.727	4.712	4
1 1 0	3.873	3.872	5
1 1 1	3.738	3.726	10
0 0 4	3.538	3.534	2
1 1 2	3.397	3.390	13
1 1 3	2.992	2.987	100
0 0 5	2.828	2.827	10
0 2 0	2.736	2.733	40
1 1 4	2.605	2.606	6
0 0 6	2.356	2.356	7
0 2 4	2.160	2.159	7
0 2 5	1.965	1.964	13
2 2 0	1.932	1.931	19
2 0 6	1.784	1.784	13
1 3 0	1.715	1.714	2
2 2 4	1.695	1.695	3
1 3 3	1.622	1.621	30
1 1 8	1.606	1.607	2
2 2 5	1.594	1.595	5
1 3 4	1.552	1.551	3
2 2 6	1.493	1.493	7
1 1 9	1.455	1.455	2
0 4 0	1.365	1.365	5
3 3 3	1.241	1.242	3
2 2 9	1.219	1.219	3

a = 5.461(1), b = 5.466(6), c = 14.138(1) Å.

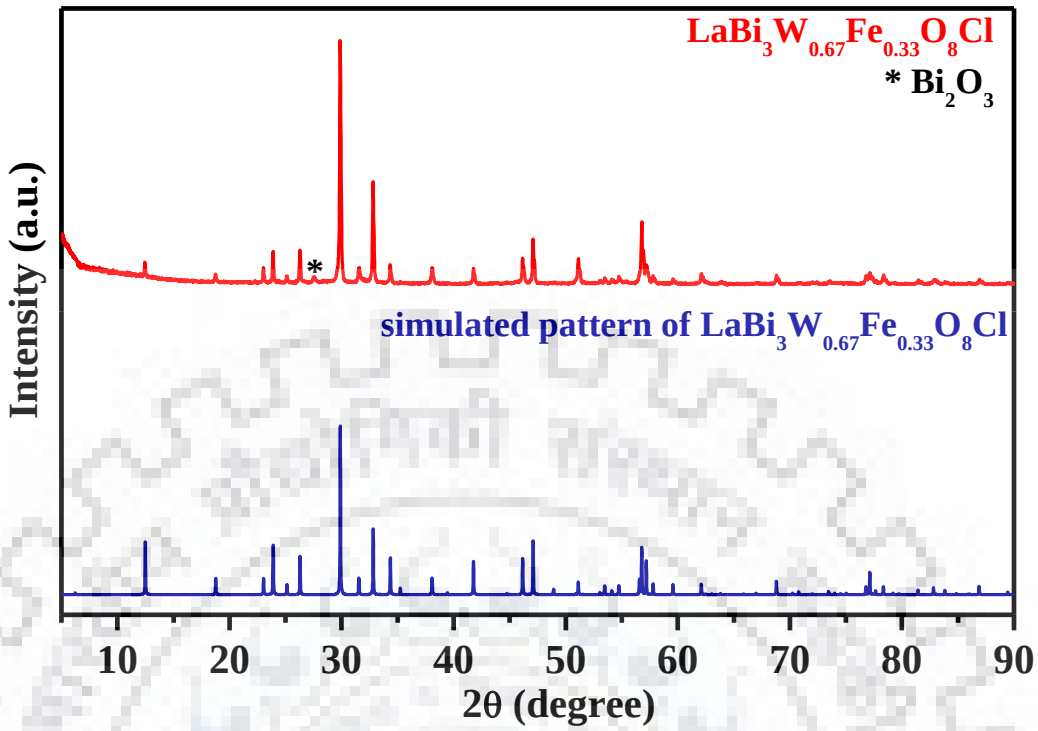

Figure 5.2 Simulated P-XRD pattern of $LaBi_3W_{0.67}Fe_{0.33}O_8Cl$ (bottom). The experimental pattern is shown in the top panel.

Table 5.4 Atomic Position, Site Occupancy and Thermal Parameters used for P-XRD Pattern Simulation of $LaBi_3W_{0.67}Fe_{0.33}O_8Cl$.

Atom	*x*	*y*	*z*	Occ.	B (temp)
Bi1	0	0.004	0.364	0.50	0.33
Bi2	0	0.528	0.181	0.25	1.60
La	0	0.0528	0.181	0.25	1.60
W/Fe	0	0.013	0	0.1666/.0833	0.30
Cl	0	0.521	0.050	0.25	0.80
O1	0	-0.083	0.117	0.5	0.80
O2	0.188	0.289	0	0.5	0.80
O3	0.233	0.266	0.296	1	0.80

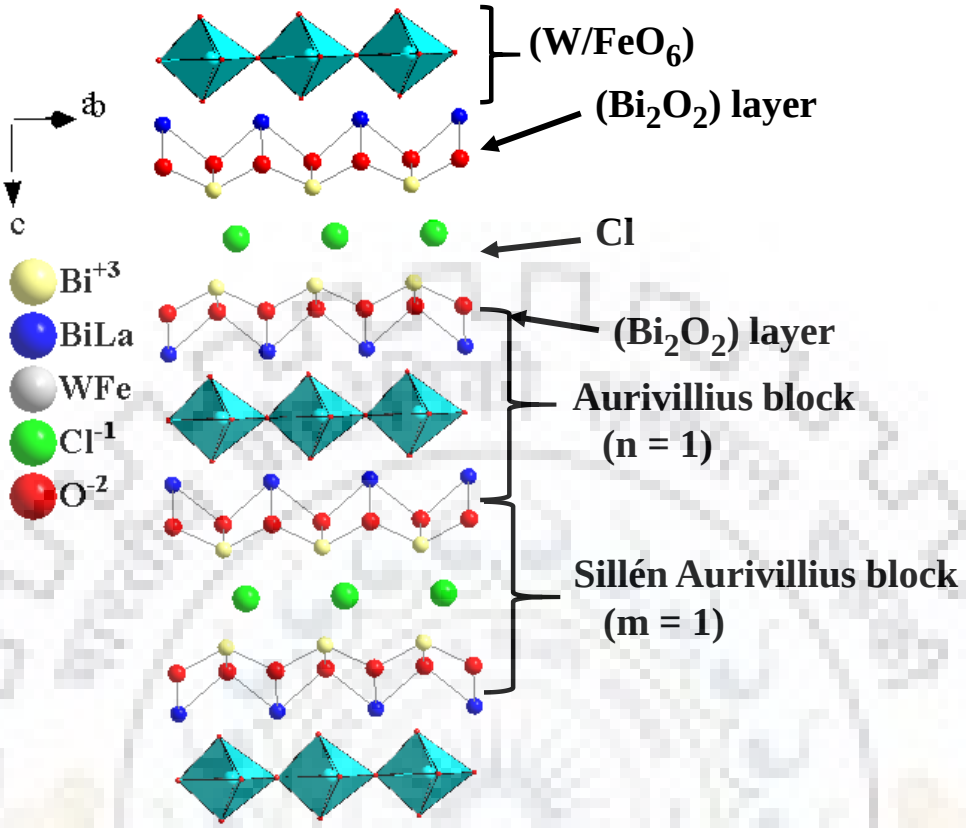

Figure 5.3 Structure of Sillén-Aurivillius perovskite, $LaBi_3W_{0.67}M_{0.33}O_8Cl$.

5.3.2 Field Emission-Scanning Electron Microscopy (FE-SEM)

The morphology and elemental composition of the samples were characterized by FE-SEM and EDS analysis, respectively. The FE-SEM images (Figure 5.4) revealed homogenous plate like morphology with agglomerated crystallites. The plate like crystal habitats are generally expected for the layered compounds. The particle size ranges from few hundred nanometers to few micrometers as seen in the FE-SEM images. According to EDS the atomic percentages in the synthesized compound are in agreement with the nominal composition. EDS mapping analysis were also carried out to know the elemental distribution in the compounds. The EDS elemental mapping images (Figure 5.5) show uniform spreading of elements in the entire region of the selected area shown in the bright field FE-SEM image.

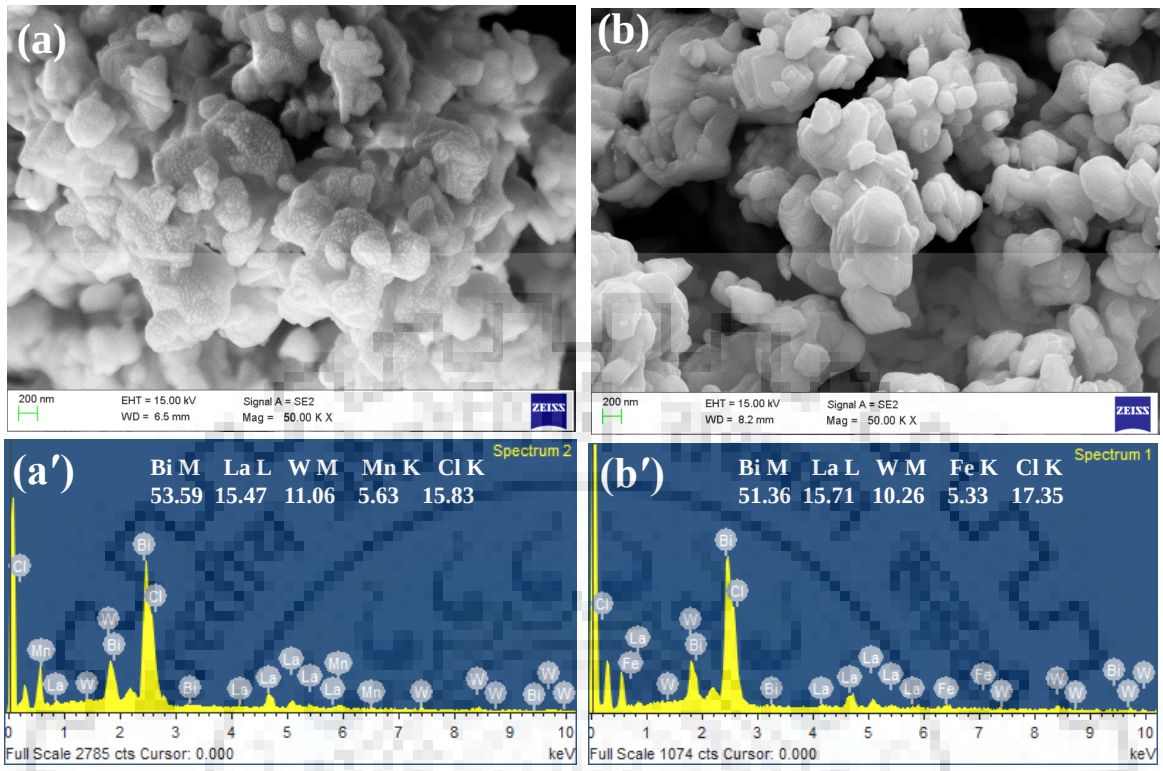

Figure 5.4 FE-SEM images and corresponding EDS data of $LaBi_3W_{0.67}Fe_{0.33}O_8Cl$ (a, a') and $LaBi_3W_{0.67}Mn_{0.33}O_8Cl$ (b, b').

5.3.3 XPS Analysis

The surface chemical states of all the elements present in the compounds were investigated by XPS, as shown in Figure 5.6. In the survey spectra, six elements (La, Bi, W, Fe or Mn, Cl and O) are detected. The high resolution XPS of Bi 4*f* show two peaks located at 164.0 and 158.8 eV, which are recognized as Bi $4f_{5/2}$ and Bi $4f_{7/2}$ of the Bi^{3+} present in the $(Bi_2O_2)^{2+}$ layer. The additional two peaks positioned at 165.3 and 160.1 eV belong to the Bi^{3+} closer to the [Bi-O-W] octahedral layer $(W_{0.67}Fe_{0.33})O_6$. In the high resolution XPS of W 4*f*, two peaks appearing at 37.1 and 34.9 eV for W $4f_{5/2}$ and W $4f_{7/2}$, respectively, indicates the presence of W in the 6+ oxidation state. For the high resolution of O1*s* spectra, the peaks at 529.5 and 532.0 eV are assigned to the crystal lattice oxygen in the [Bi-O-Bi] layer and [Bi-O-W/Fe] octahedral layer, respectively.[41] In the high resolution La spectra, peaks observed in the range of 830–840 eV is identified as peaks of doublets of La 3*d*, i.e. La $3d_{3/2}$ and La $3d_{1/2}$. The transition metal 2*p* spectra (Figure 5.6 (e) and (i)) are split into two peaks $2p_{3/2}$ and $2p_{1/2}$,

by spin-orbit coupling. The binding energy of the peaks indicate that both the transition metalsnamely, Mn and Fe are present in the single oxidation state of 3+ i.e. as M^{3+}.[42,43] Moreover, the Cl $2p_{3/2}$ and $2p_{1/2}$ peaks confirmed the presence of Cl^- in the compound.

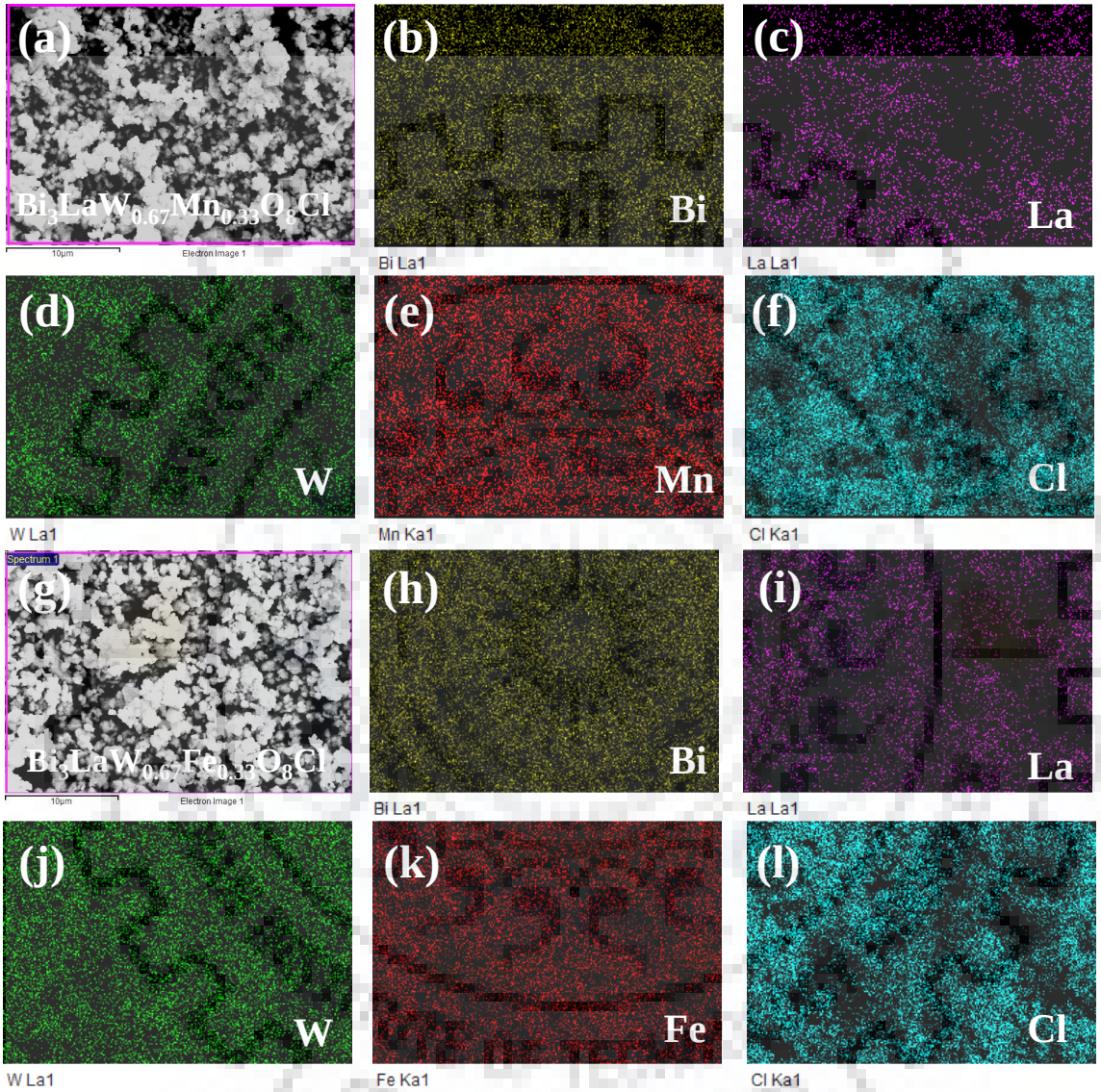

Figure 5.5 FE-SEM elemental mapping of $LaBi_3W_{0.67}Mn_{0.33}O_8Cl$ (a to f) and $LaBi_3W_{0.67}Fe_{0.33}O_8Cl$ (g to l)

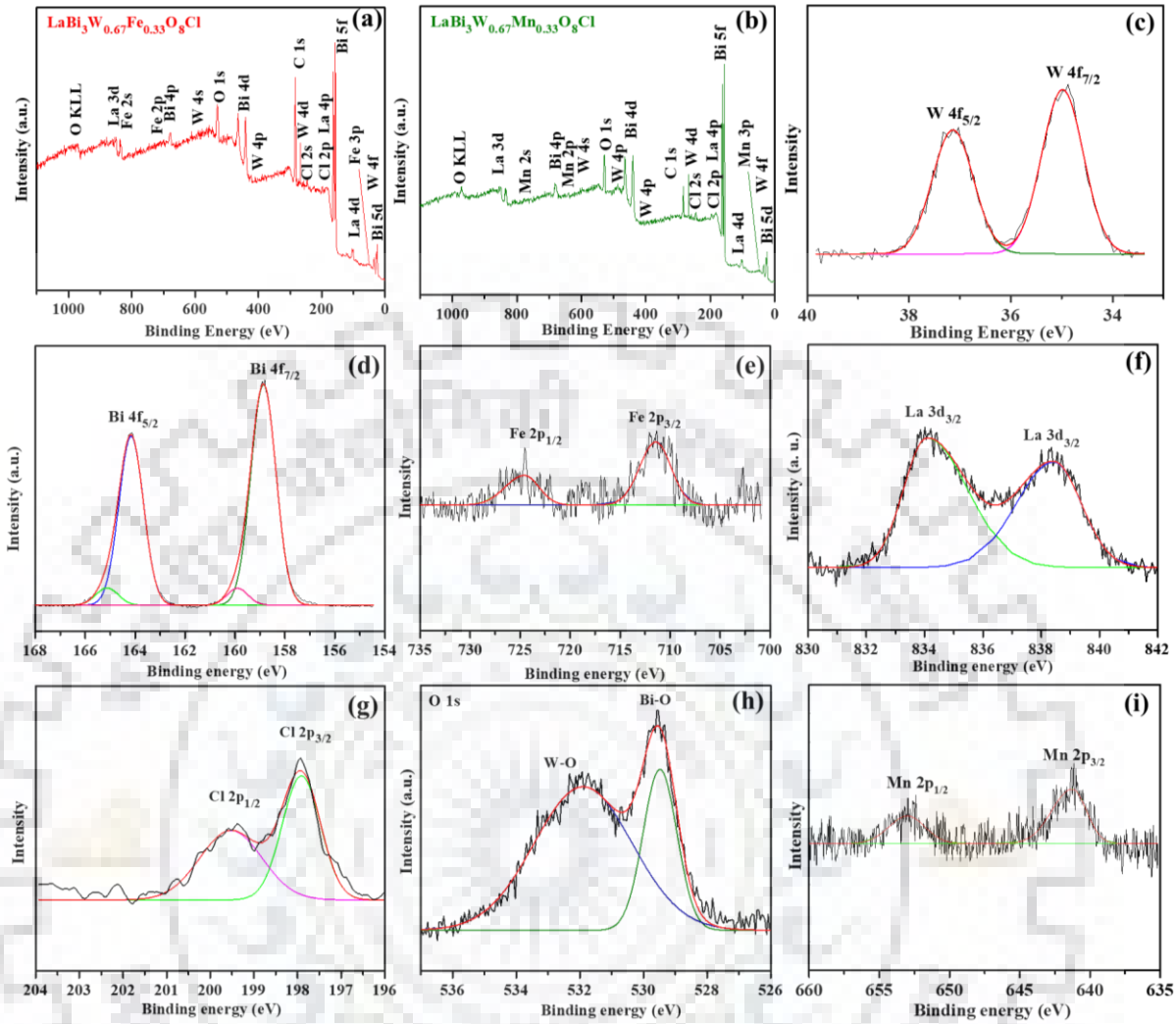

Figure 5.6 (a, b) Survey XPS of $LaBi_3W_{0.67}M_{0.33}O_8Cl$ (M = Mn, Fe), (c to i) high resolution spectra of W 4*f*, Bi 4*f*, Fe 2*p*, Cl 2*p*, O 1*s* and Mn 2*p*.

5.3.4 HR-TEM Analysis

Figure 5.7 shows the TEM images for a representative member, $LaBi_3W_{0.66}Fe_{0.33}O_8Cl$. The HR-TEM image exhibits the lattice fringes corresponding to the repeating units of the orthorhombic perovkite slabs with spacings 0.468 and 0.278 nm, conforming to the *d*-spacings of (003) and (020) plane of $LaBi_3W_{0.66}Fe_{0.33}O_8Cl$, respectively. The HR-TEM is in very good agreement with the P-XRD results. SEAD data show bright spots indicating the highly crystalline nature of the samples and the diffraction spots are indexable corresponding to the distances observed in the P-XRD as shown by indexing of few representative bright spots.

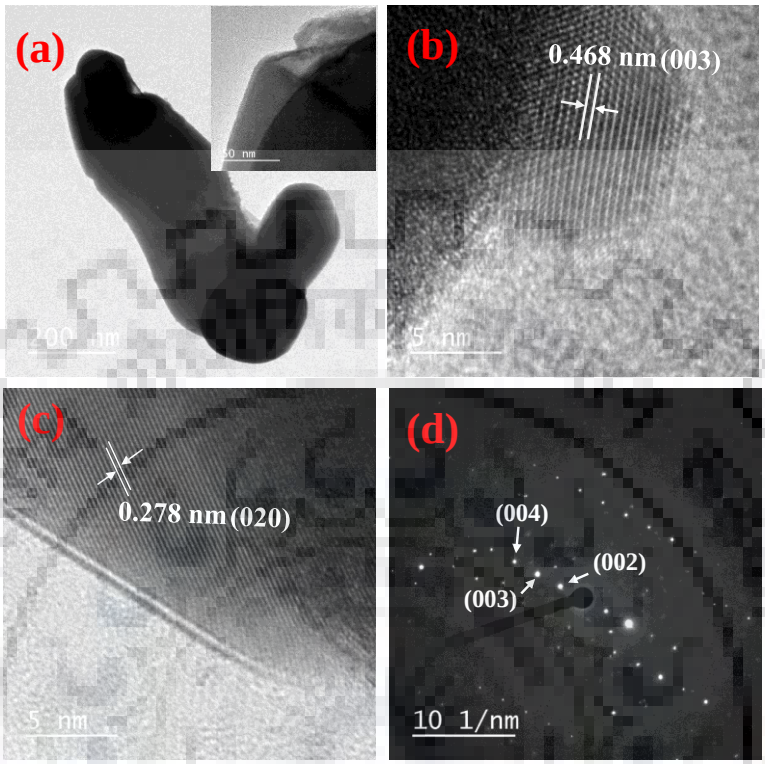

Figure 5.7 (a) TEM image (b, c) HR-TEM images and (d) SAED pattern of $LaBi_3W_{0.67}Fe_{0.33}O_8Cl$.

5.3.5 Magnetic Properties

The magnetic behavior of the as prepared $LaBi_3W_{0.67}M_{0.33}O_8Cl$ (M = Mn, Fe) are shown in Figure 5.8. The compounds show paramagnetic behavior with no indication of any magnetic phase transition in the temperature range 5-300 K. The concentration of the magnetic metal (33% magnetic cation at the B-site) in the layer is so less that nearest neighbor magnetic interaction is less likely. Moreover, owning to the presence of the (Bi_2O_2) layers, there are hardly any nearest neighbor magnetic interaction between the adjacent perovskite blocks. Therefore, the transition metal in the perovskite layer stays mostly isolated thereby prevailing paramagnetic behavior. The paramagnetic moments per formula unit (per/mole) are calculated from the inverse susceptibility vs. temperature data for the compounds. The observed magnetic moments of 5.12 and 5.81 BM for $LaBi_3W_{0.67}Mn_{0.33}O_8Cl$ and $LaBi_3W_{0.67}Fe_{0.33}O_8Cl$,

respectively, are in good agreement with the corresponding calculated magnetic moments based on spin-only formula assuming high spin states for M^{3+}.

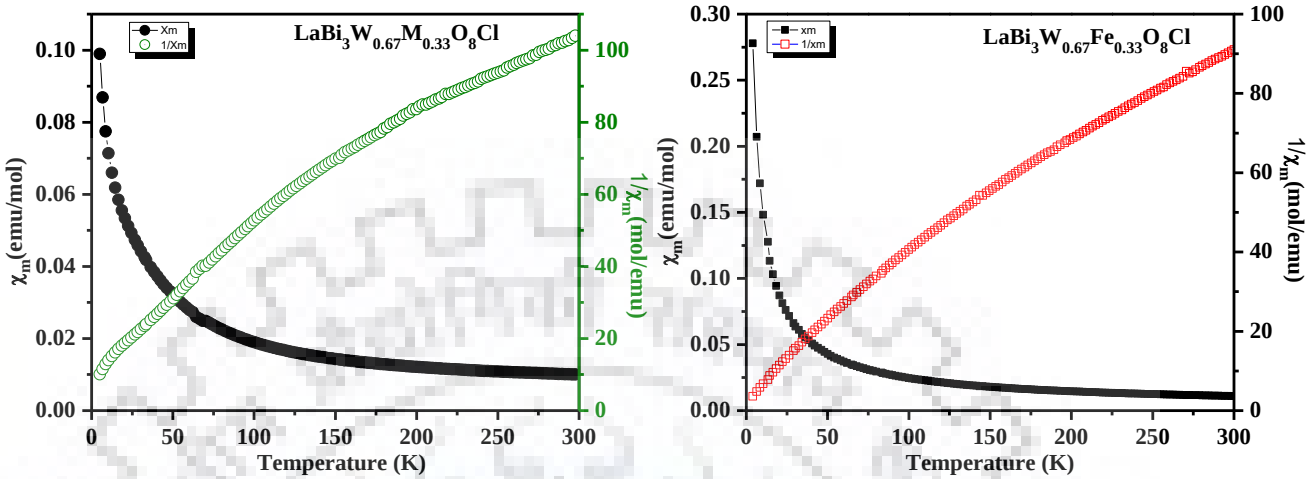

Figure 5.8 Magnetic susceptibility data for $LaBi_3W_{0.67}M_{0.33}O_8Cl$ (M = Mn, Fe).

5.3.6 UV-vis DRS Analysis

Figure 5.9 shows the optical absorption spectra of $LaBi_3W_{0.67}M_{0.33}O_8Cl$ (M = Mn, Fe). Both the compounds show sharp absorption edges above 400 nm (λ_{edges} > 400 nm) indicating visible-light absorption. While $LaBi_3W_{0.67}Fe_{0.33}O_8Cl$ shows a sharp absorption, the $LaBi_3W_{0.67}Mn_{0.33}O_8Cl$ show a two-step feature in the optical absorption. While the high energy one is attributed to the transition of the 6*s* electron of Bi to 5*d* empty orbital of W, the lower energy one is assigned to the transition from 2*p* electron of O to 3*d*-t_{2g} orbital of the transition metal.[44,45] The band gap energies of the compounds are calculated from the Tauc plot by following the equation, $\alpha h\nu = A(h\nu - E_g)^{1/n}$, where, α is the optical absorption coefficient, $h\nu$ is the photon energy, A is a proportionally constant and E_g is the band gap. The exponent, '*n*' denotes the type of transition in the semiconductor; $n = ½$ is for direct transition and $n = 2$ indicates an indirect transition. The band gap energies of the compounds are considered as indirect. The estimated band gap energies of the compounds are 2.11 eV for $LaBi_3W_{0.67}Fe_{0.33}O_8Cl$ and 2.41 eV for $LaBi_3W_{0.67}Mn_{0.33}O_8Cl$. The fact that all the compounds are visible light absorber, it is thought that their photocatalytic activity under sunlight could be interesting.

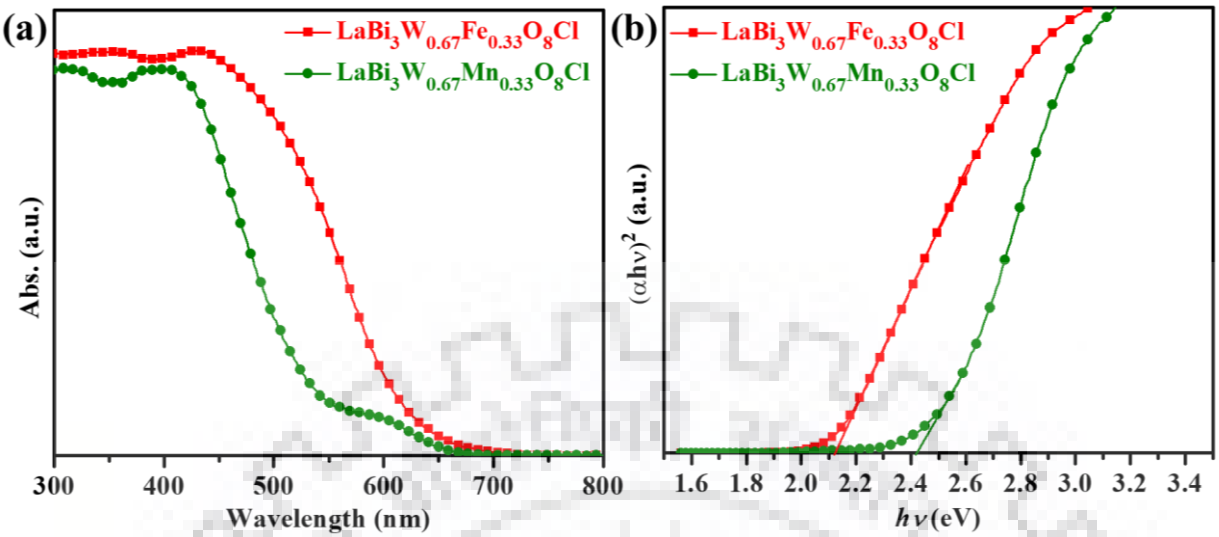

Figure 5.9 (a) UV-vis DRS and (b) Tauc plots of $LaBi_3W_{0.67}M_{0.33}O_8Cl$ (M = Mn, Fe).

5.3.7 PL Analysis

Photoluminescence spectra of the compounds recorded at room temperature are displayed in Figure 5.10. The photoluminescence emission spectra gives indirect information about the separation and migration of photogenerated charge carriers (electron and holes) in comparison to recombination. In general, the low intensity of PL means relatively lesser electron-hole recombination and hence efficient charge-carrier separation or indirectly longer lifetime of the photogenerated electron-holes. The photocatalytic activity depends on the efficiency of the catalysts to produce the electron and holes. PL emissions of the compounds are observed in the wavelength range 425-525 nm with the high intensity emission at around 471 nm. $LaBi_3W_{0.67}Mn_{0.33}O_8Cl$ shows higher PL intensity as compared to the Fe analog, indicating greater extent of electron-hole recombination in the Mn-compound. The higher emission intensity observed in the case of Mn is attributed to an intermediate energy band edge emission, which also supports the extended secondary sharp absorption edge in the UV-vis DRS of the Mn compound. The correlation between the PL peak intensity and photocatalytic activity, presumes the photocatalytic activity order as $LaBi_3W_{0.67}Fe_{0.33}O_8Cl$ > $LaBi_3W_{0.67}Mn_{0.33}O_8Cl$.

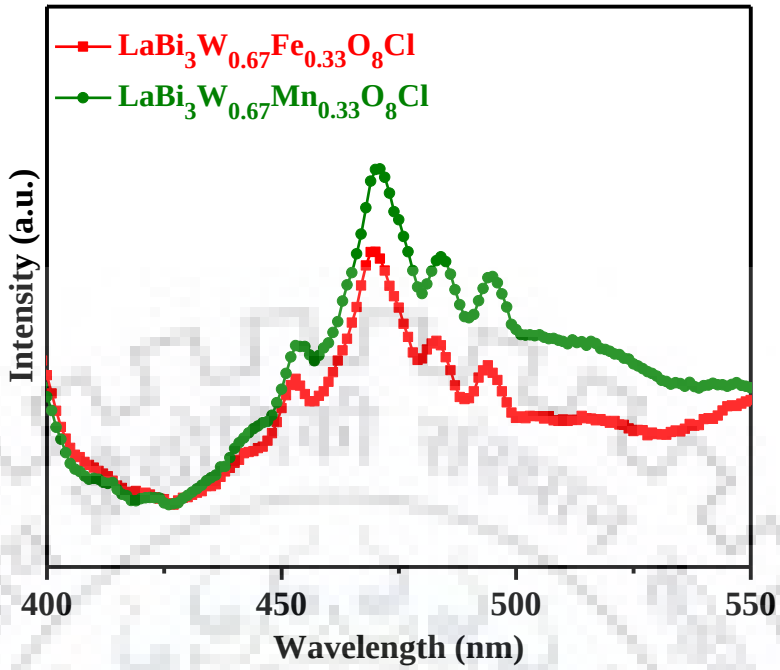

Figure 5.10 PL spectra of $LaBi_3W_{0.67}M_{0.33}O_8Cl$ (M = Mn, Fe) at room temperature.

5.3.8 EIS Analysis

EIS studies can help evaluate the charge transfer resistance (R_{CT}) and carrier separation efficiency of the catalysts. Figure 5.11 shows the Nyquist plot of $LaBi_3W_{0.67}M_{0.33}O_8Cl$ (M = Mn, Fe).Both the data consist of a semi-circular part, which provides information about the charge transfer process and a linear part with a slope, belonging to the diffusion controlled step. The Fe compound shows the smaller R_{CT} of 0.987 kΩ while higher value of 2.46 kΩ are obtained for the Mn compound. The smaller the R_{CT} value more efficient is the charge transfer. Among the catalysts, $LaBi_3W_{0.67}Fe_{0.33}O_8Cl$ show relatively smaller R_{CT} value, implying better separation efficiency of the photogenerated charge carriers. On the basis of EIS the Fe-compound is expected to show enhance photocatalytic activity as compared to that of the Mn-compound.

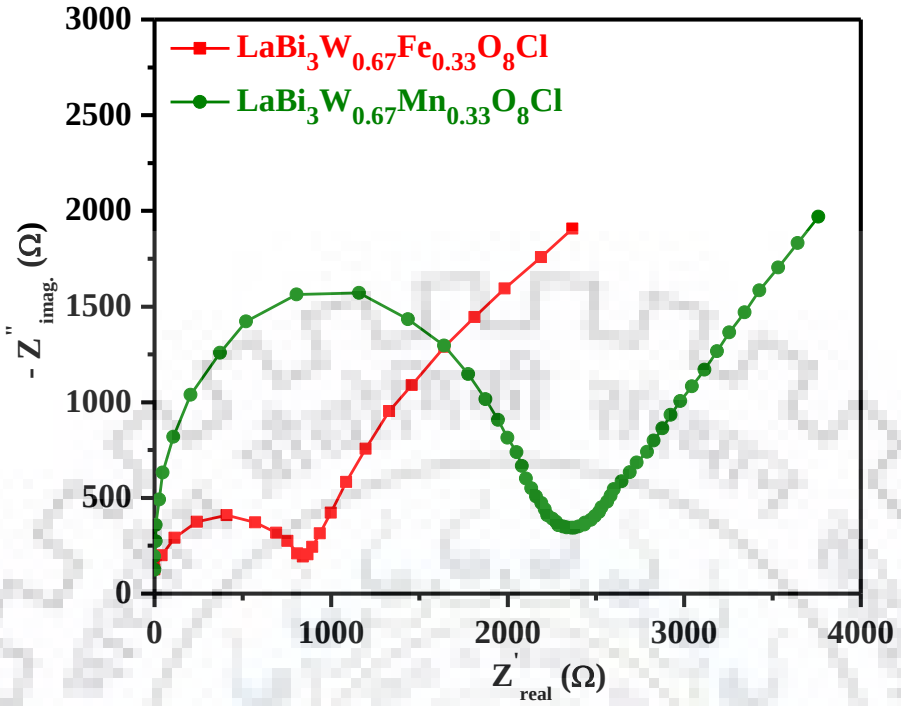

Figure 5.11 Nyquist impedance plots for $LaBi_3W_{0.67}M_{0.33}O_8Cl$ (M = Mn, Fe)

5.3.9 Photocatalytic Rhodamine B (RhB) Degradation Study

The activity of the compounds, $LaBi_3W_{0.67}M_{0.33}O_8Cl$ (M = Mn, Fe), in solar photocatalysis was evaluated by the degradation of dyes from aqueous solutions taking RhB, MO, and a mixture of RhB−MO as model systems. To evaluate the photostability of the dyes in aqueous medium at different pH (2, 7 and 11) blank tests (photodegradation of dyes without catalyst) of dyes were carried out under natural sunlight irritation. The blank studies confirmed the photostability of dye with no signature of self-photolysis of the dyes. Afterwards, degradation of dyes were carried out with catalysts and gradual decrement in the absorption intensity (λ_{max}) of the characteristic absorption peaks of RhB (at 554 nm) and MO (at 466 nm) indicated photocatalytic degradation of the dyes. The complete degradation of the dyes is indicated eventually with the disappearance of the absorption peaks. The catalysts took 90-120 min for complete degradation of RhB at pH 2 (Figure 5.12 (a) and (b)) under natural sunlight. However, 98% MO degradation (Figure 5.13 (a) and (b)) is achieved for $LaBi_3W_{0.67}Mn_{0.33}O_8Cl$ and 97% for $LaBi_3W_{0.67}Fe_{0.33}O_8Cl$ within 220 min of solar light irradiation at pH 2. The compound is considered as an efficient photocatalyst and the results

suggest that the rate of RhB degradation is three times higher than that of MO degradation over $LaBi_3W_{0.67}Fe_{0.33}O_8Cl$. Moreover, the percentage COD removal data for RhB at pH 2 are shown in Figure 5.12 (d). The data indicates complete and concordant dye mineralization for RhB.

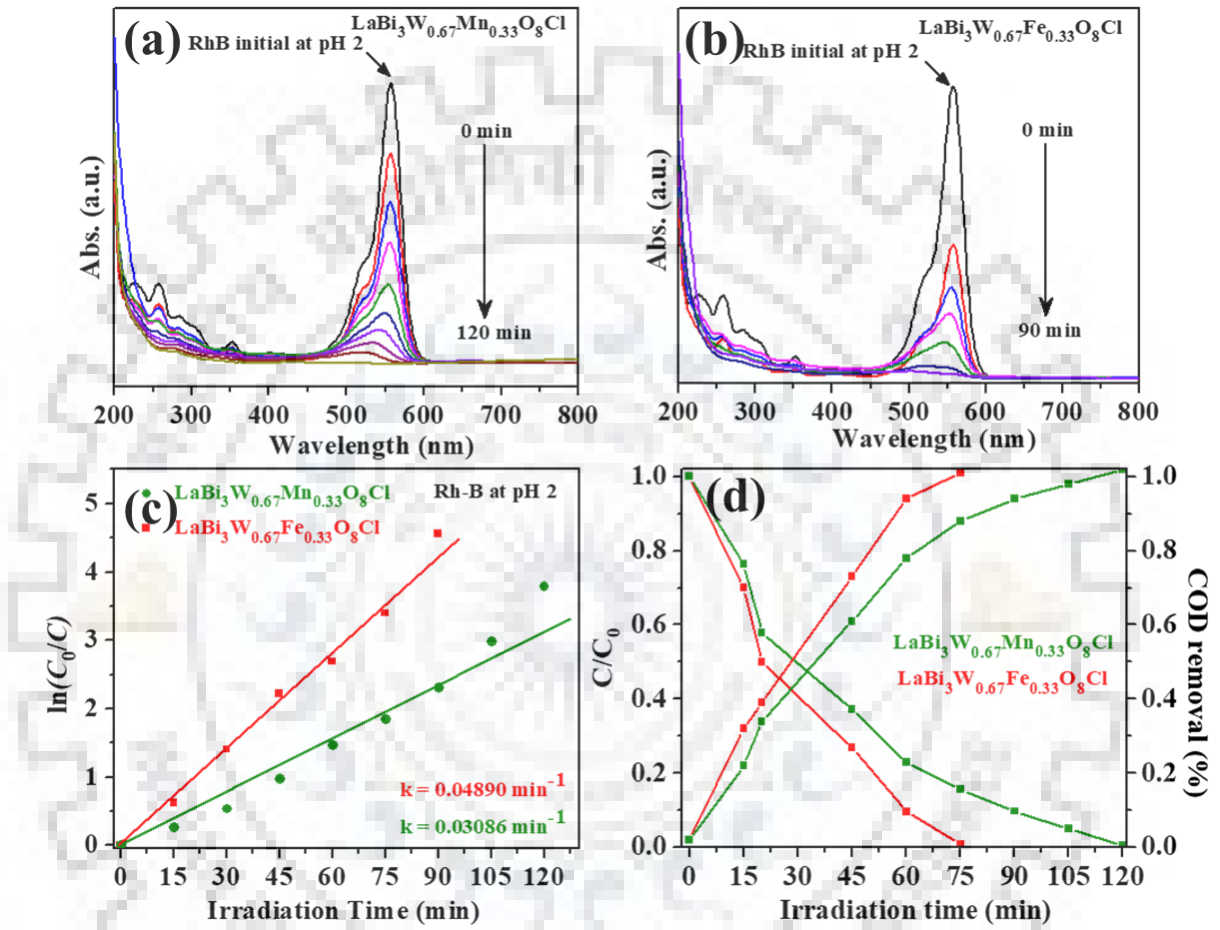

Figure 5.12 (a, b) UV-vis absorbance data for photocatalytic degradation (c) $\ln(C_0/C)$ *vs.* irradiation time plot, (d) photocatalytic degradation (C/C_0) and COD removal efficiency with time for RhB at pH 2 by $LaBi_3W_{0.67}M_{0.33}O_8Cl$ (M = Mn, Fe) under sunlight.

The photocatalytic degradation kinetics data of RhB and MO over $LaBi_3W_{0.67}M_{0.33}O_8Cl$ (M = Mn, Fe) are fitted with a Langmuir–Hinshelwood rate expression.[46]

$$\ln(C_0/C) = kt \qquad (5.2)$$

where, C_0 is the initial concentration of dye and C is the residual concentrations at different time interval and k is the rate constant. The plot between $\ln(C_0/C)$ versus irradiation time (t) for the compound is found to follow a pseudo first order kinetics. The rate constant is calculated (Figure 5.12 c) to be 0.03086 min^{-1} for $LaBi_3W_{0.67}Mn_{0.33}O_8Cl$ and 0.04809 min^{-1} for $LaBi_3W_{0.67}Fe_{0.33}O_8Cl$ in RhB degradation. Moreover, the calculated rate constants for MO degradation (Figure 5.13 d) are 0.0118 min^{-1} for $LaBi_3W_{0.67}Mn_{0.33}O_8Cl$ and 0.0126 min^{-1} for $LaBi_3W_{0.67}Fe_{0.33}O_8Cl$.

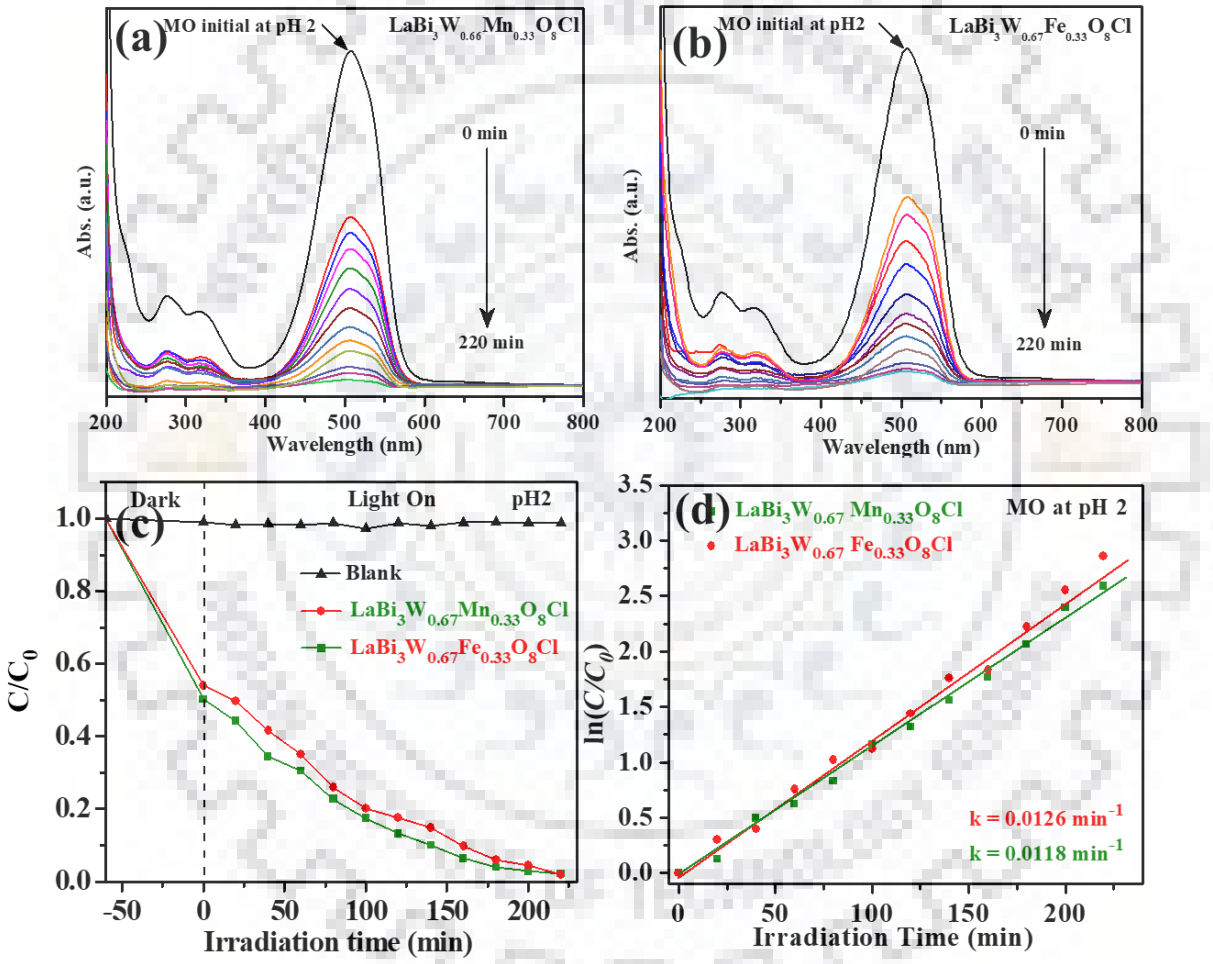

Figure 5.13 (a, b) UV-vis absorbance, (c) C/C_0 *vs.* irradiation time and (d) $\ln(C_0/C)$ as a function of time for MO degradation at pH 2 over $LaBi_3W_{0.67}M_{0.33}O_8Cl$ (M = Mn, Fe).

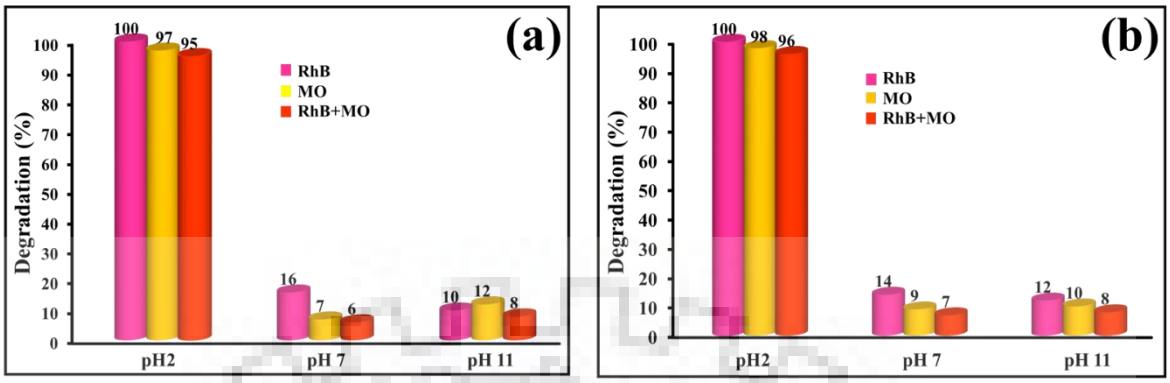

Figure 5.14 Photocatalytic degradation of (a) RhB and (b) MO at different pH.

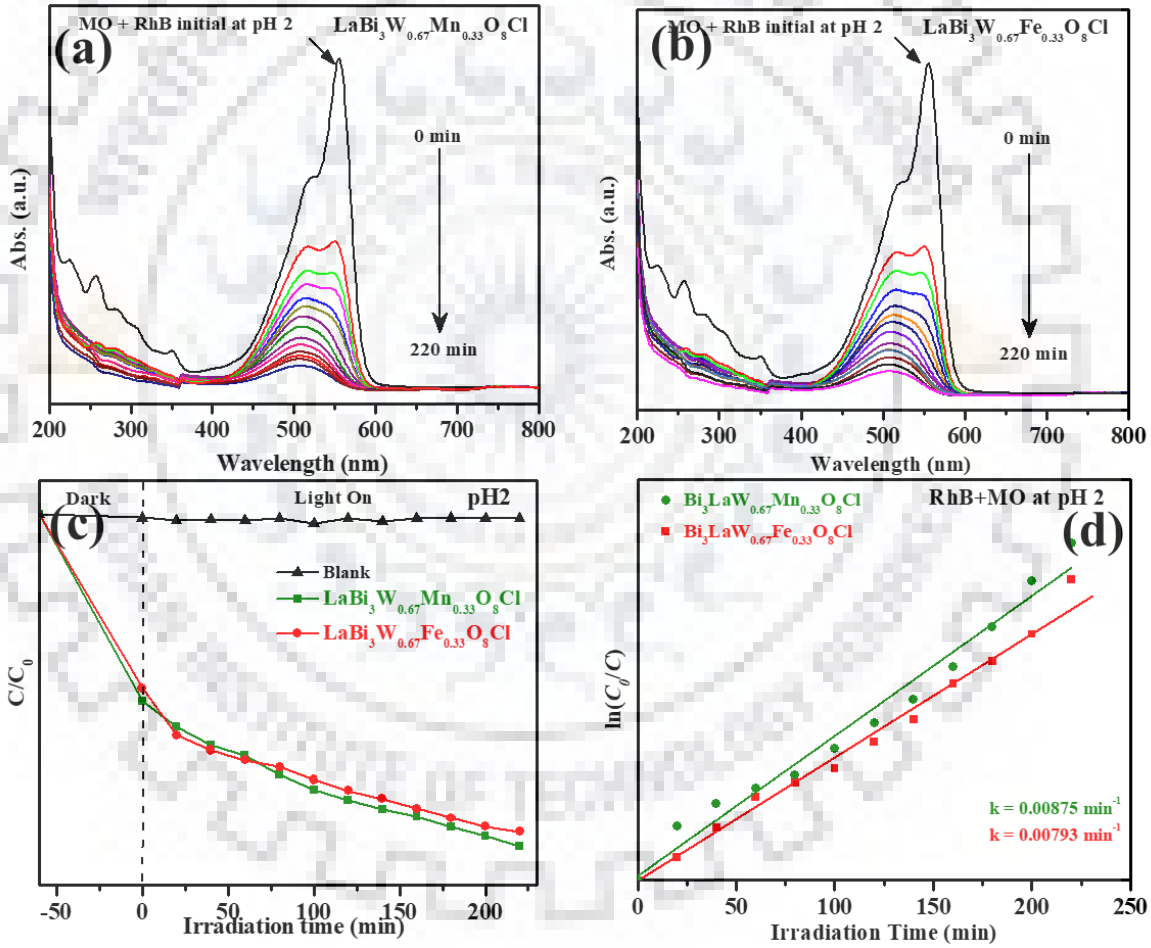

Figure 5.15 (a, b) UV-vis absorbance (c) C/C_0 *vs*. irradiation time and (d) $ln(C_0/C)$ as a function of time for collective photocatalytic degradation of RhB and MO at pH 2 over $LaBi_3W_{0.67}M_{0.33}O_8Cl$ (M = Mn, Fe).

The collective degradation of RhB and MO were also carried out over the catalysts and almost complete degradation of the mixed dye at pH 2 (Figure 5.15) was observed within 220 min. Although the data is fitted with the pseudo first–order kinetic giving an average rate constant for the mixed dye degradation, a close inspection of the kinetic data seems to indicate stepwise degradation of the dyes one after the other. The degradation experiment carried out at pH 7 (neutral) and 11 (alkaline) did not show any significant photocatalytic activity within 220 min of solar irradiation.

5.3.10 Catalyst Stability and Photocatalytic Cycle Studies

To evaluate the reusability and the stability of the photocatalysts, the cyclic test of dye degradation was carried out. Figure 5.16 shows the four successive catalytic cycle of RhB and MO degradation at pH 2 over $LaBi_3W_{0.67}Fe_{0.33}O_8Cl$ under solar irradiation. In each cycle, the RhB dye degradation is ~ 99.8 % at pH 2 within 50 min with no noticeable observable loss of activity of the catalyst. However, ~ 96% degradation of MO with negligible loss of activity of the catalyst after four successive runs are observed. The P-XRD patterns were recorded with the catalysts recovered after four cycles of degradation. The post-catalytic P-XRD pattern appear like the original catalysts, with no loss of crystalline nature and show excellent phase purity. Therefore, it is concluded that the catalysts preserve its structural integrity during the photocatalysis and do not show any photoleaching under the reaction condition.

5.3.11 Detection of Reactive Species

Generally, h^+ (holes), $^{\bullet}OH$ (hydroxyl radical) and $O_2^{\bullet-}$ (superoxide radical anions) are reactive species that are involved in the dye degradation process. To understand the role of the reactive species, which play the important role in the degradation process, scavenger tests were carried out. Tertiary butyl alcohol, benzoquinone and ammonium oxalate were used for $^{\bullet}OH$, $O_2^{\bullet-}$ and h^+ scavenger, respectively. Figure 5.17 indicate the photodegradation of RhB over $Bi_3LaW_{0.67}Mn_{0.33}O_8Cl$ in presence of ammonium oxalate. The significant inhibition of the degradation indicate the predominant role of holes in the degradation process. A noticeable reduction in the degradation efficiency is also observed on the addition of t-BuOH scavenger. A moderate role of hydroxyl radical in the RhB degradation is concluded from the scavenger experiment. Moreover, a small extent of retardation in the photodegradation of RhB is noticed

in presence of BQ. In summary, the main reactive species involved in the photodegradation of RhB over $LaBi_3W_{0.67}Mn_{0.33}O_8Cl$ are holes and $^{\bullet}OH$ radicals, while $O_2^{\bullet-}$ play an insignificant role. Moreover, the same reactive species are active for the degradation of MO in the acidic medium.

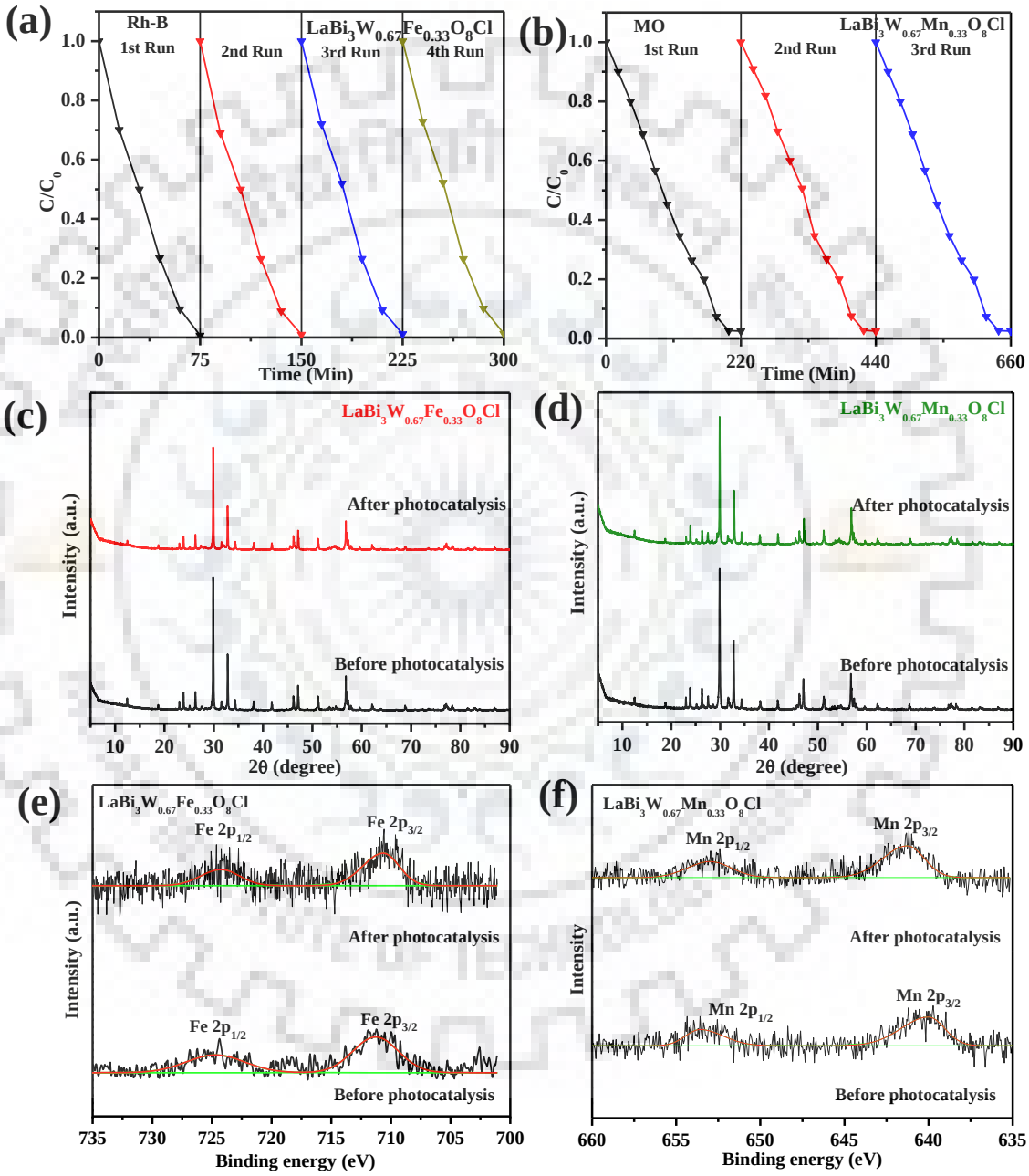

Figure 5.16 (a, b) Time profiles of RhB degradation for successive cycles with $LaBi_3W_{0.67}M_{0.33}O_8Cl$ (M = Mn, Fe), (c, d) P-XRD patterns of the catalysts before and after

the photocatalytic degradation. (e, f) high-resolution XPS of Fe 2p and Mn 2p of the catalysts before and after degradation.

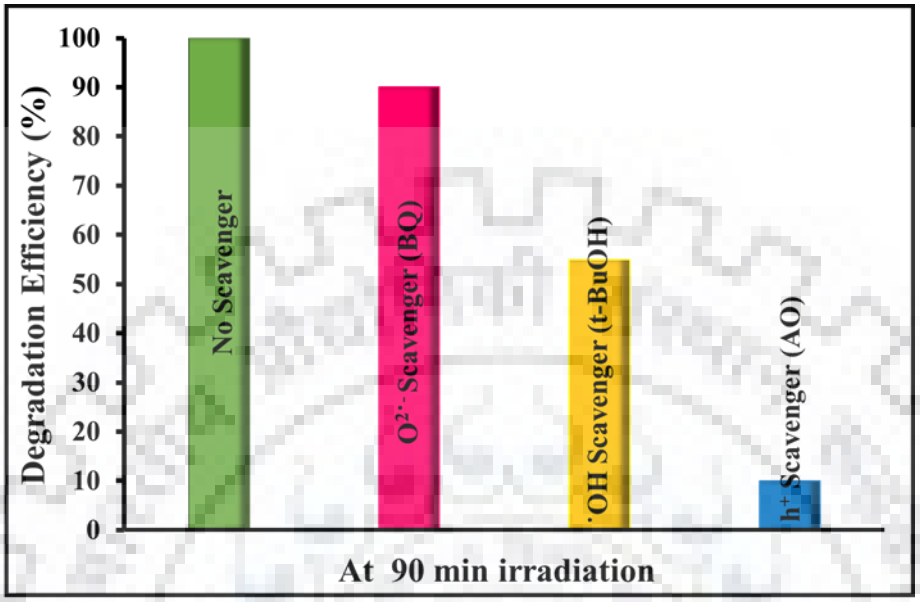

Figure 5.17 Effect of different scavengers on the degradation of RhB over $LaBi_3W_{0.67}Mn_{0.33}O_8Cl$ under sunlight-irradiation

5.3.12 ζ- Potential Measurements

The surface charge on the catalyst were measured by ζ-potential measurements. Surface charge of the catalyst play a significant role in the adsorption of dye. Change in ζ-potential of the as synthesized compounds as a function of pH are shown in Figure 5.18. The ζ- potential data indicates positive values in the acidic medium, whereas maximum negative value is shown in the basic medium and moderately negative value near natural pH. The adsorption of the RhB is maximum in the acidic medium, due to its positive value. RhB dye is considered as zwitterionic or cationic. At pH 2, the positive surface charge of the catalyst show strong electrostatic attraction for the negatively charged carboxylic group of RhB leading to enhanced adsorption. However, the catalyst surface is more negatively charged at pH 7 and 11 and a negatively charged carboxylic group of RhB will be electrostatically repelled. However, a small amount of dye adsorbed at the negatively charged catalyst at pH 7 and 11 is due to the electrostatic attraction between the negatively charged catalyst and

positively charged N-diethyl group of RhB. However, Methyl orange dye exist in quinonoid form in the acidic medium, whereas in the basic medium it exist in the benzenoid form. The adsorption of MO is higher in the acidic medium, due to the electrostatic interaction between the positively charged catalyst surface and negatively charged sulfonate ion group of Methyl orange. Moreover, the adsorption is less at pH 7 and 11, because of the strong repulsion between the negatively charge surface of catalyst and negatively charged sulfonate group of the dye.

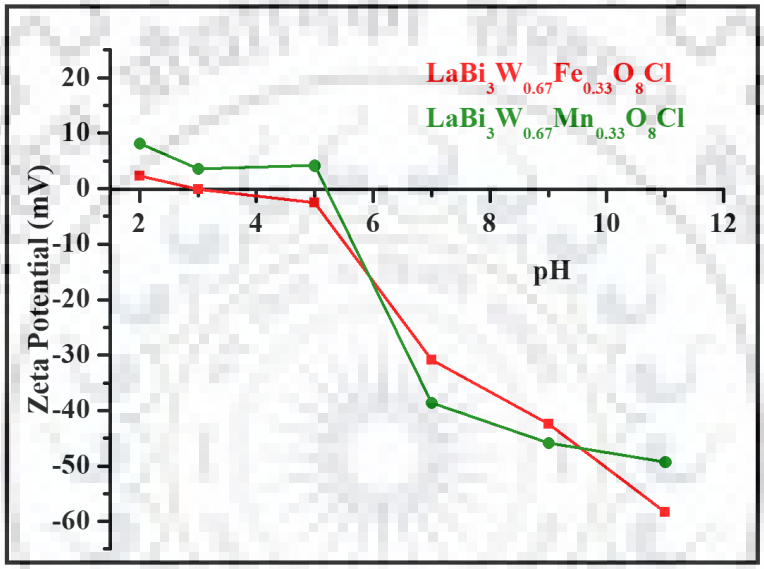

Figure 5.18 ζ- Potential of $LaBi_3W_{0.67}M_{0.33}O_8Cl$ (M = Mn, Fe) at different pH.

5.3.13 Role of Adsorption

The adsorption tests were performed at different pH in the dark. The adsorption data indicate that the adsorption of the dye is maximum in the acidic medium (pH 2) and low in natural (pH 7) and alkaline (pH 11) media. The corresponding adsorption (Figure 5.19) of RhB over $LaBi_3W_{0.67}Fe_{0.33}O_8Cl$ and $LaBi_3W_{0.67}Fe_{0.33}O_8Cl$ are 46 and 32 %, respectively, at pH 2 and a marked decrease is seen in the neutral and alkaline medium with the adsorption reaching up to a maximum of 11 % only. This definitely clarifies the higher activity of the catalyst in the acidic and very low performance in the alkaline and neutral pH. Moreover, the adsorption order of the catalysts are the same as the photoactivity of the catalyst with RhB. Therefore, $LaBi_3W_{0.67}Fe_{0.33}O_8Cl$ exhibited superior activity toward RhB degradation as compared to $LaBi_3W_{0.67}Mn_{0.33}O_8Cl$. With MO, nearly 50 % adsorption takes place in the

acidic medium (pH 2) while the adsorption is much lower in the neutral and basic medium (Figure 5.20). The adsorption results are in good agreement with the activity order showing very close rate for MO degradation by the catalysts at pH 2 while there is substantial difference in the RhB degradation at pH 2. This is consistent with the adsorption data.

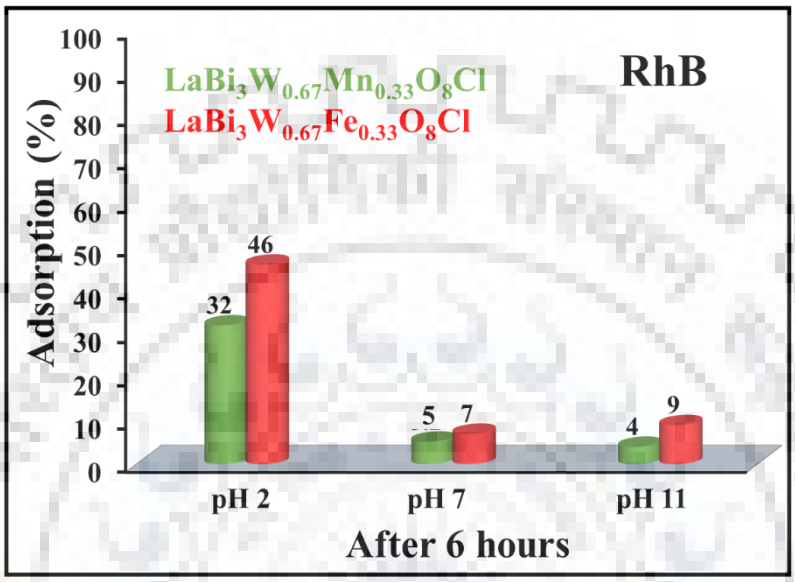

Figure 5.19 Percentage adsorption of RhB over $LaBi_3W_{0.67}M_{0.33}O_8Cl$ (M = Mn, Fe) at different pH.

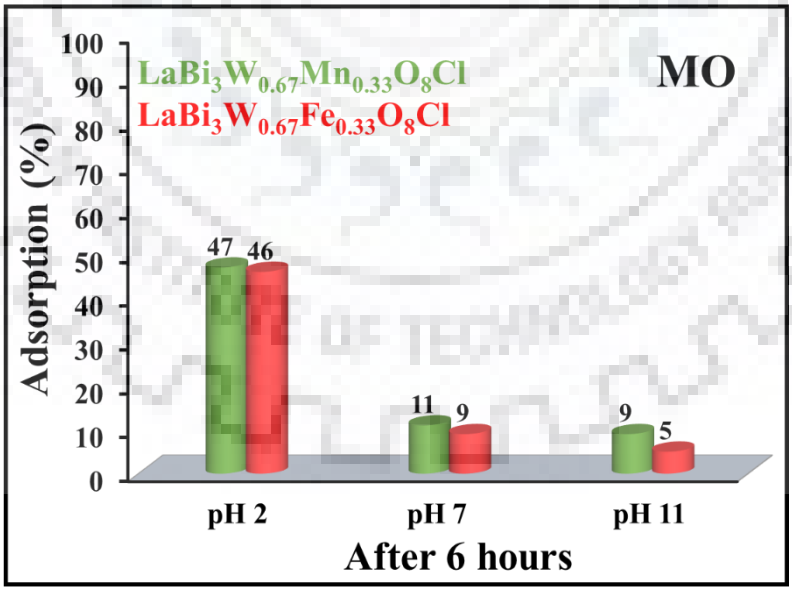

Figure 5.20 Percentage adsorption of MO over $LaBi_3W_{0.67}M_{0.33}O_8Cl$ (M = Mn, Fe) at different pH.

5.3.14 Mechanism of Photocatalysis

It is believed that adsorption of the dye on the surface of photocatalysts play an important role in photocatalysis, in addition to other general factors such as, generation of electron-hole pair on photoexcitation and creation of reactive oxygen species followed by oxidative degradation of the dye on action of ROS generated. In general, the photocatalyst first absorbs the light photons and electron gets excited from the valence to the conduction band (CB) creating holes in the valance band (VB). Subsequently, the electrons-hole pair get separated from each other and migrate to the photocatalyst surface where they take part in the generation of reactive species. In most of the cases, the electrons that are present in the CB reduces the dissolved oxygens to produce superoxide radical anions ($O_2^{\bullet-}$) and VB holes oxidizes the water to yield the $^{\bullet}OH$ radicals, that further participate in the degradation of dye. Moreover, the photogenerated holes in the valance band of the semiconductor may also oxidize the adsorbed dye molecules into CO_2 and H_2O.

To explain the mechanism of photocatalytic activity of the catalysts the VB and CB edge positions of the semiconductors are calculated using the following formula:

$$E_{CB} = \chi(A_aB_bC_c) - \tfrac{1}{2}E_g + 0.059(pH_{ZPC} - pH) + E_0 \quad (5.3)$$

$$E_{VB} = E_{CB} + E_g \quad (5.4)$$

By using the above formulas and the calculated χ value (6.18 eV), the CB (E_{CB}) and VB edge energies (E_{VB}) for $LaBi_3W_{0.67}Mn_{0.33}O_8Cl$ are calculated to be 0.46 and 2.87 eV, respectively. The potential for the generation of $^{\bullet}OH$ ($E_{\bullet OH/H2O}$= +2.68 eV *vs. NHE)* and $O_2^{\bullet-}$ ($E_{O2/O2\bullet-}$= +0.13 eV *vs. NHE*), are taken from the literature. The HOMO-LUMO levels of RhB (E_{HOMO} = 0.95 eV and E_{LUMO} = –1.42 eV) as reported in literature were used for drawing the energy level diagram.[47,48]

According to the energy level diagram, the conduction band of the catalyst is more positive than the potential of E ($O_2/O_2^{\bullet-}$) (+0.13eV *vs. NHE*), due to this the photogenerated electrons in E_{CB} of $LaBi_3W_{0.67}Mn_{0.33}O_8Cl$ cannot reduce the dissolved O_2 and help creation of $O_2^{\bullet-}$ radicals. Moreover, the E_{VB} of the $LaBi_3W_{0.67}Mn_{0.33}O_8Cl$ is more positive than the potential of E ($^{\bullet}OH/H_2O$) (+2.68eV *vs. NHE*). In addition, the E_{VB} of the semiconductor is located below the HOMO levels of RhB dye that supports the h^+ transfer from the

semiconductor to the adsorbed dye. Further, $O_2^{\bullet-}$ radicals are observed to play negligible role in the dye degradation process, indicating that the dye degradation may be driven by a dye sensitization mechanism. Accordingly, the effects of *t*-BuOH and AO scavenger test show retardation in the degradation while the BQ scavenger test indicate only negligible effect on the photodegradation of RhB.

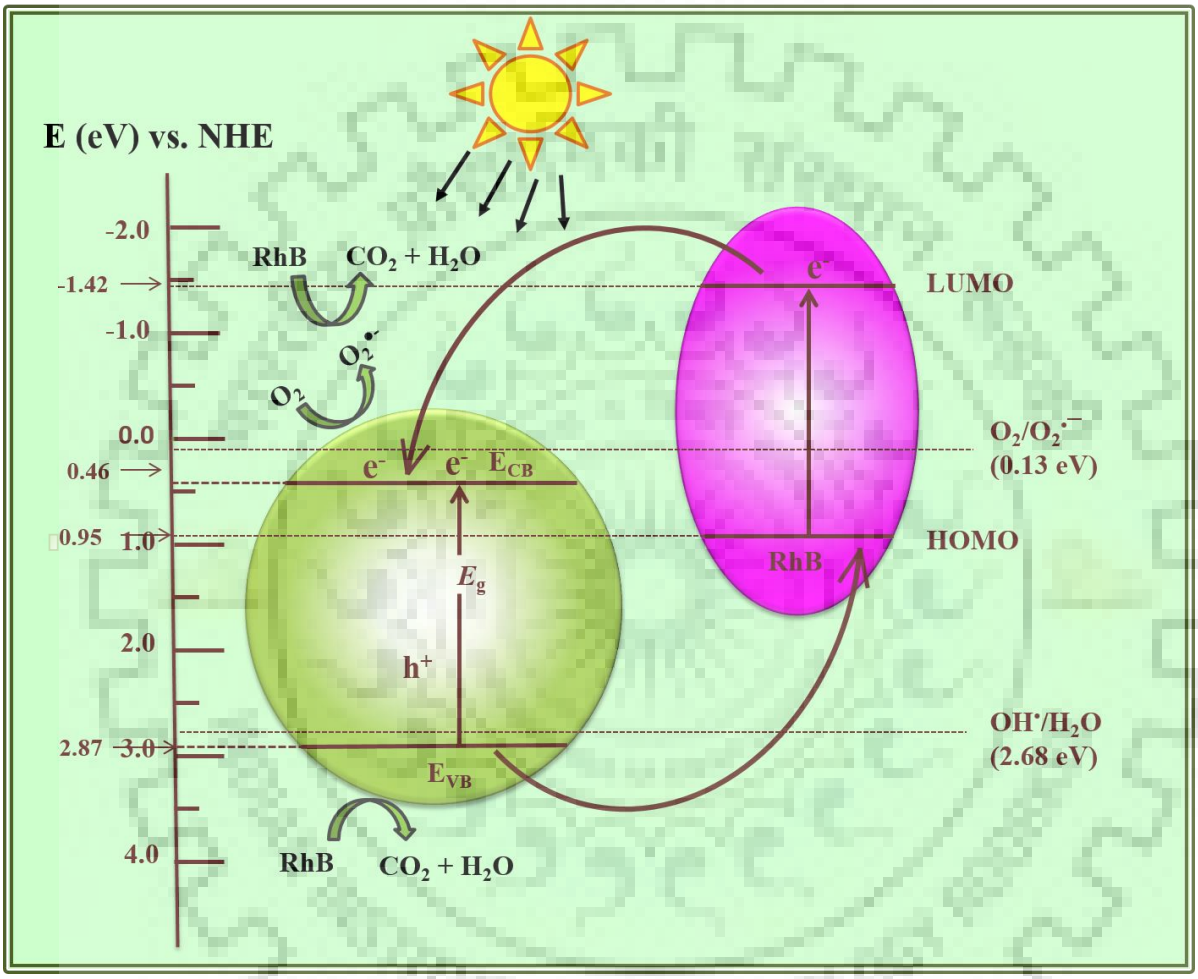

Figure 5.21 Schematic energy level diagram of $LaBi_3W_{0.67}M_{0.33}O_8Cl$ with respect to potential (vs. NHE) of $^{\bullet}OH/H_2O$, $O_2/O_2^{\bullet-}$ and the HOMO–LUMO levels of RhB.

In summary, solid-state synthesis of single-layered Sillén-Aurivillius perovskites, $LaBi_3W_{0.67}M_{0.33}O_8Cl$ (M = Mn, Fe) are reported in this chapter. The compounds are characterized by P-XRD, FE-SEM, EDS, TEM, UV-Vis DRS, PL and EIS spectroscopy. The SEM images showed homogenous morphology with quite large degree of agglomeration among the crystallites. The compounds exhibit paramagnetic behavior with no magnetic phase

transitions between 5 and 300 K. The compounds showed photocatalytic performance toward Rhodamine B and Methyl Orange. The compounds show enhanced photocatalytic degradation of RhB and MO at pH 2 as compared to the neutral and alkaline media. The major role of photogenerated holes in the RhB degradation is established by reactive species trapping experiments. The photodegradation cycle experiment indicated the catalyst to possess excellent stability and recyclability as demonstrated by five consecutive cycles of experiments. The paramagnetic behavior of the compounds will be helpful in the post-catalytic magnetic separation of the catalysts.

REFERENCES

1. Maeda, K. Photocatalytic Water Splitting using Semiconductor Particles: History and Recent Developments. *J. Photchem. Photobiol. C* **2011**, *12*, 237–268.

2. Hoffmann, M. R.; Martin, S. T.; Choi, W.; Bahnemann, D. W.; Environmental Applications of Semiconductor Photocatalysis. *Chem. Rev.* **1995**, *95*, 69–96

3. Qu, Y.; Duan, X. Progress, Challenge and Perspective of Heterogeneous Photocatalysts. *Chem. Soc. Rev.* **2013**, *42*, 2568–2580.

4. Osterloh, F. E. Inorganic Materials as Catalysts for Photochemical Splitting of Water. *Chem. Mater.* **2008**, *20*, 35−54.

5. Ye, C.; Bando, Y.; Shen, G.; Golberg, D. Thickness-Dependent Photocatalytic Performance of ZnO Nanoplatelets. *J. Phys. Chem. B* **2006**, *110*, 15146-15151.

6. Li, L.; Chu, Y.; Liu, Y.; Dong, L. Template-Free Synthesis and Photocatalytic Properties of Novel Fe_2O_3 Hollow Spheres *J. Phys. Chem. C* **2007**, *111*, 2123-2127.

7. Zhang, H.; Chen, G.; Bahnemann, D. W. Photoelectrocatalytic Materials for Environmental Applications. *J. Mater. Chem.* **2009**, *19*, 5089-5121.

8. Dong, S.; Feng, J.; Fan, M.; Pi, Y.; Hu, L.; Han, X.; Liu, M.; Sun, J.; Sun, J. Recent Developments in Heterogeneous Photocatalytic Water Treatment using Visible Light Responsive Photocatalysts: A Review. *RSC Adv.* **2015**, 5, 14610-14630.

9. Fujishima, A.; Honda, K. Electrochemical photolysis of water at a semiconductor electrode. *Nature* **1972**, 238, 37–38.

10. Banerjee, S.; Pillai, S. C.; Falaras, P.; O'Shea, K. E.; Byrne, J. A.; Dionysios D. D. New Insights into the Mechanism of Visible Light Photocatalysis. *J. Phys. Chem. Lett.* **2014**, 5, 2543−2554.

11. Kim, H. G.; Hwang, D. W.; Lee, J. S. An Undoped, Single-Phase Oxide Photocatalyst Working under Visible Light. *J. Am. Chem. Soc.* **2004**, 126, 8912−8913.

12. Kudo, A.; Miseki, Y. Heterogeneous Photocatalyst Materials for Water Splitting. *Chem. Soc. Rev.* **2009**, 38, 253−278.

13. Naresh, G.; Mandal, T. K. Excellent Sun-Light-Driven Photocatalytic Activity by Aurivillius Layered Perovskites, $Bi_{5-x}La_xTi_3FeO_{15}$ (x = 1, 2). *ACS Appl. Mater. Interfaces* **2014**, *6*, 21000-21010.

14. Naresh, G.; Mandal, T. K. Efficient COD Removal Coinciding with Dye Decoloration by Five- Layer Aurivillius Perovskites under Sunlight-Irradiation. *ACS Sustainable Chem. Eng*. **2015**, *3*, 2900–2908.

15. Pandey, A.; Naresh, G.; Mandal, T. K. Sunlight Responsive New Sillén-Aurivillius A1X1 Hybrid Layered Oxyhalides with Enhanced Photocatalytic Activity. *Sol. Energy Mater. Sol. Cells* **2017**, *161*, 197–205.

16. Oshikiri, M.; Boero, M.; Ye, Zou, Z. Kido, G. Electronic Structures of Promising Photocatalysts $InMO_4$ (M=V, Nb, Ta) and $BiVO_4$ for Water Decomposition in the Visible Wavelength Region. *J. Chem. Phys*. **2002**, *117*, 7313–7318.

17. Tang, J.; Zou, Z.; Ye, J. Efficient Photocatalytic Decomposition of Organic Contaminants over $CaBi_2O_4$ under Visible-Light Irradiation. *Angew. Chem. Int. Ed.* **2004**, *43*, 4463–4466.

18. Zhang, J.; Shi, F.; Lin, J.; Chen, D.; Gao, J.; Huang, Z.; Ding, X.; Tang, C. Self-Assembled 3-D Architectures of BiOBr as a Visible Light-Driven Photocatalyst. *Chem. Mater*. **2008**, *20*, 2937–2941.

19. Ye, L.; Su, Y.; Jin, X.; Xie, H.; Zhang, C. Recent Advances in BiOX (X = Cl, Br and I) Photocatalysts: Synthesis, Modification, Facet Effects and Mechanisms. *Environ. Sci. Nano* **2014**, *1*, 90–112.

20. Dia, J.; Xia, J.; Li, H.; Guo, S.; Dai, S. Bismuth Oxyhalides Layered Materials for Energy and Environmental Applications. *Nano Energy* **2017**, *41*, 172–192.

21. Lv, J.; Hu, Q.; Cao, C.; Zhao, Y. Modulation of Valence Band Maximum Edge and Photocatalytic Activity of BiOX by Incorporation of Halides. *Chemosphere* **2018**, *191* 427–437.

22. Kim, H. G.; Hwang, D. W.; Lee, J. S. An Undoped, Single-Phase Oxide Photocatalyst Working under Visible Light. *J. Am. Chem. Soc.* **2004**, *126*, 8912.

23. Kim, H. G.; Becker, O. S.; Jang, J. S.; Ji, S. M.; Borse, P. H. Lee, J. S. A generic Method of Visible Light Sensitization for Perovskite-related Layered Oxides: Substitution Effect of Lead. *J. Solid State Chem.* **2006**, *179*, 1214.

24. Kim, H. G.; Borse, P. H.; Jang, J. S.; Jeong, E. D.; Lee, J. S. Enhanced Photochemical Properties of Electron Rich W-Doped $PbBi_2Nb_2O_9$ Layered Perovskite Material under Visible-Light Irradiation. *Mater. Lett.* **2008**, *62*, 1427–1430

25. Bhat, S.S.M.; Sundaram, N. Photocatalysis of Bi_4NbO_8Cl Hierarchical Nanostructure for Degradation of Dye under Solar/UV Irradiation. *New J. Chem.* **2015**, *39*, 3956–3963.

26. Ackerman, J. F. The Structures of Bi_3PbWO_8Cl and Bi_4NbO_8Cl and the Evolution of the Bipox Structure Series. *J. Solid State Chem.* **1986**, *62*, 92–104.

27. Aurivillius, B. Intergrowth Compounds between Members of the Bismuth Titanate Family and Structures of the Lithium Dichlorotetraoxitribismuthate ($LiBi_3O_4Cl_2$) Type. *Chem. Scr.* **1984**, *23*, 143.

28. Kusainova, A. M.; Stefanovich, S. Y.; Dolgikh, V. A.; Mosunov, A. V.; Hervoches C. H.; Lightfoot, P. Dielectric Properties and Structure of Bi_4NbO_8Cl and Bi_4TaO_8Cl. *J. Mater. Chem.* **2001**, *11*, 1141–1145.

29. Kusainova, A. M.; Zhou, W.; Irvine, J. T. S.; Lightfoot, P. Layered Intergrowth Phases Bi_4MO_8X (X = Cl, M = Ta, and X = Br, M = Ta or Nb): Structural and Electrophysical Characterization. *J Solid State Chem.* **2002**, *166*, 148–157.

30. Kusainova, A. M.; Lightfoot, P.; Zhou, W.; Stefanovich, Y. S. Mosunov, A. V.; Dolgikh, V. A. Ferroelectric Properties and Crystal Structure of the Layered Intergrowth Phase $Bi_3Pb_2Nb_2O_{11}Cl$. *Chem. Mater.* **2001**, 13, 4731–4737.

31. Brande, D. A.; Herrero, A. G.; Cánovas, A. R. L.; Díaz, L. C. O. Synthesis, Structural and Microstructural Study of $Bi_4W_{0.5}Ti_{0.5}O_8X$ (X=Cl, Br) Sillén–Aurivillius Intergrowths. *Solid State Sciences* **2005**, *7*, 486–496.

32. Brande, D. A.; Díaz, L. C. O.; Cánovas, A. R. L.; Bals, S.; Tendeloo, G. V. A New $Bi_4Mn_{1/3}W_{2/3}O_8Cl$ Sillén–Aurivillius Intergrowth: Synthesis and Structural CharacteriSation by Quantitative Transmission Electron Microscopy. *Eur. J. Inorg. Chem.* **2006**, 1853–1858.

33. Brande, D. A.; Cánovas, A. R. L.; Díaz, L. C. O. Order-Disorder and Direct Evidence of Oxygen Vacancies in a New Family of BICUWOX Compounds. *Chem. Mater.* **2007**, *19*, 323–328.

34. Brande, D. A.; Cánovas, A. R. L.; Díaz, L. C. O. Structural Science Order, disorder and structural modulations in Bi– Fe–W–O–Br Sillén–Aurivillius intergrowths. *Acta. Cryst.* **2008**, *B64*, 438–447

35. Kusainova, A. M. Stefanovich, S. Y.; Irvine, J. T. S.; Lightfoot, P. Structure–Property Correlations in the New Ferroelectric $Bi_5PbTi_3O_{14}Cl$ and Related Layered Oxyhalide Intergrowth Phases. *J. Mater. Chem.* **2002**, *12*, 3413–3418.

36. Kato, D.; Hongo, K.; Maezono, R.; Higashi, M.; Kunioku, H.; Yabuuchi, M.; Suzuki, H.; Okajima, H.; Zhong, C.; Nakano, K. Abe, R.; Kageyama, H. Valence Band Engineering of Layered Bismuth Oxyhalides toward Stable Visible-Light Water Splitting: Madelung Site Potential Analysis. *J. Am. Chem. Soc.* **2017**, *139*, 18725−18731.

37. Kusainova, A. M.; Stefanovich, S. Y.; Dolgikh, V. A.; Mosunov, A.V.; Hervoches,C. H.; P. Lightfoot, Dielectric Properties and Structure of Bi_4NbO_8Cl and Bi_4TaO_8Cl. *J. Mater. Chem.* **2001**, *11*, 1141–1145.

38. Lin, X.; Huang, T.; Huang, F.; Wang, W.; Shi, J. Photocatalytic Activity of a Bi-based Oxychloride Bi_4NbO_8Cl. *J. Mater. Chem.* **2007**, *17*, 2145–2150.

39. Fujito, H.; Kunioku, h.; Kato, D.; Suzuki, H.; Higashi, M.; Abe, R.; Kageyama, H. Layered Perovskite Oxychloride Bi_4NbO_8Cl: A Stable Visible Light Responsive Photocatalyst for Water Splitting. *J. Am. Chem. Soc.* **2016**, *138*, 2082−2085.

40. Kunioku, H.; Higashi, M.; Tomita, O.; Yabuuchi, M.; Kato, Daichi.; Fujito, H.; Kageyama, H.; Abe, R. Strong Hybridization between Bi-6*s* and O-2*p* orbitals in Sillén–Aurivillius perovskite Bi_4MO_8X (M = Nb, Ta; X = Cl, Br), visible light photocatalysts enabling stable water oxidation. *J. Mater. Chem. A* **2018**, *6*, 3100−3107.

41. Mi, L.; Feng, Y.; Cao, L. Xue, M.; Qin, C.; Huang, Y.; Qin, L.; Seo, H. J. Photocatalytic Ability of $Bi_6Ti_3WO_{18}$ Nanoparticles with a Mix-Layered Aurivillius Structure. *J Nanopart. Res.* 2018, 20:2.

42. Kar, P,; Sardar, S.; Ghosh, S.; Parida, M. R.; Liu, B.; Mohammed, O. F.; Lemmens, P.; Pal, S. K. Nano surface engineering of Mn_2O_3 for potential light-harvesting application. *J. Mater. Chem. C*, **2015**, *3*, 8200-8211.

43. Lukashuk, L.; Yigit, N.; Rameshan, R.; Kolar, E.; Teschner, D.; Havecker, M.; Gericke, A. K.; Schlögl, R.; Föttinger, K.; Rupprechter, G. Operando Insights into CO Oxidation on Cobalt Oxide Catalysts by NAP-XPS, FTIR, and XRD. *ACS Catal*. **2018**, *8*, 8630−8641.

44. Zuo, X.; Zhu, S.; Bai, J.; He, E.; Hui, Z.; Zhang, P.; Song, D.; Song, W.; Yang, J.; Zhu, X.; Dai, J.; Enhanced Multiferroicity and Narrow Band Gap in B-site Co-Doped Aurivillius $Bi_5FeTi_3O_{15}$. *Ceram. Int.* **2019**, *45*, 137–143.

45. Li, W.; Ding, X.; Wu, H.; Yang, H.; $Bi_2Mo_xW_{1-x}O_6$ Solid Solutions with Tunable Band Structure and Enhanced Visible-Light Photocatalytic Activities. *Appl. Surf. Sci.* **2018**, *447*, 636–647.

46. Fu, H.; Pan, C.; Yao, W.; Zhu, Y. Visible-Light-Induced Degradation of Rhodamine B by Nanosized Bi_2WO_6. *J. Phys. Chem. B.* **2005**, *109*, 22432-22439.

47. Kumar, S.; Surendar, T.; Baruah, A.; Shanker, V. Synthesis of a Novel and Stable g-C_3N_4–Ag_3PO_4 Hybrid Nanocomposite Photocatalyst and Study of the Photocatalytic Activity under Visible Light Irradiation. *J. Mater. Chem. A* **2013**, 1, 5333-5340.

48. Pan, L.; Zou, J.J.; Liu, X. Y.; Liu, X. J.; Wang, S.; Zhang, X.; Wang, L. Visible−Light−Induced Photodegradation of Rhodamine B over Hierarchical TiO_2: Effects of

Storage Period and Water-Mediated Adsorption Switch. *Ind. Eng. Chem. Res.* **2012**, *51*, 12782-12786.

CHAPTER -6

Intercalative Removal of Congo Red Dye Employing Layered Dion Jacobson Perovskite

Intercalative Removal of Congo Red Employing a Layered Dion-Jacobson Perovskite

6.1 INTRODUCTION

As discussed in earlier chapters, removal of organic pollutants especially dyes are indispensable for the environmental remediation and effluent treatment purposes. Due to improper treatment of many industrial effluents such as textile, cosmetic, leather, printing and dying etc. a large amount of untreated dyes are released, while even a low concentration of these is highly toxic. Most of the dyes are organic compounds with very high chemical stability and are toxic to both aquatic organism and humans. There are various physical, chemical and biological techniques such as flocculation, membrane filtration, chemical oxidation and adsorption that are used for treatment purposes. However, adsorption is one of the most effective and useful process for removal of dyes from the aqueous solution but, it is also energy and cost intensive.[1-4]

Congo red [1-napthalenesulfonic acid, 3, 3-(4, 4-biphenylene bis (azo) bis (4-amino) disodium salt] is a benzidine based anionic diazo dye. This is known as carcinogenic and mutagenic to humans, and its exposure creates allergic problems.[5] Congo red have been chosen as a modal dye because of its limited biodegradability, complex chemical structure and high solubility in aqueous solution. The discharge of Congo red is also harmful for environment especially for the aquatic organisms.

The adaptability of the layered perovskite structure to intercalation,[6,7] and ion exchange[8-11] is well known in the solid state and material chemistry literature. In addition, the perovskite and layered perovskite like structures exhibit a wide range of other chemical and physical properties, such as, electronic/protonic-conductivity,[12] superconductivity,[13] photoluminescence,[14] dielectric behavior,[15] and photocatalytic properties.[16] Among the layered perovskites R-P phases, $A_2[A_{n-1}B_nO_{3n+1}]$, and D-J phases, $A[A_{n-1}B_nO_{3n+1}]$, are susceptible to intercalation. One of the essential features of the layered perovskite compound is the existence of negatively charged layers that stack to form a 2D structure while the positively charged cation is interleaved within the layers.[17] Figure 6.1 shows the structure of a typical member of the three-layer D-J phase, $KCa_2Nb_3O_{10}$.

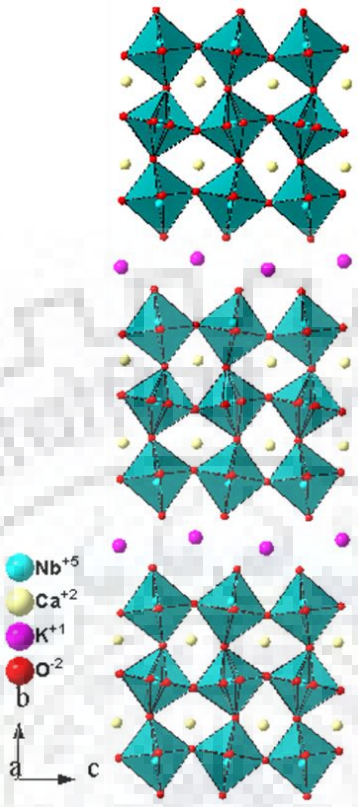

Figure 6.1 Crystal structure of $KCa_2Nb_3O_{10}$.

The rich interlayer chemistry of the D-J and R-P phases have attracted adequate attention. These layered perovskites show ion exchange and intercalation reactions via soft chemical topotactic reactions while the topological features of the reactants is retained in the products. Most of the layered compounds can be intercalated by alkali metals,[18] metal hydroxide, metal halides,[19, 20]chalcogenides,[21, 22] nanoparticles[23] and organic cations / molecules such as amines,[24-27] by replacing the interlayer cations in aqueous solution. The intercalation reaction is possible through various mechanisms such as ion-dipole interactions, hydrogen bonding and acid base reactions.[28,29] Tong *et al.* has reported the intercalation of methylene blue dye into $K_4Nb_6O_{17}$, $KTiNbO_5$, $KLaNb_2O_7$ and $KCa_2Nb_3O_{10}$ by a two-step guest-guest exchange method and studied the electrochemical properties.[30-34] The intercalation processes have been widely investigated, however less studies have focused on the deintercalation processes i.e. removal of interlayer cation after exchange reaction and conversion of intercalated compound into original layered perovskite.

In previous chapters, the coupled substitution in two layer Aurivillius and A1X1 Sillén-Aurivillius layered perovskites have been reported. The coupled substitution in three layer Dion-Jacobson phase ($KCa_2Nb_3O_{10}$) is also attempted but unfortunately, these were not successful and no single phase compounds with coupled substitution (such as, $KCa_{1.5}Bi_{0.5}Nb_{2.75}M_{0.25}O_{10}$; M = Cr, Mn, Fe) could be prepared. But, the photodegradation of Congo red was studied with the mixed phase $KCa_{1.5}Bi_{0.5}Nb_{2.75}M_{0.25}O_{10}$. During the degradation experiments, it has been observed that the Congo red (CR) dye was completely removed from the aqueous solution within 5-20 min of stirring with $KCa_2Nb_3O_{10}$ in the dark. In the present work, the removal of CR in the presence of $KCa_2Nb_3O_{10}$ in dark condition have been investigated in detail. It is found that the CR undergoes intercalation into the protonated form of the layered perovskite under acidic pH and is released back into the solution by a deintercalative mechanism in the alkaline pH. The observed peak shift at lower angles in the P-XRD pattern after intercalation, and the reserve after deintercalation/release supports the above mechanism. The intercalated and deintercalated forms of $KCa_2Nb_3O_{10}$ is further characterized by FT-IR, FE-SEM, EDS, and Raman techniques. The details are presented in the subsequent sections.

6.2 EXPERIMENTAL SECTION

6.2.1 Materials and Synthesis

$KCa_2Nb_3O_{10}$ was synthesized by a solid state reaction as reported in the literature.[35] A stoichiometric mixture of K_2CO_3 (SRL, 99%) $CaCO_3$ (Sigma Aldrich, 99.6%) and Nb_2O_5 (Sigma Aldrich, 99.6%) was ground and calcined at 800ºC for 12h. Subsequently, with the addition of 20 mole % extra K_2CO_3, the mixture was reground and fired again at 1100ºC for 24h.

6.2.2 Removal Test of Congo Red

Adsorption studies were carried out for determination of the amount of dye molecule adsorbed over the solid catalyst at pH 2. For this purpose, 100 mg of catalyst was dispersed in 100 ml of 1×10^{-5} M solution of dye and stirred in the dark for 20 min. During the stirring in the dark, 5 ml solution are withdrawn at after a regular intervals, centrifuged for 2 min to

remove the catalyst particles and the absorbance of the centrifugate is recorded. For the removal of dye in a cycle, the catalyst used in the first cycle was washed with deionized water for several times and adsorption experiments were carried out with fresh dye solution under the same experimental condition as mentioned above.

6.3 RESULTS AND DISCUSSION

6.3.1 P-XRD Analysis

In Figure 6.2, the P-XRD pattern of $KCa_2Nb_3O_{10}$ is shown and all the diffraction peaks are well matched with the orthorhombic structure (JCPDS PDF No.32.1294) with the space group *Cmcm* as reported in the literature.[35]

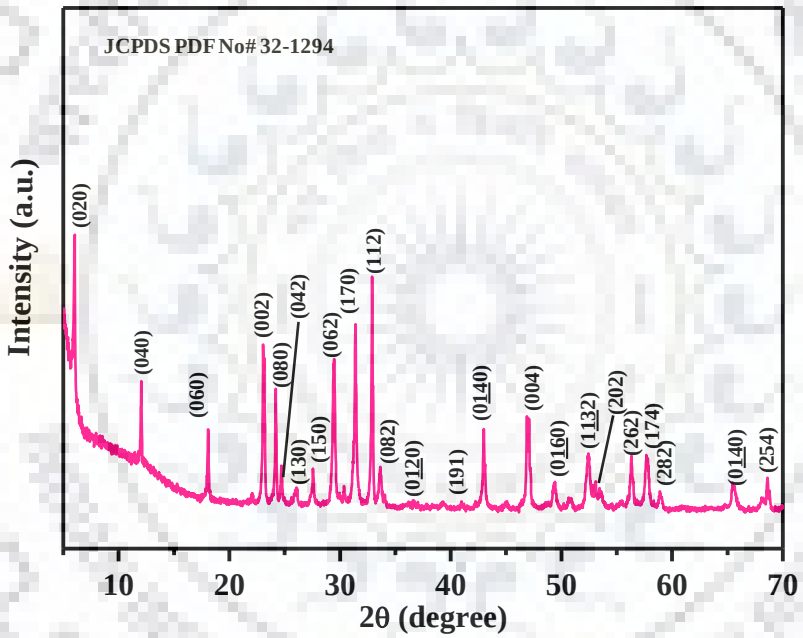

Figure 6.2 P-XRD patterns of $KCa_2Nb_3O_{10}$.

6.3.2 FE-SEM and EDS Analysis

The morphology of the samples was characterized by FE-SEM and is shown in Figure 6.3. The SEM images show plate-like morphology, often seen and expected in the layered type of oxides. Figure 6.3 (b) shows the EDS data and corresponding SEM image of the regions where the elemental compositions of the sample are determined.

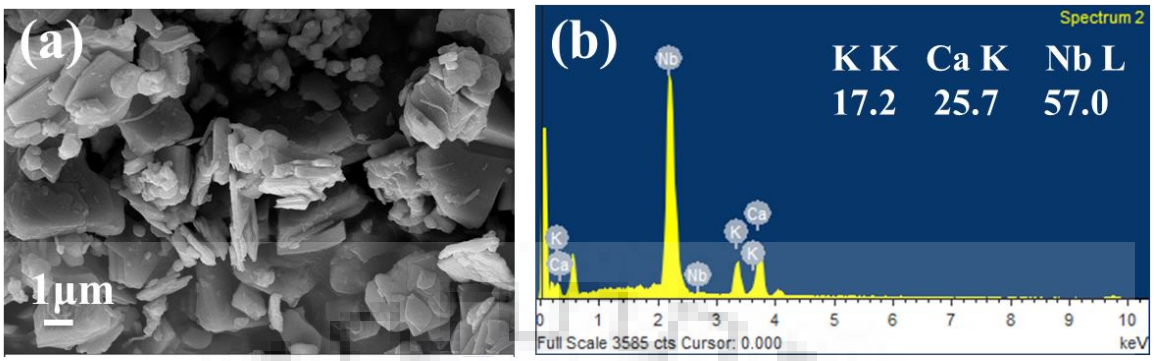

Figure 6.3 (a) SEM image and (b) EDS data of $KCa_2Nb_3O_{10}$.

6.3.3 Adsorption Test

The adsorption studies were carried out with Congo red in the acidic medium at pH 2 over the solid catalyst, $KCa_2Nb_3O_{10}$, in the dark. The absorption peak of Congo red gradually decreased with time and completely vanished within about 20 min indicating complete removal of the dye (Figure 6.4 a). The reusability of the catalysts (Figure 6.4 b) is evaluated by performing four consecutive cycles of Congo red removal over $KCa_2Nb_3O_{10}$ in the dark. The results suggest no noticeable activity loss over the cycles and up to the 4^{th} cycle.

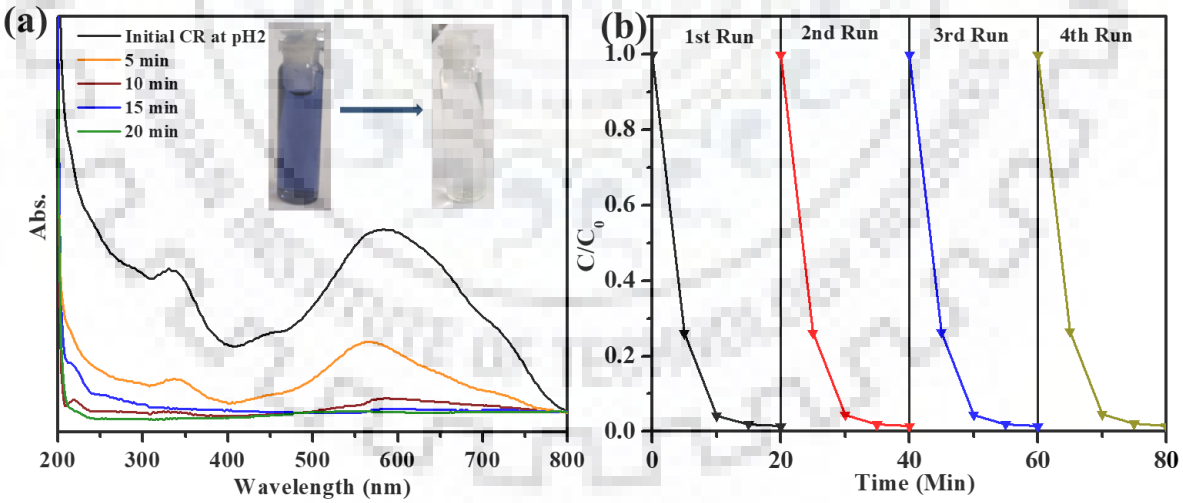

Figure 6.4 (a) UV-vis absorption spectra of Congo red as a function of time during adsorption study with $KCa_2Nb_3O_{10}$. (b) Time profiles of adsorptive cycles with $KCa_2Nb_3O_{10}$ in the dark.

The blue color of CR at pH 2 turned colorless in the presence of $KCa_2Nb_3O_{10}$, while the color of the catalyst ($KCa_2Nb_3O_{10}$) changed from white to dark blue after removal of the Congo red, favoring the hypothesis of adsorption/absorption of Congo red molecules on/by the catalysts. As this happened in the dark, the removal process is initially thought to occur by adsorptive mechanism. Afterwards, the catalyst was washed with water and dispersed in the alkaline aqueous solution. The color of the alkaline solution was converted into orange, which is the color (orange) of Congo red dye in the alkaline medium. Subsequently, the color of the catalyst was converted from dark blue violet to the light color, indicating desorption/release of the dye from the catalyst to the solution. To understand the change in the compound after removal of Congo red from the solution and its release into the solution, P-XRD patterns were recorded (Figure 6.5). Although the P-XRD patterns looked very similar, a slight shift in 2θ is observed in the diffraction peaks to lower angle after the adsorption/absorption of the dye.

A closer look at the refined lattice parameters of $KCa_2Nb_3O_{10}$ (Table 6.1) after adsorption of dye shows slight increase in the '*b*' parameter from 29.37 Å to 30.73 Å, while *a* and *c* remain almost unchanged. The difference in the '*b*' lattice parameter was about 1.35 Å. This expansion in the *b*-parameter is attributed to the intercalation of the dye molecule in interlayer space of the layered perovskite, $KCa_2Nb_3O_{10}$. However, after desorption of the dye, the lattice parameter again changed toward that of the original catalyst. Moreover, the initial increase of the *b*-lattice parameter when the adsorption occur and decrease after desorption of dye, supports the intercalative removal or deintercalative release of the dye molecule. For the confirmation of the intercalation or deintercalation, further experiments, with FE-SEM, FT-IR, and Raman were performed.

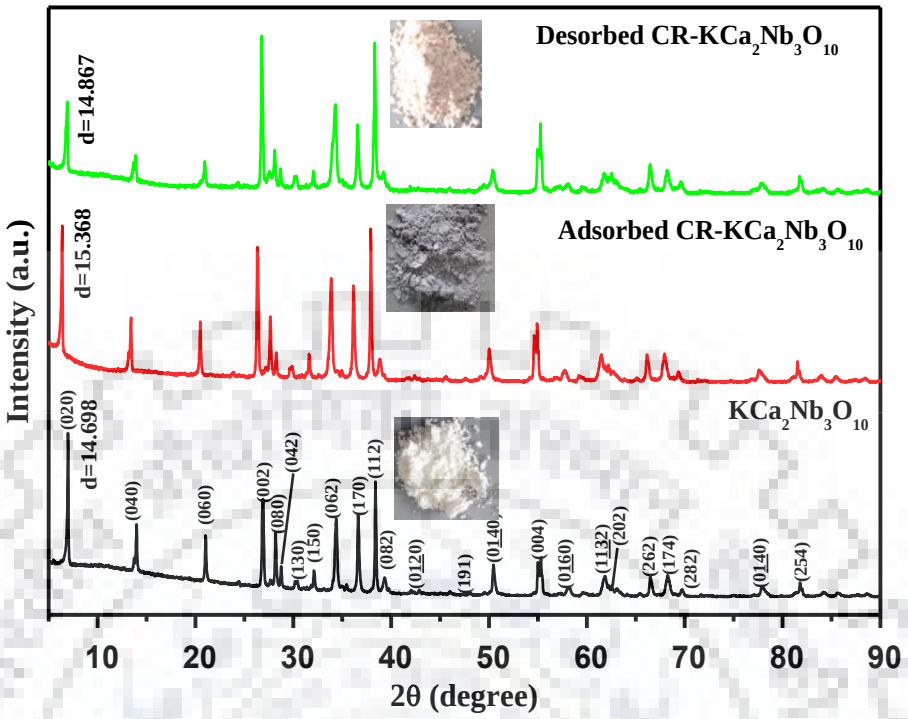

Figure 6.5 P-XRD patterns of (a) $KCa_2Nb_3O_{10}$ (pristine) (b) CR-adsorbed $KCa_2Nb_3O_{10}$, and (c) CR-desorbed $KCa_2Nb_3O_{10}$. The corresponding photographs of the compounds are also shown.

Table 6.1 Refined Lattice Parameters for $KCa_2Nb_3O_{10}$.

Compound	Lattice parameters		
	a	***b***	***c***
$KCa_2Nb_3O_{10}$ (Pristine)	3.876(1)	29.37(1)	7.705(1)
CR- Intercalated $KCa_2Nb_3O_{10}$	3.889(1)	30.73(1)	7.713(1)
CR-Deintercalated $KCa_2Nb_3O_{10}$	3.873(1)	29.47(2)	7.727(1)

Table 6.2 Indexed P-XRD Data for Pristine $KCa_2Nb_3O_{10}$.

h k l	d_{obs}(Å)	d_{calc} (Å)	I_{obs}
0 2 0	14.698	14.687	91
0 4 0	7.349	7.343	33
0 6 0	4.898	4.895	32
0 0 2	3.853	3.852	87
0 8 0	3.674	3.671	47
1 3 0	3.601	3.603	11
0 4 2	3.411	3.411	19
1 5 0	3.235	3.234	20
0 6 2	3.026	3.027	100
0 10 0	2.938	2.937	4
1 7 0	2.847	2.846	82
1 1 2	2.721	2.720	85
0 8 2	2.657	2.658	20
1 5 2	2.475	2.477	2
1 9 1	2.375	2.374	4
1 7 2	2.288	2.289	4
0 14 0	2.098	2.098	38
2 0 0	1.937	1.937	39
0 0 4	1.926	1.926	45
2 4 0	1.873	1.873	15
1 13 2	1.740	1.741	41
2 0 2	1.732	1.730	22
0 14 4	1.422	1.419	19
2 0 4	1.366	1.366	23

a = 3.876(1), b = 29.37(1), c = 7.705(1) Å.

Table 6.3 Indexed P-XRD Data for CR-Intercalated $KCa_2Nb_3O_{10}$.

h k l	d_{obs} (Å)	d_{calc} (Å)	I_{obs}
0 2 0	15.360	15.365	65
0 4 0	7.679	7.682	30
0 6 0	5.123	5.121	32
0 0 2	3.857	3.863	80
0 8 0	3.842	3.841	37
1 3 0	3.636	3.635	7
0 4 2	3.447	3.446	11
1 5 0	3.286	3.286	16
0 6 2	3.081	3.080	100
0 10 0	2.961	2.961	3
1 7 0	2.911	2.911	70
1 1 2	2.727	2.727	80
0 8 2	2.699	2.699	13
1 9 1	2.439	2.440	3
1 7 2	2.291	2.291	2
0 14 0	2.114	2.114	30
2 0 0	1.945	1.947	37
0 0 4	1.935	1.935	50
2 4 0	1.884	1.884	3
1 13 2	1.791	1.791	7
2 6 2	1.638	1.638	25
0 14 4	1.432	1.432	15
2 0 4	1.369	1.369	12

a = 3.889(1), b = 30.73(1), c = 7.731(1) Å.

Table 6.4 Indexed P-XRD Data for CR-Deintercalated $KCa_2Nb_3O_{10}$.

h k l	d_{obs} (Å)	d_{calc} (Å)	I_{obs}
0 2 0	14.867	14.739	46
0 4 0	7.370	7.369	20
0 6 0	4.917	4.913	20
0 0 2	3.862	3.863	79
0 8 0	3.684	3.684	25
1 3 0	3.609	3.603	7
0 4 2	3.428	3.421	11
1 5 0	3.241	3.237	10
0 6 2	3.033	3.033	100
0 10 0	2.945	2.945	2
1 7 0	2.850	2.850	50
1 1 2	2.725	2.723	76
0 8 2	2.665	2.666	13
1 9 1	2.500	2.501	13
1 7 2	2.291	2.291	2
0 14 0	2.102	2.103	20
2 0 0	1.938	1.937	45
0 0 4	1.928	1.928	65
2 4 0	1.843	1.843	7
1 13 2	1.741	1.741	16
2 6 2	1.631	1.632	25
0 14 4	1.422	1.419	15
2 0 4	1.366	1.366	20

a = 3.873(1), b = 29.47(2), c = 14.727(1) Å.

6.3.3.1 Post Adsorptive FE-SEM and EDS Analysis

The SEM images and EDS data of the CR-intercalated and CR-deintercalated $KCa_2Nb_3O_{10}$ are shown in Figure 6.6. Both the CR-intercalated and deintercalated $KCa_2Nb_3O_{10}$ compounds retain the plate like morphology. The elemental ratios as obtained from EDS analyses, reveals that the potassium content is less in the CR-intercalated and deintercalated compound as compared to that of the parent. Around 35-40 % of potassium is exchanged during the dye removal process. This may be attributed the proton exchange of the D-J phase, as they are well known for their proton exchange ability in the acidic medium.

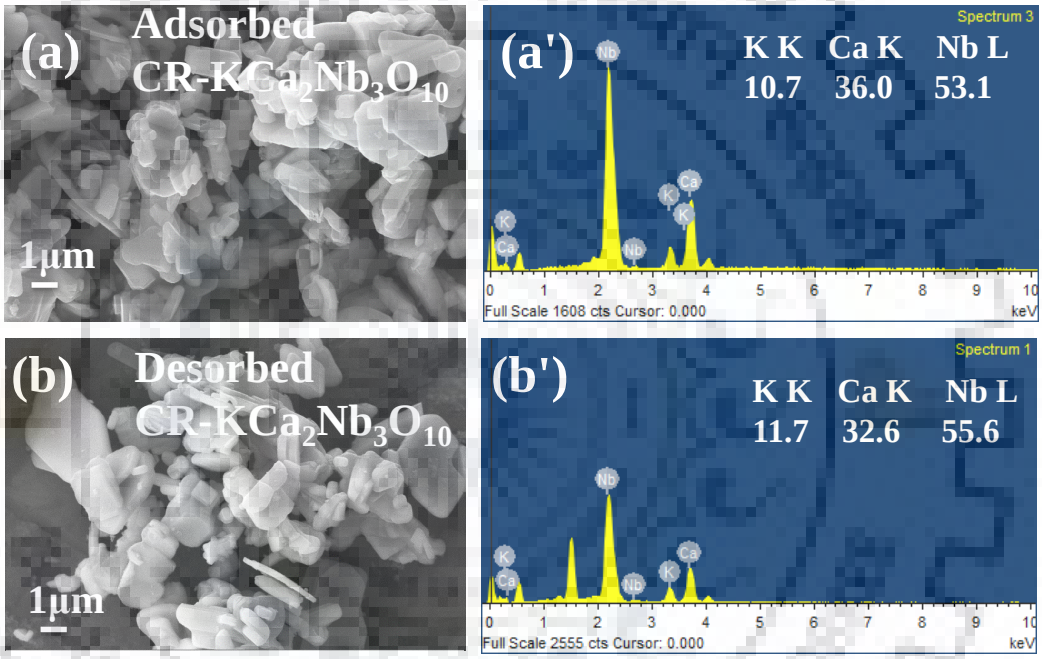

Figure 6.6 SEM and EDS data for CR-adsorbed CR- $KCa_2Nb_3O_{10}$ (a & a') and CR-desorbed $KCa_2Nb_3O_{10}$ (b & b').

6.3.3.2 Post Adsorptive FT-IR Analysis

Since, FTIR is a technique for qualitative identification of the functional groups of organic molecules, to further confirm the intercalation of the dye in $KCa_2Nb_3O_{10}$, FT-IR is employed to monitor the removal and release process of the dye. The IR spectra (Figure 6.7) of the dye intercalated compound shows some absorption peaks of Congo along with the $KCa_2Nb_3O_{10}$ peaks, as identified in the spectra. The absorption peaks at 937, 771, and 589 cm^{-1} are identified as for the stretching vibrations of $Nb–O_{terminal}$ group, asymmetric stretching

vibration of Nb–O_{bridge} in the terminal NbO_6 octahedron and asymmetric stretching vibration of Nb–O_{bridge} of the central NbO_6 octahedron.[36] Figure 6.7 also compares the characteristic absorption peak of CR corresponding to 3468 cm^{-1} for the N-H stretching of 1º amine, 1223, 1190 and 1053 cm^{-1} for the RSO^{3-} stretching and 698 cm^{-1} for the C-C bending vibration. The C-H stretching of di-substituted aromatic compound is seen at 698 cm^{-1} and 1440 cm^{-1} for the C=C stretching of the aromatic rings present in the CR as well as in the intercalated compound. The new signals detected at 1380 and 1384 cm^{-1} and sharp peak at 1616 cm^{-1} in the intercalated compound, reveals the presence of benzene ring skeletal. However, the IR-spectra shows only compound peaks after the deintercalation of the dye from $KCa_2Nb_3O_{10}$. This is supportive of near complete release of the Congo red from the interlayer space of the layered perovskite.

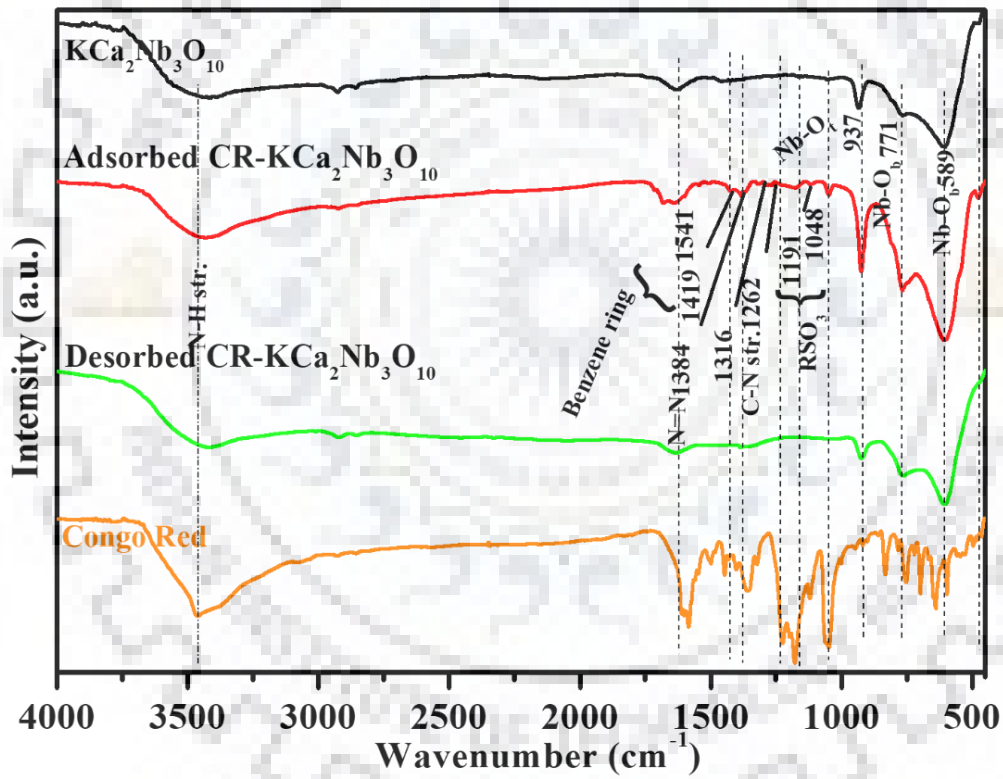

Figure 6.7 FT-IR spectra of the samples of $KCa_2Nb_3O_{10}$, CR-adsorbed $KCa_2Nb_3O_{10}$, and CR-desorbed $KCa_2Nb_3O_{10}$ and Congo Red.

6.3.3.3 Post Adsorptive Raman Analysis

Raman spectra of $KCa_2Nb_3O_{10}$ and CR-intercalated $KCa_2Nb_3O_{10}$ are shown in Figure 6.8. The characteristic Raman bands of $KCa_2Nb_3O_{10}$ are positioned at 248, 578, 761, and 935

cm^{-1}. The bands around 935, 761 and 578 cm^{-1} are assigned for the symmetric stretching vibration and asymmetric stretching vibration of Nb-O in NbO_6 octahedra, respectively.[37,38] The Raman spectra of CR-intercalated $KCa_2Nb_3O_{10}$ differ from that of the solid Congo red dye (reported in the literature).[39] All the bands of the host compounds are suppressed in the intercalated compound. The disappearance of the band at 254 cm^{-1} indicates removal of K^+ due to ion exchange during dye removal. The characteristic bands of Congo red present at 1113 cm^{-1} for SO^{3-} group, 1160 cm^{-1} for (C-N=), 1277 cm^{-1} for (C-H), 1380 cm^{-1} for (N=N), 1463 cm^{-1} for (C=C) and 1595 cm^{-1} for (C-C, aromatic ring) are observed in the intercalated compound.[39] The CR-intercalated compound have shown some additional bands, for example, the bands at 1182, 1319 and 1570 cm^{-1} indicate the asymmetric stretching of the (N-N), (C-NH_2) and (C=N-) groups, respectively, for developing the hydrazone structure. The intensity of the band at 1160 cm^{-1} for (C-N=) decreases and the band at 1295 cm^{-1} appears indicating the presence of biphenyl group. These bands are indicative of the emergence of the azo-hydrazone tautomer.

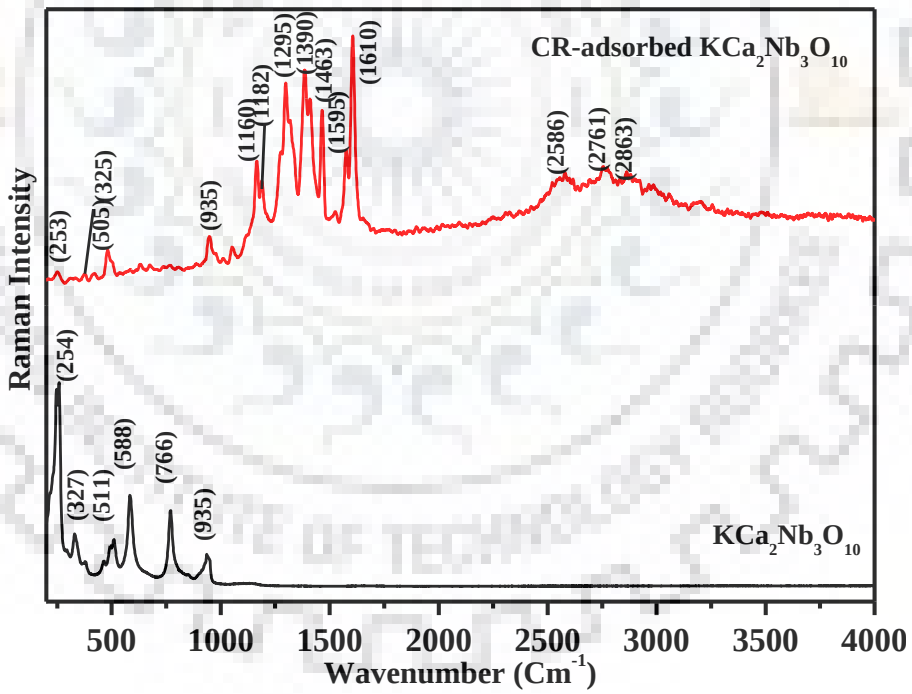

Figure 6.8 Raman spectra of the samples of $KCa_2Nb_3O_{10}$ and CR-adsorbed $KCa_2Nb_3O_{10}$.

Based on the P-XRD, FT-IR and Raman studies, the intercalation/deintercalation of dye molecule in the interlayer space of the layered perovskite, $KCa_2Nb_3O_{10}$ is proposed. As presented earlier (Figure 6.1), the structure of $KCa_2Nb_3O_{10}$ has three octahedral thick

perovskite slab, $[Ca_2Nb_3O_{10}]^-$ stacked one over the other and the K^+ ion occupy the interlayer space. The adjacent perovskite slabs are stacked along the *b*-axis with a displacement vector of a/2. The interlayer alkali metals are easily exchangeable with other metals (monovalent or divalent) and organic cation/molecules including protons. The reversible intercalation/deintercalation reactions are governed by the acid–based exchange reactions. It is well known that the Congo red dye (Figure 6.9) is a dipolar molecule that exists as cationic and anionic form in the acidic and basic medium, respectively.[40] The anionic Congo red shows red color in the basic aqueous medium, while the red color converts into dark blue in the acidic medium. It is understand that in the acidic medium the dye is protonated. Moreover, based on the results found in Raman and FT-IR analysis, the interaction of the dye with the layered perovskite has occurred through an acid-base complexation between the amine group and the proton exchanged layered $KCa_2Nb_3O_{10}$. Moreover, it is found by EDS that about ~ 40 % of dye molecule were intercalated in the interlayer space. Accordingly, an acid-base complexation between the protons of the in-situ formed proton-exchanged layered perovskite and the amine group of the CR is attributed for the intercalative removal of the dye from the aqueous medium. In the basic medium, a strong complexation of the proton with the basic OH^- frees the amine groups of the dye, which leads to the release of the CR molecules from the interlayer space of the layered perovskite. The three models (Figure 6.10) of intercalation can be proposed based on the possibilities of intercalation based on the molecular dimension (2.5 nm × 0.7 nm × 0.27 nm) of the Congo red. Since, the lattice parameter has shown an expansion perpendicular to the layer direction by about 1.35 Å, therefore, dye can only intercalate through in a lying position.

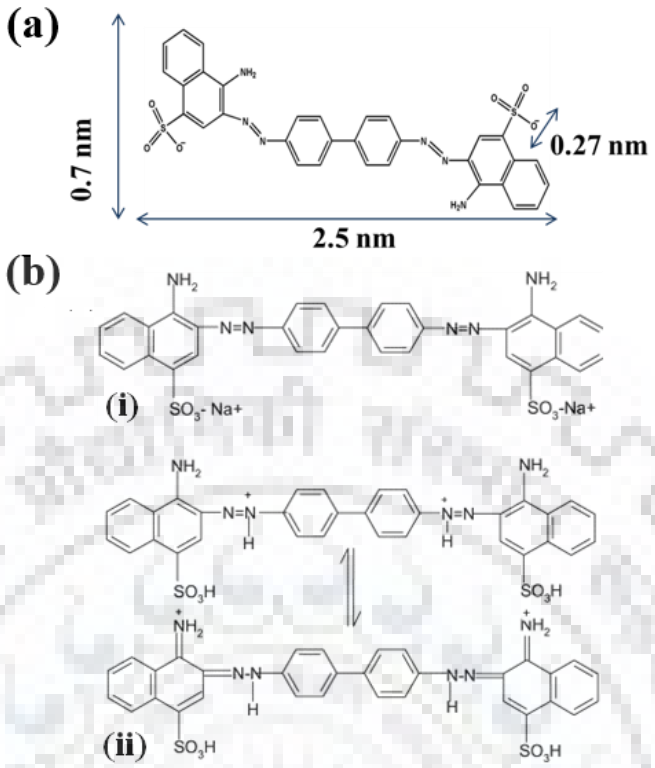

Figure 6.9 (a) Chemical structure of Congo red. (b) Structural forms of Congo red in (i) basic pH and (ii) acidic pH.

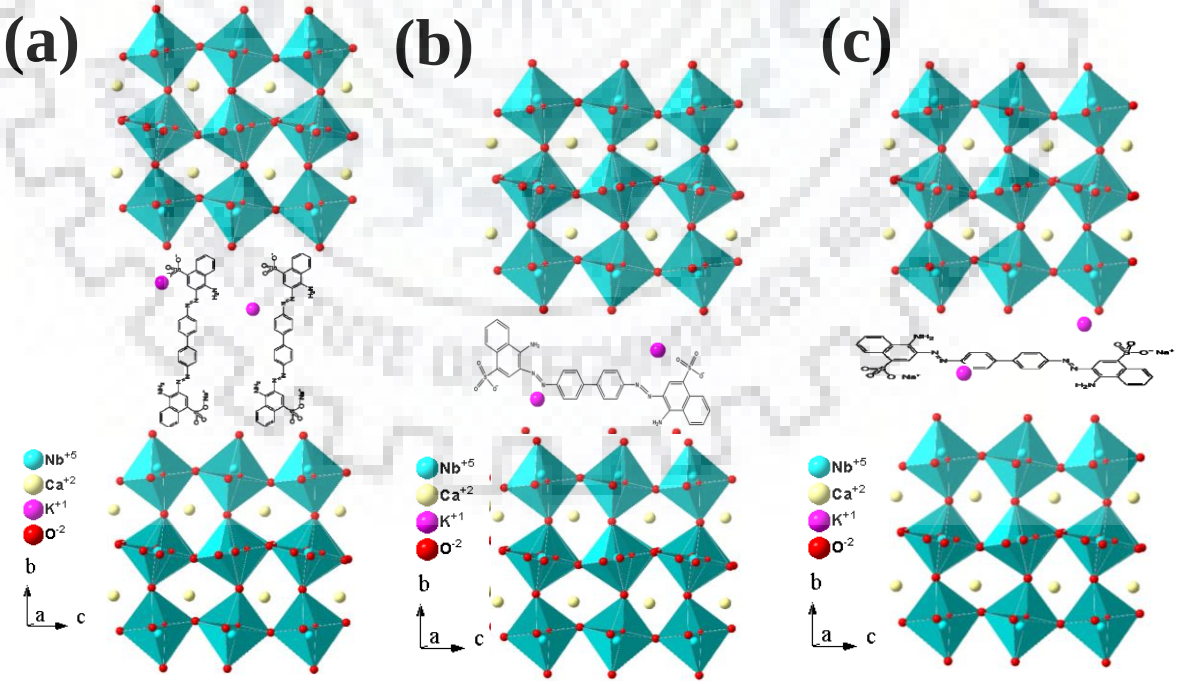

Figure 6.10 The proposed models of intercalation of CR dye in $KCa_2Nb_3O_{10}$.

There are reports of the intercalation of dye or organic compound in a two-step process.[32-34] Initially, the proton exchange reaction is carried out in a first step followed by the intercalation of the organic compound in a second step.[37] Therefore, for the confirmation of in-situ intercalation, the proton exchange and intercalation have been carried out in a two-step process. From P-XRD (Figure 6.11), it is observed that an exchange of K^+ with H^+ causes the (0k0) peaks to move to the higher angles. After the intercalation of the dye, characteristic diffraction peaks shift to the lower angle and the difference in d_{020} is about ~ 1.2 Å. In the two-step process, also a similar expansion in the interlayer space is observed.

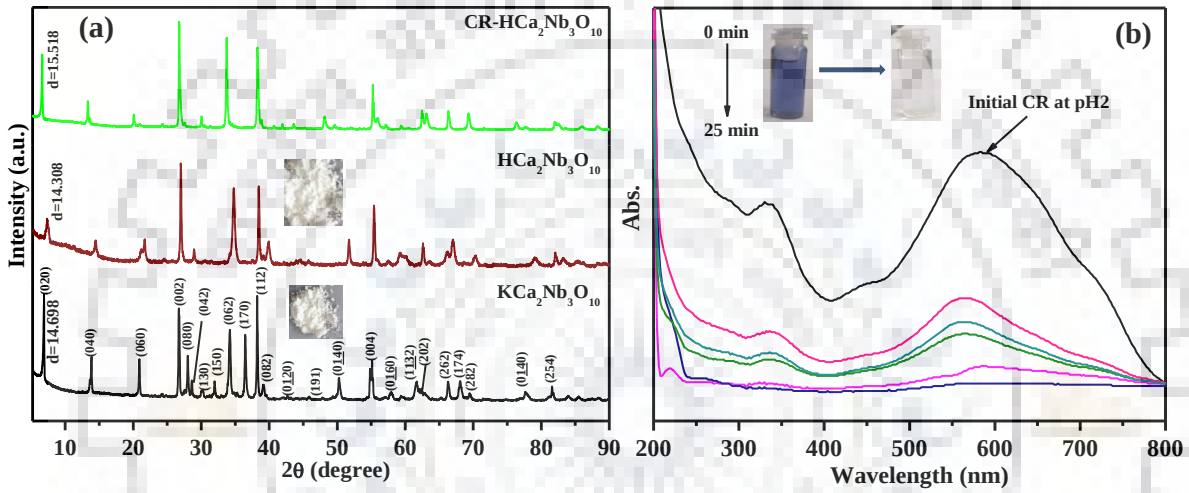

Figure 6.11 (a) P-XRD patterns of $KCa_2Nb_3O_{10}$, $HCa_2Nb_3O_{10}$, and CR- $KCa_2Nb_3O_{10}$. (b) UV-vis absorption spectra of Congo red as a function of absorption time for $HCa_2Nb_3O_{10}$.

In summary, intercalative removal and deintercalative release of Congo red dye with a three layer Dion-Jacobson phase is demonstrated. The compound, $KCa_2Nb_3O_{10}$ shows excellent removal of Congo red dye at pH 2. The removal experiment have revealed the intercalation of the dye in the interlayer space of the layered perovskite with the expansion of the lattice along the *b*-axis. In FT-IR and Raman, the compound shows characteristic peaks of the dye after the intercalation. EDS data also reveal the proton exchange in $KCa_2Nb_3O_{10}$ upto ~ 35-40 % during the dye removal process. The intercalation reactions is proposed to be directed in aqueous acidic medium by the acid–based complexation between the protons of the in-situ proton exchanged layer perovskite and the amine group of the dye. In the basic medium, the deintercalation of the dye from the interlayer space is driven by the strong complexation of the proton with the basic OH groups that frees the amine groups of the dye. The intercalation

carried out with the protonated form of the compound in a two-step process also results in similar outcome as the removal in the acidic media with the pristine layered perovskite.

REFERENCES

1. Forgacs, E.; Cserhati, T.; Oros, G. Removal of Synthetic Dyes from Wastewaters: a Review. *Environ. Int*. **2004**, *30*, 953 – 971.

2. Slokar, Y. M.; Marechal, A. M. L. Methods of Decoloration of Textile Wastewaters. *Dyes and Pigments* **1998**, *37*, 335–356.

3. Holkar, R. C.; Jadhav, A. J.; Pinjari, D. V.; Mahamuni, N. M.; Pandit, A. B.; A Critical Review on Textile Wastewater Treatments: Possible Approaches. *J. Environ. Manage*. **2016**, *182*, 351–366.

4. Ahmaruzzaman, M. Role of Fly Ash in the Removal of Organic Pollutants from Wastewater. *Energy & Fuels* **2009**, *23*, 1494–1511.

5. Ghorai, S.; Sarkar, A. K.; Panda A. B.; Pal, S. Effective Removal of Congo red Dye from Aqueous Solution using Modified Xanthan Gum/Silica Hybrid Nanocomposite as Adsorbent. *Bioresour. Technol.* **2013**,*144*, 485–491.

6. Takahashi, S.; Nakato, T.; Hayashi, S.; Sugahara, Y.; Kuroda, K. Formation of a Methoxy-Modified Interlayer Surface via the Reaction between Methanol and Layered Perovskite $HLaNb_2O_7.xH_2O$. *Inorg. Chem*. **1995**, *34*, 5065–5069.

7. Hata, H.; Kubo, S.; Kobayashi, Y.; Mallouk, T. E. Intercalation of Well-Dispersed Gold Nanoparticles into Layered Oxide Nanosheets through Intercalation of a Polyamine. *J. Am. Chem. Soc*. **2007**, *129*, 3064–3065.

8. Gopalakrishnan, J.; Bhat, V.; Raveau, B. $A^ILaNb_2O_7$: A New Series of Layered Perovskites Exhibiting Ion Exchange and Intercalation Behaviour. *Mater. Res. Bull*. **1987**, *22*, 413–417.

9. Uma, S.; Raju, A. R.; Gopalakrishnan, J. Bridging the Ruddlesden-Popper and the Dion-Jacobson Series of Layered Perovskites: Synthesis of Layered Oxides, $A_{2-x}La_2Ti_{3-x}Nb_xO_{10}$ (A = K, Rb), exhibiting Ion Exchange. *J. Mater. Chem*. **1993**, *3*, 709–713

10. Pratt, J. A.; Shepherd, A. M.; Hayward, M. A. Diamagnetic Ru^{2+} in $Na_2La_2Ti_2RuO_{10-x}$ ($0 < x < 2$): A Series of Complex Oxides Prepared by Topochemical Reduction. *Inorg. Chem*.

2015, *54*, 10993−10997.

11. Gustin, L.; Hosaka, Y.; Tassel, C.; Aharen, T.; Shimakawa, Y.; Kageyama, H.; Wiley. J. B. From Tetrahedral to Octahedral Iron Coordination: Layer Compression in Topochemically Prepared $FeLa_2Ti_3O_{10}$. *Inorg. Chem.* **2016**, *55*, 11529−11537.

12. Kobayashi, Y.; Schottenfeld, J. A.; Macdonald, D. D.; Mallouk, T. E. Structural Effects in the Protonic/Electronic Conductivity of Dion-Jacobson Phase Niobate and Tantalate Layered Perovskites. *J. Phys. Chem. C* **2007**, *111*, 3185–3191.

13. Fukuoka, H.; Isami, T.; Yamanaka, S. Superconductivity of Alkali Metal Intercalated Niobate with a Layered Perovskite Structure. *Chem. Lett*. **1997**, *8*, 703–704.

14. Ida, S.; Ogata, C.; Eguchi, M.; Youngblood, W. J.; Mallouk, T. E.; Matsumoto, Y. Photoluminescence of Perovskite Nanosheets Prepared by Exfoliation of Layered Oxides, $K_2Ln_2Ti_3O_{10}$, $KLnNb_2O_7$, and $RbLnTa_2O_7$ (Ln: Lanthanide Ion). *J. Am. Chem. Soc*. **2008**, *130*, 7052–7059.

15. Fang, M.; Kim, C. H.; Mallouk, T. E. Dielectric Properties of the Lamellar Niobates and Titanoniobates $AM_2Nb_3O_{10}$ and $ATiNbO_5$ (A = H, K, M = Ca, Pb), and Their Condensation Products $Ca_4Nb_6O_{19}$ and $Ti_2Nb_2O_9$.*Chem. Mater*. **1999**, *11*, 1519–1525.

16. Takata, T.; Furumi, Y.; Shinohara, K.; Tanaka, A.; Hara, M.; Kondo, J. N.; Domen, K. Photocatalytic Decomposition of Water on Spontaneously Hydrated Layered Perovskites. *Chem. Mater*. **1997**, *9*, 1063–1064.

17. Schaak, R. E.; Mallouk, T. E. Perovskites by Design: A Toolbox of Solid-State Reactions *Chem. Mater*. **2002**, *14*, 1455-1471.

18. Didier, C.; Guignard, M.; Suchomel, M. R.; Carlier, D.; Darriet, J.; Delmas, C. Thermally and Electrochemically Driven Topotactical Transformations in Sodium Layered Oxides Na_xVO_2. *Chem. Mater*. **2016**, *28*, 1462–1471.

19. Viciu, L.; Kodenkandath, T. A.; Wiley, J. B. Construction of a Double-Layered Tetrahedral Network within a Perovskite Host: Two-step Route to the Alkali-Metal-Halide

Layered Perovskite, (Li_xCl)$LaNb_2O_7$. *J. Solid State Chem*. **2007**, *180*, 583–588.

20. Choi, J.; Zhang, X.; Wiley, J. B. Building Alkali-Metal-Halide Layers within a Perovskite Host by Sequential Intercalation: (A_2Cl)$LaNb_2O_7$ (A = Rb, Cs). *Inorg. Chem*. **2009**, *48*, 4811–4816.

21. Montasserasadi, D.; Mohanty, D.; Huq, A.; Heroux, L.; Payzant E. A.; Wiley, J. B. Topochemical Synthesis of Alkali-Metal Hydroxide Layers within Double- and Triple-Layered Perovskites. *Inorg. Chem*. **2014**, *53*, 1773–1778.

22. Ranmohotti, K. G. S.; Montasserasadi, M. D.; Choi, J.; Yao, Y.; Mohanty, D.; Josepha, E. A.; Adireddy, S.; Caruntu G.; Wiley, J. B. Room Temperature Oxidative Intercalation with Chalcogen Hydrides: Two-step Method for the Formation of Alkali-Metal Chalcogenide arrays within Layered Perovskites. *Mater. Res. Bull*. **2012**, *47*, 1289–1294.

23. Hata, H.; Kubo, S.; Kobayashi, Y.; Mallouk, T. E. Intercalation of Well-Dispersed Gold Nanoparticles into Layered Oxide Nanosheets through Intercalation of a Polyamine. *J. Am. Chem. Soc*. **2007**, *129*, 3064–3065.

24. Matsuda, T.; Miyamae N.; Takeuchi, M. Intercalation of Various Alcohols in $HLaNb_2O_7$. *Bull. Chem. Soc. Jpn*. **1993**, *66*, 1551–1553.

25. Wang, Y.; Wang, C. H.; Wang, L. L.; Hao, Q. Y.; Zhu, X. B.; Chen X. H.; Tang, K. B. Preparation of Interlayer Surface Tailored Protonated Double-Layered Perovskite $H_2CaTa_2O_7$ with n-Alcohols, and their Photocatalytic Activity. *RSC Adv*. **2014,** *4*, 4047–4054.

26. Toihara, N.; Yoneyama, Y.; Shimada, A.; Tahara, S.; Sugahara, Y. Intercalation of Triethylphosphine Oxide bearing a Phosphoryl group into Dion–Jacobson-type Ion-Exchangeable Layered Perovskites. *Dalton Trans.* **2015**, *44*, 3002–3008.

27. Tefaghi, S. A.; Veiga, E. T.; Amand, G.; Wiley, J. B. Rapid Topochemical Modification of Layered Perovskites via Microwave Reactions. *Inorg. Chem*. **2016**, *55*, 1604–1612.

28. Jacobson, A. J.; Johnson J. W.; Lewandowski, J. T. Interlayer Chemistry between Thick Transition-Metal Oxide Layers: Synthesis and Intercalation Reactions of $K[Ca_2Na_{n-}$

$_3Nb_nO_{3n+1}$] ($3 \leq n \leq 7$). *Inorg. Chem*. **1985**, *24*, 3727–3729.

29. Treacy, M. M. J.; Rice, S. B.; Jacobson A. J.; Lewandowski, J. T. Electron Microscopy Study of Delamination in Dispersions of the Perovskite-related Layered Phases $K[Ca_2Na_{n-3}Nb_nO_{3n-1}]$: Evidence for Single-Layer Formation. *Chem. Mater*. **1990**, *2*, 279–286.

30. Zhang, X.; Feng, D.; Chen, M.; Ding, Z.; Tong, Z. Preparation and Electrochemical Behavior of Methylene Blue Intercalated into Layered Niobate $K_4Nb_6O_{17}$. *J Mater Sci*. **2009**, ***44***, 3020–3025.

31. Zhang, X.; Liu, C.; Zhang, D.; Zhang, T.; Tong, Z. Intercalation of Methylene Blue into Layered Potassium Titanoniobate $KTiNbO_5$: Characterization and Electrochemical Investigation. *J Mater Sci*. **2010**, *45*, 1604–1609.

32. Shao, F.; Zhuo, M.; Han, G.; Zhang, X.; Liu, L.; Too T.; Tong. Z. Synthesis and Electrochemical Properties Study of Novel Intercalation Compound of $KCa_2Nb_3O_{10}$ with Cationic Methylene Blue. *Micro & Nano letters* **2013**, *8*, 788–791.

33. Zhang, X.; Shen, L.; Wang, M.; Siqin, G.; Tong, Z.; Xu, R.; Zhang, D.; Ma, J.; Liu, L. A Novel Glucose Biosensor Constructed by Glucose Oxidase Immobilized with Methylene Blue Intercalated Layered Lanthanum Niobic Acid Nanocomposite. *Mater. Lett.* **2014**, *135*, 39–42.

34. Ma, J.; Zhang, Z.; yang, M.; Wu, Y.; Feng, X.; Liu, L.; Zhang, X.; Tong, Z. Intercalated Methylene Blue between Calcium Niobate Nanosheets by ESD Technique for Electrocatalytic Oxidation of Ascorbic Acid. *Microporous and Mesopourous Mater*. **2016**, *221*, 123–127.

35. Igarashi, S.; Sato, S.; Takashima, T.; Ogawa, M. Preparation of Finite Particles of Layered Niobate ($KCa_2Nb_3O_{10}$) for Improved Materials Performance. *Ind. Eng. Chem. Res.* **2013**, *52*, 3329–3333.

36. Chen, Y.; Zhao, X.; Mac, H.; Ma, S.; Huang, G.; Makita, Y.; Bai, X.; Yang, X. Structure and Dehydration of Layered Perovskite Niobate with Bilayer Hydrates Prepared by Exfoliation/Self-assembly Process. *J. Solid State Chem.* **2008**, *181*, 1684–1694.

37. Sun, C.; Peng, P.; Zhu, L.; Zheng, W.; Zhao, Y. Designed Reversible Alkylamine Intercalation–Deintercalation in the Layered Perovskite-Type Oxide $KCa_2Nb_3O_{10}$. *Eur. J. Inorg. Chem.* **2008,** 3864–3870.

38. Zhong, Z.; Ding, W.; Chen, Y. The Ferroelectricity of Perovskite-type Oxides with Alkylamine Interlayer. *Appl. Phys. Lett*. **1999**, *75*, 1958–1960.

39. de Souza M. L.; Tristão, D. C.; Corio, P. Vibrational Study of Adsorption of Congo red onto TiO_2 and the LSPR effect on its Photocatalytic Degradation Process. *RSC Adv*. **2014**, *4*, 23351–23358.

40. Purkait, M. K.; Maiti, A.; Gupta, S. D.; De, S. Removal of Congo red using Activated Carbon and its Regeneration. *J. Hazard. Mater*. **2007**, *145*, 287-295.

CHAPTER -7

Conclusions and Future Prospects

Conclusions and Future Prospects

Layered perovskites with the Aurivillius, Ruddlesden-Popper (R-P) and Dion-Jacobson (D-J) structures are important class of materials owing to their interesting physicochemical properties that include magnetic, catalytic, photocatalytic, ion exchange, intercalation, Bronsted acidity and so on. While many oxides with the perovskite structure can be stabilized with 3*d*, 4*d* or 5*d* transition metals with d^n electronic configuration, the layered perovskites are mostly composed of d^0 metal cations of Ti, Nb, Ta, Mo or W. Thus, layered perovskites composed of transition metals with d^n electron configuration are rare in the D-J and Aurivillius structure, although a plenty of them exist with the R-P structure.

In connection with the magnetic and visible-light-driven photocatalytic properties, the d^0 metal containing layered niobates, titanates and tungstates are not very useful as they mostly are devoid of unpaired *d* electrons and absorb in the UV region. Research efforts have been devoted toward the devolvement of new layered niobates, titanates and tungstates that can have reduced band gap with visible-light absorption ability and at the same time can exhibit paramagnetism at room temperature, so that the compounds may act as magnetic photocatalysts. While the visible light absorption can help in the sunlight-driven photocatalysis, the magnetic properties can facilitate their post-catalytic magnetic separation from the reaction medium.

In the present investigation, synthesis of new niobates, titanates and tungstates are envisaged with the incorporation of d^n transition metals following a coupled substitution strategy so that transition metals with lower oxidation states can be incorporated with suitable cationic charge compensation. Moreover, considering earlier reports on La-substituted Aurivillius phases, La-substitution is also employed as a strategy in enhancing the photocatalytic activity of the layered perovskite based photocatalysts. Herein, a few series of new layered perovskites with Aurivillius and Sillén-Aurivillius (S-A) structures are synthesized and characterized by an array of advanced analytic technique including P-XRD, FE-SEM, HR-TEM, XPS, UV-Vis DRS, FT-IR, Raman and PL. The compounds are investigated for their photocatalytic activity by way of dye degradation and the magnetic properties are studied with the help of a SQUID magnetometer.

In the first section of the thesis, lead free new double-layer Aurivillius niobates are reported. The compositions, $LaBi_2Nb_{1.5}M_{0.5}O_9$ (M = Cr, Mn, Fe, Co), are designed by a coupled substitution strategy and the compounds are synthesized by the conventional solid-state reaction. Rietveld structure refinements based on P-XRD data of the compounds ascertained their formation in the orthorhombic $A2_1am$ space group, isostructural with the parent $SrBi_2Nb_2O_9$. The compounds exhibit extended visible-light absorption up to ~ 650 nm with band gap ranging from 2.25 - 2.94 eV. Interestingly, all the transition metal ions adopt HS configuration, while the Mn compound stabilize with a LS configuration. This is attributed to the Jahn-Teller (J-T) nature of Mn^{3+} (d^4), where the J-T elongation is suppressed by the dominating second order J-T effect of the Nb ($4d^0$) cations. The observed magnetic moment corroborate very well with the LS configuration. This is also supported by the substantial decrease in the *c*-parameter of the Mn compound. The compounds showed photocatalytic RhB degradation at pH 2 within 50-110 minutes under natural sunlight irradiation and the degradation time reduced to 15-30 min when irradiated with 250 W MP-MVL. The strategy adopted herein is believed to be useful in designing other visible light active magnetic photocatalysts with enhanced sunlight harvesting ability. The other advantage is that the strategy adopted here is lead free and do not use expensive silver, thereby, making them environment friendly and cheaper.

The idea of coupled substitution is extended further for the synthesis of new double-layered Aurivillius titanates. A series of double-layered perovskite titanates, $Bi_{3-x}La_xTi_{1.5}W_{0.5}O_9$ (x = 0, 1) and $Bi_{3-x}La_xTiW_{0.67}Fe_{0.33}O_9$ (x = 0, 1), are prepared by conventional solid-state reactions and their photocatalytic activity are evaluated by dye degradation. The coupled substitution strategy involving Fe, Ti and W in $Bi_{3-x}La_xTi_{1.5}W_{0.5}O_9$ (x = 0, 1) resulted in substantial decrease in the band gap of the compounds (E_g of 2.63 & 2.72 eV from that of ~3.0 eV for the parent $Bi_{3-x}La_xTi_{1.5}W_{0.5}O_9$; x = 0, 1). The Fe-substitution appeared to help in the suppression of the photogenerated e^-–h^+ recombination as evidenced by the PL spectra and as a result enabled complete RhB degradation under sunlight irradiation, while $Bi_{3-x}La_xTi_{1.5}W_{0.5}O_9$ (x = 0, 1) showed only negligible to little RhB degradation in the acidic aqueous medium. To our surprise, the La-substituted compound showed inferior activity as compared to its Bi-analogs. This is in contrary to the results observed in other higher order

layered Aurivillius titanates, where the La-substitution has resulted in an enhanced photocatalytic activity.

Extending the same idea of coupled substitution in a hybrid layered perovskite of the Sillén−Aurivillius A1X1 structure, the layered tungstates, $LaBi_3W_{0.67}M_{0.33}O_8Cl$ (M = Mn, Fe), are synthesized. The compounds, $LaBi_3W_{0.67}M_{0.33}O_8Cl$ (M = Mn, Fe), crystallized in the *Cm2m* space group as adopted by the parent $Bi_4W_{0.67}Mn_{0.33}O_8Cl$, while the refined lattice parameters indicated slight contraction in their *c*-parameter on La substitution. The compounds exhibited paramagnetic behaviour between 5 and 300 K indicating absence of any magnetic phase transitions in the temperature interval, while the UV-vis DRS established the compounds as visible-light-active semiconductors with much lower band gaps (2.11-2.41 eV) as compared to that of the double layered titanates and niobates. The photocatalytic activity studies toward individual RhB and MO and their mixture demonstrated complete to near complete degradation of the dyes in the acidic aqueous medium (pH 2) under natural sunlight irradiation. All the catalysts reported herein are robust and reusable in consecutive cycles of individual or collective RhB and MO degradation in the acidic medium without showing any noticeable loss of activity, as evidenced by the cycle tests and their post catalytic P-XRD and XPS analyses. It is believed that the paramagnetic nature for all the compounds will be helpful in the post catalytic magnetic separation from the solution phase.

While the same strategy in the triple-layered D-J phase, $KCa_2Nb_3O_{10}$, have not been quite successful in the formation of phase pure D-J compounds with nearly 16 % doping of transition metals at the Nb-site, in the course of this investigation, a rapid removal of Congo red dye was observed with the pristine $KCa_2Nb_3O_{10}$. Detail investigation of the removal process of CR revealed intercalation of CR in the interlayer space of the layered perovskite with concomitant expansion of the lattice along the *c*-axis and the process is nearly reversible as demonstrated by the de-intercalative release of the CR dye in the alkaline aqueous medium. Analysis of $KCa_2Nb_3O_{10}$ before and after CR removal by P-XRD, FT-IR, EDS and Raman supported the intercalative removal and de-intercalative release of the dye. It is believed that the concomitant proton exchange in the parent $KCa_2Nb_3O_{10}$ mediates the intercalation through an acid-base complexation of the protons of the layered perovskite with the amine group of the CR. Likewise, a strong complexation of the proton with the basic OH^- in the alkaline medium mediated its release. The above mechanism of CR removal is in line with earlier

reports of Methylene Blue intercalation on protonated-layered perovskites and the present study with the protonated forms of the Dion-Jacobson perovskite.

The work reported herein can further be extended to other series of layered compounds containing higher member of perovskite layers as well as their S-A hybrids. This may not only help in extending their visible-light absorption but also introduce interesting magnetic or multiferroic properties in them. This is envisaged based on their inherent dielectric nature due to the presence of d^0 transition metals together with the newly incorporated d^n metals in the structure. With appropriate valance manipulation of cations, coupled substitution of 4*d* and 5*d* transition metals can also be investigated. While some of the 4*d* and 5*d* metals as co-catalysts show enhanced photocatalytic activity, they may well be incorporated in the same structure and their effect on the catalytic and or photocatalytic property can be investigated.

Moreover, apart from dye degradation, other photocatalytic reactions or conversions, such as, water splitting, CO_2 reduction, peroxide generation etc. can also be investigated with the synthesized compounds reported herein. It is believed that the work reported here leaves many opportunities for future exploration. The demonstration of intercalative removal of pollutants is a quite new concept and may further be investigated in other systems to test its generality and other applications.